Hydrogen gas explosions in pipelines - modeling and experimental investigations

Vegeir Knudsen

Thesis submitted for the degree of Philosophiae Doctor.

Porsgrunn, December 2006.

Faculty of Technology
Telemark University College
Norway

Faculty of Engineering Science & Technology
Norwegian University of Science and Technology
Norway

Preface

The present work was carried out during the years from 2003 to 2006 at the Faculty of Technology, Telemark University College, Porsgrunn, Norway.

Acknowledgments Several persons have supported me in the work with this thesis and I would like to express my sincere gratitude to them.

First of all, I want to thank my supervisor Professor Dag Bjerketvedt for accepting me as his student and for introducing me to the field of combustion. His enthusiasm, great insight and clear thinking is greatly appreciated. I further want to thank my second advisor Doctor Randi Toreskås Holta for her assistance and constant interest in my work. The financial support from The Norwegian Defense Estates Agency and Strategisk Høgskole-program - The Research Council of Norway, is also gratefully acknowledged.

A special thank goes to my fellow Ph.D. student and laboratory companion Knut Vågsæther. Much of the experimental work was carried out in collaboration with him. A special thank also goes to Divisional engineer Talleiv Skredtveit, Senior engineer Hildegunn Hegna Haugen and Divisional engineer Eivind Fjelddalen, for their contribution to the experimental setup. I also want to thank M.Sc. Knut Tommy Løyland for assisting me in the experimental work with carbon monoxide.

It is a pleasure to thank both the administrative staff and colleagues at the Faculty of Technology, for providing a constructive and friendly working environment. Ole Kristian Sommersel and Nina Bjerkebo Brovig who have been my fellow Ph.D. students, deserve a special thank. Others that deserve to be thanked are the weight lifters in “Grenland Atletklubb”, the Center for Information Technology Services at the University of Oslo and M.Sc. Caspar Wohlfahrt.

I would in particular like to express my sincere gratitude to my partner and best friend Ingrid Fjøsne. Her support, understanding and encouragements have been of great importance for me.

Publications Two conference papers have been published. The first paper was presented at the European Combustion Meeting in Belgium 2005 and the second paper was presented at the First Baltic Combustion Meeting in Poland 2005. Both papers are given in Appendix A.

Porsgrunn, November 2006
Vegeir Knudsen

Abstract

Gas explosions in closed pipes with a single obstacle have been investigated both numerically and experimentally. Most of the work is related to hydrogen and air mixtures, but other fuels have also been used. At the present time there does not exist a software tool or a numerical method that single-handedly can cover the whole range of phenomena in gas explosions. Computational fluid dynamics is also a developing field, even for fluid flow without chemical reactions. The objective of this work was to develop numerical models that can be applied in predictive simulations of gas explosions in pipes and tunnels. Such predictive tools are important since they can expand the knowledge of gas explosions and thereby reduce the risk and consequences of gas explosion accidents.

The experiments were performed with premixed fuel and air at atmospheric conditions in three closed steel pipes. The pipes had an inner diameter of 107 mm and inner lengths of 3.0, 4.0 and 7.0 m. The various gas mixtures were ignited at the center of one end wall by a weak ignition source. Both the 4.0 and the 7.0 m pipe had an obstacle installed inside the pipe 1.0 m from the ignition wall. Four different fuels and seven different obstacles were used in the experiments. The obstacles had opening diameters ranging from 5 to 80 mm and the fuels were hydrogen, propane, methane and blends of hydrogen and carbon monoxide. Two types of Kistler pressure transducers were distributed along the pipes to measure the experimental overpressure. The experimental work has provided a unique data set which includes combustion regimes ranging from laminar flames to detonations. Several conditions which affect the flame propagation and transition to detonation in single obstructed pipes have been found.

The numerical work has been related to the one dimensional code RCMLAB. New numerical models have been developed and applied in the numerical simulations with this code. (The primary focus of these simulations were the flame propagation between the ignition wall and the obstacle.) The numerical simulations showed a high level of similarity between the measured experimental overpressure and the simulated overpressure at the various pressure transducer positions in the pipe. RCMLAB can therefore be used to enhance the understanding of gas explosions in pipes. Important parameters in the combustion process, such as the average burning rate, can be quantified by this numerical code. The numerical work performed in this thesis have also brought RCMLAB closer to becoming a predictive numerical code for simulation of gas explosions in pipes and tunnels.

Contents

Chapter 1

Introduction

Processing, transportation and storage of combustible gases or evaporating liquids, such as hydrogen and liquid propane, represents a potential hazard for fires and gas explosions [21, 156, 175]. A combustible mixture of fuel and air can be formed if the fuel is accidently released into the atmosphere or if air is allowed to enter the containment. The containment can for example be process equipment such as a storage tank or a transportation pipeline. From a safety point of view, the worst case scenario occurs when the fuel and the oxidizer have been mixed prior to ignition [21, 93]. Such premixed gases can under the right conditions experience a flame speed of more than 1.5 km/s and an explosion overpressure of more than 1.5 MPa.

1.1 Gas explosions

There appears to be no fixed definition of a gas explosion. Bjerketvedt et al. [21] point out that the term "gas explosion" is just one of several other names that are used for the phenomenon. Terms like "fuel-air explosion", "vapor cloud explosion" and "gaseous explosion" are also used in the literature. Bjerketvedt et al. [21] define a gas explosion as a process where combustion of a premixed gas cloud, i.e. fuel-oxidizer, is causing a rapid increase of pressure. Reference [172] on the other hand, describes a gas explosion as the sudden generation and expansion of gases associated with an increase in temperature and an increase in pressure capable of causing structural damage. As a comparison, a premixed combustion process which only produces negligible overpressure is referred to as a flash fire [21, 172].

1.1.1 Historical summary

This subsection presents a short historical summary of gas explosions in pipes. The summary is based on the literature review presented in Chapter 2 and the main focus is therefore directed towards studies where the premixed gas was ignited at a closed end of the pipe. The reader is further asked to look into Chapter 2 for definitions and additional information.

The first scientific studies of gas explosions in pipes were performed at the end of the 19th century. The work of Mallard and Le Chatelier [94] showed that a flame which is

ignited at the end wall of a long pipe with one open end, will propagate with inversions and that these inversions will be in the axial direction of the pipe. The first photographic pictures of inverted flame fronts were presented by Ellis [86] in 1928. Several explanations and discussions of inverted flame propagation have been presented over the years [100, 97, 2, 1], but Dunn-Rankin and Sawer [95] proposed that the inverted flame phenomenon is a combination of various processes. The experimental study of Ellis [86] also revealed that the initial flame propagation in a pipe consists of several stages and that the flame structure in these stages can be affected by the length of the pipe. Similar observations were done in the experimental study of Popov [87]. Popov's study [87] also showed that the flame speed in the radial direction right after the ignition, varied as the inverse of the pipe length for short and closed pipes. Studies of flame propagation in obstructed pipes have been performed by Combe et al. [88], Guénoche [2] and Evens et al. [89] among others. These experiments revealed that the mean axial velocity between the ignition wall and the obstacle generally is reduced, if the blockage ratio of the obstacle is increased. The schlieren photographs from the experimental study of Markstein [100] in 1956, showed that an interaction between a shock wave and a laminar flame could lead to the formation of an instable flame. But there also exists other flame instability mechanisms. Barrére and Williams [116] divide these mechanisms into phenomena that either are 1) a result of external influence or 2) a result of internal conditions in the flame.

Turbulent flame propagation in obstacle filled tubes have been studied by Dorofeev et al. [126] and Lee et al. [73], among others. These studies have shown that turbulent combustion can be divided into a quenching regime, a subsonic regime (slow turbulent flames) and a choked regime (fast turbulent flames). The studies of Dorofeev et al. [128] and Kuznetsov et al. [134], indicate that the final turbulent flame propagation regime (at a sufficiently large scale) mainly depends on the expansion ratio of the gas mixture. (The expansion ratio is the density of the unburned gas divided by the density of the burned gas.) They also suggested that the expansion ratio had to be above some critical value to achieve strong flame acceleration and a fast turbulent flame.

A transition to detonation has been observed in many situations. The first scientific studies of the phenomenon were also performed at the end of the 19th century [143, 94]. Stroboscopic schlieren records obtained in the experiments of Urtiew and Oppenheim [76] in 1966, indicated that the detonation starts as an "explosion in the explosion". Zeldovich et al. [68] presented in 1970 a theory that describes the onset of detonation through an ignition delay gradient in the unburned gas mixture. A similar theory was proposed by Lee et al. [74] in 1978. This theory is based on an induction time gradient and shock wave amplification by coherent energy release (SWACER). Several empirical criteria for a deflagration to detonation transition have been established as a result of the work of numerous researches. Such criteria are mostly related to the length scale of the containment and the reactivity of the gas mixture, such as the detonation cell size. Dorofeev [12] on the other hand, states that supersonic combustion should be developed before a transition to detonation is possible in areas with strong confinement and heavy obstructions.

There exists several computational fluid dynamics codes today that can perform predictive analysis of gas explosions. But it is important to keep in mind that these software packages only apply empirical models for the turbulent combustion. The various computational fluid dynamics codes should therefore be used with caution outside their area

Figure 1.1: A photograph from the hydrogen gas explosion that occurred at a Norwegian ammonia plant (Norsk Hydro Ammonia NI) in 1985 [22].

of validation [172]. Numerical simulations of flames are on the other hand a growing research area and it is a powerful tool that gives important contributions to our understanding of combustion [170].

1.1.2 Industrial Accidents

Industrial gas explosion accidents differ greatly in size and damage extent, but serious gas explosions occur worldwide every year [21]. There are also a large number of near accidents and minor gas explosions. Two examples of severe gas explosions are given below. A deflagration to detonation transition did most likely occur in these two incidents [22, 177] and this phenomenon is also an important subject in this thesis.

Porsgrunn, Telemark, Norway, 1985

A hydrogen gas explosion occurred at a Norwegian ammonia plant in 1985 [22]. The event started as a result of a mechanical failure in a water pump. The mechanical failure allowed hydrogen to be discharged from a nearby high pressure vessel and into a $100\times10\times7$ m^3 building. The hydrogen was discharged for approximately 20 or 30 seconds before the hydrogen and air mixture was ignited by a hot bearing. It has been estimated that the total amount of discharged hydrogen was from 10 to 20 kg. The explosion was very violent and it caused broken window glasses up to 700 m away from the explosion center. The explosion was followed by a large jet fire from the high pressure vessel. Two people later died from injuries caused by the explosion. A photograph of the buildings north side wall, is shown in Figure 1.1.

Port Hudson, Missouri, USA, 1970

A propane gas explosion occurred in Port Hudson, Missouri in 1970 [21]. (Port Hudson is also called the Franklin county.) The event started as a rupture in a pipeline which transported liquid propane. Large amounts of liquid propane were released from the ruptured pipe line and a combustible cloud of evaporated propane and air flowed into a valley. (Propane is more dense than air.) Approximately 20 minutes after the release had started, the unconfined gas cloud exploded violently. Houses within a radius of about 3.2 km were extensively damaged [176]. The explosion started most likely in a concrete block warehouse [177].

1.1.3 Hydrogen and the future

Large quantities of hydrogen are produced in the industry today (e.g. in the production of ammonia and in refineries), but hydrogen is not commonly used for non-industrial energy purposes. This will most likely change in the future. It is both a Norwegian [178, 179], a European [181] and an international [180] political strategy to make hydrogen the energy carrier of the future. This strategy is mostly founded on the need of a reduction of the local and global pollution problems, but also on the need of a more reliable and independent energy supply. The introduction of hydrogen as an energy carrier for the general public, will on the other hand make great demands on all aspects of safety. This can be illustrated by the matrix shown in Figure 1.2, which outlines the structuring of the work performed by HySafe [181] to facilitate a safe introduction of hydrogen as an energy carrier. A wider knowledge of the explosion characteristics of hydrogen, will in this regard be an important contribution to the development of codes, standards and regulations related to hydrogen safety.

1.2 Specific objectives

A one dimensional numerical code named RCMLAB [17, 18] has been developed at Telemark University College. This code was created with the intention of 1) to make a tool for simulation of gas explosions in pipes and 2) to develop a model for deflagration to detonation transition. Kristoffersen et al. [23, 24] have previously used RCMLAB to simulate deflagrations in unobstructed and partly closed pipes. They used premixed propane and air and premixed acetylene and air at various equivalence ratios.

The main objective of this work was to develop numerical models that could be used with RCMLAB to simulate flame acceleration and transition to detonation in obstructed pipes. Various gas explosion experiments were therefore performed in closed and single obstructed pipes to create a set of data for validation of the numerical simulations. But the first phase of this work revealed that more knowledge of the initial stages of the explosions were necessary before the transition to detonation phenomenon could be modeled numerically. The primary focus of both the numerical and the experimental work has therefore been to see how the flame propagation between the ignition wall and the obstacle in this type of confinements is affected by the obstacle opening diameter. Most of the work is related to hydrogen and air mixtures since 1) hydrogen and air mixtures

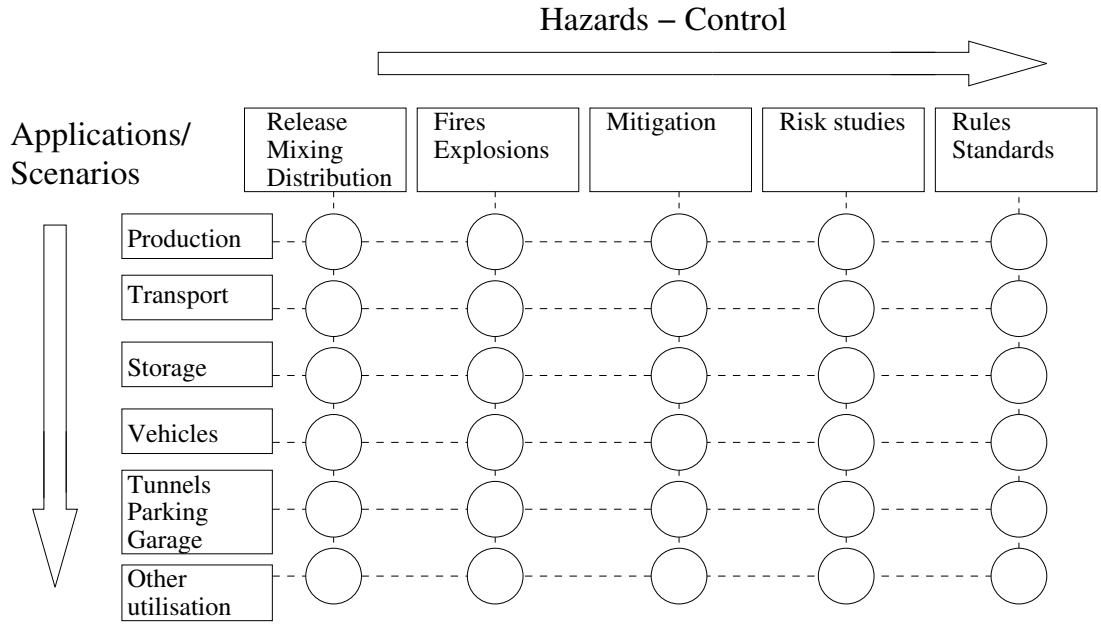

Figure 1.2: An activity matrix that illustrates the structuring of the work performed by HySafe [181, 182].

detonates relatively easy and 2) more knowledge of the explosion characteristics of hydrogen and air mixtures is needed. Our knowledge of gas explosions and DDT is limited and there does not exist a set of general criteria which, if they are met, can state that a DDT necessarily will occur. Both dispersion, ignition, flame acceleration and DDT are important events in gas explosions. In the presented work only factors related to flame acceleration and transition to detonation are studied. Other fuels than hydrogen, have also been used in this thesis. These fuels were used to make references to the hydrogen and air gas explosions within the same geometry.

Kristoffersen et al. [23, 24] used experimental pressure records together with RCM-LAB to estimate the burning velocity of deflagrations in pipes. An objective of this thesis has also been to investigate if the burning velocity estimation method applied by Kristoffersen et al. [23, 24] can be used to characterize different fuels.

1.3 Document structure

This document consists of five chapters. The various chapters are further divided into sections and subsections. Some of the subsections are also divided into sub subsections, but these are neither included in the numbering scheme of the document nor shown in the table of contents.

Chapter 1 outlines the background and motivation for this work. Chapter 2 presents a literature review on gas explosions in pipes, whereas Chapter 3 gives a description of the experimental setup and a presentation of the experimental results. The numerical work is presented in Chapter 4 and the conclusions with some recommendations for future work are presented in Chapter 5.

Chapter 2

Review on gas explosions in pipes

This chapter gives a selective review on gas explosions in pipes. A short introduction to the chapter is given Section 2.1. Some basic theory on the different premixed combustion regimes are given in Section 2.2. Section 2.3 gives a presentation of flame propagation experiments in pipes and Section 2.4 gives a presentation of Computational Fluid Dynamics (CFD) codes used in gas explosion simulations.

2.1 Introduction

Numerous experiments have shown that a flame, which is initiated by a weak ignition source in a pipe, in most practical cases will have a positive flame acceleration. Even though this increased burning rate is a result of complicated interactions between turbulence, chemical reactions and the compressible flow at a variety of length and time scales, most of the mechanism is qualitatively well understood. The expansion of the hot reaction products can lead to various flame instabilities and create a turbulent flow in the unburned gas right in front of the flame. These mechanisms increase the flame acceleration by increasing both the flame surface area and the local transport of heat and reactants in the reaction zone. Since an increase in the burning velocity results in an increase of the turbulence in the unburned gas flow, a positive feedback loop is established between the turbulence and the reaction zone. The result is a continuously accelerating flame which under the appropriate conditions can undergo a transition from deflagration[1] to detonation[2]. Obstacles of various kinds are known to increase the flame acceleration and the probability of a transition to detonation. Dorofeev [12] states that confinements and obstructions provide the most effective means for the flame acceleration and the development of hazardous explosion regimes. A firmer discussion of the various stages that occur during the flame acceleration process in a premixed gas from the ignition to the transition to detonation, is given in Section 2.3. The main focus has been directed towards gas explosions in closed or partly closed pipes.

[1] A deflagration is a combustion process where the flame propagation is sub sonic relative to the unburned gas right in front of the flame. This includes both laminar and turbulent combustion.

[2] A detonation is a combustion process where the flame propagation is super sonic relative to the unburned gas right in front of the flame.

2.2 Premixed combustion

This section gives an overview of the different regimes in premixed combustion. These regimes are further related to gas explosions in pipes in Section 2.3. Subsection 2.2.1 describes the ignition process and Subsection 2.2.2 describes the laminar combustion. Then Subsection 2.2.3 describes turbulent combustion and Subsection 2.2.3 describes detonations.

2.2.1 Ignition

A combustible gas mixture, which would not ignite by itself, can be ignited locally by an ignition source. This process is called an induced [49] or a forced [50] ignition. The principle is to raise a small volume of the mixture to a high enough temperature so that auto ignition can take place. The raised temperature must be high enough to cause a continued flame propagation even after the energy source is removed. An electrical spark is the most common type of an igniter. But also other energy sources like hot inert gases, hot surfaces, glow plugs, pilot flames, lasers, explosive charges and shock waves can be used.

Williams [40] relates the strength of the ignition source to the temperature raise caused by the source. The amount of released energy into the mixture also determines the combustion regime that is initiated by the source. In some extreme cases may a strong ignition source like a high explosive lead to a direct initiation of a detonation. Only a weak ignition source which initiates a laminar combustion process, is used in this work.

2.2.2 Laminar flame

The premixed laminar flame structure consists of several zones. Figure 2.1 shows the profile of a plane, stationary and premixed methane and air flame that is perpendicular to the unburned gas flow [62]. The first part of the flame is the preheat zone which is chemically inert. The rest of the flame is build up by several reaction layers. The first reaction layer is the inner layer. This reaction layer consumes the fuel and keeps the reaction process alive. The inner layer also consumes the radicals (i.e. molecules with an unpaired electron) by chain branching reactions and produces CO and H_2. The oxidation layer then oxidizes CO and H_2 to CO_2 and H_2O. Other consumption layers also exist, but they are omitted here.

In Figure 2.1 T_u is the temperature of the unburned gas, T_0 is the temperature of the inner layer, T_b is the temperature of the burned gas and δ_L is the characteristic flame thickness. The inner layer thickness δ_δ is a fraction δ of the flame thickness and can be written as $\delta_\delta = \delta \cdot \delta_L$. Correspondingly the oxidation layer thickness can be written as $\delta_\varepsilon = \varepsilon \cdot \delta_L$. A definition of the flame thickness is given by Peters [10, 11] as

$$\delta_L = \frac{(\lambda/c_p)_0}{(\rho \cdot S_L)_\mathrm{u}}, \tag{2.1}$$

where $(\lambda/c_p)_0$ is the heat conductivity divided by the specific heat capacity at the inner layer temperature T_0 and $(\rho \cdot S_L)_\mathrm{u}$ is the product of the density and the laminar burning

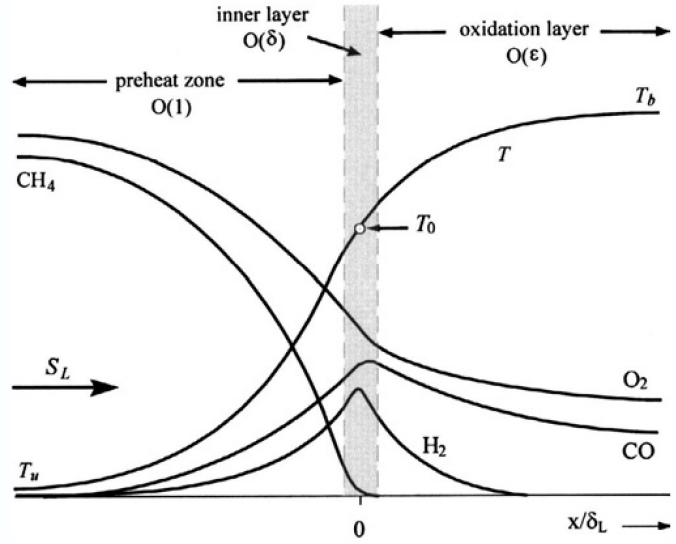

Figure 2.1: The structure of a premixed methane and air flame [62].

velocity of the unburned gas. The burning velocity is the flame speed relative to the unburned gas right in front of the flame. Peters [11] has estimated that the flame thickness δ_L of a stoichiometric methane and air flame at 1.0 atm is 0.175 mm and that the corresponding δ is 0.1. The size of the oxidation layer is often three times the size of the inner layer. A stoichiometric mixture of fuel and air for hydrocarbons generally has a laminar burning velocity of about 0.4 - 0.5 m/s, but a stoichiometric mixture of hydrogen and air has a burning velocity of approximately 2.5 m/s. The burning velocity depends on the fuel type, mixture ratio, pressure and temperature [56].

2.2.3 Turbulent flame

The interaction between a flame and a turbulent premixed gas flow depends on the length and the time scales of both the flame and the turbulent flow. The length scale of the flame can be given as the laminar flame thickness δ_L and time scale of the flame can be given as the laminar flame thickness divided by the laminar burning velocity, i.e. $\tau_L = \delta_L / S_L$. The turbulent flow on the other hand is a continuous distribution of length and time scales. The integral length scale l_0 is the dimension of the largest turbulent eddies which are less than the characteristic length scale L of the confinement. The Kolmogorov length scale l_k, represents the dimension where the smallest turbulent eddies are dissipated by viscosity into thermal energy. The corresponding time scales for the integral and Kolmogorov length scales, i.e. the eddy turnover times, are denoted as τ_0 and τ_k.

The effects of turbulent flow on premixed combustion, can be summarized in a diagram of combustion regimes. Such diagrams are commonly called Borghi diagrams and Figure 2.2 shows an example of a Borghi diagram after Warnatz et al. [49]. This diagram is a double logarithmic plot where the vertical axis has the *rms* value of the velocity fluctuations u' (i.e. the turbulence intensity) divided by the laminar burning velocity. The horizontal axis has the integral length scale divided by the laminar flame thickness. This diagram consists of five combustion domains. The next paragraph contains just a brief

discussion of the various domains. Because of the large spectrum of scales in turbulence, a flame is most likely best represented by a region in a Borghi diagram, rather than a single point. Some examples of other types of Borghi diagrams can be found in Reference [10, 50, 40, 64].

In Figure 2.2 the domains with turbulent combustion are separated from the laminar flame domain by the line $\mathrm{Re_T} = 1$. $\mathrm{Re_T}$ is the turbulent Reynolds number and it is defined by Reference [49] as $\mathrm{Re_T} = [(u' \cdot l_0 \cdot \rho)/\mu]^2$. The first turbulent domain has $u' < S_L$. This means that the turbulent intensity u' is smaller than the laminar burning velocity S_L. The turbulence is therefore slow compared to the flame advancement and the turbulence only wrinkles the flame. Two other lines, $\mathrm{Ka} = 1$ and $\mathrm{Da} = 1$, are also used to separate the turbulent combustion domains. Ka is the turbulent Karlovitz number defined as $\mathrm{Ka} = \tau_L/\tau_k$ and Da is the turbulent Damköler number defined as $\mathrm{Da} = \tau_0/\tau_L$. If $\mathrm{Ka} < 1$ and $u' > S_L$, then the flame thickness is smaller than the Kolmogorov eddies and the turbulent intensity is larger than the laminar burning velocity. This kind of turbulence wrinkles the flame in such a way that one part of the flame front interacts with another part of the flame front. This interaction creates pockets of unburned and burned gas. Peters [10] calls this domain, the corrugated flamelets domain. If $\mathrm{Ka} > 1$ and $\mathrm{Da} > 1$, then the Kolmogorov eddies are smaller than the flame thickness. Since the smallest vortices now are able to modify the inner flame structure, the flame can no longer be a laminar flame front. If the flame stretch caused by the Kolmogorov eddies also becomes too large, then there will be a local quenching of the flame front. This domain is known as the distributed reaction zone domain or the torn flame fronts domain. The last domain in Figure 2.2 has $\mathrm{Da} < 1$. This means that the chemistry is relatively slow compared to the turbulence intensity. Even the larger eddies are embedded in the reaction zone and they are faster than the laminar burning velocity. This situation gives well stirred combustion.

2.2.4 Detonation

Deflagrations are combustion processes where the flame propagation velocity relative to the unburned gas right in front of the flame, are subsonic. This includes both laminar and turbulent combustion. The combustion process in a deflagration is dominated by molecular and turbulent transport processes, i.e. the nature of the turbulent flow relative to the mixture properties. Detonations are on the contrary combustion processes with supersonic flame propagation. A detonation consists of a lead shock followed by a reaction zone. The lead shock compresses and heats the unburned gas. This causes the premixed gas to auto ignite after an induction time τ_d. The rapid heat release caused by the chemical reactions expands the gas and the expansion process supports the lead shock. This creates a coupling between the lead shock and the reaction zone. A detonation is therefore a self sustaining process.

Mathematical predictions of the detonation velocities v_{CJ} can be made with the classical model of Chapman [65] and Jouguet [66]. This model treats the detonation wave as a one dimensional reacting discontinuity, i.e. as a control volume where the lead shock is directly followed by a reaction zone with infinitive reaction rate. The one dimensional conservation equations (see Equation 4.16, 4.17 and 4.21 in Subsection 4.2.2) are used together with the assumption that the burned gas velocity right behind the detonation is

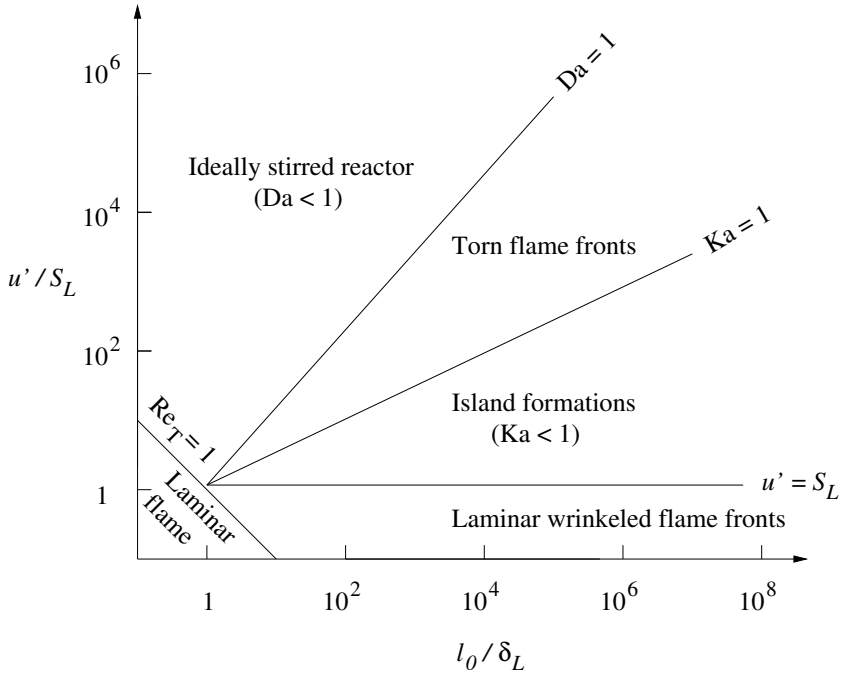

Figure 2.2: Borghi diagram after Warnatz et al. [49]. u' is the turbulence intensity, S_L is the laminar flame burning velocity, l_0 is the integral length scale and δ_L is the laminar flame thickness.

sonic. The applied reference frame defines the unburned gas flow to be in the direction towards the detonation and that the detonation wave is locked in space (i.e. zero velocity). The Chapman-Jouguet theory (CJ theory) also relates the burned states in a CJ detonation to be the tangential intersection of the Rayleigh line on the Hugoniot curve. Even though there are no knowledge of the chemical kinetics in the model, there is still good agreement between experimental and theoretical detonation velocities [50].

Another classical model for detonations is the model of Zeldovich [67], von Neumann [70] and Döring [71] (ZND). As in the CJ theory, the detonation wave is assumed to consists of a planar lead shock which propagates with the CJ velocity. But the ZND theory assumes a finite reaction rate. Some knowledge of the chemical kinetics is therefore required. It is the rate of the chemical reactions that gives the induction distance l_e between the lead shock and the reaction zone.

Both the CJ and the ZND model assume that the detonation front are one dimensional and planar. But numerous experiments have shown that the detonation front is three dimensional and strictly instable. The instability is created by secondary shock structures that propagate transversally to the main front. These transverse waves collide with each other in a periodically manner and makes the detonation front oscillate. The junction between a transverse wave and the lead shock is called a triple point. Several studies, such as the pioneering work performed by Denisov and Torsin [108, 109, 110] and Voitsekhovsky et al. [111], have shown that the characteristic patterns observed on soot foils in gaseous detonation experiments are created by the triple point regions in the lead shock[3]. The soot

[3]Section 3.2 in Reference [112] gives a historical review on the soot track method.

foil inscriptions are therefore the triple points trajectories, but the exact mechanism that creates the inscriptions is not known. If the soot foil is directed in the overall direction of the detonation, for example on the pipe wall in tube, then the detonation can create a regular cell pattern similar to the one shown in Figure 2.3. The length of such cells are L_c and the hight (or width) are λ_d. The hight of the cells are also referred to as the cell size and they are used as a length scale to describe detonations.

A cell apex is created by the collision between two triple points. Such collisions increase the heat and the pressure in the neighboring gas and the lead shock becomes locally strengthened and overdriven. Figure 2.3 also shows the structure of the lead shock at two different times during the cell cycle for cell number III. At the time t_1 the triple points are moving away from each other and the lead shock decays and becomes less curved as it approaches $L_c/2$. The lead shock is called a Mach stem in the first half of the cell cycle. When the triple points are close to $L_c/2$ they collides with neighboring triple points. These collision marks the beginning of neighboring cells and they create new Mach stems outside cell III. This last event also changes the lead shock in cell III from a Mach stem shock to an incident shock. The rest of the cell cycle is dominated by the transient waves that are approaching each other and the decaying lead shock. Even though the lead shock velocity changes through the cell cycle, the average propagation velocity is still the CJ detonation velocity v_{CJ}. Lee [72] has reported that the lead shock may have a propagation velocity that is 1.6 times the CJ detonation velocity at the beginning of the cell cycle and 0.6 times the CJ detonation velocity at the end of the cell cycles.

The upper right corner in Figure 2.3 shows a triple point where the transverse shock is propagating downwards. The illustration is a simplified version of a double Mach reflection model after Lee [72]. The triple point is at the junction between the transverse shock, the Mach stem shock and the incident shock. Both the Mach stem shock and the incident shock are strong enough to cause chemical heat release in the premixed and unburned gas. But the Mach stem shock is stronger than the incident shock and the induction length l_e between the lead shock and the reaction front is therefore shortest for the Mach stem shock. The transverse shock which propagates with almost the speed of sound in the hot products, is too weak to cause chemical heat release. According to Williams [40], even the incident shock in a self sustaining detonation may not be sufficiently strong to initiate chemical heat release in the time avaliable.

The classical ZND model together with constant volume processes have been used by Westbrook [78] in calculations of the induction length l_e. These calculations show proportionality to the experimental cell sizes only for a limited range of gas mixtures. A linear relationship like $\lambda_d = A \cdot l_e$ [77], where A is a fuel specific constant, is therefore generally not well suited to make detonation cell size calculations. Measurements from soot foils are used instead to determine the detonation cell sizes. But the accuracy of the cell size measurements may be uncertain because of poor regularity in the cell pattern [91].

2.3 Gas explosions in pipes

Breitung et al. [63] have divided the possible stages of a gas explosion into five combustion regimes. These regimes are shown in Figure 2.4. The exact development of a gas

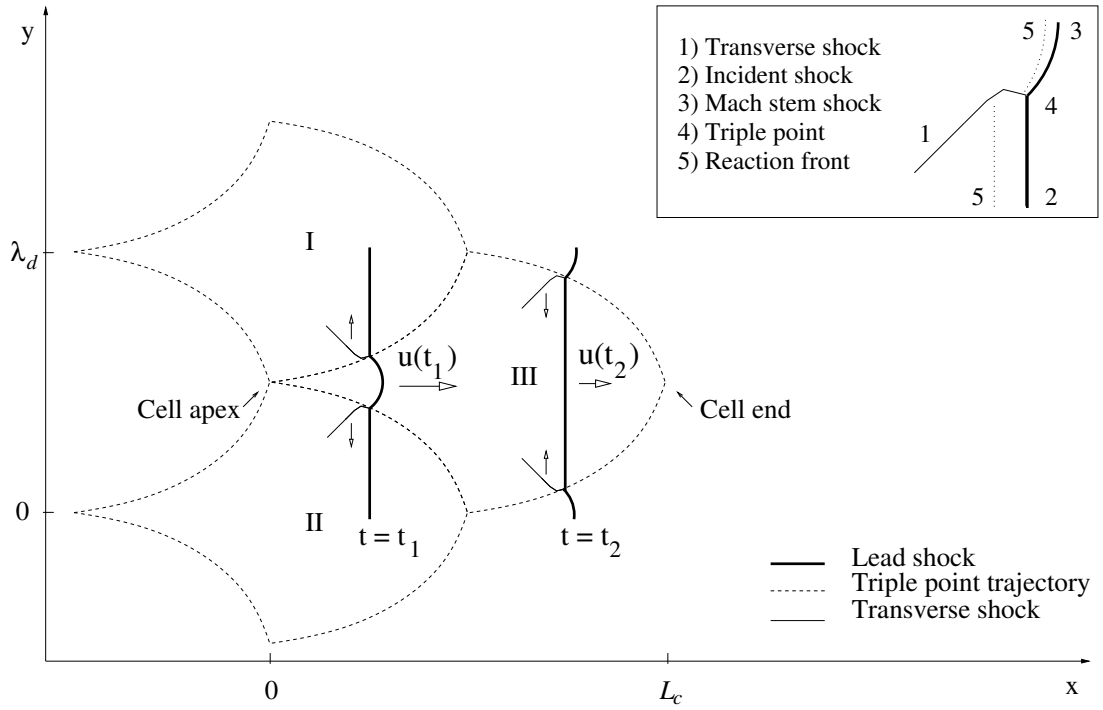

Figure 2.3: Triple point trajectories and the structure of the lead shock at two different times during one cell cycle. This illustration has been based on the descriptions of the detonation front presented by Reference [21, 40, 60, 50, 72].

explosion depends on both the gas mixture properties and the confinement geometry. If a combustible gas mixture is ignited by a weak ignition source, then the first phase of the flame propagation is laminar. The flame speed (i.e. relatively to a fixed observer) in this initial phase, depends only on the laminar burning velocity and the expansion ratio. The expansion ratio is given as

$$\sigma = \frac{\rho_{\mathrm{u}}}{\rho_{\mathrm{b}}} \,, \tag{2.2}$$

where ρ_{u} is the unburned density and ρ_{b} is the burned density. But the combustion induced gas flow together with the discontinuities over the flame, makes the flame intrinsically unstable. The result is a wrinkled or cellular flame structure. This third combustion regime occurs relatively shortly after the ignition. The flame wrinkling increases the burning rate because of an increased flame surface area. But even though the burning velocity at this stage in the explosion may become several times larger than the laminar burning velocity, the flame acceleration is still slow [12].

The fourth combustion regime in Figure 2.4 involves turbulent combustion. The turbulence is created in the combustion induced flow by the confinement and/or obstacles. Obstacles like orifice plates are often used in gas explosion experiments to increase the turbulence. The turbulence enhances the burning velocity by increasing both the flame surface area and the local transport of energy and mass in the reaction zone. The enhanced burning velocity will then increase the velocity of the combustion induced flow and therefore increase the turbulence in the flow. The result is a positive feedback loop

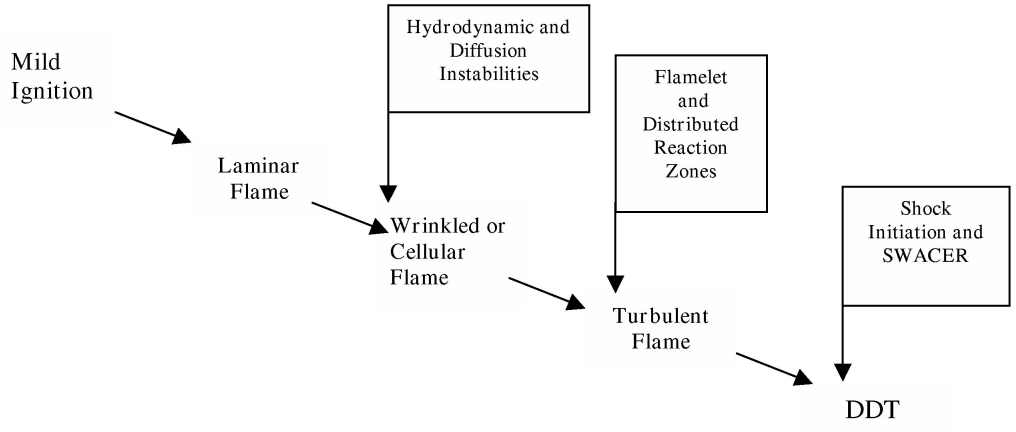

Figure 2.4: The various combustion regimes between the ignition and the transition to detonation in a premixed gas explosion [63].

which gives a continuous flame acceleration. But the positive flame acceleration process is not unlimited. A too high turbulence intensity will reduce the burning velocity. The reduced burning velocity is caused by a too large flame stretch and a too rapid mixing of the hot burned gas with the cold unburned gas. A local quenching of the flame is possible if the temperature in the reaction zone becomes too low. It is these two competing effects of turbulence, i.e. an increase or a reduction of the burning rate, that lead to the maximum turbulent burning velocity $S_{T,M}$. Shy et al. [79] found the magnitude of $S_{T,M}$ to be ten times the laminar burning velocity for both propane and air mixtures and for methane and air mixtures. But this result is almost a factor of two smaller than the one that was found by Bradley et al. [80][4]. Obstacles may also have a non turbulent related "geometrical" effect on the flame propagation. The flow around obstacles increases the flame surface area. The increased flame surface area will increase the combustion induced flow around the obstacle and the result is a positive feedback loop which gives a continuous flame acceleration. This "geometrical" effect also contributes to the overall flame propagation in both the wrinkled flame regime and the turbulent flame regime.

Abdel-Gayed et al. [81] have studied the turbulent burning velocity S_T of premixed fuel and air at various equivalence ratios in a fan stirred bomb. Figure 2.5 shows the turbulent burning velocity of premixed propane and air as a function of the turbulent intensity u'. The figure shows that S_T increases initially with increasing u' and reaches a maximum before it starts to decrease again. The termination of the curve indicates that the flame was quenched for higher turbulent intensities and the shadings in the figure indicates the quenching regions. Abdel-Gayed et al. [81] did also perform experiments with premixed hydrogen and air, but those experiments are less illustrative because no quenching occurred.

Dorofeev [12] includes two critical branching points for the turbulent combustion regime in areas with strong confinement and heavy obstructions. The first branching point distinguishes between weak and strong flame acceleration, where the weak flame

[4]Bradley et al. [80] based their calculations of $S_{T,M}$ on the measurements of S_T in Reference [82, 83].

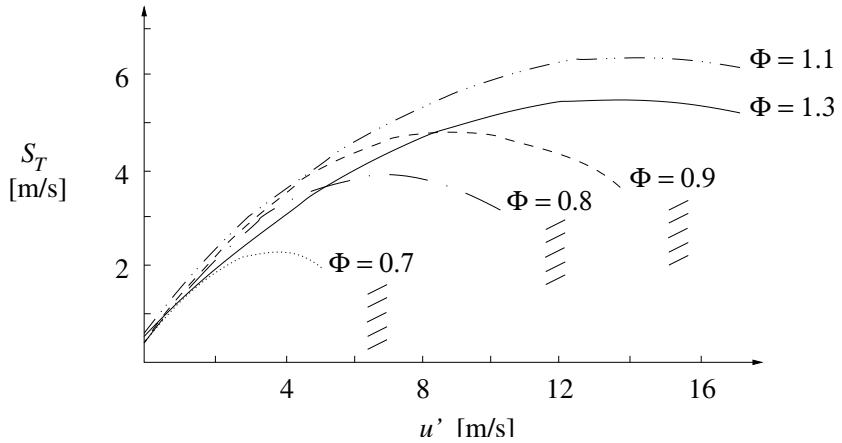

Figure 2.5: Turbulent burning velocities after Abdel-Gayed et al. [81] at five equivalence ratios of premixed propane and air. The burning velocities are given as a function of the turbulent intensity and the shadings shows the quenching regions.

acceleration gives a subsonic flame propagation and a strong flame acceleration gives a supersonic flame propagation. The supersonic flame propagation consists of a single or several lead shocks and a turbulent flame brush. But such supersonic flames are still dominated by molecular and turbulent transport processes as in ordinary deflagrations. The second branching point states that if these supersonic deflagrations are given the right conditions, then they might experience a deflagration to detonation transition. A deflagration to detonation transition is also the last combustion regime in Figure 2.4.

2.3.1 Initial flame propagation in pipes

This subsection describes the initial stages of gas explosions in pipes. The subsection is divided into four parts. The first part describes the initial flame propagation in unobstructed pipes, whereas the second part describes the initial flame propagation in obstructed pipes. Only closed or partly closed pipes where the ignition of the premixed gas is done at the center of an end wall, are considered. The two last parts of this subsection describe different flame instabilities that might occur during the laminar flame propagation.

Unobstructed pipes

Clanet and Searby [1] have used a high speed camera together with pressure transducers to study flame propagation in circular pipes with one open end. They used premixed propane and air at various equivalence ratios and ignited the gas mixtures at the closed end of the pipe. According to this study the flame propagation can be divided into four stages. The first stage starts right after the ignition and has a small flame which propagates hemispherically. The expansion of the flame is isotropic. The flame is quenched at the contact surfaces with the end wall, but it is unaffected by the presence of the pipe wall in the radial direction. As the flame gets closer to the pipe side wall, it will at some point experience a reduced radial flame speed because of the hindering of the flow of the

unburned gas in the radial direction [2]. This event marks the beginning of the second stage. A formula that predicts the time t_h at which stage one ends, is presented by Clanet and Searby [1] as

$$t_h = \frac{D_p}{2S_L} \cdot (0.1 \pm 0.02), \tag{2.3}$$

where D_p is the inner diameter of the pipe and S_L is the laminar burning velocity.

In the second stage of the flame propagation the flame shape is changing from a hemisphere to an elongated semi ellipsoid. This change in the flame shape is caused by a higher flame speed in the axial direction than in the radial direction. In the literature, this flame structure is also referred to as a finger shaped flame. The second stage lasts until the flame reaches the pipe wall in the radial direction. Both the axial velocity of the flame tip and the pressure have an exponential growth during this stage. The time t_w at which the flame reaches the pipe wall in the radial direction, is given by Clanet and Searby [1] as

$$t_w = \frac{D_p}{2S_L} \cdot (0.26 \pm 0.02). \tag{2.4}$$

The relative error in this equation is in the order of five percent.

During the third stage of the flame propagation, the flame surface area is decreasing as a consequence of the quenching of the flame at the contact surfaces with the pipe side wall. The reduced flame surface area also reduces the flame speed and initiates a flame inversion process. This flame inversion process will be discussed more firmly in part three of this subsection. The time at which the actual inversion occurs, was also fund by Clanet and Searby [1] to be only a linear function of the pipe diameter and the laminar burning velocity. The equation can be written as

$$t_i = \frac{D_p}{2S_L} \cdot (0.33 \pm 0.02). \tag{2.5}$$

Clanet and Searby [1] have also made a first order model to the flame tip position x_f during the initial flame propagation. This model is based on a geometrical approximation of the flame shape. The model assumes that the flame surface area can be represented by a cylinder and a hemispherical tip. The equation can be given as

$$x_f = \frac{D_p}{2} \cdot e^{(t-t_h)/\tau}, \quad t \ \in < 0, t_w > \tag{2.6}$$

where $\tau = D_p/(4\sigma S_L)$ and σ is the gas expansion ratio given by Equation (2.2). This formula shows good approximation with the experimental data and gives that the trajectory of the flame tip x_f is exponential for times between t_h and t_w.

The fourth stage of the flame propagation is related to the continuing flame propagation after the first inversion process. This stage of the flame propagation depends on the pipe geometry and the properties of the gas mixture. The flame may be dominated by acoustic effects and propagate both as a fast turbulent flame or as a slower oscillating flame.

Slow and oscillating flames with several following flame inversions, have been reported by Schmidt et al. [84]. They used a steel pipe with four windows and one open

end. The pipe had a quadratic cross section area of 576 mm^2 and a length of 1.09 m. Based on schlieren photographs, they related the initiation of the turbulent combustion regime to the turbulence generated in the unburned gas flow at the pipe side walls. In one of the experiments they measured the flame speed, i.e. relative to the pipe wall, to be 50 m/s in a stoichiometric mixture of propane and air. They further proposed that more than 90 percent of this flame speed was due to the combustion induced flow of the unburned gas mixture.

Jones and Thomas [85] have studied flame propagation in premixed natural gas and air. They conducted their experiments in a long rectangular pipe with one open end. These experiments were further analyzed based on both pressure measurements and flame front motions. The flame front motions were measured by photodiodes. Jones and Thomas [85] observed an oscillating flame propagation and proposed that the oscillations were caused by acoustic interactions. They also observed rapid flame accelerations and related them to the turbulence generated by the interaction between the propagating pressure waves and the density discontinuity at the flame front. It was further concluded by Jones and Thomas [85] that the shear generated turbulence may play a role in the overall flame acceleration.

Closed and obstructed pipes

The four flame propagation stages discussed in the previous paragraphs, were described for a simplified quasi constant pressure configuration in a half open pipe. How is the initial flame propagation affected if the pipe is closed at both ends and/or if an obstacle is placed inside the pipe? Because of the numerous possible combinations of pipe geometries, premixed gas properties and obstacle configurations, only some general effects are pointed out here.

Ellis [86] used premixed carbon monoxide and oxygen to study flame propagation in pipes closed at both ends. The pipes had an inner diameter of 50 mm and lengths of 95, 120, 170 and 195 mm. A stroboscopic picture of the flame propagation from an experiment in the 170 mm long pipe, is shown in Figure 2.6. This picture shows that the flame grows out as a hemisphere after it has been ignited at the left end wall. But as the flame approaches the side wall of the pipe, it is elongated into a finger shaped flame. The flame is then quenched at the contact surfaces with the side wall of the pipe. This quenching process rapidly flattens the flame before it becomes inverted, i.e. concave towards the unburned gas. The flame then stays inverted through out the rest of the combustion process. This development is similar to the flame propagation stages described by Clanet and Searby [1]. The experiments of Ellis [86] did further show that the length of a closed pipe could influence the structure of the flame also during the first stages of the flame propagation. But since pipes unlike discs have a radius which is smaller than the pipe length L, i.e. $D_p/2L \ll 1$, the first stage of the flame propagation in pipes is unaffected by the pipe length. (Remember that it is the influence of the pipe side wall on the flame that ends the first stage of the flame propagation.) A short pipe may on the contrary influence the rest of the flame propagation. In the second stage of the flame propagation, where the flame is an elongated semi ellipsoid, the end wall in front of the flame will impede the axial propagation of the unburned gas. Guénoche [2] states that the effects of the impeded gas flow in a short pipe, are a less elongated flame, a reduced axial flame speed and a smaller

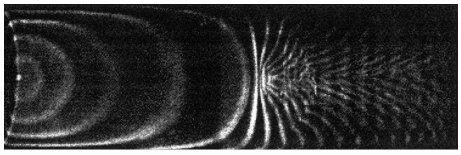

Figure 2.6: Flame propagation in a closed pipe filled with premixed carbon monoxide and oxygen. Stroboscopic image by Ellis [86].

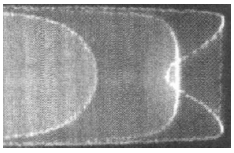

Figure 2.7: Flame inversion in a partly closed pipe filled with premixed propane and air. High speed video photographs by Clanet and Searby [1].

flame surface area than in a longer pipe. On the contrary, if the pipe is long enough, then the initial flame development will be independent of the pipe length.

Popov [87] did also use premixed carbon monoxide and oxygen at various equivalence ratios to study flame propagation in closed pipes. The pipes in these experiments had a diameter of 50 mm and lengths L ranging from 0.24 to 2.25 m. Popov's study [87] showed that the flame speed in the radial direction varies as $1/L$ for short pipes. As an example, the flame did reach the pipe side wall approximately 1.2 times faster in the 0.24 m pipe than it did in the 2.25 m pipe.

If a device which will affect the flow of the gas, i.e. an obstacle, is installed in the pipe, then the effect of the device on the flame propagation will be drastic [2]. Only pipe configurations where the obstacle has a centered flow passage will be considered here. Combe et al. [88] have studied the flame propagation in obstructed pipes. They used premixed benzene (C_6H_6) and air in a closed pipe. The pipe had a total length of 970 mm and consisted of two tubes connected together by a centered channel. The two tubes had a diameter of 52 mm and lengths of 200 and 745 mm. The interconnecting channel, which can be regarded as the obstacle, had a length of 25 mm and diameters of 0, 4, 8, 11, 25 and 52 mm. This gives blockage ratios[5] ranging from 0 to 100. The premixed gas was further ignited at the end wall of the 200 mm long tube and the flame propagation was filmed with a drum camera. These experiments showed 1) that the axial flame speed towards the obstacle decreased and 2) that the maximum axial flame speed was reached closer to the ignition wall, when the obstacle opening diameter decreased. According to Guénoche [2] these two effects will also occur if the blockage ratio of the obstacle is held constant and the distance between the obstacle and the ignition wall decreases. But this development requires that the distance between the obstacle and the ignition wall is larger than the position of the flame tip x_f at the time t_w when the flame reaches the pipe side wall for the case without a constriction.

Figure 2.8 shows a schematic comparison of the flame shape between the ignition wall and an obstacle at three different times for a given pipe at four different obstacle configurations [2]. The premixed gas is ignited at the center of the lower end wall in all the four configurations. In situation '(a)', '(b)' and '(c)' the distance between the ignition wall and the obstacle is unchanged, but the obstacle opening area increases from '(a)' to '(c)'. The constriction in front of the flame hinders the flow of unburned gas in the axial direction. The level of constriction depends on the obstacle opening diameter and the

[5]See Equation (3.1) for an example on how to calculate the blockage ratio for a circular pipe with a circular obstacle opening.

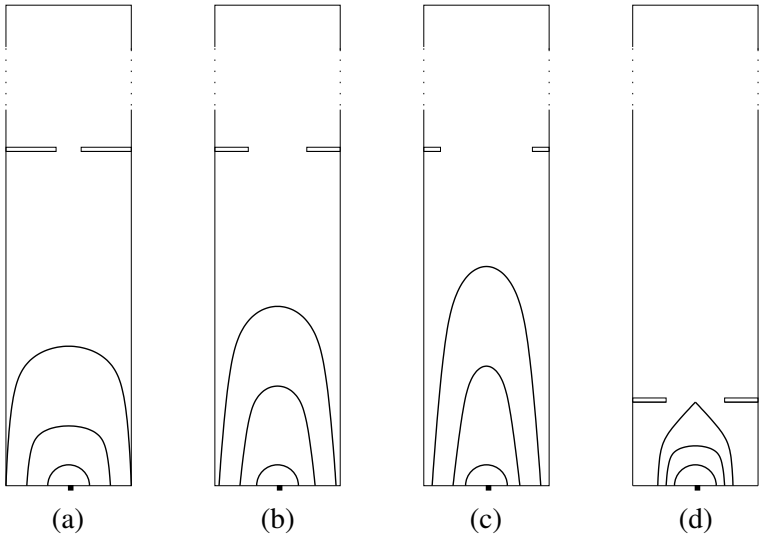

Figure 2.8: Flame shapes illustrations after Guénoche [2]. Situation '(a)', '(b)' and '(c)' has the same distance between the ignition wall and the obstacle, but the blockage ratio of the obstacles is different. In situation '(d)' the distance between the ignition wall and the obstacle is short.

constriction is strongest for the smaller opening areas. As for the situation in a short and closed pipe described in the previous paragraph, the flame will reach the pipe wall sooner and get a reduced flame surface area for the smaller obstacle opening areas. The mean axial flame speed of the flame tip is also reduced with a reduced obstacle opening area. It is important to keep in mind that for sufficiently short pipes also the end wall on the opposite side of the obstacle might affect the flame propagation between the ignition wall and the obstacle.

In Situation '(d)' in Figure 2.8, the distance between the ignition wall and the obstacle is short. This means that the flame tip x_f reaches the obstacle x_o before the flame skirt reaches the pipe side wall, i.e. $t_o < t_w$ where t_o is the time when the flame reaches the obstacle. The short distance between the obstacle and ignition wall causes an elongation of the flame in the axial direction when the flame is close to the obstacle. The elongation occurs mainly in the parts of the flame that is close to the center of the pipe. Illustration '(d)' is made according to the high speed schlieren filming images presented by Evens et al. [89]. They used both premixed propane (C_3H_8) and air and premixed n-butane (C_4H_{10}) and air in a squared Pyrex pipe. The dimensions of the pipe were, after being transformed from inches, approximately $1.83 \times 0.09 \times 0.09$ m^3. The obstacle, which was a grid of three rectangular nozzles placed in line, was installed 79 mm from the ignition wall. The nozzles had a depth of 7 mm and a square opening area of 250 mm^2. Situation '(d)' in Figure 2.8 can be regarded as the situation where the three nozzles are placed in the line of sight.

The combustion process between the ignition wall and the obstacle induces a flow of unburned gas through the obstacle. But, this unburned gas flow depends both on the mixture properties of the unburned gas and on the pipe and obstacle configuration. For the case of an obstacle with a single centered opening, a turbulent jet is created behind

the obstacle when the pressure difference over the obstacle is high enough[6]. Unless the turbulent intensity in the jet is so high that it causes global or local quenching of the flame, the flame will experience a positive flame acceleration behind the obstacle. A deflagration to detonation transition is also possible in the turbulent jet [6]. The mechanisms behind the turbulent flame acceleration and the transition to detonation, are discussed further in Subsection 2.3.2 and Subsection 2.3.3.

Flame inversion

The inverted flame shape has been presented in many publications. Mallard and Le Chatelier [94] were the first to observe the phenomenon [1]. They found that a flame which was ignited at the end wall of a long pipe with one open end, would propagate with inversions and that these inversions would be in the axial direction of the pipe. This oscillating motion was referred to as the "jerky movement" or "movement saccadé" [2]. But it was the development of the rotating shutter camera and the closed tube experiments performed by Ellis [86], that gave the first photograph of the inverted flame front. Figure 2.6 shows a stroboscopic image of the inverted flame front obtained by Ellis [86].

Salamandra et al. [97] used moving image photographs to study how shock waves in front of the flame influenced the deflagration to detonation transition in closed combustion chambers. They used premixed hydrogen and oxygen in long tubes. Both tubes with a circular cross section and tubes with a squared cross section were used. The tubes with a circular cross section had a diameter of 42 mm and the tubes with squared cross section had a cross section area of 36.5×36.5 mm^2. They observed the inversion of the flame during the initial stages of the flame propagation and described the flame shape as "tulip like". Today the tulip name is also used for the inverted flames both in tubes with an open geometry and in short and closed tubes [95].

Many explanations together with analytical and numerical models of the tulip flame phenomenon, have been proposed. But the process is difficult to resolve from a single configuration or from the experimental evidence in the literature. The tulip flame phenomenon might therefore be a combination of various processes [95]. Several physical mechanisms like pressure waves and flame interaction, flame instability and rotational flow behind the flame have been used to describe the process [96]. Some selected studies of the tulip flame formation are presented in the next paragraph.

Markstein [100] studied the interaction between shock waves and laminar flames in stoichiometric butane and air mixture. The shock waves were produced independently of the combustion process and they interacted with the flame just before the flame reached the pipe wall in the radial direction. The experiments were done in a tube which consisted of a high pressure chamber, a central portion and a combustion chamber with an internal cross section of 76.2×76.2 mm^2. The combustion chamber in the tube had a length of approximately 0.3 m. The schlieren photographs from these experiments show that the interactions between the shock waves and the flame led to the formation of a inverted flame. The time from the shock flame interaction to the formation of the inverted flame,

[6] According to White [16] the laminar jet profiles are unstable and undergoes a transition to turbulence for Reynolds numbers as low as 30, when the Reynolds number is based on the exit slot diameter and the mean slot velocity.

was further found to decrease with increasing shock pressure strength. These inversions were explained with a modified version of the Taylor instability [103]. Salamandra et al. [97] on the other hand, concluded that the tulip flame formation in their experiments were caused by the development of the pressure difference over the flame. At this stage in the flame propagation the pressure in front of the flame had became larger than the pressure behind the flame. The result of this difference was the initiation of a flow of gas in the opposite direction to the flame propagation. Guénoche [2] gives a discussion of the phenomenon and points out that flame inversions occurs both in closed pipes and in pipes with one open end. The study of Dunn-Rankine et al. [96] indicates that hydrodynamics of the combustion induced flow alone is sufficient to cause a tulip flame. They combined laser Doppler anemometry (LDA) experiments with two dimensional numerical simulations to study the interaction between the flame front and the combustion induced flow in a closed pipe. The experiments were carried out in a 155 mm long plexiglass pipe with a squared cross section of 38×38 mm^2. The numerical simulations were performed with the constrain of no vorticity formations, i.e. inviscid flow, but they still managed to reproduce the experimental flame inversions. Clanet and Searby [1] on the other hand, found that the inversion process occurred approximately at the same time for pipes with different lengths. This observation indicates that the inversion phenomenon is independent of acoustic waves. They also reproduced the experiment of Pocheau and Kwon [104] and concluded that boundary layers are not directly involved in the tulip flame phenomenon. This experiment shows that an array of igniters in a premixed gas can create an array of inverted flames with no physical boundaries between the flames. Clanet and Searby [1] also found that Richmyer's model of the Taylor instability [105] gave a good estimation of the flame front inversion time τ_i in Markstein's shock wave experiment [100]. An example of the formation of a tulip flame from the experiments of Clanet and Searby [1], is shown in Figure 2.7. The figure is a superposition of three images showing the flame front just before, during and just after the tulip flame formation of a premixed propane and air flame with an equivalence ratio of 0.70.

Salamandra et al. [97] also observed that the flame could become asymmetrical relative to the tube axis. The upper parts of the flame front did in those situations propagate faster in the axial direction than the lower part of the flame front. They observed this phenomenon during the positive flame acceleration, when the flame once more turned convex towards the unburned gas after the tulip formation. Salamandra et al. [97] explained this phenomenon with the density difference between the burned and unburned gas and the gravity force. The heavier unburned gas spreads in the lower parts of the tube, whereas the lighter burned gas rises to the upper part of the tube. This effect increases the acceleration of the flame in the upper part of the tube and slows it down in the lower part of the tube. This type of asymmetrical development of a premixed flame in horizontal tubes, can also be seen in the photographs presented in Reference [98, 84] among others. It is also interesting that Markstein [100], in the study of flame front and shock wave interactions, did place the tube vertically with the combustion chamber at the bottom to avoid these asymmetrical flame shapes. The effect of gravity on the flammability limits of premixed propane and air, in both a closed cubic vessel and a shortened standard flammability open tube, has been studied by Pu et al. [99]. They compared the flammability limits for the system under normal gravity $1.0g$ with the ones that were achieved under micro grav-

ity μg conditions. A drop tower with a falling assembly of 0.8×0.8×0.8 m^3 was used to create the micro gravity conditions. Both high speed video, temperature and pressure measurements together with a schlieren system, were used during the experiments. Pu et al. [99] found that in the closed vessel both the lower and upper flammability limits were unaffected by the gravity difference. For the open tube on the other hand, the lower flammability limit was unaffected, but the upper flammability limit became slightly lower under micro gravity conditions. They also found that the closed vessel had a slightly wider flammability range than the open tube.

Flame stability

The field of laminar flame instability is huge and it is beyond the scope of this thesis to go into the details of all the aspects of this field. The following paragraphs are therefore just intended to give a short outline of some of the mechanisms. A more detailed description of instability mechanisms in premixed combustion, can be found in Reference [64, 101, 113, 114, 115].

Barrére and Williams [116] state that combustion instabilities can occur as a result of both external influence and internal conditions in the flame. Examples of external influences that may cause flame instability are acoustic waves, shock waves and the establishment of the flow pattern in the combustion chamber, i.e. fluid dynamic conditions. The instabilities that occur in a flame without any external influence are a result of instabilities which are inherent to the reactants themselves. Examples of such intrinsic instabilities are chemical kinetic[7], diffusive-thermal, Landau-Darrieus and acceleration or buoyancy instabilities. These instabilities have different length scales and they are listed with an increasing length scale in the previous sentence. Five different instability mechanisms common for a premixed combustion in a pipe are presented below.

- **Diffusive - Thermal:** As the name implies, the mechanism is related to the thermal and molecular diffusivities of the premixed gas. The mechanism can both stabilize and destabilize the reaction zone. Liñán and Williams [117] give a qualitative description of this instability phenomenon based on the Lewis number. The Lewis number can be written as

$$Le = \frac{\alpha}{D} = \frac{\lambda}{D \cdot \rho \cdot c_p}, \tag{2.7}$$

  where α is the thermal diffusivity, D is the molecular diffusivity, ρ is the density, c_p is the specific heat capacity and λ is the heat conductivity. There is an increased conductive heat loss to the unburned gas in the parts of a perturbed flame that is convex towards the unburned gas. But if the Lewis number is equal to unity, then the normal components of the thermal and molecular diffusivities from the flame are equal. This means that the increased heat loss at the convex parts of the flame is balanced by an increased diffusion rate of reactants into the flame. The result

[7] Instability created by chemical kinetics is not going to be described here, but according to Barrére and Williams [116], this instability mechanism just means that the set of equations that represents the combustion kinetics exhibits unstable solutions.

is an unchanged flame temperature and burning velocity. If the Lewis number is larger than one, i.e. weakly diffusing reactants, then the generated heat from the diffusion of reactants is less than the heat lost by conduction. The result is then a reduced flame temperature and a reduced burning velocity and therefore also a reduction of the instability. On the contrary, if the Lewis number is smaller than one, i.e. strongly diffusing reactants, then the generated heat from the diffusion of reactants is larger than the heat lost by conduction. The result in this case is an increased flame temperature and an increased burning velocity and therefore also a growth in the instability. Based on this description, it can generally be stated that a planar flame is unstable due to the diffusive-thermal instability if $Le < 1$ and stable if $Le \geq 1$. A corresponding argumentation can be applied to the parts of the flame that is concave towards the unburned gas.

- **Landau - Darrieus:** This instability mechanism is purely hydrodynamic[8] [117] and it was first studied by Landau [118] and Darrieus [119]. Landau and Darrieus considered 1) the flame as a surface of discontinuity between two fields of non-viscous incompressible flow and 2) both the burning velocity S and the expansion ratio σ as constant [102]. The continuity of the tangential component of the fluid velocity over a perturbed flame front, implies that the streamlines diverge in front of the flame and converges on the burned gas side of the flame, for the parts of the flame that are convex towards the unburned mixture. Mass conservation over a variable area flow states that the product $\rho u A$ is constant, when A is the cross section area, ρ is the density and u is the fluid velocity. As the cross section area of the fluid flow increases, i.e. the stream lines diverge, at the positions where the flame is convex towards the unburned gas, the gas flow velocity is decreased. The velocity is decreased both in front of and behind the flame. But the burning velocity is regarded as constant and the part of the flame that is convex towards the unburned gas will therfore move further upstream. A corresponding argumentation can also be applied on the parts of the flame that is concave towards the unburned gas, but in this case the flame front moves further downstream. The net effect of this mechanism is that the perturbation grows.

- **Rayleigh - Taylor:** Rayleigh [106] studied the stability of fluids in a gravitational field and Taylor [103] adapted the problem to accelerating fluids. This instability mechanism states that if two fluids of different densities are accelerated in a direction perpendicular to their interface, this surface becomes stable or unstable depending on the direction of the acceleration. If the acceleration is directed from the heavier to the lighter fluid, then the surface will be stable and vice versa.

- **Richtmyer - Meshkov:** This instability mechanism is closely related to the Rayleigh-Taylor instability and it occurs when an interphase between two fluids of different densities has an impulsive acceleration [31, 121]. Shock waves are known to create such accelerations. If the acceleration on the other hand is steady like the acceleration created by gravity, then the instability process is known as the Rayleigh-Taylor instability [32]. But the Richtmyer-Meshkov instability differs qualitatively from

[8] Hydrodynamics is the science of forces acting on or exerted by fluids [107].

the Rayleigh-Taylor instability because it destabilizes the interface either the acceleration is from the light fluid to the heavier fluid or vice versa [31]. This instability mechanism was first predicted theoretically by Richtmeyer [105] and then studied experimentally by Meskhov [120].

- **Kelvin - Helmholtz:** The theory of this instability mechanism was first developed by Helmholtz [124] and Kelvin [123]. The instability is related to the shear forces created by fluid velocity differences. One of the simplest cases in which this instability can occur, is at the interface between two superimposed, non-mixable, incompressible, ideal and parallel flowing fluids with constant but non equal velocities [125].

Zhdanov [122] describes a situation where a material interface of two fluids of different density is influenced by both the Kelvin-Helmholtz and the Rayleigh-Taylor instabilities. This situation occurs when the heavier fluid is placed over the lighter fluid. The lighter fluid will then, because of buoyancy, accelerate the material interface in the direction from the lighter to the heavier fluid. This acceleration process destabilizes the interface according to the Rayleigh-Taylor instability and allows "fingers" of the light fluid to penetrate upwards and into the heavier fluid and vice versa. But the interface between the two fluids at the growing "fingers", will become unstable according to the Kelvin-Helmholtz instability, because the velocity of the two fluids are different. A similar argument can also most likely be applied to a premixed planar flame which propagates away from the ignition wall in a horizontal pipe. The expansion of the combustion products will make the flame unstable according to the Rayleigh-Taylor instability and the Kelvin-Helmholtz instability will destabilize the flame at the growing "fingers". But the pipe is horizontal and the growing "fingers" will therefore create regions of unburned gas over burned gas and vice versa. It is therefore possible that the Kelvin-Helmholtz instability is strengthened or weakened by the Rayleigh-Taylor instability at these interfaces. This extension of Zhdanov's example [122] shows that several stability and/or instability mechanisms of various length scales, can simultaneously act on a premixed flame.

2.3.2 Turbulent flame propagation in pipes

The previous subsection gave a short introduction to laminar flame propagation in closed and partly closed pipes. But, as it was pointed out in the beginning of this section, the flame propagation may also become turbulent as a result of obstacles and/or boundary layers. Breitung et al. [63] divide the turbulent flame propagation into three combustion regimes. These three combustion regimes have been studied firmly in obstacle filled pipes [134, 128] and they are separated from each other by a jump in the magnitude of the turbulent flame speed. These turbulent combustion regimes are further referred to as the subsonic combustion regime, the choked combustion regime and the quenching regime. The final turbulent flame speed depends on a variety of parameters, including the mixture properties and the geometry of the confinement and obstacles. But Dorofeev [12] states that a transition to detonation can only occur for supersonic deflagrations.

This Subsection has been divided into two parts. The first part gives a short introduction to the various turbulent combustion regimes, whereas the last part shows the influence

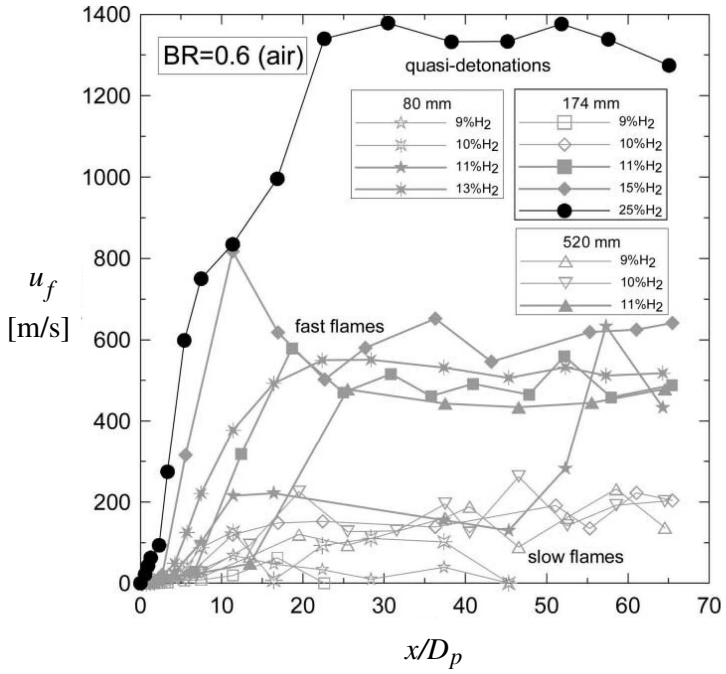

Figure 2.9: Turbulent flame and detonation speeds u_f along tubes as a function of the distance to pipe diameter ratio x/D_p. Experimental results obtained by Dorofeev et al. [126] for premixed hydrogen and air at atmospheric conditions. The empty gray points are slow flames, the closed gray points are fast flames and the black points are quasi detonations.

of pipe confinement on the overall turbulent flame acceleration.

Turbulent combustion regimes

Dorofeev et al. [126] have performed gas explosion experiments with lean mixtures of premixed hydrogen and air in obstructed pipes. The blockage ratio of the obstacles were 0.6 and the pipes had diameters D_p of 80, 174 and 520 mm. The turbulent flame and detonation speeds u_f obtained in these experiments are shown in Figure 2.9 as a function of the distance to pipe diameter ratio x/D_p. Three different flame speed regimes are viewable in the figure. The slow and fast flames correspond respectively to the subsonic and choked combustion regimes. An experiment with a transition to detonation is also shown in Figure 2.9, but this phenomenon is discussed in Subsection 2.3.3.

As described in the beginning of this subsection, turbulent mixing processes may also cause local or global quenching of the flame, i.e. zero terminal flame speed. Thibault et al. [133] investigated quenching of premixed flames propagating from one combustion chamber to another through an orifice. They found that the quenching criteria for a flame in a given gas mixture was dependent both on the blockage ratio of the obstacle and on the pressure difference across the obstacle. They also achieved choking conditions for the flow inside the orifice when the pressure difference across the orifice reached a ratio of approximately 1.8.

Lee et al. [73] did also study turbulent flame propagation in obstructed pipes. They

used various fuel and air mixtures in closed steel pipes with lengths ranging from 11.0 to 17.0 m and diameters of 50, 150 and 300 mm. The obstacles, which were circular orifice plates, were spaced one pipe diameter D_p apart and they had blockage ratios of 0.28, 0.39 and 0.44. Lee et al. [73] observed that for large blockage ratios the flame first accelerated and then quenched after a certain number of orifice plates. They referred to this situation as the quenching regime.

According to Breitung et al. [63] total quenching of a hydrogen and air flame is not always possible. The competitive aspects of turbulence on the combustion process may in such situations result in a subsonic flame speed. Breitung et al. [63] also state that such flames are very unstable and that a slight change in the physical conditions may cause the flame to jump to another combustion regime, i.e. cause a total quenching of the flame or accelerate it to a fast turbulent flame. Dorofeev [127] states that slow turbulent flames will, in spite of their name, still have a significant increase in the flame speed compared to the laminar flame situation. But the flame speed stays far below the speed of sound in the burned gas.

Lee et al. [73] found that if the blockage ratio of the orifice plates were such that quenching did not occur, then the flame speed would reach a terminal quasi steady state. This quasi steady state was further found to be dominated by gas dynamic choking of the combustion induced flow within the orifices[9]. They also observed that the flame speed was close to the local speed of sound of the burned gas for these fast flames. Gamezo et al. [132] state that this choking regime has a flame speed typically ranging from 1/3 to 1/2 of the CJ detonation velocity. The flame acceleration in this combustion regime has therefore been strong enough to generate pressure and shock waves in front of the flame that leads to a supersonic combustion [127]. But the flame is still decoupled from the lead shock and the combustion process is maintained by molecular and turbulent transport processes [132].

Reference [127] gives a short description of the work performed by Dorofeev et al. [128] and Kuznetsov et al. [134] to find dimensionless parameters that influence the positive feedback mechanism for turbulent flame acceleration in obstructed pipes. They suggested, based on the difference between slow and fast turbulent flames, that the turbulent flame acceleration could be characterized as weak or strong. In situations with a weak turbulent flame acceleration the terminal combustion regime is a slow turbulent flame and vice versa. Dorofeev et al. [128] and Kuznetsov et al. [134] further found that the final flame propagation regime at a sufficiently large scale mainly depends on the expansion ratio σ and they proposed a critical condition for strong flame acceleration. This critical condition is given as

$$\sigma > \hat{\sigma}(\beta), \tag{2.8}$$

where the critical expansion ratio $\hat{\sigma}$ is a function of the dimensionless Zeldovich number [127]. The dimensionless Zeldovich number is given as $\beta = E_a(T_\mathrm{b} - T_\mathrm{u})/T_\mathrm{b}^2$, where E_a is the effective activation energy in Kelvin [K], T_u is the initial temperature of the unburned gas and T_b is the adiabatic temperature of the flame. Not all aspects of the critical conditions for strong flame acceleration are known [127], but the critical expansion ratio

[9] Lee et al. [73] referred to this fast turbulent flame regime as the choking regime.

decreases with increasing initial temperature [63]. An increase in the initial temperature also decreases the Zeldovich number [126]. The dimensionless Zeldovich number is related to the critical conditions for strong flame acceleration, through the suppressing of the burning rate. A high Zeldovich number provides qualitatively a larger ability for the turbulent mixing process to quench the combustion process locally [127]. The critical expansion ratio is between 2.0 - 4.0 for hydrogen and air mixtures, depending on the initial temperature and equivalence ratio [63].

Influence of confinement

The turbulent flame propagation of a premixed flame in an obstructed pipe, is very sensitive to the degree of pipe confinement [63]. As it has been pointed out earlier in this section, there exists a positive feedback loop between turbulent flame acceleration and the generated turbulence in the unburned gas in front of the flame. Chan et al. [138] have investigated the influence of different degrees of confinement on a turbulent flame propagating in a pipe filled with obstacles. Their experiments were conducted with premixed methane and air at stoichiometric proportions in a 1220 $\times$ 127 $\times$ 203 mm^3 pipe. The obstacles were baffle type obstacles with heights of 32, 50 and 76 mm. Chan et al. [138] controlled the level of confinement by perforating the top plate of the pipe with different opening areas. They found that the maximum flame speed achieved $u_{f,M}$, is relatively low (less than 5.0 m/s) when the level of confinement of the top plate is less than 50 percent. In the case of venting through the top perforated plate, the flow ahead of the flame is reduced. This reduced flow velocity will further cause a reduction of the turbulent intensity [138, 63].

Alekseev et al. [139] have performed experiments with hydrogen mixtures[10] in pipes with transverse venting. Two pipes with lengths of approximately $63D_p$, were used in those experiments. D_p is the inner pipe diameter which was equal to 46 and 92 mm respectively. The pipes were further filled with ring shaped obstacles. These obstacles had a blockage ratio of 0.6 and they were placed one pipe diameter apart from each other. The experiments were conducted with vent ratios of 0.2 and 0.4. (The vent ratio is given as the total vent area to the total tube area ratio.) Alekseev et al. [139] found that the flame acceleration was significantly affected by the transverse venting and that an increase in the vent ratio required an increase in the mixture reactivity for achieving fast turbulent flames. If this result is related to the critical condition for strong flame acceleration presented in Equation (2.8), then $\hat{\sigma}_v > \hat{\sigma}$ when $\hat{\sigma}_v$ is the critical value for the vented pipe and $\hat{\sigma}$ is the critical value for the closed pipe.

Pressure waves generated from the combustion process in closed pipes may reflect off the end walls and/or obstacles and interact with the reaction zone. These acoustic interactions might result in an increased turbulent burning velocity through various instability mechanisms [63]. Layer and Manson [141] studied the development of vibratory flame propagation in closed tubes filled with premixed propane, oxygen and nitrogen at various initial pressures. The tubes used in these experiments were between 0.10 and 0.80 m long and some of them had Plexiglas windows for schlieren cinematography. Layer and Man-

[10] Alekseev et al. [139] used hydrogen and air mixtures and stoichiometric mixtures of hydrogen and oxygen diluted with nitrogen.

son [141] observed a vibratory flame propagation in the pipes and related the vibratory motions to the rarefaction waves which are created when the flame reaches the pipe side wall[11]. They further proposed that the rarefaction waves and therefore also the vibratory flame propagation, would be amplified by structural changes in the flame, i.e. instability mechanisms, if the rarefaction wave was larger than a threshold value. Layer and Manson [141] also observed that the vibratory propagation of a flame was significantly damped when the pipe side walls were coated with a rough insulation.

The turbulent vented gas explosion experiments performed by Tamanini and Chaffee [140], have shown that the presence of a sound absorbing material on the vessel walls can eliminate the flame instabilities induced by acoustic waves. On the contrary, with only bare pipe walls, these acoustic instabilities were observed to enhance the flame acceleration and to manifests themselves as exponentially growing pressure oscillations mainly at the fundamental frequency of the vessel. These experiments were performed with stoichiometric mixtures of fuel and air in a 1.35 m^3 spherical vessel with venting. The fuels were either propane or methane and the experiments were further performed with three different vent ratios and four different levels of turbulence. Turbulent combustion was ensured by a rapid injection of the premixed gas into the vessel just prior to the ignition. The gas was further ignited at the center of the sphere. In regard of the experiments performed with propane and methane, as explained in Subsection 3.3.3 and Subsection 3.3.4, it can be pointed out that Tamanini and Chaffee [140] found no major differences in the behavior between the two gas mixtures.

A pressure wave which has been generated from a flame propagating in a tube, may also steep into a shock wave [101]. Markstein [100] was the first to show how an interaction between a shock wave and the flame front could lead to an increased burning rate [142]. The experiments performed by Markstein [100] have previously been mentioned under the “flame inversion” part of Subsection 2.3.1. But these experiments also showed that the flame structure did change from laminar to turbulent, after the interactions with an incident and reflected shock wave.

2.3.3 Detonations in pipes

The previous subsections have outlined the possible evolvement of premixed gas explosions in closed or partly closed pipes; Starting with the laminar flame propagation that follows a weak ignition, through the positive flame acceleration caused by the turbulent feedback loop, to the quasi steady regime of fast turbulent flames. This last combustion regime, i.e. fast turbulent flames, can also under the right conditions experience a transition from deflagration to detonation [12].

The first scientific investigations of the detonation phenomenon were done independently by two pairs of French scientists in the late 19th century. Mallard and Le Chatelier [94] are often credited with the actual discovery, because they were the first to propose that the supersonic combustion primarily was a result of gas compression and not molecular transport processes [145]. But Mallard and Le Chatelier [94] gave credit to Berthelot

[11] According to Guénoche [2], it has been conclusively shown that vibratory flame propagation arises from longitudinal acoustic vibrations of the gas mass contained in the tube and from their action on the flame.

and Vielle [143] for the discovery [76].

A deflagration to detonation transition has been observed in a large variety of experiments. These observations have shown that the phenomenon depends on parameters such as the mixture composition, the initial conditions, the geometrical configuration and the physical scale of the apparatus [12]. But the observations have also resulted in a set of well documented data for detonation initiation, transition and propagation. This dataset has further been used to establish a set of necessary deflagration to detonation transition criteria [144]. Such criteria can be used on the initial and boundary conditions to evaluate the possibility of a transition to detonation. But the criteria are largely empirical and there does not exist a numerical tool which can cover the whole range of phenomena associated with flame acceleration and deflagration to detonation transition [12]. Each criterion is further necessary in the sense that a transition should not be expected if one criterion is unfulfilled. But on the other hand, the criteria can not guarantee that a transition to detonation is to be initiated even if all of them are met. This reservation is related to the possibility that there might exist one or several unknown requirements [63]. The transition to detonation criteria are therefore most useful to evaluate when a transition to detonation will not occur [12].

It has been shown through numerous experiments that the detonation cell size λ_d is a useful parameter to qualitatively describe the detonability or reactivity of a gas mixture. A mixture with large cells is less sensitive to DDT than a mixture with small cells [144]. The detonation cell size might also be used as a length scale in a deflagration to detonation transition criteria. Such a criterion can on a general form be given as

$$L \geq \alpha \cdot \lambda_d, \tag{2.9}$$

where L is the characteristic length scale of the apparatus and α is a constant that is equal to or larger than one, depending on the geometry of the apparatus [12]. Different values of α for some types of confinement configurations are presented later in this subsection. Figure 2.10 shows the detonation cell sizes for premixed hydrogen and air as a function of the equivalence ratio Φ. The cell size data in this figure are obtained from four different studies[12]. Generally the detonation cell size is known to vary with the initial pressure and temperature, the mixture composition and the tube diameter [144].

This subsection has been divided into four parts. The first part presents some theories for the underlying mechanisms for deflagration to detonation transition. The three following parts describe some selected studies on deflagration to detonation transition in pipes and jets.

Transition to detonation mechanisms

A transition to detonation can occur in a large variety of situations. Breitung et al. [63] have divided the processes that lead to onset of detonation for an accelerating flame in a pipe, into two categories. The first category includes situations where shock reflection or shock focusing results in an auto ignition of the unburned gas. Such types of detonation initiations are comparable to direct initiation processes and therefore require 1) that the

[12]Figure 2.10: The '$\Diamond$' data set is from Guirao et al. [3], the '$+$' dataset is from Tieszen et al. [129], the '$\Box$' dataset is from Ciccarelli et al. [130] and the '$\times$' dataset is from Benedick et al. [131].

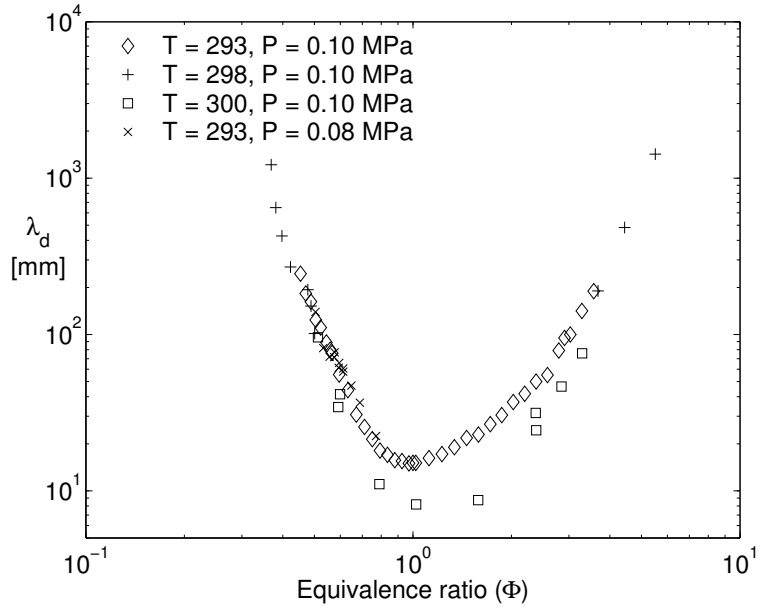

Figure 2.10: Detonation cell sizes λ_d for hydrogen and air mixtures as a function of the equivalence ratio Φ, after Reference [4].

energy which is released into the unburned gas is fast and of such an amount that it can create a shock wave that is comparable to the shock wave in a CJ detonation and 2) that the time scale of the created shock wave is equal to or larger than the induction time of the chemical reactions [144]. The second category of detonation onset processes includes deflagration to detonation transitions caused by a variety of flame instabilities and mixing processes. Examples of such processes are transitions caused by explosions of pockets of unburned gas and transitions caused by flame interactions with the confinement or shock waves.

Gas explosion experiments with premixed hydrogen and oxygen in a closed tube have been performed by Urtiew and Oppenheim [76]. Both the initial pressure and the equivalence ratio of the gas mixture were changed in the experiments. The tube had a cross section area of approximately 25×38 mm^2 and the mixtures were ignited at a closed end of the tube. The ignition was performed either with an electrical spark or with a glow coil. Stroboscopic schlieren records obtained in these experiments revealed that the onset of detonation could occur 1) between the lead shock and the flame, 2) at the flame front, 3) at the lead shock front and 4) at a discontinuity formed by the coalescence of shocks in front of the flame. Urtiew and Oppenheim [76] further found that the onset of detonation was dependent on the structure of the shock front. They therefore argued that the transition to detonation process is not reproducible in its detailed development, since the shock front is created by nonlinear acceleration of a turbulent flame. Urtiew and Oppenheim [76] also observed that the onset of detonation was common for the four situations listed above. The detonations started as an "explosion in the explosion" and propagated from the point of origin and into the shock compressed medium as a spherical detonation, before it developed the structure of a self sustaining detonation.

Zeldovich et al. [68] have studied the development of a detonation in a non-uniformly

preheated gas. This study resulted in a concept that describes the onset of detonation through the mechanism of an ignition delay gradient in the unburned gas mixture. An unburned gas which has been preheated by a shock wave, will according to this concept self ignite at the location where the induction time is shortest. The self ignition process will thereafter continue at the locations with longer induction times. As the velocity of this "self ignition wave" reaches the local speed of sound in the unburned gas, a shock wave is created. This shock wave will first result in a spontaneous coupling between the exothermic reaction and the shock wave and eventually in a transition to detonation [144]. Bartenev and Galfand [146] refer to the area within the domain with the lowest induction time as the initiating center. They further define such centra as a spatial non-uniformity (or a hot spot) which depends on several parameters. Examples of such parameters are the mixture composition, the temperature distribution and the concentration of active radicals.

Lee et al. [74] have performed experiments where a photochemical process was used to initiate gaseous detonations. They exposed various gas mixtures in a combustion vessel to ultraviolet radiation generated from a xenon flash and observed that the development of the detonations occurred in the vicinity of the vessel window. The electromagnetic radiation used in these experiments created a number of free active radicals which were sufficient to ignite the gas mixtures. But the concentration of the active free radicals becomes highest close to the vessel window and decreases exponentially with the distance from the vessel window. There existed therefore a gradient in the concentration of active free radicals at the time of ignition. The various gas mixtures used in these experiments were 1) acetylene and air, 2) hydrogen and air and 3) hydrogen and chlorine. Lee et al. [74] proposed a mechanism for the observed detonation initiations which was based on the induction time gradient and the shock wave strengthening through coherent energy release. The mechanism was called "shock wave amplification by coherent energy release" (SWACER) and it can be described by the following three steps:

1. The gas layer with the shortest ignition delay is ignited first.

2. The shock wave of the primary explosion propagates to the next layer, which has an induction time that is slightly longer than in the previous layer.

3. The shock wave reduces the ignition delay time of the new layer and initiates the explosion of it. The energy release from the explosion strengthens the shock wave further before it advances to the next layer. This step is then repeated until a transition from deflagration to detonation occurs.

Breitung et al. [63] point out the similarity between the two mechanism presented by Zeldovich et al. [68] and Lee et al. [74]. They also list seven different detonation initiation phenomena where the SWACER mechanism is believed to be the underlying process. Such phenomena include transition to detonation in turbulent jets and obstacle filled tubes.

Transition to detonation in smooth pipes

An experimental study of the run-up distance x_d for gaseous detonations in smooth pipes has been performed by Steen and Schampel [147][13]. They used premixed propane and air and premixed ethylene and air, in pipes with one open end. The gas mixtures were ignited with a weak ignition source at the closed end of the pipes and the following flame propagation were measured with ionization probes. The distance between each ionization probe were 2.0 m. Steen and Schampel [147] referred to the position of transition to detonation as being the point of intersection between the curve of increasing deflagration velocities and the relatively stable detonation velocity[14]. This intersection point can be determined by plotting the measured flame positions along the pipe as a function of the time, i.e. the pipe length [m] along the vertical axis and the time [ms] along the horizontal axis as illustrated in Figure 2.11. This study indicated a linear relationship between the pipe diameter D_p and run-up distance x_d. According to Steen and Schampel [147] this linear relationship has also been showed for methane and air mixtures and for hydrogen and air mixtures in the studies presented in Reference [149, 150], for pipes with $25 < D_p < 500$ mm. The linear relationship indicates that the run-up distance to the pipe diameter ratio, i.e. x_d/D_p, is unchanged for various pipe diameters. But Steen and Schampel [147] also point out that the x_d/D_p ratio for a specific gas mixture increases with increasing initial temperature [151] and decreases with both increasing initial pressure [151, 152, 154] and increasing turbulence [153, 155].

Figure 2.11 gives the x_d/D_p ratio to be approximately equal to 66 for a stoichiometric mixture of ethylene and air. Chatrathi et al. [156] used the same method of determination for x_d as Steen and Schampel [147] and found the corresponding ratio for stoichiometric hydrogen and air to be 59. A stoichiometric mixture of propane and air was on the other hand found to have a x_d/D_p ratio of approximately 72. Chatrathi et al. [156] conducted their experiments at atmospheric conditions in partly closed pipes and measured the flame arrival times with photodiodes. The pipes had a pipe length to pipe diameter ratio, i.e. L/D_p, of 98 and the pipe diameters were approximately 152 and 254 mm. The gas mixtures were further ignited at the closed end of the pipes.

The run-up distance for the onset of detonation in a smooth and closed tube as a function of the initial pressure, has bee studied experimentally by Kuznetsov et al. [135]. They used premixed hydrogen and oxygen at stoichiometric proportions in a 24 m long tube with an inner diameter of 105 mm. The length of the tube relative to the reactivity of the gas mixture, was sufficient to avoid any influence on the deflagration to detonation transition process from pressure waves reflected off the end wall. The gas mixtures were ignited by a glow plug at initial overpressures ranging from 0.08 to 0.80 MPa. Both measurements from pressure transducers and photodiodes were used in the diagnosis of the experiments. Kuznetsov et al. [135] found that the run-up distance decreased with increasing initial pressure as expressed by Equation (2.10)[15].

[13]Run-up distance: The distance propagated by a flame from the spatial point of ignition to the spatial point where the flame has a deflagration to detonation transition.

[14]Li et al. [148] gives an uncertainty analysis of three adopted methods used to estimate the run-up distance for gaseous detonation in smooth pipes. They also points out that there are no standard definition or apparatus to measure x_d.

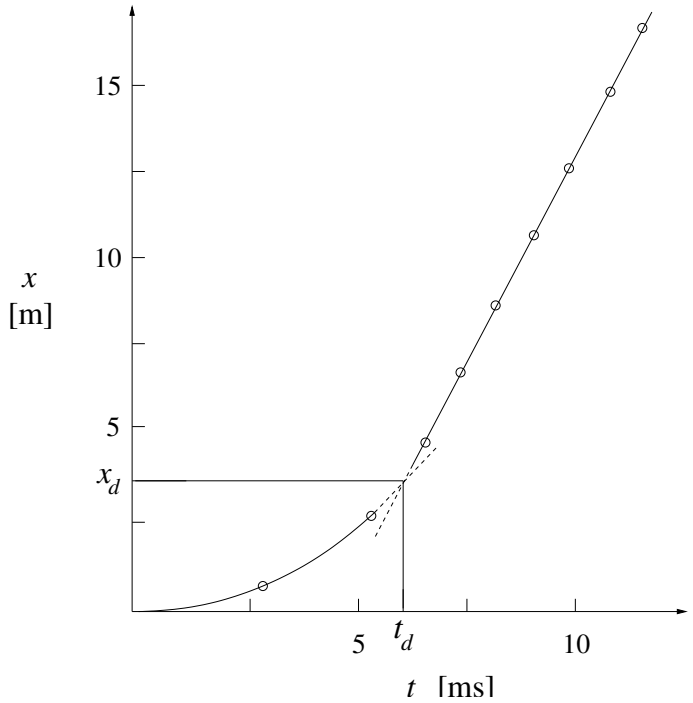

Figure 2.11: A distance-time diagram after Steen and Schampel [147]. The diagram shows a deflagration to detonation transition in a smooth pipe with one open end. The gas mixture had 6.5 volume percentage of ethylene in air and the pipe diameter was 50 mm.

$$x_d \sim p^{-1.117} \tag{2.10}$$

The experimental study of Kuznetsov et al. [135] does also support the criterion proposed by several researches (Reference [63, 12, 160] among others); That the reaction zone has to become a fast turbulent flame (supersonic combustion) before it can experience a deflagration to detonation transition.

A scaling analysis of the critical conditions for a deflagration to detonation transition caused by turbulent mixing in a turbulent flame brush, has been performed by He [157]. This analysis used the detonation initiation within a non-uniformly heated gas mixture as an analogy. The analysis shows that a transition to detonation depends on both the time and the length scales of the turbulent mixing process. If the integral length scale is below some critical length l_c or if the mixing intensity is lower than some critical turbulent intensity u'_c, then a transition to detonation should be unexpected. This result makes the initiation of a detonation possible only in the upper part of a Borghi diagram. (See Figure 2.2.) He [157] also points out that less reactive gas mixtures may experience various quenching phenomena in this part of the Borghi diagram. A typical value of u'_c has been suggested to be 500 m/s when the integral length is 0.05 m.

[15] A possible linear proportionality between the laminar flame thickness δ_L and the run-up distance x_d, was also proposed by Kuznetsov et al. [135].

Transition to detonation in obstructed pipes

Lee et al. [75] have carried out gas explosion experiments with premixed hydrogen and air at atmospheric conditions in a closed steel tube. A glow plug or an electrical spark was used to ignite the various gas mixtures at a closed end of the pipe. Three different obstacle sections with a blockage ratio of either 0.44 or 0.6 and a total length of 3.0 m, were installed at the ignition end of the pipe. These obstacle sections were either created by a Shchelkin spiral with a pitch equal to the pipe diameter or by an orifice plate array with an internal spacing of one pipe diameter. The tube had further an inner diameter of 0.05 m and a total length of 11.0 m. Ionization probes or pressure transducers were installed at every 0.5 m down the pipe, to measure the flame speed or the pressure development in the experiments. The volume percentages of hydrogen were ranging from 10 to 45 percent. Lee et al. [75] found that only gas mixtures with a detonation cell size smaller than the pipe diameter could experience a transition to a normal CJ detonation in part of the pipe that were without obstacles, i.e. downstream of the obstacle section. Based on this observation, a critical criterion for a deflagration to detonation transition in smooth pipes was stated as

$$D_p \geq \lambda_d. \tag{2.11}$$

A similar criterion was, according to Lee et al. [73], proposed by Vasiliev [159].

The necessary criteria for transition to detonation in closed and obstacle filled tubes, have been studied by Peraldi et al. [160]. Three 18.0 m long tubes with an inner diameter of respectively 0.05, 0.15 and 0.30 m, were used in these experiments together with premixed fuel and air at atmospheric conditions. The fuels were hydrogen, acetylene, ethylene, propane and methane. A glow wire at a closed end of the tubes was used to ignite the gas mixtures and the obstacles were orifice rings spaced one tube diameter apart. A blockage ratio of approximately 0.4 was used in all the three tubes. The flame speeds were measured with ionization probes spaced 0.5 or 1.0 m apart. Peraldi et al. [160] found that the orifice opening diameter D_o had to be larger than the detonation cell size of the specific gas mixture, to achieve a detonation initiation in the tubes. This observation lead to the criterion for a deflagration to detonation transition in a obstacle filled tube that can be given as

$$D_o \geq \lambda_d. \tag{2.12}$$

But Lindstedt and Michels [5] have observed transition to detonation within Shchelkin spirals for a detonation cell size to the obstacle opening diameter ratio (i.e. λ_d/D_o) as high as 1.4. They used stoichiometric mixtures of hydrocarbons and air. The Shchelkin spirals were placed at the ignition end of the pipe and a composite spark source of 100 mJ was used to ignite the various gas mixtures. The pipe was approximately 11.2 m long and had a diameter of about 51 mm. The flame velocities were measured with ionization probes. Lindstedt and Michels [5] also observed that the most optimum conditions for flame acceleration in the obstructed part of the pipe, were achieved for a blockage ratio of 0.44 and a pitch distance of 45 mm.

Lee et al. [73] have performed experiments with approximately the same experimental configuration and gas mixtures as Peraldi et al. [160]. Lee et al. [73] observed that the

detonations propagated with a sub CJ detonation velocity within the obstacle arrays, when the obstacle opening diameter D_0 was less than a multiple of the detonation cell size of the specific gas mixture. They referred to such detonations as quasi detonations and stated that they propagate with a velocity which is typically larger than fast turbulent flames, but slower than the CJ detonation velocity due to momentum losses. These observations were used by Lee et al. [73] to propose a detonation propagation regime criterion. This criterion states that a detonation which propagates in an obstacle filled tube, will propagate as a quasi detonation when

$$\lambda_d \leq D_o \leq 13\lambda_d. \tag{2.13}$$

Lee et al. [73] did also observe that the propagation of detonations in this types of pipes were unaffected by wall effects and the obstacles, i.e. they propagated with the CJ detonation velocity, when

$$D_o > 13\lambda_d. \tag{2.14}$$

Gamezo et al. [132] state that the propagation velocity of a quasi detonation increases with an increase in the D_m/λ_d ratio, when D_m is the characteristic length scale of the smallest cross section of the channel.

An experimental study of the propagation mechanisms of quasi detonations has been performed by Teodorczyk et al. [161]. This study indicated that the detonation wave was diffracted over the obstacles before it was re-initiated through shock reflections from the tube side walls. There is therefore a temporary decoupling between the lead shock and the reaction zone in a quasi detonation [132]. Teodorczyk et al. [161] did use stoichiometric mixtures of fuel and oxygen at subatmospherical initial pressures ranging from $1.3 \cdot 10^{-3}$ to $21.3 \cdot 10^{-3}$ MPa. The various fuels were hydrogen, ethylene and propane. The tube was 1.5 m long and had a cross section area of 61.8×61.8 mm^2. Three different obstacle arrays with constant spacing were used in the experiments. The obstacles were aluminium angels with a hight of 25.4 mm and a blockage ratio of 0.5. The internal distance between the obstacles were respectively 32.1, 64.2 and 128.4 mm in the three different arrays. A direct initiation of a detonation in the various gas mixtures were created by a high voltage electrical spark or by an exploding wire at a closed end of the tube. Both velocity measurements from photo diodes and photographs from high speed schlieren photography were used in analysis of these experiments.

Critical tube diameter and transition to detonation in jets

The previous subsections have shown that both the pipe configuration and the level of confinement affect the evolvement of a gas explosion in a pipe. The following discussion is related to the required criteria for 1) a transmission of a planar detonation into an unconfined volume and 2) a deflagration to detonation transition in a jet of hot combustion products. A jet can for example occur when a combustion process propagates through an orifice plate and into an explosion chamber or from a pipe end and into an unconfined volume.

Experimental studies of gaseous detonations emerging from a circular tube and into an unconfined region, have indicated the existence of a critical tube diameter D_c. (According

to Reference [93], the first observation of this phenomenon was made by Zeldovich et al. [69].) A planar detonation is transformed into a spherical detonation in the unconfined region, when the pipe diameter D_p is larger than D_c. Likewise does the detonation fail, i.e. it is transformed to a spherical deflagration, when D_p is smaller than D_c [72]. Mitrofanov and Soloukhin [162] have studied the diffraction of planar detonation waves emerging from a circular tube and into the same gas mixture in an unconfined volume. They used a stoichiometric mixture of acetylene and oxygen at initial pressures less than $13.3 \cdot 10^{-3}$ MPa. These experiments of Mitrofanov and Soloukhin [162] showed that there is a correlation between the detonation cell size and the critical tube diameter. The relationship between the two quantities can be expressed as

$$D_c \approx 13\lambda_d. \tag{2.15}$$

Mitrofanov and Soloukhin [162] also found the critical width W_c for squared tubes to be approximately ten times the detonation cell size [72]. The validity of Equation (2.15) has also been confirmed by the experiments of Moen et al. [92], who used various stoichiometric mixtures of ethylene and oxygen diluted with nitrogen at atmospheric conditions. But Moen et al. [91, 93] later concluded that D_c is only $13\lambda_d$ for the majority of fuel and air mixtures, i.e. mixtures with an irregular cell structure. The experimental determined D_c depends on the properties of the exploding gas mixture, but it is between 10 and 30 detonation cell widths [93].

The previous paragraph dealt with the situation where a stable detonation in a pipe suddenly emerges into an unconfined region. But what are the criteria for a deflagration to detonation transition, when the emerging combustion process is a deflagration? Knystautas et al. [52] have studied the direct initiation of a spherical detonation by a hot turbulent gas jet. They used equimolar mixtures of acetylene and oxygen in an apparatus which consisted of a spherical flame chamber interconnected with a cylindrical detonation chamber. Obstacles of various types were mounted in the passage between the two chambers to manipulate the fluid flow. The initial pressures were less than $26.6 \cdot 10^{-3}$ MPa and the premixed gas was ignited by a weak electrical spark at the center of the spherical chamber. Streak and schlieren photography were used together with measurements from both pressure transducers and ionization probes, to analyze the experiments. Knystautas et al. [52] observed that a spherical detonation could be initiated in the turbulent jet downstream of the obstacle. They stated that these transitions to detonation were caused by intense mixing of the hot combustion products and the unburned gas, i.e. shockless initiation of detonation [158]. The combustion induced flow creates a turbulent flow field of unburned gas behind the obstacle. When the flame enters this region, hot combustion products are rapidly mixed with the unburned gas. This mixing process might result in an auto ignition and eventually the onset of detonation. But Knystautas et al. [52] list three criteria that have to be fulfilled before the turbulent mixing process can lead to a deflagration to detonation transition:

1. Large scale energetic eddies of unburned gas have to be generated in the turbulent flow field behind the obstacle.

2. The small scale turbulence has to be sufficiently intense to ensure that there is a mixing of the hot combustion products and the unburned gas entrained inside the

large eddies.

3. An induction time gradient field has to be generated inside an eddy to give shock wave amplification by coherent energy release. (The SWACER mechanism.)

Moen et al. [6] have investigated the transition to detonation in a large turbulent flame jet both experimentally and numerically. They used various mixtures of acetylene and air, where the acetylene volume percentage was ranging from 4.9 to 8.1. The experimental apparatus consisted of a 11.0 m long tube and a 8.0 m long plastic bag. The diameter of the tube was 0.66 m and the diameter of the plastic bag was 2.0 m. A match head was used to ignite the various gas mixtures at one end of the tube, whereas the other end of the tube was connected to the plastic bag. The pipe was closed at the ignition end and open at the other end. But some experiments were also conducted with various obstacles mounted at the open end. Both pressure recordings from pressure transducers and films from high speed cameras were used to analyze the experiments. Moen et al. [6] concluded that the initiation of detonation in a hot gas jet reported by Knystautas et al. [52], also applies for acetylene and air mixtures when the scale is large enough. The diameter of the jet had to be approximately five times the critical tube diameter. But the scale requirement on the turbulent jet could be significantly reduced by placing obstacles at the tube exit. They further reported the onset of detonation as a result of a localized explosion somewhere in the turbulent flame jet. But the presence of a pressure reflecting boundary, i.e. the ground or the plastic bag, could also set off a local explosion that lead to the onset of detonation. These detonation transitions could also occur for jet to critical tube diameter ratios smaller than five.

Experimental and numerical investigations of flame jet ignition of premixed fuel and air clouds, have also been performed by Mackay et al. [163]. The fuels were acetylene, ethylene, propane and vinyl chloride monomer (C_2H_3Cl). Mackay et al. [163] used an experimental apparatus which is comparable to the apparatus used by Moen et al. [6]. The pipe was 7.8 m long and the cylindrical plastic bag was 8.0 m long. The diameter of the tube was 0.9 m and the diameter of the plastic bag was either 1.8 or 2.0 m. The various gas mixtures were ignited by a spark close to the closed end of the tube. A centered circular disc with an opening area ratio of either 1.00, 0.78 or 0.59, was mounted at the open end of the tube. Circular and centered obstacles with constant spacing were also mounted inside the tube. As in the experiments of Moen et al. [6], the analysis were based on recordings from pressure transducers and high speed cameras. Mackay et al. [163] proposed that the critical conditions for a transitions to detonation were established by the absolute jet velocity. It was assumed that a minimum flame jet velocity of 600 m/s was required for obtaining detonation initiation in a sensitive fuel and air mixture. This velocity would also increase with a decreasing mixture sensitivity. It can be pointed out that Mackay et al. [163] only observed a transition from deflagration to detonation in experiments with premixed acetylene and air.

The experimental study performed by Üngüt and Shuff [164] indicates that the minimum required tube diameter for obtaining a DDT in a turbulent jet, is smaller than the critical tube diameter for a detonation transmission. This means that a given gas mixture in the essentially unconfined volume behind the tube exit, will detonate more easily if the emerging combustion process is a fast turbulent flame and not a detonation. Üngüt

and Shuff [164] used stoichiometric mixtures of fuel and oxygen diluted with nitrogen. The premixed gases were ignited by a spark plug at the closed end of a circular steel pipe which was interconnected with a semi-spherical detonation chamber. The initial pressure in the apparatus was either 0.10 or 0.04 MPa and the fuels were propane and methane. Various short length pipes added to the open end of the pipe were used to vary the diameter of the jet. The unobstructed pipe had an inner diameter of 140 mm. Recordings from both soot foils, ionization probes, pressure transducers and high speed cameras were used to analyze the experiments. Üngüt and Shuff [164] observed a deflagration to detonation transition in the turbulent jet when the average flame speed at the pipe exit was larger than 450 m/s. But the experiments also indicated the existence of a pipe exit diameter to detonation cell size ratio limit, for which a transition is possible, no matter what the deflagration speed is at the pipe exit. This detonation transition criteria was observed to be $D_o/\lambda_d \geq 7$ for propane and oxygen mixtures, when D_o is the pipe exit diameter.

2.4 Computational Fluid Dynamics codes

Appendix B gives an introduction to the partial differential equations for conservation of mass, momentum and energy. Computational Fluid Dynamics (CFD) codes use these equations to solve various types of fluid flow problems in a solution domain which is discretized in time and space. The conservation equations are often referred to as the Navier-Stokes equations and they can also be applied to turbulent flow simulations. But the computational power required to simulate turbulent flow in detail at high Reynolds numbers is absent to the present time. This situation might change some time in the future with the help of parallel programming and faster supercomputers, but today most of the turbulent fluid flow simulations are performed with various empirical turbulence models. Such turbulence models are less computationally intensive and they have been divided into the following six categories by White [16]: zero, one and two equation models, Reynolds stress models, almost model free and model free. The four first categories are also refereed to as Reynolds averaged Navier-Stokes (RANS) equation closures or just RANS models. Three turbulence models commonly used in CFD codes are listed below.

1. k-ε model: This is a two equation model where k is the turbulent kinetic energy relation and ε is the turbulent kinetic energy dissipation rate, i.e the rate at which the turbulent kinetic energy is transfered to heat.

2. Large eddy simulation (LES): Only the effect of the small scale turbulence is modeled in this type of simulations. The effect of the larger turbulent structures is explicitly simulated. This approach is relatively computational intensive and it is based on the assumption that the small scale turbulence behaves in a universal manner, whereas the large scale turbulence are related to the geometry of the system [169]. White [16] categorizes such turbulence simulations as almost model free.

3. Direct numerical simulation (DNS): This type of simulations use a grid resolution which is high enough to handle even the smallest structure scales and the fastest velocity fluctuations in a turbulent flow. The approach does not include any turbulence

modeling, but it is extremely computationally intensive. Direct numerical simulations are therefore often limited to fluid flows at low Reynolds numbers [171].

As the previous sections have shown, turbulence is an important parameter in the evolvement of a gas explosion. Various computational fluid dynamics codes have been developed to simulate the effects of turbulent combustion in gas explosions. But the turbulent combustion processes occur at a scale which is unresolved in the simulations, i.e. at a sub grid level, which means that the combustion process needs to be modeled. This sub grid combustion problem is present either the CFD code is using a LES or a RANS turbulence model. Combustion models used in RANS codes can after a modification also be used with LES codes [170]. Most turbulent combustion models calculate the combustion process based on a description of the mean flow field. These flow field descriptions can further be based on 1) a geometrical approach as with flame surface density models, 2) a statistical approach as with probability density functions or 3) turbulent mixing models [169]. Both G-equation models, flame surface density models and thickened flame models are common combustion models in LES codes, whereas Eddy-break-up models are common combustion models in RANS codes [169, 170]. An introduction to these combustion models and other commonly used models for turbulent premixed combustion, can be found in Reference [64, 169, 170].

A CFD code has to be validated before it can be used in predictive analysis. For gas explosion simulation tools the validation is normally done against experimental data, such as the overpressure [173]. But the models are empirical, i.e they are based on assumptions and simplifications. It is therefore important to be aware of the possible danger of miss calculations if these codes are used outside their range of validation against test data [172]. Both FLACS [165], EXSIM [166] and AutoReaGas [167] are examples of computational fluid dynamics codes which are used in predictive simulations of gas explosions. These three software packages are all three dimensional and they use a standard k-ε turbulence model [172][16].

RCMLAB [17, 18, 23, 24] which has been used in this thesis, differs somewhat from the numerical codes described above. The turbulent combustion is incorporated into the simulations through experimental pressure data. The turbulent burning velocity is then calculated by comparing the simulated and experimental overpressures at the various time steps. RCMLAB is a one dimensional code and it uses the random choice method (RCM) to solve the local Riemann problems (RP) between each grid cell. The random choice method has the advantage that discontinuities such as shock waves, are treated as true discontinuities, i.e they remain sharp throughout the simulation. Other methods tend to smear the discontinuities over several grid cells [36]. A more detailed description of RCMLAB is given in Section 4.2.

Detailed descriptions of the various codes and the various turbulence and combustion models are not presented here, since the main objective of this section is just to give a brief introduction to common computational fluid dynamics codes used in gas explosion simulations. But it should however be pointed out that 1) computational fluid dynamics is still a developing field even for non reactive fluid flow simulations and 2) there does not exist

[16] More information about FLACS [165], EXSIM [166] and AutoReaGas [167] can be found in Reference [172, 174], which also gives a description of other predictive gas explosion software packages.

a numerical method or a software tool that single-handedly can cover the whole range of phenomena that are associated with flame acceleration and transition to detonation [12].

Chapter 3

Experiments

This chapter describes the experimental work. First there is a short introduction to the chapter in Section 3.1 before the experimental setup is described in Section 3.2. The experimental results with some references to other comparable studies are presented in Section 3.3 and Section 3.4 gives the conclusions derived from the experimental work.

3.1 Introduction

Gas explosion experiments have been performed to enhance the understanding of flame propagation in pipes. The experiments were carried out with premixed fuel and air at various equivalence ratios (Φ) in circular, closed and single obstructed pipes. The primary focus of the experimental work was to see how the blockage ratio (BR) of the obstacle and the equivalence ratio of the premixed fuel and air affected the flame propagation.

Obstacles are often used to increase the turbulence in gas explosion experiments. It is well known that turbulent flow right in front of a flame in a combustible gas mixture, may lead to strong flame acceleration and increased burning velocity. The turbulence increases the transport of heat and reactants in the reaction zone, but it also increases the flame surface area. If the flame acceleration is sufficiently large, a deflagration to detonation transition (DDT) can take place. Different types of obstacles create different levels of turbulence and flow patterns for the reactive flow. The experiments in this study have been done with one single obstacle in closed pipes. These pipe configurations were chosen both to ensure strong turbulence inside the pipe and to keep the geometrical complexity at a fairly low level. The upper pipe in Figure 3.1 shows the main experimental setup as it appears in the laboratory. The premixed gas is ignited by a weak ignition source at the right end wall.

Pressure transducers have been used to measure the experimental overpressures. These pressure measurements can be used to find pressure peaks, shock pressures, shock speeds, detonation velocities and detonation pressures. The pressure recordings are often plotted as a function of both the time and the pressure transducer position in the pipe. These types of plots are very informative and they are powerful tools in the analysis of the experiments.

The main objective of performing the experiments, was to provide a set of data for validation of numerical simulations. Chapter 4 describes how the validation is done and

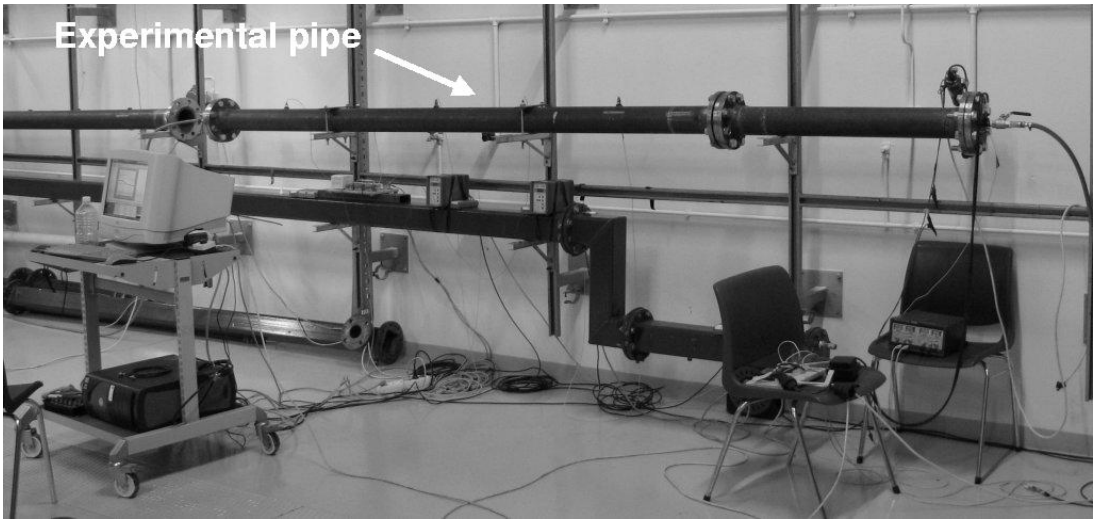

Figure 3.1: A photograph of the main experimental setup at the laboratory.

how the experimental pressure recordings have been used as input to a one dimensional numerical code for estimation of the burning velocity.

3.2 Experimental setup

This section gives an overview of the experimental equipment and how the data collection was performed. The section has been divided into five subsections. The various pipe types are described in Subsection 3.2.1. Subsection 3.2.2 describes the mechanisms of the ignition unit and Subsection 3.2.3 describes the gas handling unit. The data acquisition and recording unit is explained in Subsection 3.2.4 and the data post processing methods are presented in Subsection 3.2.5.

3.2.1 Pipe types

Three different pipes have been used in the experiments. These pipes were closed, smooth and circular steel pipes with an inner diameter of 107 mm. The total inner length of the pipes were 3.0, 4.0 and 7.0 m. The 4.0 m pipe can be regarded as the main pipe configuration. Most of the experiments were performed with this pipe. The 3.0 and 7.0 m pipes were created by removing or adding pipe modules to the 4.0 m pipe.

The 4.0 m pipe was constructed by putting a 1.0 m long and a 3.0 m long pipe together. Both pipes had the same inner diameter of 107 mm. The merged pipe was further closed at both ends and an obstacle was installed in the junction between the 1.0 m pipe and the 3.0 m pipe. Rubber rings (O-rings) were placed in the junctions to prevent leakage of gas from the pipe. The obstacle was an orifice plate with a single centered opening. Both of the end walls were plane and they had a manual valve for gas flow control. The end wall closest to the obstacle had a centered mounting point for an ignition source. A total of 6 pressure transducers were distributed in the pipe. One pressure transducer (P0) was installed on the end wall close to the ignition source. The rest of the transducers

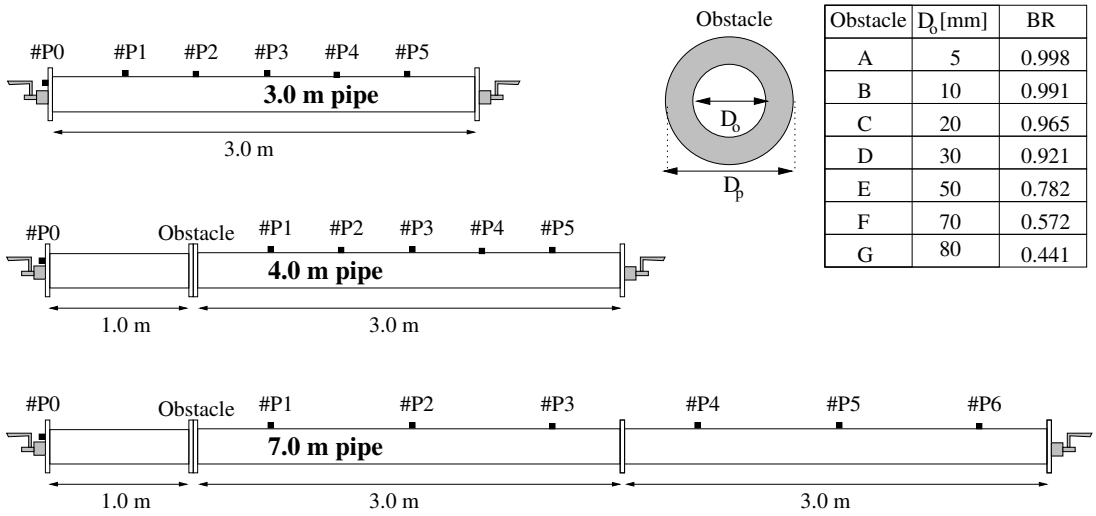

Obstacle	D_o [mm]	BR
A	5	0.998
B	10	0.991
C	20	0.965
D	30	0.921
E	50	0.782
F	70	0.572
G	80	0.441

Figure 3.2: The three different pipes used in the experiments with an overview of the various obstacles used together with the 4.0 and 7.0 m pipe.

were mounted 1.5 m from the ignition source (P1) and every 0.5 m down the pipe (P2 - P5). Seven different obstacles were used. The obstacle opening diameters were ranging from 5 to 80 mm. This is equivalent to blockage ratios ranging from 0.996 to 0.441. The blockage ratios are given by

$$\mathrm{BR} = \frac{A_p - A_o}{A_p} = 1 - \left(\frac{D_o}{D_p}\right)^2, \tag{3.1}$$

where A_p and A_o are the internal pipe and obstacle opening cross section areas. D_p and D_o are the internal pipe and obstacle opening diameters, respectively.

The 3.0 and 7.0 m pipes were constructed by removing or adding pipe modules from or to the 4.0 m pipe. The 3.0 m pipe was constructed by removing the obstacle and the 1.0 m pipe. The 7.0 m pipe was constructed by adding an additional 3.0 m pipe between the 3.0 m pipe and the end wall. In the case of the 7.0 m pipe, the pressure transducer distribution was changed. The number of pressure transducers was increased to a total of seven. The distance between the transducers after the obstacle (P1 - P6) was also increased to be 1.0 m. Figure 3.2 gives a sketch of the three different steel pipes and their pressure transducer distributions. An overview of the various obstacles used together with the 4.0 and 7.0 m pipe is also given in the figure.

3.2.2 Ignition unit

The ignition unit ignites the premixed gas and sends a trigger signal to the data acquisition and recording unit. Two different types of ignition systems have been used. Both systems generated a spark in the center of the left end wall of the pipes shown in Figure 3.2. This end wall will be referred to as the ignition wall. The first ignition system used a spark plug together with a 12 V Diamond ignition coil. This system was later replaced by a spark electrode and a SIEMENS ZM 20/10 220 V transformer together with a small control circuit. A sketch of the two systems are given in Figure 3.3 and Figure 3.4. The output

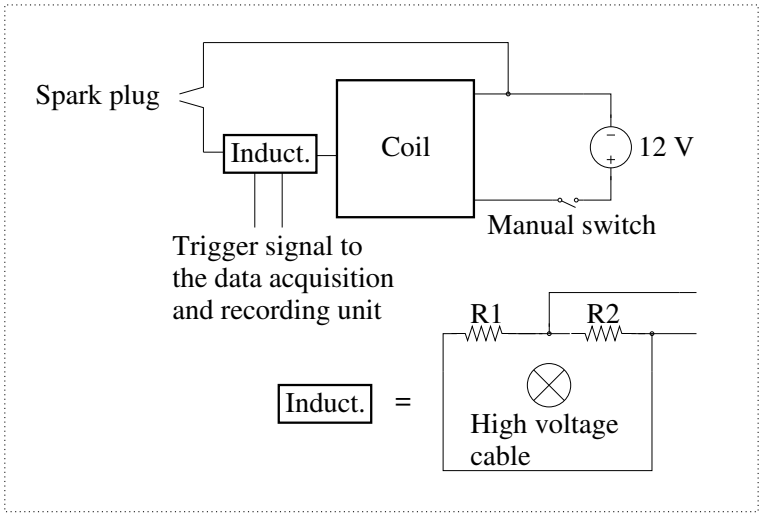

Figure 3.3: The initial ignition unit.

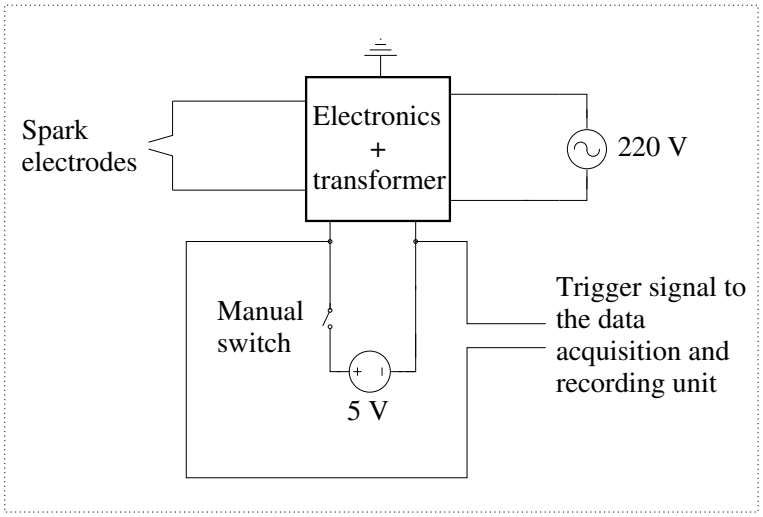

Figure 3.4: The second ignition unit.

voltage of the Diamond ignition coil is less than 30 kV and approximately 5 kV for the SIEMENS ZM 20/10. The distance between the electrodes used in the second ignition system, was approximately 2 mm. Both ignition sources are regarded as weak.

The trigger signal to the data acquisition and recording unit was generated differently by the two ignition systems. In the initial setup the trigger signal was induced in an insulated wire. The insulated wire had two serial resistors and made a closed loop around the high voltage cable of the ignition coil. In the second system the trigger signal was generated directly by the manual switch and the 5 V driving the control circuit. Both systems had a non constant time delay between the closing of the manual switch and the ignition of the gas. The actual ignition time had to be determined by an analysis of the pressure record from the pressure transducer closest to the ignition source (P0). The ignition signal would appear as a very sharp peak, often only four or five sampling points wide, in the beginning of the pressure record.

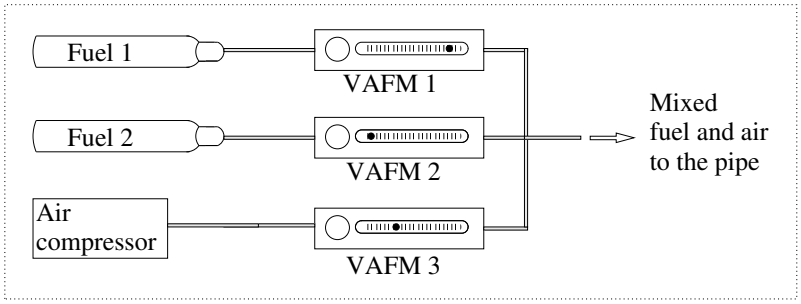

Figure 3.5: The gas handling unit.

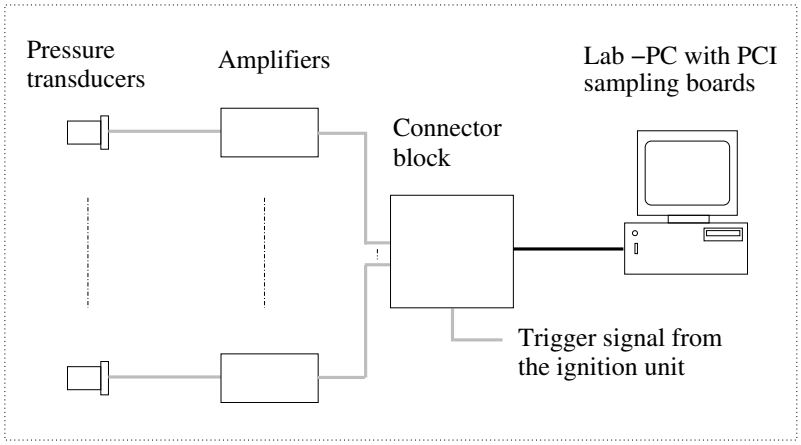

Figure 3.6: The data acquisition and recording unit.

3.2.3 Gas handling unit

The gas handling unit made homogenous gas mixtures of fuel and air at the correct equivalence ratio. The gas compositions were controlled by variable area flow meters (VAFM). The VAFM were calibrated by a Ritter TG10/1 or a Ritter TG05/1 drum-type gas meter. (The TG10/1 has a maximum of 20 l/min and the TG05/1 has a maximum of 1 l/min.) Based on the calibration results, a first or a second order polynomial was found to describe the volume flow through the VAFMs as a function of the VAFM marker position. All gases entered the VAFMs at an overpressure of 0.15 or 0.20 MPa. The compressed air was supplied from a compressor in the laboratory and the commercial graded fuels were supplied from high pressure gas cylinders. Fuel and air were mixed after passing through the VAFMs and transported to the pipe in a 7-10 meter long transport tube. A sketch of the gas handling unit is given in Figure 3.5.

3.2.4 Data acquisition and recording unit

The data acquisition and recording unit measured the experimental overpressures and saved the digital pressure records on the hard drive of the laboratory computer. The unit was build up by pressure transducers, a trigger signal, amplifiers, connector blocks, sampling boards and a laboratory computer. A schematic diagram of the data acquisition and recording unit is given in Figure 3.6.

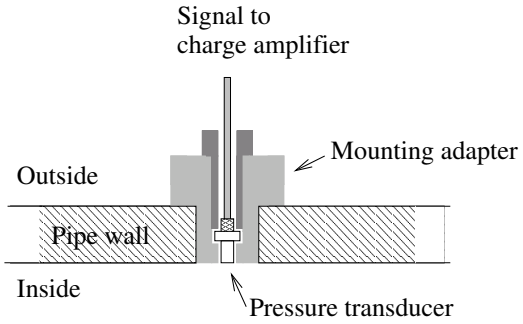

Figure 3.7: The mounting of a pressure transducer inside the pipe.

Table 3.1: Pressure transducer specifications from the manufacturer.

Transducer	603B	7001
Range [bar]	0-200	0-250
Natural frequency [kHz]	400	570
Sensor diameter [mm]	5.5	9.5
Material	Quartz	Quartz

Pressure transducers and amplifiers

The experimental overpressures have been measured with Kistler 7001 and Kistler 603B pressure transducers. These pressure transducers are hermetically sealed and have a stainless steel sensor body. Both senor models are designed in such a way that the measured pressure is acting on a piezo electrical quartz crystal through a stainless steel diaphragm. The quartz crystal transforms the pressure p [bar] into an electrical charge Q [pC]. The response times, the outer diameters and the measuring ranges of the two sensor types, are given in Table 3.1. Each pressure transducer is calibrated by the manufacturer and have a unique sensitivity [pC/bar].

The pressure transducers are placed in a mounting adapter before they are put inside the pipe. A sketch of a pressure transducer and a mounting adapter inside the pipe, is shown in Figure 3.7. The sketch shows the pipe and the pressure transducer in the axial direction.

Each pressure transducer was connected to a charge amplifier. Both Kistler 5011 and Kistler 5041 charge amplifiers were used. The specific sensitivity of the pressure transducers have to be fed in to the amplifiers. All the amplifiers were configured to give 1 or 10 bar/V as the output signal.

Sampling boards

Each charge amplifier was connected to a shielded connector block. The Kistler 5011 amplifiers were connected to a National Instruments BNC 2110 connector block and all the Kistler 5041 amplifiers were connected to a National Instruments SCB-68 connector block. The trigger signal from the ignition unit was also connected to the BNC 2110 connector block. Each connector block was further connected to a National Instruments 6110 PCI sampling board. It was these sampling boards that converted the analog voltage signals into digital signals. The sampling boards tolerate input signals in the range of $\pm$ 42 V and they have 4 input channels which can be sampled at a sampling rate up to 5 Mega samples per second [MHz]. The two sampling boards were installed in a laboratory computer running Windows. Initially the laboratory computer had a limitation in the sampling frequency. It could not perform samples at a frequency higher than 0.5 MHz. But this computer was later replaced with a DELL gx280. Sampling rates up to 1.5 MHz were used with this new computer. The communication between the operator,

the operational system and the sampling boards, was controlled by a LabView interface developed at Telemark University College. This interface allows the operator to configure things like the sampling rate, the total number of samples , the number of pre trigger samples and the project name. The interface starts the recording when a signal appears on the trigger channel and saves the pressure records as both binary and ASCII files on the hard drive of the laboratory computer. These files contains eight columns of the measured pressure at each time step. A typical file contains 0.5 M samples and has the size of 37.8 M bytes in the ASCII format and 7.7 M bytes in the binary format.

3.2.5 Data post processing

The post processing of the experimental pressure records have been done with MATLAB [27] on a Dell gx280 computer running Linux. The pressure transducers create a considerable amount of noise in the experiments with a strong deflagration and in the experiments with a transition to detonation. Many of the pressure records therefore had to be filtered before they could be analyzed. Various types of MATLAB scripts have been written to analyze the pressure records.

The pressure records from the various experiments have been backed up at a separate file server which was located in another building. This file server was accessible via internet to the whole research group. The uploading and downloading of pressure records to or from the server were done through the two file transfer programs *scp* and *sftp* [28].

3.3 Results and discussion

Gas explosion experiments with premixed fuel and air have been performed. Three different pipes and four different fuels at various fuel concentrations were used. The fuels were hydrogen, propane, methane and a mix of hydrogen and carbon monoxide. The pipes had an inner diameter of 107 mm and lengths of 3.0, 4.0 and 7.0 m. Both the 4.0 and 7.0 m pipes had an obstacle placed inside the pipe 1.0 m from the ignition source. The experimental overpressures were measured with Kistler pressure transducers. A more detailed description of the experimental setup is given in Section 3.2. Table 3.2 gives an overview of the various combinations of fuels and pipes that were used in the experiments. A dark bullet ('•') in this table represents an experiment and a circle ('○') represents no experiment. All the experiments were done at atmospheric conditions and at room temperature. Before each experiment the pipes were filled with the premixed gas at the right equivalence ratio for a time larger than the time it took to fill the pipe volume three times. The hand valves at the end walls and the VAFM were closed just prior to ignition. All the pipes had the ignition end slightly elevated. Usually two or more parallels were taken for each experiment. The primary focus of this experimental work was to see how the blockage ratio of the obstacle and the equivalence ratio of the premixed fuel and air affected the flame propagation.

This section has been divided into five subsections. There is one subsection for each fuel type (Subsection 3.3.1 - 3.3.4) plus one subsection which gives a brief discussion of the uncertainties in the experiments (Subsection 3.3.5).

Table 3.2: The various fuel and pipe combinations used in the experiments. A dark bullet ('•') represents an experiment and a circle ('○') represents no experiment.

Fuel	Pipe types		
	3.0 m	4.0 m	7.0 m
H_2	•	•	•
$CO + H_2$	○	•	○
C_3H_8	○	•	○
CH_4	○	•	○

Table 3.3: The various hydrogen concentrations used in the experiments.

Mixture	Φ	% volume
1	0.26	10
2	0.42	15
3	0.60	20
4	0.79	25
5	1.02	30
6	1.28	35
7	1.59	40
8	1.95	45
9	2.38	50

3.3.1 Hydrogen and air

The majority of the experiments were performed with premixed hydrogen and air. Nine different equivalence ratios and three different pipes were used. The volume concentration of hydrogen was ranging from 10 to 50 percent. This is equivalent to equivalence ratios ranging from 0.26 to 2.38. The pipes had lengths of 3.0, 4.0 and 7.0 m. Pressure transducers were used to measure the experimental overpressures. The overall reaction of hydrogen and air as a function of the equivalence ratio, can be written as[1]

$$\begin{aligned} 2\Phi H_2 + (O_2 + 3.762N_2) &\longrightarrow 2\Phi H_2O + (1-\Phi)O_2 + 3.762N_2 \quad \text{, if } \Phi \leq 1 \\ 2\Phi H_2 + (O_2 + 3.762N_2) &\longrightarrow 2H_2O + 2(\Phi - 1)H_2 + 3.762N_2 \quad \text{, if } \Phi \geq 1 \end{aligned} \tag{3.2}$$

Table 3.3 gives an overview of the different fuel concentrations used in the experiments. The experimental results are presented separately for each pipe length.

3.0 m pipe

Gas explosion experiments with premixed hydrogen and air have been carried out in a 3.0 m long steel pipe with an inner diameter of 107 mm. The pipe was smooth, circular and closed. Six pressure transducers were distributed along the pipe to measure the experimental overpressures. One pressure transducer was located at the end wall close to the ignition source (P0) and the rest of the transducers were located at each half meter down the pipe (P1 - P5). The objective of these experiments was to enhance the understanding of flame propagation in a closed and unobstructed pipe.

The first 25 ms of the recorded overpressure from a gas explosion experiment in the 3.0 m pipe with 35 volume percentage of hydrogen, is shown in Figure 3.8 and Figure 3.9. Figure 3.8 shows the overpressure at pressure transducer P0. The first overpressure in this

[1]It is assumed for simplicity that the products are only H_2, O_2, N_2 and H_2O.

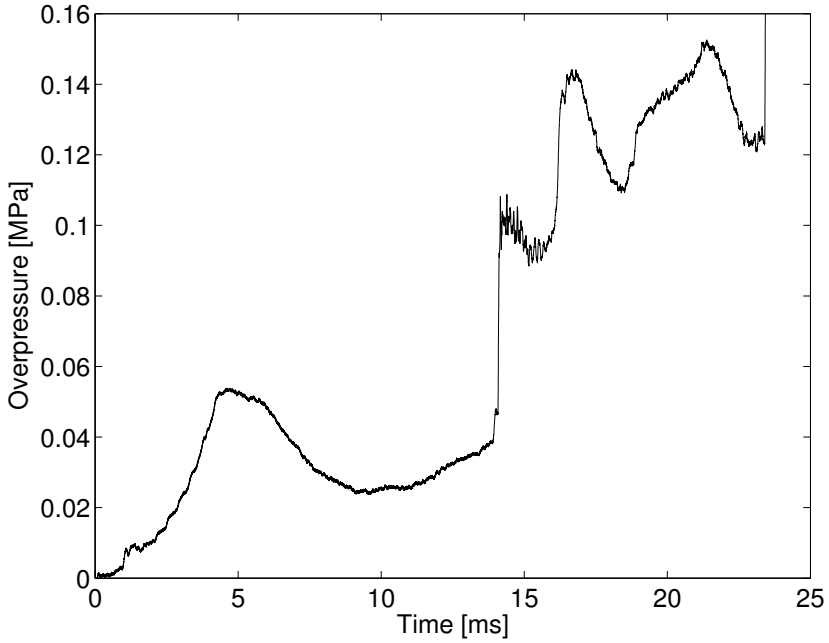

Figure 3.8: Experimental overpressure at pressure transducer P0 in the 3.0 m pipe. The hydrogen volume percentage was 35.

experiment is recorded by P0 after approximately 1.0 ms. The recorded overpressure then increases exponentially until it reaches a local maximum at approximately 4.5 ms. Thereafter the overpressure decreases for several milliseconds until it slowly increases again. At approximately 14 ms a small pressure wave and a shock wave are registered by the transducer. The build up and fall of the recorded overpressure around 4.5 ms can be related to the second and third flame propagation stages described by Clanet and Searby [1]. (See Subsection 2.3.1.) After the ignition the flame propagation in the axial direction is much faster than in the radial direction. The flame therefore gets an increasing elongated semi-ellipsoid shape. This leads to an exponential growth of both the flame surface area and the pressure. The flame continues to grow until the parts of the flame that is burning in the radial direction is quenched at the contact surfaces with the pipe side wall. The local pressure maximum at 4.5 ms can be related to the beginning of this quenching. Both the flame surface area, the pressure and the flame propagation will now be reduced as larger parts of the flame is being quenched. According to Clanet and Searby [1] the flame will now go through an inversion process. The local pressure minimum at 8.5 ms can be related to this inversion process. When the flame has completed the inversion process, it starts to propagate with an increasing elongated semi-ellipsoid shape again. This will once more give an exponential growth of both the flame surface area and the pressure. In this experiment the flame interacts with the two reflected pressure waves that is recorded by pressure transducer P0 after approximately 14 ms.

Figure 3.9 shows the recorded overpressure at all the six pressure transducers used in the experiment. The overpressures have been multiplied by two and they are plotted as a function of both time and the pressure transducer position in the pipe. A pressure wave is reflected by both the end walls and the flame. But a pressure wave can also interact with

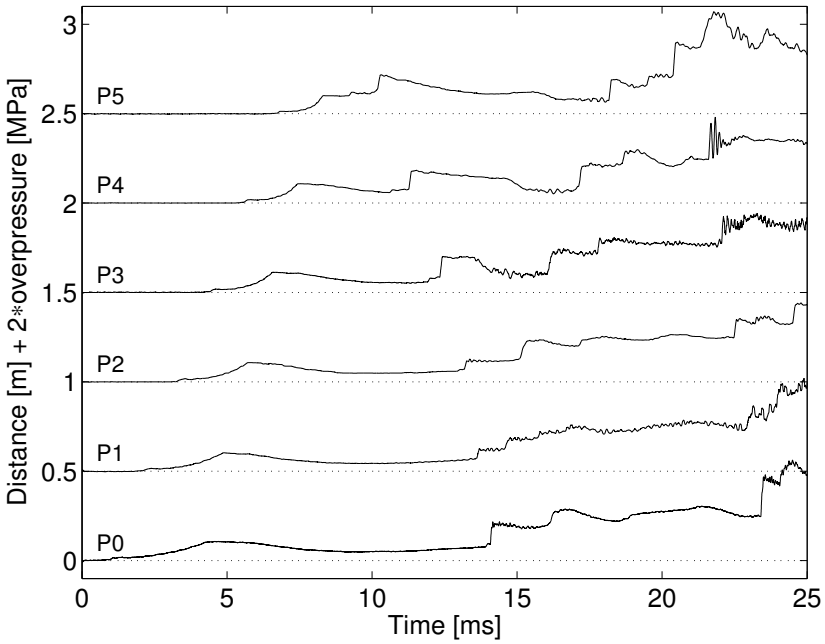

Figure 3.9: Experimental overpressures at pressure transducer P0 - P5 in the 3.0 m pipe for a hydrogen volume percentage of 35. The overpressures have been multiplied by two and they are shifted along the vertical axis to indicate the pressure transducer positions in the pipe. (1.0 m corresponds to 1.0 MPa.)

the flame and change the burning rate and the structure of the flame. The complexity of the system therfore increases very fast as the flame propagates down the pipe. The first two pressure structures described in Figure 3.8 (at 1.0 and 4.5 ms), can be traced in Figure 3.9 as they propagate down the pipe. The first pressure structure propagates down the pipe as a sonic pressure wave and reflects off the opposite end wall at approximately 8.0 ms. This gives a velocity of about (3.0 m)/(7.0 ms) = 429 m/s. SuperSTATE [25] gives the sound of speed in the unburned gas to be 419 m/s for the initial conditions of 0.1 MPa and 300 K. The second wave structure is reflected off the end wall as a fully developed shock at approximately 9.0 ms. This shock wave has a higher velocity than the sonic pressure wave and the distance between the two waves therfore decreases as they propagates back up the pipe. The time difference between the two waves are approximately 0.4 ms at pressure transducer P3 and 0.2 ms at pressure transducer P0. The two wave structures can be spotted in Figure 3.8 at approximately 14.0 ms as they are reflected off the ignition wall. It can also be seen from Figure 3.9 that the two wave structures propagate much faster in the products than in the reactants. This is the main reason why the first wave structure only uses approximately 14.0 ms - 8.0 ms = 6.0 ms to propagate back up the pipe. SuperSTATE gives the speed of sound in the products to be 1141 m/s.

The local pressure maximum described in Figure 3.8 appears at different times and with different magnitudes for the various fuel concentrations. Table 3.4 shows the time and magnitude of this first local pressure maximum at pressure transducer P0 for the various hydrogen volume percentages. It was stated in Chapter 2 that the flame propagation right after the ignition is laminar. Both the time of appearance and the magnitude of the

local pressure maximum, mirrors the laminar burning velocity for the various equivalence ratios.

Table 3.4: The various times and overpressures for the first local pressure maximum at pressure transducer P0 in the 3.0 m pipe.

H_2 (% volume)	Overpressure [MPa]	Time [ms]
20	0.01	14.0
25	0.03	7.5
30	0.04	5.5
35	0.05	4.5
40	0.05	4.5
45	0.04	5.0
50	0.03	5.5

The maximum recorded overpressure at pressure transducer P2 and P4 as a function of the hydrogen volume percentage, is shown in Figure 3.10. The constant volume combustion (CVC) pressure calculated by SuperSTATE, is also plotted in the figure. The experimental pressures are lower than the theoretical, but they show a similar behavior for the various volume percentages of hydrogen. There is also an increasing difference between the experimental and theoretical pressures for the less reactive mixtures. This difference can be related to the nature of the pressure transducers and the heat conduction to the surroundings. The piezo electrical material in the pressure transducers can not hold their charge for a long period of time. If the flame propagation in the pipe is slow compared to the rate in which the pressure transducers are loosing charge, then the recorded pressure will be lower than the actual experimental pressure. A deflagration to detonation transition was not observed in any of the experiments with the 3.0 m pipe.

4.0 m pipe

A closed steel tube with a single internal obstacle has been used to study gas explosions in premixed hydrogen and air. The pipe was 4.0 m long and had an inner diameter of 107 mm. The experimental overpressures were measured with six pressure transducers. One pressure transducer was located at the end wall close to the ignition source (P0). The rest of the transducers were located 1.5 m from the ignition source (P1) and at every 0.5 m down the pipe (P2 - P5). These experiments were performed to enhance the understanding of flame propagation in a closed and single obstructed pipe.

Obstacles of various kinds are known to provide good conditions for positive flame acceleration and an increased burning velocity. A strong flame acceleration may also under the right conditions result in a deflagration to detonation transition [12]. The combustion induced flow increases the flame surface area around obstacles and obstacles generate turbulence in the combustion induced flow. Turbulence increases the burning rate by increasing the flame surface area and the local transport of heat and reactants in the reaction zone. But turbulence which is too intense, may also cause local or global quenching of the flame.

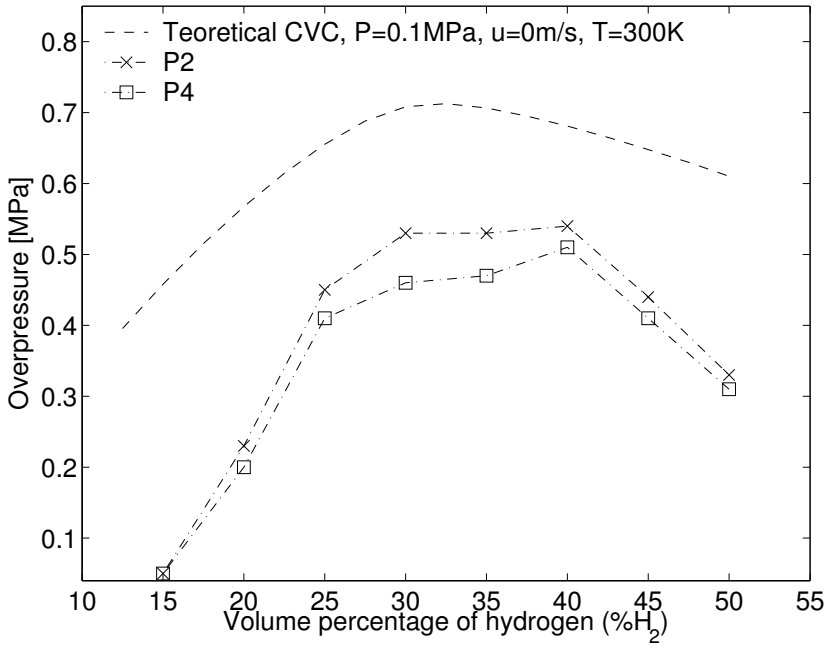

Figure 3.10: Maximum overpressure at pressure transducer P2 and P4 for the various volume percentages of hydrogen in the 3.0 m pipe. (CVC is an abbreviation for constant volume combustion.)

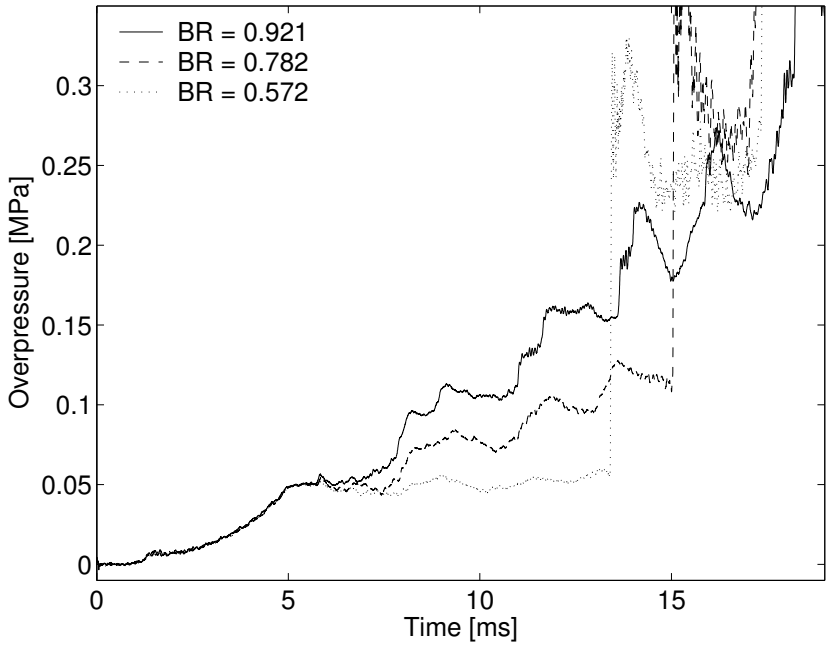

Figure 3.11: Experimental overpressures at pressure transducer P0 in the 4.0 m pipe. The experiments were performed with a hydrogen volume percentage of 30 and with obstacle opening diameters of 30, 50 and 70 mm.

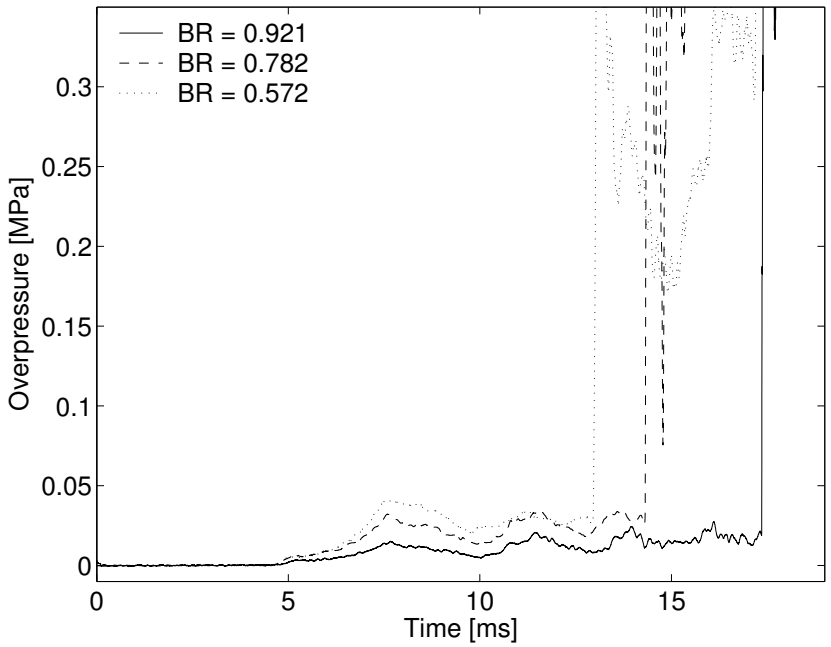

Figure 3.12: Experimental overpressures at pressure transducer P1 in the 4.0 m pipe. The experiments were performed with a hydrogen volume percentage of 30 and with obstacle opening diameters of 30, 50 and 70 mm.

Figure 3.11 and Figure 3.12 show the experimental overpressures at pressure transducer P0 and P1 for three different blockage ratios and a hydrogen volume percentage of 30. The obstacle opening diameters are 30, 50 and 70 mm. The first overpressures in Figure 3.11 are recorded by pressure transducer P0 after 1.3 ms. The pressures then increase exponentially until approximately 5.0 ms after the ignition. This pressure evolvement is similar to the one described in Figure 3.8 for the unobstructed 3.0 m pipe. The small pressure peak that is superimposed on the pressure after about 5.7 ms, is the reflected pressure wave from the obstacle. SuperSTATE gives the speed of sound to be 405 m/s for the unburned gas mixture. This first pressure wave should therfore use less than (2.0 m)/(405 m/s) = 4.9 ms to propagate the distance from P0 to the obstacle and back again. This implies that the first 5.7 ms of the pressure recordings in Figure 3.11 are independent of the obstacle. The magnitude of the obstacle reflected pressure wave depends on the blockage ratio of the obstacle. Figure 3.11 also shows that the pressure recordings at pressure transducer P0 after 5.7 ms, increase with decreasing obstacle opening diameter. Guénoche [2] has reported that the mean axial flame speed between the ignition wall and the obstacle, tends to decrease with increasing blockage ratio. The reduced flame speed is explained by the hindering of the flow of unburned gas in the longitudinal direction towards the obstacle. This results in a pressure build up in front of the flame. The pressure build up both flattens the flame and makes it reach the pipe side wall in the radial direction sooner than it does without a constriction. Both of these two effects result in a reduced flame surface area and a reduced burning rate.

The flow of unburned gas in front of the flame passing through the obstacle, will create a turbulent flow field on the other side of the obstacle. If this turbulent flow field is not

too intense, it will accelerate the flame and in some cases lead to a DDT. The reduction of the mean axial velocities of the flame as a function of the blockage ratio, is illustrated by Figure 3.11 and Figure 3.12. The obstacle caused shocks arrive later at both pressure transducer P0 and P1 for the higher blockage ratios. It is therefore interesting to note that the increase in the recorded overpressure at pressure transducer P0 for the higher blockage ratios, is mainly caused by the hindering of the flow of unburned gas through the obstacle and not by an increased burning rate.

Examples of three typical wave patterns obtained in the gas explosion experiments with hydrogen and air, are shown in Figure 3.13, 3.14 and 3.15. Figure 3.13 is an example of a pressure record with a DDT after the obstacle and a propagating detonation. The volume percentage of hydrogen was 35 and the obstacle opening diameter was 70 mm in this experiment. The maximum overpressure at pressure transducer P2 is approximately 1.83 MPa and it was recorded after 12.0 ms. In this type of experiments the obstacle caused shock propagated down the pipe with an overpressure of approximately 1.4 to 2.0 MPa. These shock waves often gave the highest recorded overpressure for each transducer. Figure 3.14 is an example of a pressure record with a strong deflagration after the obstacle and a DDT close to the end of the pipe. The transition to detonation is most likely caused by the interaction between the flame and the obstacle caused shock wave that is reflected off the end wall. The volume percentage of hydrogen was 30 and the obstacle opening diameter was 70 mm in this experiment. Approximately 25.2 ms after the ignition the overpressure at pressure transducer P2 is about 0.43 MPa. But the maximum overpressure at pressure transducer P5 is 1.72 MPa after about 28.1 ms. This phenomenon occurred only for strong deflagrations with a volume percentage of hydrogen close to the stoichiometric percentage. Figure 3.15 is an example of a pressure record with a deflagration after the obstacle. The volume percentage of hydrogen was 20 and the obstacle opening diameter was 80 mm in this experiment. The maximum overpressure at pressure transducer P5 is approximately 0.27 MPa and it was recorded after 41.7 ms. The recorded overpressures are strongly related to the strength of the deflagration for this type of experiments. But the shock waves are much weaker and they propagate at a much lower velocity than the shock waves in the experiments with a detonation.

The set of blockage ratios and volume percentages of hydrogen that gave a DDT after the obstacle, is shown by the DDT matrix in Table 3.5. A circle ('$\circ$') represents an experiment without a DDT, a cross ('$\times$') represents an experiment with parallels both with a DDT and without a DDT (critical values) and a dark bullet ('$\bullet$') represents an experiment with a DDT. This matrix shows that there is a higher concentration of DDTs on the rich fuel side of the gas mixtures and that the results are almost symmetrically distributed around a hydrogen volume percentage of 35. An experiment may not be reproducible due to the stochastic nature of turbulence. This can give experimental parallels both with a DDT and without a DDT. The experiments were marked as a DDT in Table 3.5 when the velocity of the obstacle caused shock wave was close to the theoretical CJ detonation velocity and if the pressure peak of this shock wave was 1.4 MPa or higher.

Both the experimental and the theoretical CJ detonation velocities are shown in Figure 3.16 as a function of the volume percentage of hydrogen. The theoretical velocities are obtained from SuperSTATE with the initial conditions of zero fluid flow, a temperature of 300 K and a pressure of 0.1 MPa. The experimental velocities are given relative

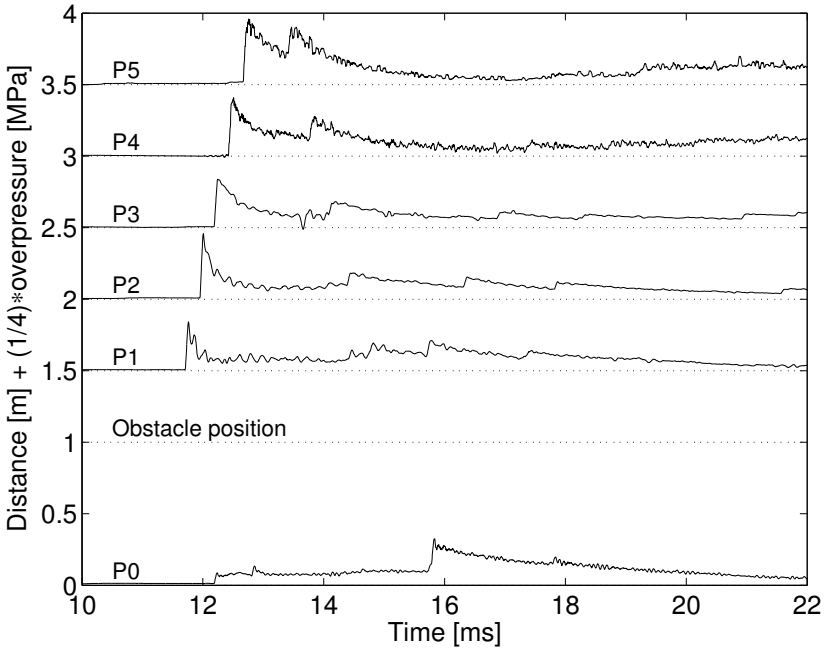

Figure 3.13: An experimental pressure record with a DDT after the obstacle and a propagating detonation in the 4.0 m pipe for $D_o = 70$ mm and $\Phi = 1.28$. The overpressures have been divided by four and they are shifted along the vertical axis to indicate the pressure transducer positions in the pipe. (1.0 m corresponds to 1.0 MPa.)

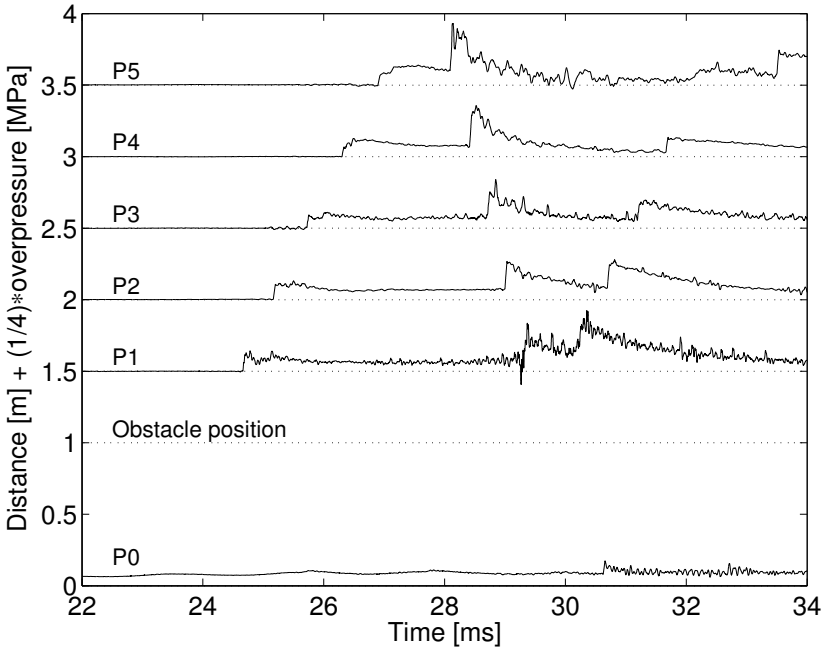

Figure 3.14: An experimental pressure record with a deflagration wave after the obstacle and a DDT close to the pipe end in the 4.0 m pipe for $D_o = 70$ mm and $\Phi = 1.0$. The overpressures have been divided by four and they are shifted along the vertical axis to indicate the pressure transducer positions in the pipe. (1.0 m corresponds to 1.0 MPa.)

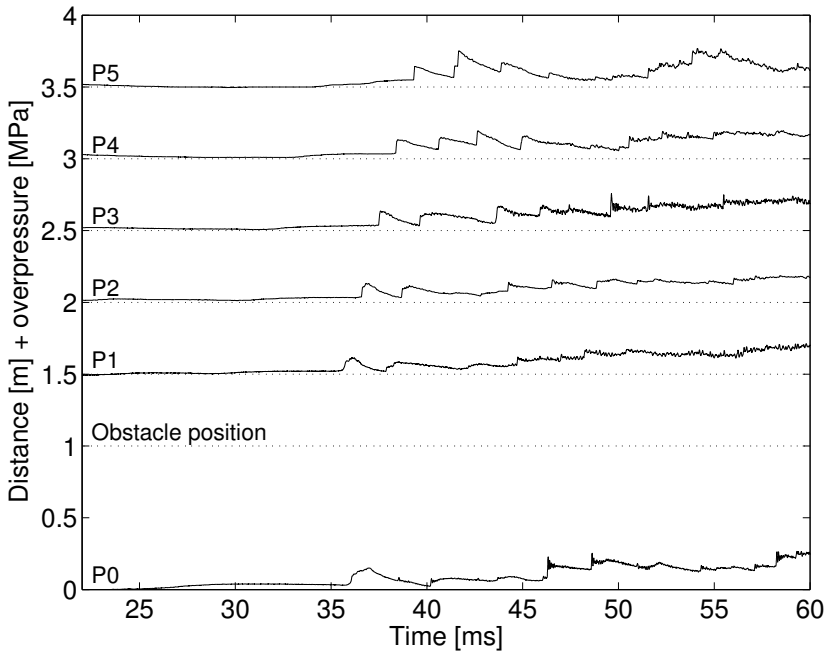

Figure 3.15: An experimental pressure record with a deflagration wave after the obstacle in the 4.0 m pipe. The obstacle opening diameter was 80 mm and the hydrogen volume percentage was 20. The overpressures are shifted along the vertical axis to indicate the pressure transducer positions in the pipe. (1.0 m corresponds to 1.0 MPa.)

Table 3.5: The experimental DDT matrix for the 4.0 m pipe. A circle ('$\circ$') represents an experiment without a DDT, a cross ('$\times$') represents an experiment with parallels both with a DDT and without a DDT, and a dark bullet ('$\bullet$') represents an experiment with a DDT.

Blockage ratio	Obstacle opening diameter [mm]	H_2 (% volume)								
		10	15	20	25	30	35	40	45	50
0.998	5	$\circ$	$\circ$	$\circ$	$\circ$	$\circ$	$\circ$	$\circ$	$\circ$	$\circ$
0.991	10	$\circ$	$\circ$	$\circ$	$\circ$	$\circ$	$\circ$	$\circ$	$\circ$	$\circ$
0.965	20	$\circ$	$\circ$	$\circ$	$\circ$	$\times$	$\times$	$\circ$	$\circ$	$\circ$
0.921	30	$\circ$	$\circ$	$\circ$	$\times$	$\bullet$	$\bullet$	$\bullet$	$\times$	$\circ$
0.782	50	$\circ$	$\circ$	$\circ$	$\circ$	$\bullet$	$\bullet$	$\bullet$	$\circ$	$\circ$
0.572	70	$\circ$	$\circ$	$\circ$	$\circ$	$\circ$	$\times$	$\circ$	$\circ$	$\circ$
0.441	80	$\circ$	$\circ$	$\circ$	$\circ$	$\circ$	$\circ$	$\circ$	$\circ$	$\circ$

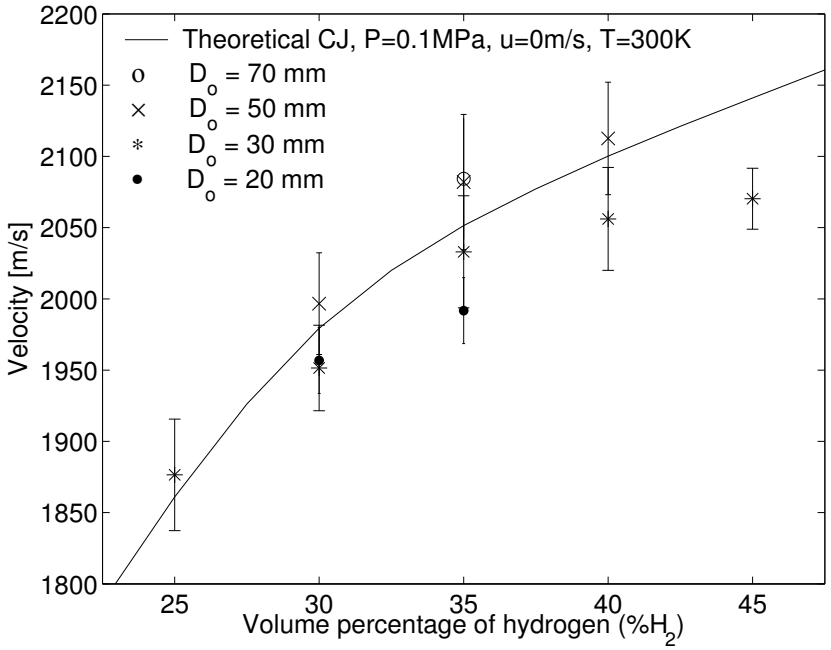

Figure 3.16: Experimental and theoretical CJ detonation velocities. The experimental velocities are given as the mean axial velocities of the detonations between the pressure transducers in the 4.0 m pipe.

to the pipe. The error bars on the experimental velocities indicate the standard deviation for each combination of blockage ratio and volume percentage of hydrogen. The figure shows that the experimental detonation velocities decrease with increasing blockage ratio. This may be caused by pressure waves in front of the flame. Figure 3.12 shows that the number of small pressure waves in front of the obstacle caused shock at pressure transducer P1 is increasing with an increasing blockage ratio. Table 3.6 lists the time difference in milliseconds between the first pressure wave and the detonation at pressure transducer P2. A circle ('$\circ$') in the table represents an experiment without a DDT. This table shows that also the time difference between the first pressure wave and the detonation increases with increasing blockage ratio. A detonation with a velocity of 2.0 km/s uses (0.5 m)/(2.0 km/s) = 0.25 ms from one pressure transducer to another. SuperSTATE gives the speed of sound to be 405 m/s for a stoichiometric mixture of hydrogen and air. This means that the first pressure wave uses (0.5 m)/(405 m/s) = 1.23 ms between each sensor. The detonation wave will therefore reduce the time difference with approximately 1.0 ms for each half meter down the pipe. But this is not sufficient for the detonation to pass the first pressure wave before it has reached the end of the pipe. The premixed gas was therefore already preheated and moving when the detonation was recorded by the pressure transducers.

Figure 3.17 shows the experimental DDT results as a function of both the obstacle opening diameter to detonation cell size ratio (D_o/λ_d) and the hydrogen volume percentage. This figure uses the same notation as Table 3.5 and the data for λ_d are obtained from [3, 4]. The figure shows that experiments with a DDT after the obstacle have a D_o/λ_d in the range from 0.9 to 3.9. This does almost meet the DDT criterion presented by Peraldi

Table 3.6: The time differences between the first sonic pressure wave and the detonation at pressure transducer P2 in the 4.0 m pipe. A circle ('$\circ$') represents an experiment without a DDT. The times are given in milliseconds.

Blockage ratio	Obstacle opening diameter [mm]	H_2 (% volume)				
		25	30	35	40	45
0.965	20	$\circ$	10.4	9.2	$\circ$	$\circ$
0.921	30	17.0	11.6	9.0	10.2	10.9
0.782	50	$\circ$	9.2	7.1	7.4	$\circ$
0.572	70	$\circ$	$\circ$	6.1	$\circ$	$\circ$

et al. [160] for an obstacle filled tube, i.e. that D_o has to be equal to or larger than λ_d. (See Equation (2.12).) Lindstedt and Michels [5] have on the other hand reported values of D_o/λ_d as low as approximately 0.71 for DDTs in stoichiometric mixtures of hydrocarbons and air. They used Shchelkin spirals with varying lengths in a 11.2 m long pipe. Lindstedt and Michels [5] also found that a blockage ratio of 0.44 gave the most optimum conditions for flame acceleration. Table 3.5 shows that a blockage ratio of 0.921 is the most efficient blockage ratio for our experimental setup. Another comparable study performed by Moen et al. [6] reports that DDTs in acetylene and air mixtures can occur as local explosions both in the flame jet and near the boundary of the gas confinement. They used a 11.0 m long tube connected to a 8.0 m long plastic bag. Moen et al. [6] observed that both turbulent mixing in the jet and reflected pressure waves from the physical boundaries, i.e. the ground or the plastic bag, could trigger the onset of a detonation. Since our experiments were done in a non-transparent steel tube, it is hard to know where the transitions actually took place. This needs to be investigated further.

Figure 3.18 shows the experimental results from Table 3.5 and the two curves $D_o/\lambda_d = 1$ and $(D_p - D_o)/2\lambda_d = 1$, as a function of both the obstacle opening diameter and the hydrogen volume percentage. The detonation cell size data are obtained from [3, 4] and the quantity '$(D_p - D_o)/2$' gives the radial distance between the pipe side wall and the obstacle opening. The intersection between the two curves gives the area where both D_o and $(D_p - D_o)/2$ are larger than λ_d. Figure 3.18 indicates that D_o is the limiting length scale for a DDT behind the obstacle when D_o is smaller than approximately 35 mm and that $(D_p - D_o)/2$ is the corresponding limitation when D_o is larger than approximately 35 mm. But the correspondence between the $(D_p - D_o)/2\lambda_d = 1$ curve and the experimental results for $D_o > 35$ mm, is observed to be best for the rich gas mixtures. The deviation on the lean side needs to be investigated further, but it might be related to the applied cell size data or to the physical conditions in the pipe. Figure 3.18 also shows that the experiments with a DDT meet the criterion in Equation (2.11), i.e. that the pipe diameter is larger than the detonation cell size.

An isentropic gas flow in a Laval nozzle throat will become choked (i.e. the Mach number is one), if the ratio of the upstream to the downstream pressure is equal to or larger than some critical value [188][2]. This critical value is approximately 1.9 for the

[2]Reference [188] gives the critical pressure ratio for choked flow in a Laval nozzle to be $(P1/P0) = [2/(\gamma+1)]^{\frac{\gamma}{\gamma-1}} = 0.528$, when $\gamma = 1.40$. (Table C.1 lists some γ values.)

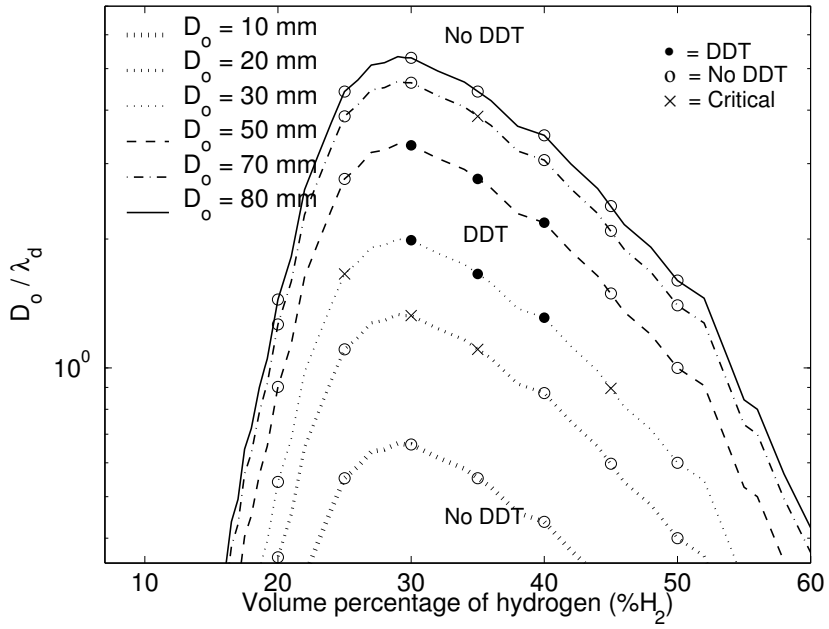

Figure 3.17: The experimental DDT results from Table 3.5 versus the detonation cell size. A circle ('$\circ$') represents an experiment without a DDT, a cross ('$\times$') represents an experiment with parallels both with a DDT and without a DDT and a dark bullet ('$\bullet$') represents an experiment with a DDT.

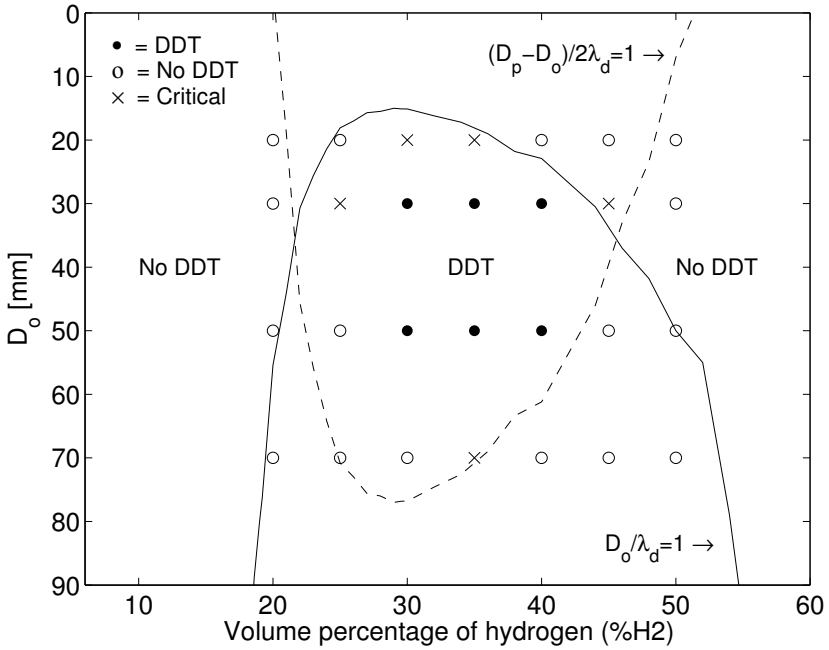

Figure 3.18: The experimental DDT results from Table 3.5 versus the three length scales D_o, $(D_p - D_o)/2$ and λ_d. A circle ('$\circ$') represents an experiment without a DDT, a cross ('$\times$') represent an experiments with parallels both with a DDT and without a DDT and a dark bullet ('$\bullet$') represents an experiment with a DDT.

Table 3.7: The ratio of the absolute pressures recorded at pressure transducer P0 and P1 (i.e. P0/P1) for the experiments with a DDT after the obstacle in the 4.0 m pipe. A circle ('○') represents an experiment without a transition to detonation.

Blockage ratio	Obstacle opening diameter [mm]	H_2 (% volume)				
		25	30	35	40	45
0.965	20	○	4.5	4.5	○	○
0.921	30	2.1	3.1	3.1	3.2	2.9
0.782	50	○	1.7	1.7	1.7	○
0.572	70	○	○	1.2	○	○

hydrogen and air mixtures used in this study. Table 3.7 gives the ratio of the absolute pressures recorded at pressure transducer P0 and P1 (i.e. P0/P1), for the experiments with a transition to detonation after the obstacle. The pressures used in this table are the overpressures recorded just prior to the obstacle caused shock with the addition of one atmosphere. For a blockage ratio of 0.782, this corresponds to an absolute P0 of approximately 0.22 MPa at 14.5 ms in Figure 3.11 and an absolute P1 of approximately 0.13 MPa at 14.0 ms in Figure 3.12. If the pressure ratios in Table 3.7 are used as a first approximation of the pressure ratio across the obstacle at the time when the flame goes through the obstacle, then the majority of the experiments had a choked flow in the obstacle at that time. The most significant exception occurs for the experiment with a hydrogen volume percentage of 35 and an obstacle opening diameter of 70 mm. The recorded overpressures at pressure transducer P0 and P1 in this experiment, indicate that a transition to detonation can occur behind the obstacle in a single obstructed pipe, even when the unburned gas flow in the obstacle is subsonic. Choked combustion (i.e. supersonic combustion) is on the other hand a DDT criterion in areas with strong confinement and heavy obstructions, such as obstacle filled tubes [12]. Thibault et al. [133] have reported choking conditions in an orifice for fuel and air mixtures, when the pressure ratio across the orifice reached approximately 1.8.

The strength of the obstacle caused shock depends both on the blockage ratio of the obstacle and on the equivalence ratio of the gas mixture. The velocities of the propagating detonations were shown in figure 3.16 and it was stated in Chapter 2 that a detonation is a self sustaining process where the reaction zone is coupled with the lead shock. Figure 3.19 and 3.20 show the piecewise mean axial velocity of the obstacle caused shocks for various obstacle opening diameters. None of the experiments had a DDT after the obstacle and the volume percentage of hydrogen was 20 in Figure 3.19 and 45 in Figure 3.20. The velocities are taken as the mean axial velocity between the pressure transducers. These two figures show that for some of the experiments there is a significant drop in the velocities as the shock propagates down the pipe. This velocity drop is generally strongest for the first 1.5 m after the obstacle. Examples of this are the experiments with an obstacle opening diameter of 20 and 30 mm in Figure 3.19 and the experiments with an obstacle opening diameter of 30 and 50 mm in Figure 3.20. Other experiments had little variation in the mean axial velocity of the obstacle caused shock. Examples of this are the experiments with an obstacle opening diameter of 10 and 80 mm in Figure 3.19

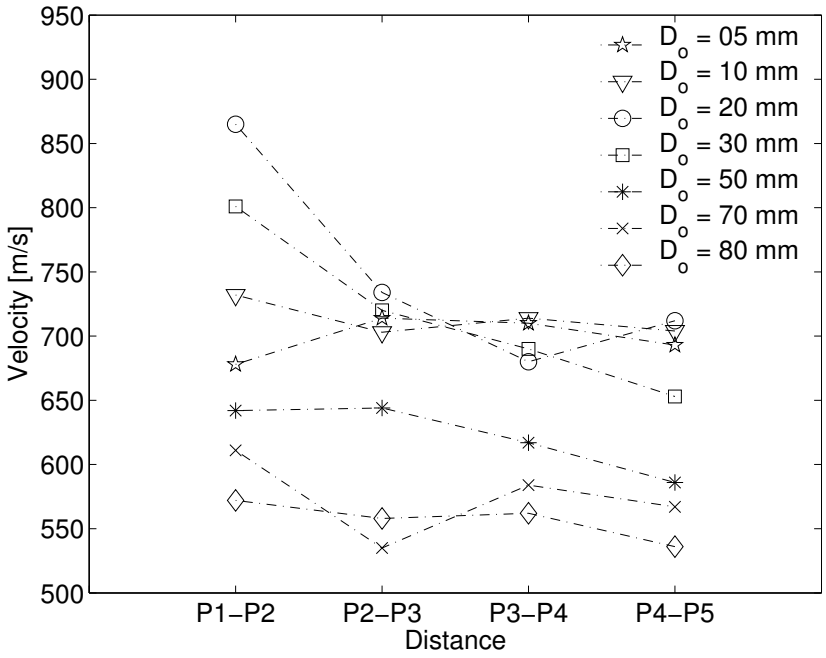

Figure 3.19: Mean axial shock velocities between the pressure transducers in the 4.0 m pipe for the various obstacle opening diameters. The hydrogen volume percentage was 20.

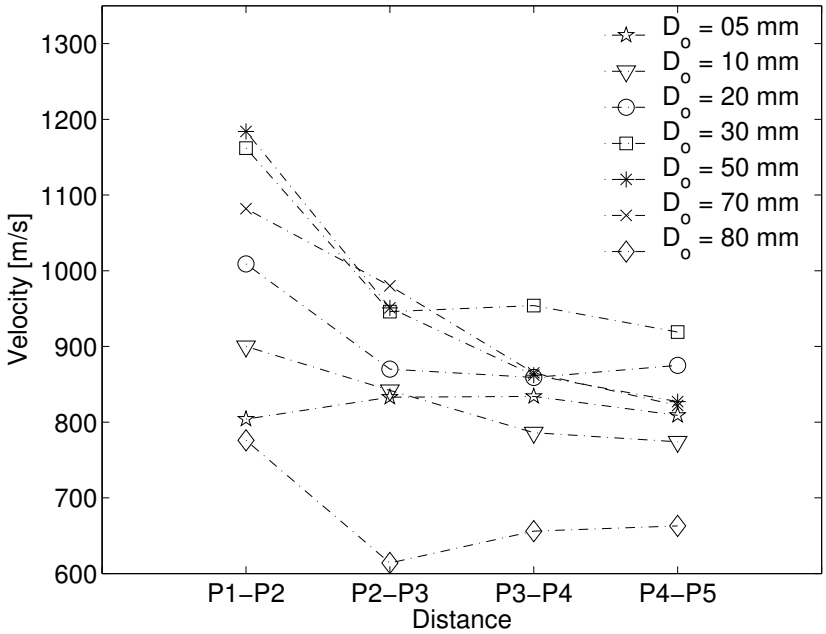

Figure 3.20: Mean axial shock velocities between the pressure transducers in the 4.0 m pipe for the various obstacle opening diameters. The hydrogen volume percentage was 45.

and the experiments with an obstacle opening diameter of 5 mm in Figure 3.20. Chue et al. [58] have reported that there is a higher degree of coupling between the leading shock and the reaction zone for deflagrations with small lead shock velocity variations compared to deflagrations with larger variations in lead shock velocity. The experiments with an obstacle opening diameter of 5 mm had the smallest variation in the mean axial velocity of the obstacle caused shock. These experiments also had the smallest variation in the shock velocities between the different equivalence ratios.

7.0 m pipe

A 7.0 m long and closed steel tube with a single internal obstacle has been used to study gas explosions in premixed hydrogen and air. The pipe had an inner diameter of 107 mm and seven pressure transducers were distributed along the pipe to measure the experimental overpressures. One pressure transducer was located at the end wall close to the ignition source (P0). The rest of the transducers were located 1.5 m away from the ignition source (P1) and at every 1.0 m down the pipe (P2 - P5). These experiments were performed to investigate how pressure waves that have been reflected off the pipe end wall affect the flame propagation.

The experimental overpressures at pressure transducer P0 and P1 from pairwise corresponding experiments with the 4.0 and the 7.0 m pipe, are plotted in Figure 3.21 and Figure 3.22. All the four experiments were performed with an obstacle opening diameter of 50 mm. The hydrogen volume percentage was 20 in Figure 3.21 and 30 in Figure 3.22. In Figure 3.21 the first overpressure was recorded by pressure transducer P0 after approximately 3.5 ms. SuperSTATE gives the speed of sound to be 381 m/s for the unburned gas mixture. This first pressure rise will therfore use less than (8.0 m)/(381 m/s) = 21.0 ms for the 4.0 m pipe and (14.0 m)/(381 m/s) = 36.7 ms for the 7.0 m pipe, to propagate down the pipe and back up again. The first 24 ms of the pressure evolvement at pressure transducer P0 and P1 for the two pipes are similar. But the pressure recordings at P0 then show that there is a delay of approximately 14 ms on the pressure evolvement of the 7.0 m pipe compared to the 4.0 m pipe. These 14 ms are equal to a sonic wave propagation distance of (381 m/s)·14 ms = 5.3 m, which is close to the total difference in the propagation distance between the two pipes. This implies that the flame propagation between the ignition wall and the obstacle in these two experiments, is affected by the difference in pipe lengths. It also implies that that first reflected pressure wave is important for the flame acceleration. Both of these two experiments had a deflagration after the obstacle.

In Figure 3.22 the first overpressure is recorded after approximately 1.4 ms at pressure transducer P0. SuperSTATE gives the speed of sound to be 405 m/s for the unburned gas mixture. The first recorded overpressure will therfore use less than (8.0 m)/(405 m/s) = 19.8 ms for the 4.0 m pipe and (14.0 m)/(405 m/s) = 34.6 ms for the 7.0 m pipe, to propagate down the pipe and back. It will further take 17.3 ms for this pressure rise to reach the obstacle from the other side in the 4.0 m pipe. But Figure 3.22 shows that the obstacle caused shock is recorded by transducer P1 already after 14.9 ms. This indicates that the flame propagation between the ignition wall and the obstacle is unaffected by the difference in pipe lengths in these two experiments. This observation is also in good agreement with the experimental results. Both of these two experiments had a DDT and a propagating detonation after the obstacle.

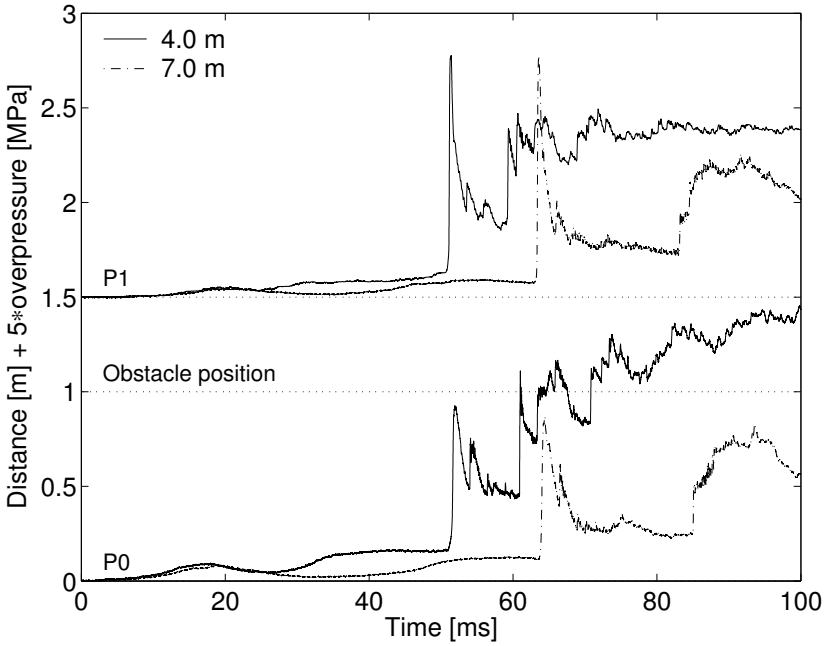

Figure 3.21: Experimental overpressure at pressure transducer P0 and P1 in the 4.0 and 7.0 m pipe for $D_o = 50$ mm and a hydrogen volume percentage of 20. The overpressures have been multiplied by five and P1 is shifted 1.5 MPa along the vertical axis to indicate the pressure transducer position in the pipe. (1.0 m corresponds to 1.0 MPa.)

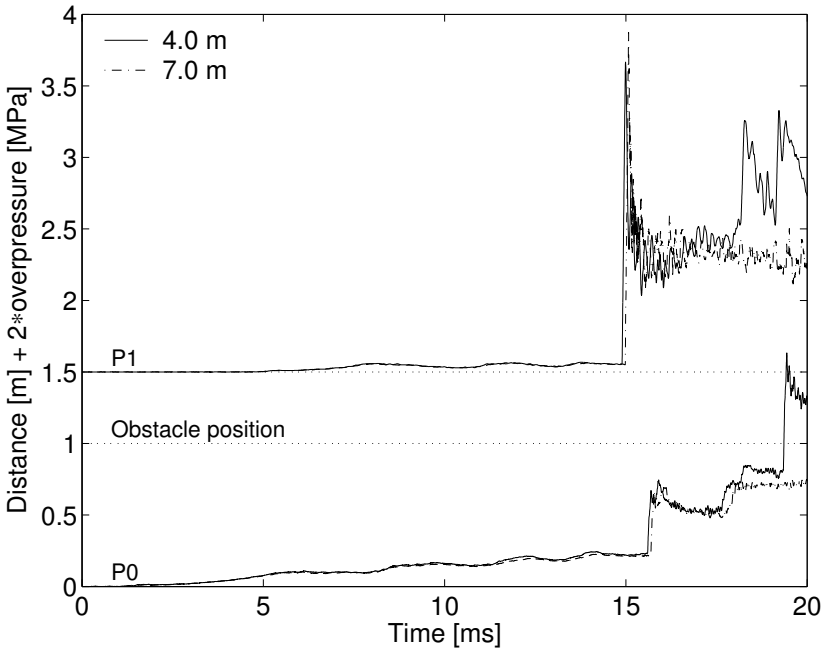

Figure 3.22: Experimental overpressure at pressure transducer P0 and P1 in the 4.0 and 7.0 m pipe for $D_o = 50$ mm and a hydrogen volume percentage of 30. The overpressures have been multiplied by two and P1 is shifted 1.5 MPa along the vertical axis to indicate the pressure transducer position in the pipe. (1.0 m corresponds to 1.0 MPa.)

3.3.2 Hydrogen, carbon monoxide and air

A 4.0 m long steel tube with a single internal obstacle has been used to study gas explosions with premixed hydrogen, carbon monoxide and air. The pipe was closed at both ends and had an inner diameter of 107 mm. Six pressure transducers were distributed along the pipe to measure the experimental overpressures. One pressure transducer was located at the end wall close to the ignition source (P0). The rest of the transducers were located 1.5 m from the ignition source (P1) and at every 0.5 m down the pipe (P2 - P5). A more detailed description of the experimental setup is given in Section 3.2 and a sketch of the pipe can be found in Figure 3.2. The overall reaction of stoichiometric hydrogen, carbon monoxide and air as a function of the mole fraction of hydrogen in the fuel, can be written as

$$\begin{aligned} 2x\mathrm{H_2} + 2(1-x)\mathrm{CO} + (\mathrm{O_2} + 3.762\mathrm{N_2}) \longrightarrow \\ 2x\mathrm{H_2O} + 2(1-x)\mathrm{CO_2} + 3.762\mathrm{N_2} \end{aligned} \quad , \tag{3.3}$$

where 'x' is the mole fraction of hydrogen in the fuel.

Carbone monoxide is a flammable, colorless and odorless gas. It is often produced industrially during gasification [183, 184] and it can be regarded as a product of an incomplete combustion of carbon containing components. Experimental data on the explosion characteristics of carbon monoxide are scant [7]. There are mainly three reasons for this. Carbon monoxide is not used as a commercial fuel, carbon monoxide does rarely occur as a significant constituent in accidental gas releases and carbon monoxide is seriously toxic [8][3].

It is known that even small amounts of added hydrogen to a carbon monoxide and air mixture, will change the explosion characteristics of the mixture. Two different series of experiments have therefore been performed to investigate the explosion and transition to detonation characteristics of various gas mixtures of hydrogen, carbon monoxide and air. These experiments were performed with an obstacle opening diameter of 30 mm, which is the same obstacle configuration that gave the most optimum conditions for a DDT after the obstacle for the hydrogen experiments described in Subsection 3.3.1. The first series of experiments were performed with a constant fuel composition of hydrogen and carbon monoxide, but with various volume percentages of the fuel. The second series of experiments were performed with a stoichiometric mixture of fuel and air, but with various volume percentages of hydrogen in the fuel.

Figure 3.23 shows the recorded maximum overpressure at transducer P2 and P4 as a function of the fuel volume percentage in the gas mixture. The constant volume combustion (CVC) overpressures calculated by SuperSTATE, are also plotted in the figure. A fuel compound consisting of 10 volume percentages of hydrogen and 90 volume percentages of carbon monoxide was used in the experiments. (This fuel compound is interesting from an industrial point of view.) As for the results with hydrogen and air in Figure 3.10, the experimental overpressures are lower than the theoretical constant volume combustion

[3] A T40 Rattler^{TM} CO gas meter was used in the laboratory at all times for safety reasons. The gas meter was also used to inspect the pipe and the gas filling unit. The inspections were conducted both under the gas filling process and after each experiment. The gas meter never gave any indications of a gas leak in the pipe or in the gas filling unit.

overpressures for the less reactive mixtures. This can probably be related to the nature of the pressure transducers and the heat conduction to the surroundings.

The lower and upper flammability limits for carbon monoxide in standard air are 12.5 and 74.0 volume percentages of carbon monoxide [50, 56]. The corresponding limits for hydrogen are 4.0 and 75.0 for an upward propagating flame [50, 56, 185]. Le Chatelier's rule [55] can in general predict the lower flammability limit of blended gases [57]. Le Chatelier's rule is given as

$$\frac{1}{f_{\mathrm{l}}} = \sum_{i}^{n} \left(\frac{x_i}{f_i} \right), \tag{3.4}$$

where f_{l} is the lower flammability limit of the gas blend, n is the number of gases in the fuel compound, x_i is the fuel mole fraction of the fuel component i and f_i is the flammability limit of fuel component i in air. According to Le Chatelier's rule the lower flammability limit is 10.3 volume percentages of fuel in air for the fuel compound in Figure 3.23. This value is relatively close to the 11.2 volume percentage predicted from the experimental results of Karim et al. [186]. The corresponding upper flammability limit was found to be 77.4 by Løyland [187]. Both Reference [186] and Reference [187] performed their experiments with an upward propagating flame at atmospheric conditions. The experimental overpressures in Figure 3.23 show that the applied fuel compound did ignite for a volume percentage of fuel ranging from 13.0 to 74.0. This range is less wide than the range created by the flammability limits mentioned above. The deviation may be related to the ignition source and the horizontal orientation of the pipe (i.e. not an upward propagating flame).

It is also shown in Figure 3.23 that the largest overpressures occurred for a fuel volume percentage of 40. These overpressures are 0.85 MPa at pressure transducer P2 and 1.05 MPa at pressure transducer P4. A transition to detonation after the obstacle was not observed in any of the experiments in Figure 3.23. Austin and Shepherd [59] have reported that the detonation cell size (λ_d) for a stoichiometric mixture of air and the fuel compound in Figure 3.23, is 32 $\pm$ 11 mm. This means that the pipe diameter is approximately three times larger than the detonation cell size at stoichiometric conditions. Figure 3.18 on the other hand indicated that also the obstacle opening diameter and the radial distance between the pipe side wall and the obstacle opening, could be limiting length scales. An obstacle opening diameter of 30 mm makes both D_o and $(D_p - D_o)/2$ about the same size as the detonation sell size.

Figure 3.24 shows the recorded maximum overpressure and the magnitude of the obstacle caused shock at transducer P2 and P4, as a function of the hydrogen volume percentage in the fuel. The constant volume combustion pressures calculated by SuperSTATE, are also plotted in the figure. The lines that are labeled 'P2' and 'P4' are the maximum recorded overpressures, and the lines that are labeled 'P2′' and 'P4′' are the magnitude of the obstacle caused shocks. The fuel was mixed with air at stoichiometric concentrations for all the experiments, but the composition of the fuel was changed. The hydrogen volume percentage in the fuel ranged from 0 to 90 percent. For a fuel volume percentage of hydrogen equal to 90, there was a transition to detonation after the obstacle. This detonation propagated down the pipe with a velocity of 1886 $\pm$ 8 m/s and the maximum recorded overpressure at pressure transducer P4 was 1.56 MPa. A hydrogen volume

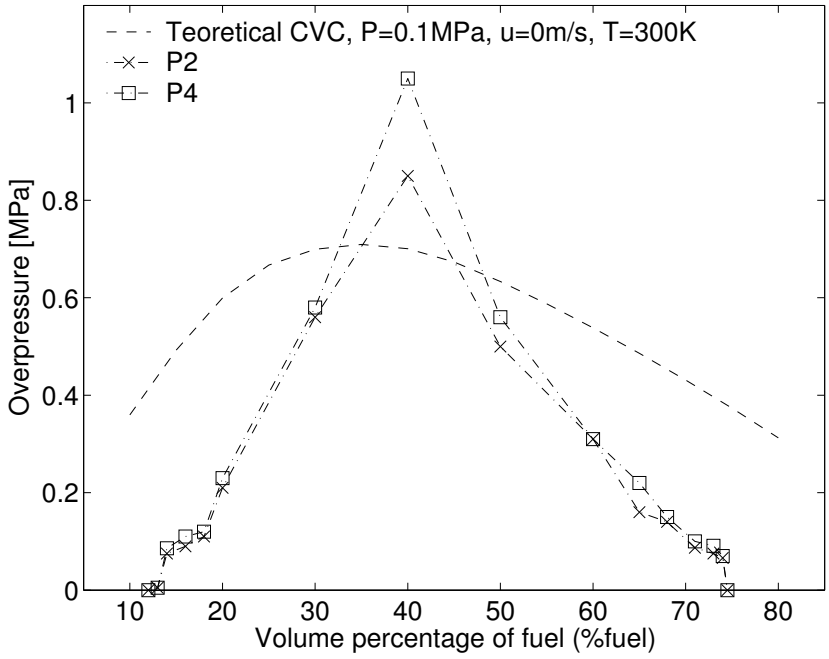

Figure 3.23: Maximum overpressure at pressure transducer P2 and P4 for various volume percentages of fuel in the 4.0 m pipe. The fuel consisted of 10 volume percentages of hydrogen and 90 volume percentages of carbon monoxide. ($D_o = 30$ mm and CVC = constant volume combustion.)

percentage of 90 in the fuel is equivalent to a hydrogen volume percentage of 27 in the gas mixture. Table 3.5 shows that an obstacle opening diameter of 30 mm and a hydrogen volume percentage of 25 gives parallel experiments with and without a DDT after the obstacle. It can therefore be stated that the added carbon monoxide did not change the DDT sensitivity of the hydrogen in these experiments.

The lower left part of Figure 3.24 have been enlarged in Figure 3.25. Figure 3.25 shows that there is almost a doubling of the experimental maximum overpressure at pressure transducer P2 and P4, if one percent of the carbon monoxide in the stoichiometric carbon monoxide and air mixture is replaced by hydrogen. This result shows that even small amounts of added hydrogen changes the explosion characteristics of premixed carbon monoxide and air.

3.3.3 Propane and air

The 4.0 m long steel pipe described in Section 3.2 has been used to study gas explosions in stoichiometric mixtures of propane and air. Six pressure transducers were distributed along the pipe to measure the experimental overpressures. A sketch of the pipe with the pressure transducer distribution is given in Figure 3.2. Five different obstacles with opening diameters of 10, 20, 30, 50 and 70 mm were used. The main objective of performing the experiments was to get comparable data to the hydrogen and air gas explosion experiments described in Subsection 3.3.1. The primary focus has been directed towards the flame propagation between the ignition wall and the obstacle.

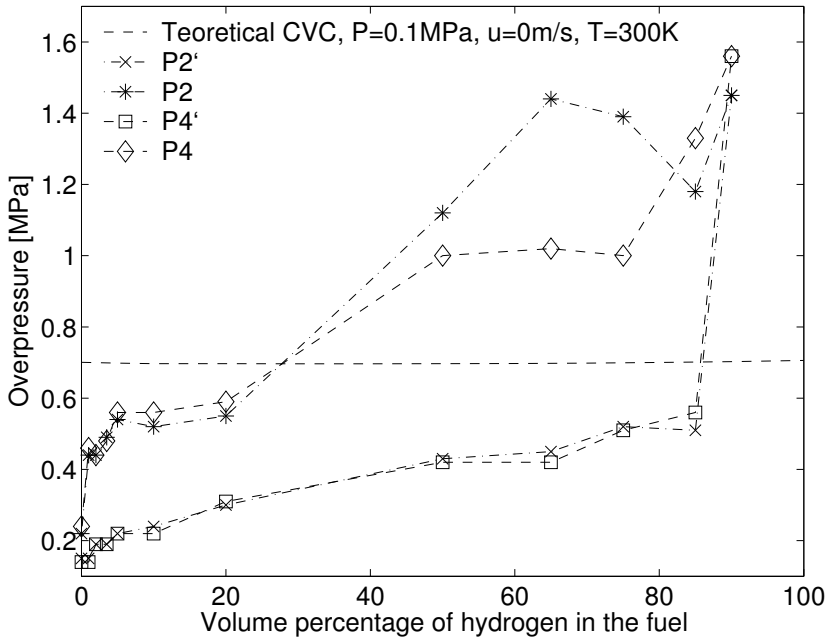

Figure 3.24: Experimental overpressures at pressure transducer P2 and P4 in the 4.0 m pipe for various volume percentages of hydrogen in a stoichiometric mixture of hydrogen, carbon monoxide and air. 'P2' and 'P4' are the maximum recorded overpressures, whereas 'P2′' and 'P4′' are the magnitudes of the obstacle caused shocks. ($D_o = 30$ mm and CVC = constant volume combustion.)

Propane is one of several hydrocarbons in Natural gas. The laminar burning velocity of propane is approximately one fifth of the laminar burning velocity of hydrogen [50]. A stoichiometric mixture of propane and air requires a propane volume percentage of 4.03 and the detonation cell size is between 52.9 mm [51, 4] and 75.2 mm [53, 4] at atmospheric conditions. The corresponding detonation cell size for hydrogen is 15.1 mm [3, 4]. Equation (3.5) shows the overall reaction of propane and air at stoichiometric conditions.

$$C_3H_8 + 5(O_2 + 3.762N_2) \longrightarrow 3CO_2 + 4H_20 + 18.81N_2 \tag{3.5}$$

Figure 3.26 and 3.27 show the recorded overpressure at pressure transducer P0 for the various blockage ratios. (Figure 3.26 enlarges the initial phase in Figure 3.27.) The first significant overpressure is recorded by the pressure transducer at approximately 6.0 ms. The overpressure then evolves similarly for the various blockage ratios up to about 12.0 ms. The rest of the pressure recordings depend on the blockage ratio of the obstacle, but all the experiments have an exponential growth in the pressure followed by a local pressure maximum. The only exception is the recorded pressure for a blockage ratio of 0.991. For this experiment the pressure continues to grow even after the first exponential phase. Both the magnitude and the time of appearance for this first local pressure maximum, are listed in Table 3.8 for the various blockage ratios. The local pressure maximum generally appears later and with a higher magnitude for the higher blockage ratios.

SuperSTATE gives the speed of sound in the unburned mixture to be 340 m/s at atmo-

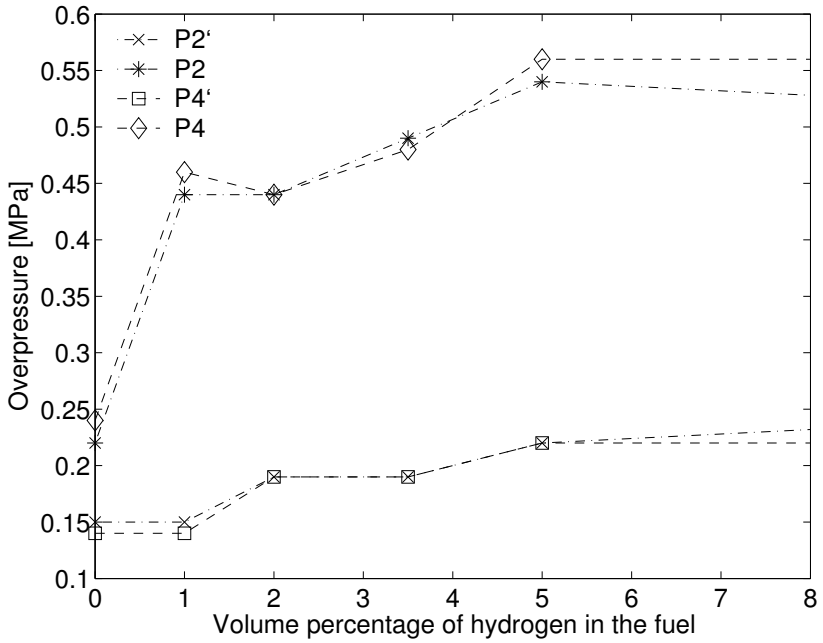

Figure 3.25: Experimental overpressures at pressure transducer P2 and P4 in the 4.0 m pipe for various volume percentages of hydrogen in a stoichiometric mixture of hydrogen, carbon monoxide and air. 'P2' and 'P4' are the maximum recorded overpressures, whereas 'P2′' and 'P4′' are the magnitudes of the obstacle caused shocks. This figure is an enlargement of the lower left corner in Figure 3.24. ($D_o = 30$ mm.)

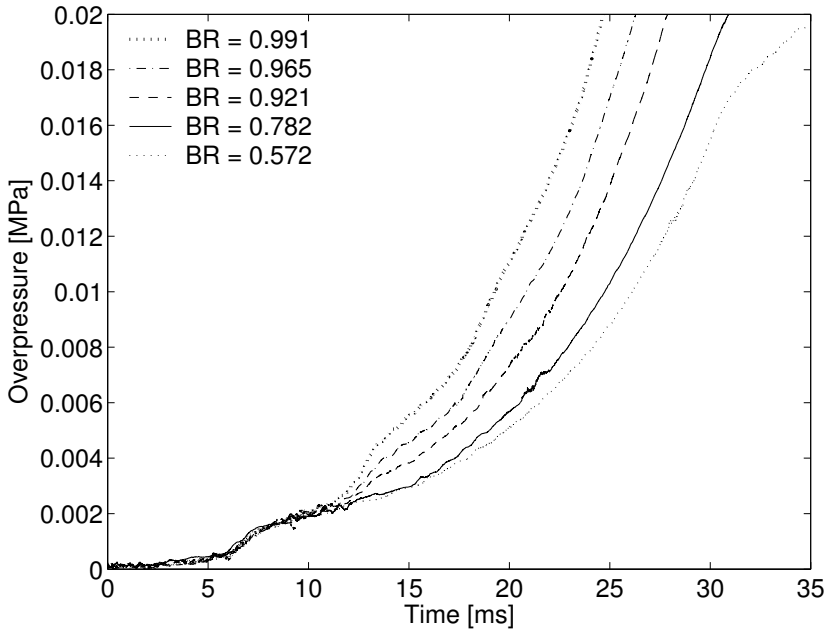

Figure 3.26: Experimental overpressure at pressure transducer P0 in the 4.0 m pipe for stoichiometric mixtures of propane and air. The obstacle opening diameters were 10, 20, 30, 50 and 70 mm. (The first 35 ms of the pressure recordings in Figure 3.27.)

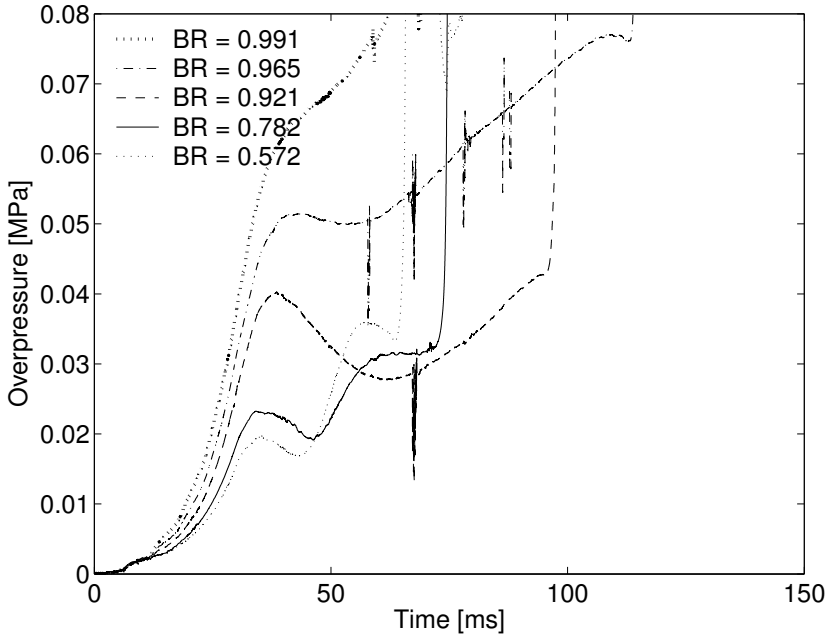

Figure 3.27: Experimental overpressure at pressure transducer P0 in the 4.0 m pipe for stoichiometric mixtures of propane and air. The obstacle opening diameters were 10, 20, 30, 50 and 70 mm.

Table 3.8: Experimental overpressure and the time of appearance for the first local pressure maximum recorded by pressure transducer P0 for stoichiometric mixtures of fuel and air. The fuels are propane and methane. (BR is an abbreviation for the blockage ratio and D_o is the obstacle opening diameter.)

BR	D_o	C_3H_8		CH_4	
	[mm]	Time [ms]	Pressure [MPa]	Time [ms]	Pressure [MPa]
0.572	70	35.5	0.020	41.3	0.016
0.782	50	34.2	0.023	39.2	0.020
0.921	30	38.6	0.040	42.0	0.031
0.965	20	43.5	0.051	40.8	0.040
0.991	10	–	–	–	–

spheric conditions. This means that a pressure wave will use less than (2.0 m)/(340 m/s) = 5.9 ms to propagate from the ignition wall to the obstacle and back. The first recorded overpressure in Figure 3.26 will therefore interact with the flame at a time less than 6.0 ms + 5.9 ms = 11.9 ms after the ignition. This pressure wave will also be superimposed on the recorded overpressure. The discussion in the previous paragraph showed that the recorded overpressures start to evolve differently after approximately 12.0 ms for the different blockage ratios. The observed differences in the recorded overpressures for times larger then 12.0 ms can therefore be related to the first pressure wave that is reflected off the obstacle. The strength of the reflected pressure wave depends on the blockage ratio of the obstacle.

A second wave structure also interacts with the flame. The first pressure wave uses less than (8.0 m)/(340 m/s) = 23.5 ms to propagate from the ignition wall to the opposite end wall and back. This pressure wave will therfore interact with the flame at a time less than 6.0 ms + 23.5 ms = 29.5 ms. The experiment with a blockage ratio of 0.572 has the earliest appearance of the first pressure maximum in Figure 3.27. For that experiment it appeared 35.5 ms after the ignition. In Figure 3.8 and Figure 3.11 the first local pressure maximums were directly related to the reduced flame surface area which occurs when the flame reaches the pipe wall in the radial direction. The first pressure maximum in those experiments could be related to this quenching phenomenon, because the local pressure maximum occurred at a time when the flame could not have been affected by any pressure waves that had been reflected off the end wall or the obstacle. As explained by the discussion above, this is not the case for the experiments with propane. In these experiments the first pressure maximum is affected by pressure waves that are reflected both between the ignition wall and the obstacle and between the two end walls. The overpressures and the times listed in Table 3.8 can therefore not be related directly to the quenching of the flame at the contact surfaces, when the flame reaches the pipe wall in the radial direction.

Only one of the two types of propagating pressure waves described in the previous paragraphs, can be seen in Figure 3.27. The oscillations created by pressure reflections between the ignition wall and the obstacle, i.e. a period less than or approximately equal to 5.9 ms, can not be seen in any of the pressure recordings. But they should be strongest for the higher blockage ratios. The oscillations created by pressure reflections between the ignition wall and the opposite end wall, i.e. periods less than or approximately equal to 23.5 ms, can be seen for an obstacle opening diameter of 50 and 70 mm. These oscillations are strongest for the lower blockage ratios. Even though the pressure recordings have been filtered, there is still a considerable amount of noise in small intervals of the various pressure recordings from pressure transducer P0. This noise is most likely created by the high voltage cable used by the ignition source.

Figure 3.28 shows the recorded overpressures at the first pressure transducer after the obstacle (P1) for the various blockage ratios. The recorded overpressure at this pressure transducer also depends on the blockage ratio. But unlike the results at pressure transducer P0, it is the lowest blockage ratios that give the fastest pressure build up. The oscillations that are superimposed on the pressure recordings can be related to pressure waves that propagate both between the ignition wall and the end wall and between the obstacle and the end wall. The pressure wave that propagates between the obstacle and the end wall will have a period that is less than or approximately equal to (6.0 m)/(340 m/s) = 17.6 ms.

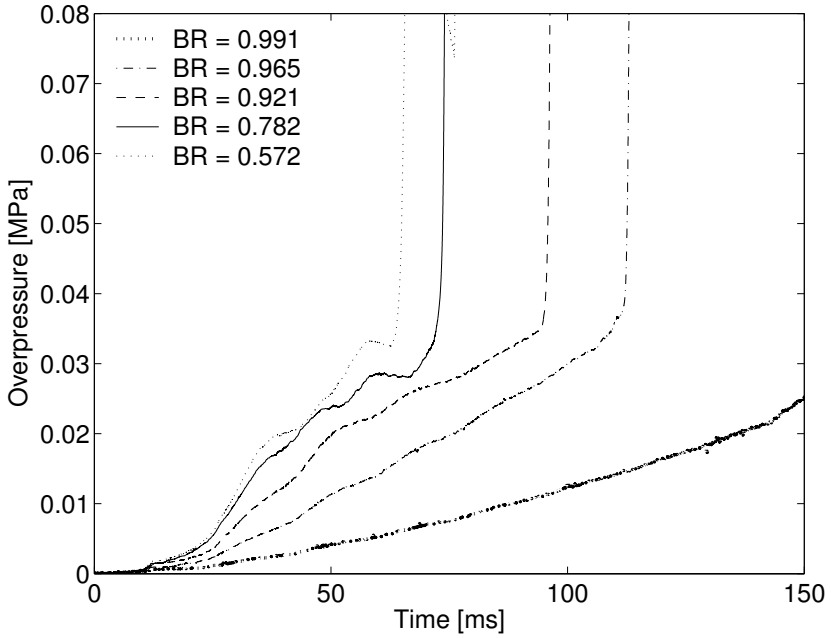

Figure 3.28: Experimental overpressure at pressure transducer P1 in the 4.0 m pipe for stoichiometric mixtures of propane and air. The obstacle opening diameters were 10, 20, 30, 50 and 70 mm.

The oscillations are strongest for the lower blockage ratios.

Both Figure 3.27 and Figure 3.28 show that the obstacle caused shock arrives later at the pressure transducers for the higher blockage ratios. The same tendency was also observed for the hydrogen and air experiments described in Subsection 3.3.1. This delay is caused by a lower mean axial velocity of the flame between the ignition wall and the obstacle. The reduced velocity is caused by the hindering of the flow of the unburned gas in the axial direction towards the obstacle [2]. A more detailed description of the phenomenon is given in Subsection 3.3.1. The main increase of the experimental pressure at pressure transducer P0 for the higher blockage ratios, is therefore most likely caused by the hindering of flow through the obstacle and not by an increase in the burning rate of the flame.

Figure 3.29 shows the maximum recorded overpressure and the overpressure of the obstacle caused shock at pressure transducer P2 and P4 as a function of the blockage ratio. The lines that are labeled ’P2’ and ’P4’ give the maximum recorded overpressures and the lines that are labeled ’P2′’ and ’P4′’ give the magnitude of the obstacle caused shocks. Both the maximum overpressure and the magnitude of the obstacle caused shock increase with increasing blockage ratio. The highest recorded overpressure was 0.73 MPa and it was recorded for an obstacle opening diameter of 20 mm. SuperSTATE gives the constant volume combustion overpressure for a stoichiometric mixture of propane and air at atmospheric conditions to be 0.85 MPa. But the maximum overpressures in Figure 3.29 are lower and for a blockage ratio of 0.572 it is only half of the theoretical constant volume combustion overpressure. As for the hydrogen and air experiments presented in Figure 3.10, some of this difference may be related to the time response of the pressure

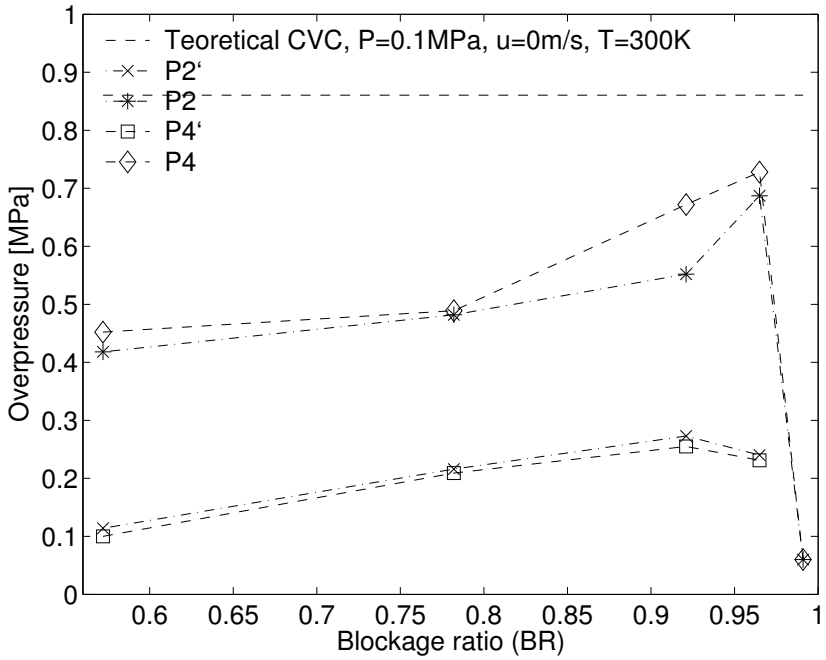

Figure 3.29: Maximum overpressure and the overpressure of the obstacle caused shock recorded at pressure transducer P2 and P4 for stoichiometric mixtures of propane and air. 'P2' and 'P4' are the maximum recorded overpressures, whereas 'P2′' and 'P4′' are the magnitude of the obstacle caused shock. The obstacle opening diameters were 10, 20, 30, 50 and 70 mm.

transducers and the heat conduction to the surroundings. It is further interesting to observe that the maximum recorded overpressure drops to 0.06 MPa and that there is no obstacle caused shock for a blockage ratio of 0.991. These two observations indicate that the flame is quenched at the obstacle. A similar observation was not made for any of the experiments performed with hydrogen and air. This quenching phenomenon needs to be investigated further[4]. Thibault et al. [133], who investigated quenching of premixed flames propagating from one combustion chamber to another through an orifice, found that the quenching criteria were dependent on both the blockage ratio of the obstacle and the pressure ratio across the obstacle. The maximum recorded overpressure at pressure transducer P0 for a blockage ratio of 0.991, was 0.26 MPa.

The diameter of the 4.0 m pipe is about one and a half or two times the detonation cell size for a stoichiometric mixture of propane and air at atmospheric conditions. This means that the 4.0 m pipe at least meets the physical requirement described by Equation (2.11) for obtaining a transition to detonation after the obstacle. But as indicated by the overpressures in Figure 3.29, non of the experiments with propane and air did have a deflagration to detonation transition. This might be related to the two length scale

[4]Dorofeev [127] have used a simplified analytical model to study the critical conditions for thermal quenching of turbulent mixed pockets of reactants and products. This analytical study shows qualitatively that the critical Karlovitz number (Ka) for thermal quenching 1) increases with both increasing expansion ratio (σ) and an increase in the overall reaction order and 2) decreases with both increasing Zeldovich number (β) and increasing Lewis number (Le).

criteria discussed in Subsection 3.3.1, i.e $D_o \geq \lambda_d$ and $(D_p - D_o) \geq 2\lambda_d$. These two criteria are not met at the same time in any of the experiments with propane and air, when $52.9 \leq \lambda_d \leq 75.2$ mm [51, 53, 4].

3.3.4 Methane and air

Figure 3.2 gives a sketch of the 4.0 m pipe with the pressure transducer distribution. This closed and single obstructed pipe has been used in gas explosion experiments with stoichiometric mixtures of methane and air, to get a set of comparable data to the experiments with hydrogen and air described in Subsection 3.3.1. Five different obstacles with obstacle opening diameters ranging from 10 to 70 mm were used. These experiments are identical to the experiments performed with propane and air in Subsection 3.3.3. The discussion of the methane and air experiments, is therefore done relative to those with propane and air. In the rest of this subsection the experiments with stoichiometric mixtures of methane and air are referred to as the methane experiments. Similarly the experiments with stoichiometric mixtures of propane and air presented in Subsection 3.3.3 are referred to as the propane experiments.

Methane is created by anaerobic bacterial decomposition of organic matter and it is therefore an important component in biogas. Methane is also the major component in Natural gas. The overall reaction of methane and air for Φ = 1.0, is shown by Equation (3.6). This equation gives that stoichiometric proportion between methane and air is achieved with a methane volume percentage of 9.50. The laminar burning velocity of methane is almost the same as for propane [49] and the detonation cell size is between 279.5 mm [53, 4] and 349.5 mm [54, 4] at atmospheric conditions.

$$CH_4 + 2(O_2 + 3.762N_2) \rightarrow CO_2 + 2H_20 + 7.524N_2 \tag{3.6}$$

Figure 3.30 and Figure 3.31 show the recorded overpressure at pressure transducer P0 and P1 for the various blockage ratios. These pressure recordings follow the same stages of evolvement and are relatively similar to those obtained in the propane experiments in Figure 3.27 and Figure 3.28. The experimental overpressures in Figure 3.30 show that there is a first phase that is similar for the various obstacle opening diameters. This first phase is then followed by a phase with an exponential growth of the pressure. The exponential phase is highly dependent on the blockage ratio of the obstacle and an increase in the blockage ratio increases the exponential growth of the pressure. The pressure growth then starts to decrease and a local pressure maximum is created. The only exception occurs for a blockage ratio of 0.991, for which the experimental pressure continues to increase. The same stages of evolvement have been described more firmly for the propane experiments in Subsection 3.3.3.

The small oscillations that are superimposed on the recorded overpressure for a blockage ratio of 0.991 in Figure 3.30, are from a pressure wave that is reflected between the ignition wall and the obstacle. Similar oscillations can not be seen in the corresponding overpressure for propane in Figure 3.27. It can be noted that the pressure evolvement for a blockage ratio of 0.965 in Figure 3.30, deviates from the pressure evolvement for the other blockage ratios. It is believed that this deviation is caused by the high voltage cable connected to the spark electrodes. (See Figure 3.4.) The electrical field around the high

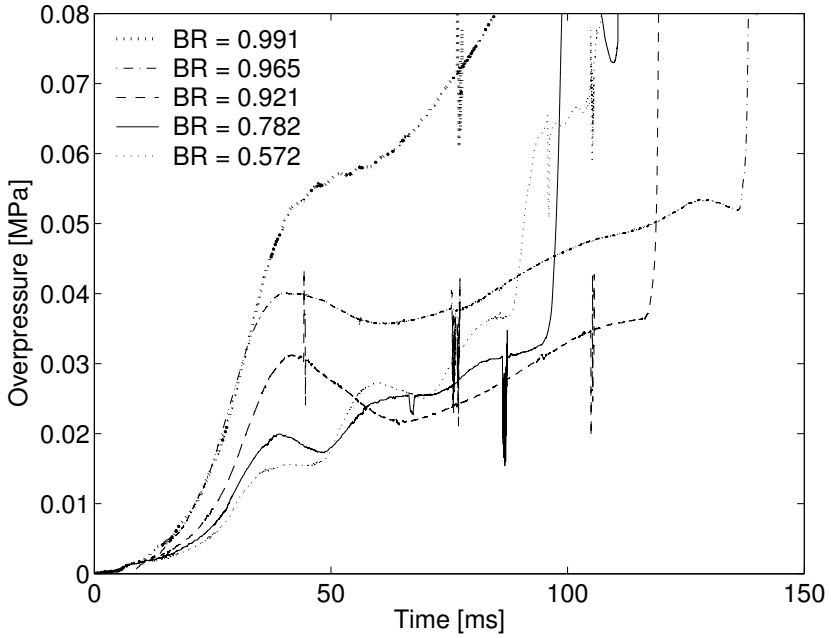

Figure 3.30: Experimental overpressure at pressure transducer P0 in the 4.0 m pipe for stoichiometric mixtures of methane and air. The obstacle opening diameters were 10, 20, 30, 50 and 70 mm.

voltage cable has most likely affected the measured overpressure in such a way that 1) it is slightly shifted at the time of ignition and that 2) it increases too fast for the first 30 ms of the experiment.

Table 3.8 also lists the time of appearance and the magnitude of the first local pressure maximum at pressure transducer P0 for the methane experiments. By comparing the experimental results for propane and methane in the table, it can be seen that the magnitude of the local pressure maximum is slightly lower for methane than for propane. The local pressure maximum also occurs generally later for methane than for propane. But it is interesting to observe that the first local pressure maximum occurs earlier for methane than for propane with an obstacle opening diameter of 20 mm. Figure 3.28 and Figure 3.31 show that the obstacle caused shock occurs sooner for the propane experiments than for the corresponding methane experiments. This indicates that the flame has a higher mean axial velocity in the experiments with propane compared to those with methane.

Both the maximum overpressure and the overpressure of the obstacle caused shock recorded at pressure transducer P2 and P4, are shown in Figure 3.32 for the various blockage ratios. The lines that are labeled 'P2' and 'P4' give the maximum recorded overpressures and the lines that are labeled 'P2′' and 'P4′' give the magnitude of the obstacle caused shocks. The theoretical constant volume combustion overpressure calculated by SuperSTATE is also plotted in the figure. The different overpressures in Figure 3.32 are relatively similar to the corresponding overpressures obtained for propane in Figure 3.29. But the magnitude of the overpressures for methane are lower than those for propane. It is especially interesting to observe that for a blockage ratio of 0.991, the methane experiment has the same pressure drop for 'P2' and 'P4' as the propane experiment. This might

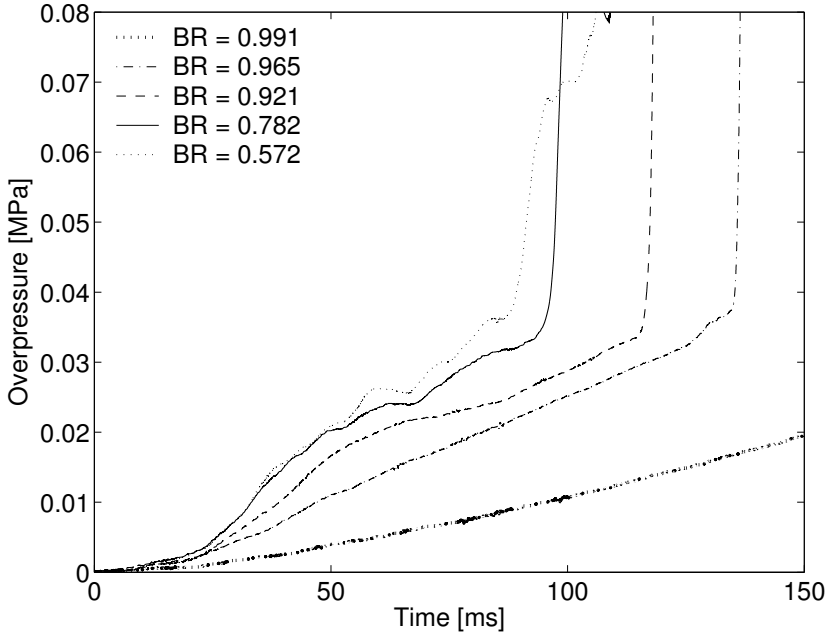

Figure 3.31: Experimental overpressure at pressure transducer P1 in the 4.0 m pipe for stoichiometric mixtures of methane and air. The obstacle opening diameters were 10, 20, 30, 50 and 70 mm.

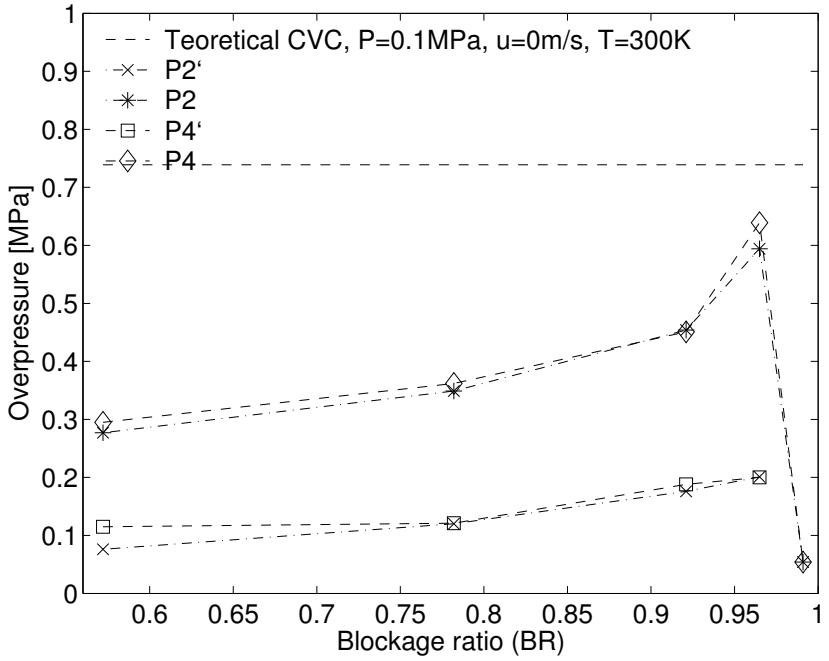

Figure 3.32: Maximum overpressure and the overpressure of the obstacle caused shock recorded at pressure transducer P2 and P4 for stoichiometric mixtures of methane and air. ’P2’ and ’P4’ are the maximum recorded overpressures, whereas ’P2′’ and ’P4′’ are the magnitude of the obstacle caused shock. The obstacle opening diameters were 10, 20, 30, 50 and 70 mm.

indicate that also the methane and air flame was quenched at the obstacle for this blockage ratio.

None of the experiments with methane did experience a transition to detonation. This result is as expected, since the pipe diameter to the detonation cell size ratio is less than one. (See Equation (2.11).) But Kuznetsov et al. [137] have reported DDT and propagating quasi detonations for stoichiometric mixtures of methane and air, in an obstacle filled tube with an inner diameter of 174 mm. Cell size measurements from soot foils in these experiments, indicated that the detonation cell size was 210 $\pm$ 80 mm. The experiments of Kuznetsov et al. [137] were conducted at the initial conditions of 0.1 MPa and 300 K.

3.3.5 Error sources

This subsection gives a short discussion of what are assumed to be the main sources of error in the experimental work. Both the gas mixtures, the diagnostic system and the post processing of the experimental data are discussed.

Gas mixtures

The equivalence ratio of the premixed gases is a possible error source. The commercially graded gases are very pure and often higher than 99.9 percent, so the main uncertainty is related to the mixing of the reactants. The method presented in the next paragraph has been used to estimate the accuracy of the gas concentrations in mixtures of hydrogen and air.

The volume flow (in liters per minute [L/min]) through the calibrated VAFMs can be described as $\dot{Q}_{air} = 1.65 \times R_{air}$ and $\dot{Q}_{\mathrm{H_2}} = 0.123 \times R_{\mathrm{H_2}}$. In these linear expressions R_{air} and $R_{\mathrm{H_2}}$ are the VAFM marker position for air and hydrogen, respectively. If the VAFM marker for air is held constant at 7.5, then the VAFM marker for hydrogen can be used in the range from 0 to 100, to get the right equivalence ratios. But there might be an uncertainty associated with the actual position of the VAFM marker. Unsteady flow inside the VAFMs can for example cause the marker to bounce up and down in a randomly manner. Equation (3.7) gives the volume percentage of hydrogen, as a function of the hydrogen marker position, for a flow of hydrogen and air. In this equation R_{air} is held at 7.5 at all times. Equation (3.7) further assumes that the exact VAFM marker positions can be determined with the accuracy of $\pm$ 0.1 for air and $\pm$ 1.0 for hydrogen. Figure 3.33 is based on Equation (3.7) and shows the deviation in the volume percentage of hydrogen at four worst case scenarios. The results in Figure 3.33 give the expected error in the hydrogen volume percentage to be less than $\pm$ 1.0 percent.

$$\dot{Q}_{\%\mathrm{H_2}} = \frac{0.123 \cdot (R_{\mathrm{H_2}} \pm 1.0)}{0.123 \cdot (R_{\mathrm{H_2}} \pm 1.0) + 1.65 \cdot (7.5 \pm 0.1)} \cdot 100 \tag{3.7}$$

The temperature of the premixed gases is assumed to be at room temperature when they entered the pipe, i.e about 293 K. But a series of experiments conducted in the same pipe, will gradually heat the pipe walls. (This increase in the pipe wall temperature was observed qualitatively by placing a hand on the pipe wall.) The highest observed pipe wall temperature prior to ignition, was not much higher than the human body temperature. It

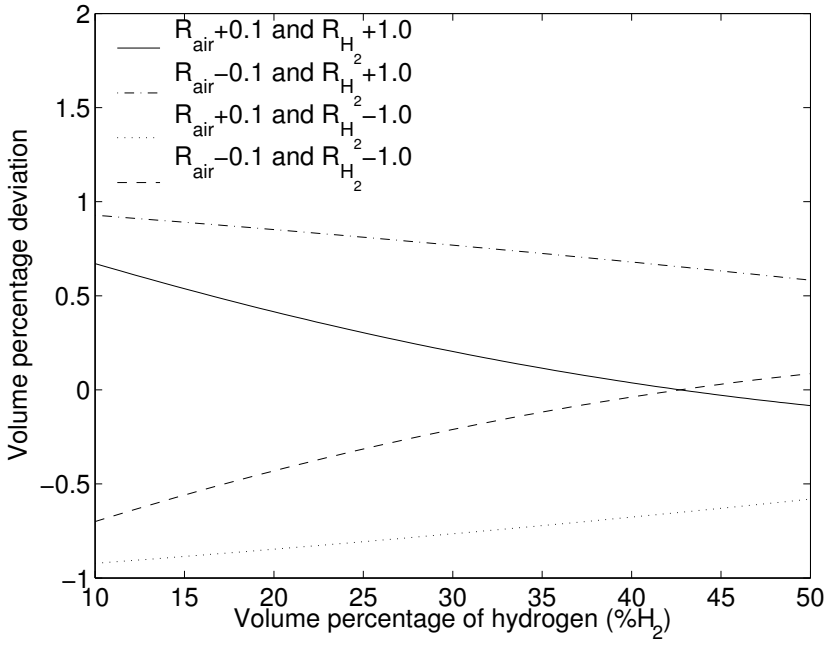

Figure 3.33: Deviation in the volume percentage of hydrogen at various hydrogen volume percentages for four different scenarios of the VAFM marker positions. (See Equation (3.7).)

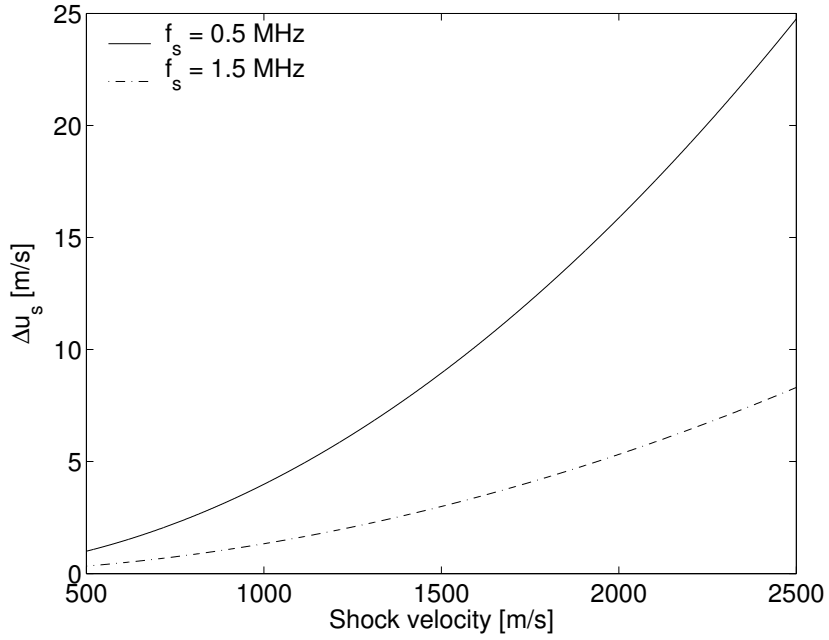

Figure 3.34: Resolution in the measured shock velocity as a function of the actual shock velocity, for two different sampling frequencies. (See Equation (3.8).)

is therefore assumed that the temperature of the premixed gas prior to ignition, did not differ much from 293 K and that it was less than 310 K.

The gas filling time of the pipes was always larger than the time it took to fill the whole pipe at least three times. This means that the first 1.0 m of the pipe was filled at least ten times. It is assumed that this filling time was sufficient to went out all the combustion products from the previous experiment. But there was condensation of water on the pipe wall after each experiment. The gas filling time was not sufficient to remove all the moisture from the pipe. It is not known if this moisture has affected the flame propagation or the detonation velocities. This needs to be investigated further.

The volume flow $\dot{Q}_{mix}$ of the gas mixture in the supply tube, was in the range from 12.0 to 24.0 liters per minute, i.e. from $2.0 \cdot 10^{-4}$ to $4.0 \cdot 10^{-4}$ m^3/s. The inner diameter of the supply tube D_t was 9.0 mm and a gas mixture element travels a distance $l = Q_{mix}/[\pi(D_t/2)^2]$ per second. This gives flow velocities of the gas mixture in the range from 3.1 to 6.3 m/s. For a stoichiometric mixture of hydrogen and air the viscosity is $1.34{\cdot}10^{-5}$ N·s/m. (See Table C.1.) This gives approximated Reynolds numbers $\mathrm{Re} = |(\rho u D_t)/\mu|$ in the range from 1800 to 3600, when the density ρ is 0.845 kg/m^3. This indicates that the flow in the supply tube is turbulent. A weak sound could also be heard from the supply tube during the filling of the pipes. It is therefore assumed that gas homogeneity was secured by a sufficient mixing of the reactants in the supply tube. It is also assumed that this homogeneity was conserved prior to ignition because of the small elevation of the ignition end of the pipe.

Diagnostic system

The uncertainties related to the diagnostic system lies both in the pressure transducers and in the sampling frequency. As shown by Table 3.1, the two pressure transducer models used in the experiments did have different physical specifications. The experimental results also showed that the Kistler 7001 model generally recorded a higher overpressure than the Kistler 603B model. The mean axial shock velocities were calculated under the assumption that the recorded overpressures were generated at the same position on each transducer. But this may not be the case. The pressures could have been measured in the center of the transducer, but also close to the transducer boundary. It was also assumed that any turbulence that might have been created by the pressure transducers, was negligible for the overall flame propagation.

The sampling frequency f_s and the number of samples X_s it takes for a shock wave to propagate the distance x_d between two pressure transducers, were used to calculate the experimental shock velocities. These velocities are relative to the pipe wall. The sampling frequency controls the resolution of the measured shock velocities. Let us assume that the velocity u_s of the shock is known. The number of samples it takes for the shock wave to propagate from one pressure transducer to another, can then be written as $X_s = t \cdot f_s = (x_d/u_s) \cdot f_s$. In an experiment u_s is unknown and X_s can be extracted form the pressure records. The experimental shock velocities can therfore be written as $u_s = (x_d \cdot f_s)/X_s$. Equation (3.8) gives an estimate of the resolution in the calculated shock velocities as a function of both the shock velocity and the different sampling frequencies. The velocity resolution at various shock velocities for the two sample frequencies of 0.5 and 1.5 MHz,

are shown in Figure 3.34. A detonation which propagates at 2.0 km/s has a resolution of 15.9 m/s and 5.3 m/s for sampling frequencies of 0.5 MHz and 1.5 MHz, respectively.

$$\begin{aligned} \Delta u_s &= \left(\frac{1}{X_s} - \frac{1}{X_s + 1} \right) x_d \cdot f_s \\ &= \frac{u_s^2}{x_d \cdot f_s + u_s} \end{aligned} \tag{3.8}$$

Post processing

Some of the experimental pressure records contained a considerable amount of noise. A filter program was therefore used on these pressure records to reduce the noise. The applied filter used a type of averaging that lead to a reduction of the pressure peaks. But the shock waves that propagated in the direction from the ignition wall to the end wall, were kept sharp. It was further observed that the Kistler 7001 pressure transducers produced more noise than the Kistler 603B pressure transducers. The calculation of all the mean axial velocities were done with as little filtering as possible and all the detonation velocities were calculated without any filtering at all.

3.4 Conclusions

The main conclusions of the experimental work can be summarized as follows:

1. Experimental pressure records from gas explosion experiments in closed and single obstructed pipes with premixed fuel and air at various equivalence ratios have been obtained. Various combinations of four different fuels, three different pipes and seven different obstacles have been used in the experiments. Kistler pressure transducers distributed along the pipes were used to measure the experimental overpressure. The four fuels were hydrogen, mixes of carbon monoxide and hydrogen, propane and methane. The three pipes had inner lengths of 3.0, 4.0 and 7.0 m.

2. The set of blockage ratios and hydrogen and air equivalence ratios that gives a DDT after the obstacle for the 4.0 m pipe, has been found. DDTs were observed for blockage ratios ranging from 0.572 to 0.965 and for equivalence ratios ranging from 0.79 to 1.95. This is equivalent to obstacle opening diameters ranging from 70 to 20 mm and hydrogen volume percentages ranging from 25 to 45. The various combinations that give a DDT are almost symmetrical around a hydrogen volume percentage of 35 and the most optimum conditions for a DDT is created with a blockage ratio of 0.921.

3. The length scale of the detonation cell size (λ_d), the pipe diameter (D_p) and the obstacle opening diameter (D_o) are critical parameters for deflagration to detonation transitions in obstacle filled tubes [160]. On the other hand, the experiments with hydrogen and air in the 4.0 m pipe, indicate that the radial distance between the pipe side wall and the obstacle opening is also an important length scale for DDTs

in these experiments. This criterion can be expressed as $(D_p - D_o) \geq 2\lambda_d$. But experiments with a higher resolution in both the hydrogen volume percentages and the obstacle opening diameters, need to be performed before this criterion can be confirmed further. Detonation cell size measurements should also be performed in such an experimental study.

4. The flame propagation between the ignition wall and the obstacle depends on the blockage ratio of the obstacle. The obstacle controls the level of pressure build up in front of the flame. The increasing overpressure at pressure transducer P0 with increasing blockage ratio, is mainly caused by the hindering of fluid flow in front of the flame and not by an increased burning rate. The mean axial flame speed between the ignition wall and the obstacle will therefore generally decrease with increasing blockage ratio.

5. It has been showed that the flame propagation between the ignition wall and the obstacle can be affected by pressure waves reflected off the opposite end wall. It can therefor be stated that the total pipe length is an important parameter for flame propagation in closed and single obstructed pipes.

6. The experiments with carbon monoxide, hydrogen and air at stoichiometric proportions in the 4.0 m pipe, have shown that small amounts of added carbon monoxide to a hydrogen and air mixture, do not change the detonability of hydrogen. A DDT was observed in the carbon monoxide, hydrogen and air mixture for a hydrogen volume percentage of 27, whereas a critical DDT was observed in the hydrogen and air mixture for a hydrogen volume percentage as low as 25.

7. The ignition limits for a specific fuel compound of hydrogen and carbon monoxide in air, have been found for the 4.0 m pipe. The fuel volume percentage of hydrogen was 10 and the fuel volume percentage of carbon monoxide was 90. The premixed fuel and air did ignite for a volume percentage of air ranging from 13.0 to 74.0. This interval is in good agreement with the experimentally determined flammability limits presented by Karim et al. [186] and Løyland [187]. A DDT was not observed with this fuel composition.

8. Experiments with stoichiometric propane and air and with stoichiometric methane and air in the 4.0 m pipe, have shown that the explosion characteristics of the two fuels are relatively similar for the various blockage ratios. But the experiments with propane had both a higher overpressure and a higher mean axial flame speed between the ignition wall and the obstacle.

9. An interesting observation was made in the experiments with propane and methane. (The fuels were mixed with air at stoichiometric conditions.) The experimental pressure recordings indicated that the flame was quenched at the obstacle for these two gas mixtures, when the blockage ratio of the obstacle was 0.991. This phenomenon was not observed in any of the experiments with hydrogen and air.

10. The experiments with propane and methane had a much slower flame propagation than the corresponding experiments with hydrogen in the 4.0 m pipe. In stoichio-

metric mixtures of hydrogen and air the flame reached the pipe side wall in the radial direction before it interacted with pressure waves that were reflected off the obstacle or the end walls. This was not the case for propane and methane. In the experiments with propane and methane the flame interacted with reflected pressure waves from both the obstacle and the end walls, before it reached the pipe side wall in the radial direction.

Chapter 4

Numerical simulations

In this chapter the numerical work is described. An introduction to the chapter is given in Section 4.1 before the numerical code and models are described in Section 4.2. Section 4.3 presents the numerical results and the conclusions of the numerical work are given in Section 4.4.

4.1 Introduction

Numerical simulations of gas explosions in pipes have been performed with a one dimensional code named RCMLAB. The simulations were performed for closed and single obstructed pipes with various equivalence ratios of premixed fuel and air. The experimental results presented in Chapter 3 were used to validate the numerical simulations. The main objective of the work was to test and develop new models for simulation of gas explosions in pipes.

Peters [10] states that one of the most important unresolved problems in premixed turbulent combustion, is the determination of the turbulent burning velocity. The burning velocity depends on local mean quantities and it gives the propagation speed of the mean flame front relative to the flow field of the unburned gas right in front of the flame. Two different types of models have been used to calculate the burning velocity in the numerical simulations. One model used experimental pressure records as input and the other model used the flow field right in front of the flame in combination with the laminar burning velocity.

Even though the phenomena of flame acceleration and flame inversion are fairly well described from experiments [12, 13, 14], there is still little quantitative information of the average burning rates [kg fuel/(m^2s)] in gas explosions. RCMLAB can make such estimates of the average burning rates with the use of experimental pressure measurements.

Most Computational Fluid Dynamics (CFD) codes today have two or three space dimensions. But there are still scenarios when a numerical code with only one space dimension can be favorable. This is especially true for simulations of gas explosions in long pipes. The amount of grid cells for a two or three dimensional code could soon become unmanageable in such simulations.

4.2 RCMLAB

RCMLAB is a one dimensional numerical code designed to simulate gas explosions in pipes and tunnels. It uses the Random Choice Method (RCM) to solve the homogeneous Euler equations for an inviscid and compressible gas with combustion. RCMLAB is developed at Telemark University College and it is written in MATLAB [27] syntax. The first version of the software was presented by Bjerketvedt et al. [17, 18] and Kristoffersen et al. [23, 24]. RCMLAB has previously been used in gas explosion simulations with various propane-air and acetylene-air mixtures in unobstructed pipes with one open end.

Some changes have been made to RCMLAB. The heat transfer model has been updated and a model for the area change caused by an obstacle has been added. A new model for the calculation of the burning velocity has also been tested. RCMLAB has gone through a 'cleaning process'. This means that unused code have been removed and that comments have been made in the code. The different variables have also been categorized and grouped in different vectors and matrixes to ease the communication between the various functions. A method for 'checkpoint and restart' has been implemented into RCMLAB. This means that RCMLAB now has the ability to periodically save a copy of the computer's memory (i.e. a checkpoint) to the hard drive and to recover (i.e. restart) from a memory copy after a crash or a termination of the program. Since the use of MATLAB requires the purchase of a license, some attempts were made to run RCMLAB in the free and MATLAB compatible environment of Octave [26]. But this was not given a high priority and RCMLAB still needs some modifications to work efficiently with Octave.

The rest of this section presents the major modules of the RCMLAB program. Subsection 4.2.1 gives a short description of the Random Choice Method. Subsection 4.2.4 describes the obstacle model and Subsection 4.2.5 describes the heat transfer model. Subsection 4.2.3 presents the two burning velocity models that were used in the simulations.

4.2.1 The Random Choice Method

Glimm [30] presented the Random Choice Method in 1965 and Chorin [33, 34] both implemented the method numerically and extended it to combustion problems. The method operates on a finite volume grid with piecewise-constant data. The local Riemann problems at each cell interface are then solved and a single state contained in the local solutions is chosen at random for each grid cell. The random choice method has the computational advantage that shocks remain sharp [38]. This feature is a result of the sampling of the local solutions. In Godunov's method [29] the local Riemann solutions are averaged and discontinuities can therfore be smeared over several computing cells. A major disadvantage with the Random Choice Method is that the method is not exactly conservative. This feature is also caused by the random sampling of the local solutions. The method may also create some numerical noise, but it was observed during the numerical work that the numerical noise tends to decrease with decreasing cell size.

A brief presentation of the major parts of the Random Choice Method used in RCMLAB will be given in this subsection . A more detailed description of the Random Choice Method, can be found in [35, 36, 37].

The Riemann problem

A Riemann problem is an initial value problem. The problem consists of the given equations together with the initial data. The initial data is a piecewise-constant function with a single jump discontinuity. The Riemann problem for the one dimensional Euler equations (see appendix B) can be written as

$$\begin{aligned} &\mathrm{U}_t + \mathrm{F}(\mathrm{U})_x = 0 \\ &\mathrm{U}(x,0) = \mathrm{U}_0(x) = \begin{cases} \mathrm{U_l} & \text{if} \quad x < 0 \\ \mathrm{U_r} & \text{if} \quad x > 0 \end{cases} \end{aligned} \tag{4.1}$$

where

$$\mathrm{U} = \begin{bmatrix} \rho \\ \rho u \\ E \end{bmatrix}, \ \mathrm{F} = \begin{bmatrix} \rho u \\ \rho u^2 + p \\ u(E+p) \end{bmatrix}. \tag{4.2}$$

This Riemann problem has the discontinuity located at $x = 0$. The part of the domain that is located in $x < 0$ gets the initial condition $\mathrm{U_l}$ and the part of the domain that is located in $x > 0$ gets the initial condition $\mathrm{U_r}$. The subscripts 'l' and 'r' refer to left and right hand side of the Riemann problem. A polytrophic ideal gas has $E = p/(\gamma - 1) + (1/2)\rho u^2$, where γ is the ratio of specific heats[1].

Solution of the Riemann problem

When no vacuum is present, the solution of a Riemann problem for the Euler equations consists of a contact discontinuity and two nonlinear waves. The nonlinear waves are either a shock or a rarefaction wave. The solution depends on the initial conditions $\mathrm{U_l}$ and $\mathrm{U_r}$. An example of a solution is shown in Figure 4.1. Starting from the left in the figure: the 1-wave and the 3-wave are nonlinear waves and the 2-wave is the contact discontinuity. There are a total of four possible wave patterns for the solution.

Since both the velocity u and the pressure p are constant across the contact discontinuity, it is common to work with the primitive variables $\mathrm{W} = [\rho, u, p]^T$ instead of the conserved variables $\mathrm{U} = [\rho, \rho u, E]^T$. But the conserved variables have to be used when the Rankine-Hugoniot condition is enforced at shocks. The Rankine-Hugoniot condition can be written as $S_s(\mathrm{U_l} - \mathrm{U_r}) = \mathrm{F}(\mathrm{U_l}) - \mathrm{F}(\mathrm{U_r})$, where S_s is the shock speed.

Two new constant states are introduced in the solution. They are denoted as $\mathrm{W_l^*} = [\rho_\mathrm{l}^*, u^*, p^*]^T$ and $\mathrm{W_r^*} = [\rho_\mathrm{r}^*, u^*, p^*]^T$. The superscript '*', refers to the term 'star region'. The two states $\mathrm{W_l^*}$ and $\mathrm{W_r^*}$ differ with only a jump in the density (i.e. $\rho_\mathrm{l}^* \neq \rho_\mathrm{r}^*$). Since the initial states $\mathrm{W_l}$ and $\mathrm{W_r}$ are known, it is necessary to determine $\mathrm{W_l^*}$ and $\mathrm{W_r^*}$ in such a way that 1) $\mathrm{W_l}$ and $\mathrm{W_l^*}$ are connected by a 1-wave, 2) $\mathrm{W_l^*}$ and $\mathrm{W_r^*}$ are connected by a 2-wave and finally 3) $\mathrm{W_r^*}$ and $\mathrm{W_r}$ are connected by a 3-wave.

RCMLAB solves the Riemann problem for the Euler equations according to a method presented by Toro [36]. This method uses a Newton-Raphson iterative process to find the pressure p^*. If p^* is known, then u^*, ρ_l^* and ρ_r^* can be calculated.

[1] A polytrophic gas is a gas where the internal energy is linearly dependent on the temperature ($e = c_v T$), i.e. c_v is constant.

The first estimate of the pressure in the star region is done with

$$p_0 = \max(\breve{p}, \min(p_\mathrm{l}, p_\mathrm{r})), \tag{4.3}$$

where $\breve{p}$ is given by

$$\breve{p} = \frac{1}{2}(p_\mathrm{l} + p_\mathrm{r}) - \frac{1}{8}(u_\mathrm{r} - u_\mathrm{l})(\rho_\mathrm{l} + \rho_\mathrm{r})(c_\mathrm{l} + c_\mathrm{r}). \tag{4.4}$$

The pressure is changed between each iteration and the iteration procedure can be written as

$$p_{(\mathrm{z})} = p_{(\mathrm{z}-1)} - \frac{f(p_{(\mathrm{z}-1)}, \mathrm{W_l}, \mathrm{W_r})}{f'(p_{(\mathrm{z}-1)}, \mathrm{W_l}, \mathrm{W_r})}. \tag{4.5}$$

$p_{(\mathrm{z})}$ is the z-th iterate of the pressure and the two functions $f(p, \mathrm{W_l}, \mathrm{W_r})$ and $f'(p, \mathrm{W_l}, \mathrm{W_r})$ are given as

$$f(p, \mathrm{W_l}, \mathrm{W_r}) = f_\mathrm{l}(p, \mathrm{W_l}) + f_\mathrm{r}(p, \mathrm{W_r}) + u_\mathrm{r} - u_\mathrm{l} \tag{4.6}$$

$$f'(p, \mathrm{W_l}, \mathrm{W_r}) = f'_\mathrm{l}(p, \mathrm{W_l}) + f'_\mathrm{r}(p, \mathrm{W_r}). \tag{4.7}$$

$f'(p, \mathrm{W_l}, \mathrm{W_r})$ is the first derivative of $f(p, \mathrm{W_l}, \mathrm{W_r})$ with respect to p. The functions $f_\mathrm{k}(p, \mathrm{W_k})$ and $f'_\mathrm{k}(p, \mathrm{W_k})$ when $\mathrm{k} = [\mathrm{l}, \mathrm{r}]$, are further given by

$$f_\mathrm{k}(p, \mathrm{W_k}) = \begin{cases} (p - p_\mathrm{k}) \left[\frac{A_\mathrm{k}}{p + B_\mathrm{k}}\right]^{\frac{1}{2}} & \text{if } p > p_\mathrm{k} \text{ (shock)} \\ \\ \frac{2c_\mathrm{k}}{(\gamma-1)} \left[\left(\frac{p}{p_\mathrm{k}}\right)^{\frac{\gamma-1}{2\gamma}} - 1\right] & \text{if } p \leq p_\mathrm{k} \text{ (rarefaction)} \end{cases} \tag{4.8}$$

$$f'_\mathrm{k}(p, \mathrm{W_k}) = \begin{cases} \left(\frac{A_\mathrm{k}}{B_\mathrm{k}+p}\right)^{\frac{1}{2}} \left[1 - \frac{p-p_\mathrm{k}}{2(B_\mathrm{k}+p)}\right] & \text{if } p > p_\mathrm{k} \text{ (shock)} \\ \\ \frac{1}{\rho_\mathrm{k} c_\mathrm{k}} \left(\frac{p}{p_\mathrm{k}}\right)^{-\frac{(\gamma+1)}{2\gamma}} & \text{if } p \leq p_\mathrm{k} \text{ (rarefaction)} \end{cases} \tag{4.9}$$

where $c_\mathrm{k} = ((\gamma p_\mathrm{k})/\rho_\mathrm{k})^{1/2}$ is the speed of sound and the constants A_k and B_k are given by

$$A_\mathrm{k} = \frac{2}{(\gamma+1)\rho_\mathrm{k}}, \; B_\mathrm{k} = \frac{(\gamma-1)}{(\gamma+1)} p_\mathrm{k}. \tag{4.10}$$

The functions $f_\mathrm{k}(p, \mathrm{W_k})$ describe how u varies as p is adjusted in a state (p,u) that can be connected to $\mathrm{W_k}$ by a nonlinear wave. If p is the theoretical value of p^*, then Equation 4.6 equals to zero.

The pressure iterations continue until the relative pressure change is below a small prescribed tolerance value. In RCMLAB the iterations are stopped when

$$\frac{|p_{(\mathrm{z})} - p_{(\mathrm{z\text{-}1})}|}{\frac{1}{2}[p_{(\mathrm{z})} + p_{(\mathrm{z\text{-}1})}]} < 1 \cdot 10^{-6}. \tag{4.11}$$

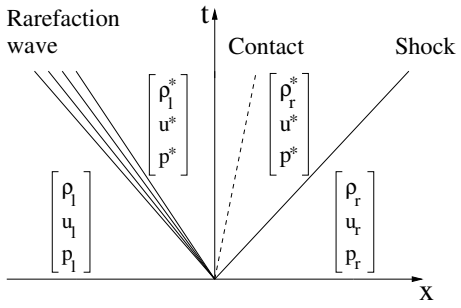

Figure 4.1: An example of a solution to a Riemann problem for the Euler equations.

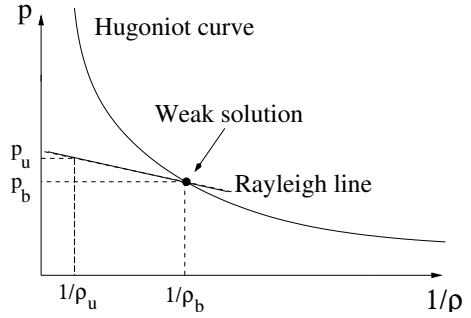

Figure 4.2: A sketch of a Hugoniot curve together with a Rayleigh line.

When the pressure p^* is known, the velocity in the star region is given by

$$u^* = \frac{1}{2}\left(u_{\mathrm{l}} + u_{\mathrm{r}} + f_{\mathrm{r}}(p^*, \mathrm{W}_{\mathrm{r}}) - f_{\mathrm{l}}(p^*, \mathrm{W}_{\mathrm{l}})\right) \tag{4.12}$$

and the densities ρ_{l}^* and ρ_{r}^* are given by

$$\rho_{\mathrm{k}}^* = \begin{cases} \rho_{\mathrm{k}} \left[\dfrac{\left(\frac{\gamma-1}{\gamma+1}\right) + \left(\frac{p^*}{p_{\mathrm{k}}}\right)}{\left(\frac{\gamma-1}{\gamma+1}\right)\left(\frac{p^*}{p_{\mathrm{k}}}\right) + 1} \right] & \text{if } p^* > p_{\mathrm{k}} \text{ (shock)} \\ \rho_{\mathrm{k}} \left(\dfrac{p^*}{p_{\mathrm{k}}}\right)^{\frac{1}{\gamma}} & \text{if } p^* \leq p_{\mathrm{k}} \text{ (rarefaction)} \end{cases} . \tag{4.13}$$

The Random Choice Method on a staggered grid

RCMLAB discretizes the one dimensional domain [0,L] into m grid cells. The length of the domain is L and the grid cell sizes are $\Delta x = \mathrm{L}/\mathrm{m} = x_{i+1/2} - x_{i-1/2}$, with $i = 1, ..., \mathrm{m}$. The location of the cell center is given as $x_i = (i - 1/2)\Delta x$. A piecewise constant distribution of the data in the domain is achieved by assuming that the given data at the cell center is constant throughout the respective cell. This gives $\mathrm{W}(x, t^n) = \mathrm{W}_i^n$ in each cell at the time $t = t^n$. Neighboring cells then define local Riemann problems. An illustration of the staggered grid with the solution procedure for a single time step, is shown in Figure 4.3. First the Riemann problems $RP(\mathrm{W}_{i-1}^n, \mathrm{W}_i^n)$ and $RP(\mathrm{W}_i^n, \mathrm{W}_{i+1}^n)$ are solved to find the respective solutions. These solutions are randomly sampled at a stable time $\Delta t^{n+1/2}$. Then the Riemann problems $RP(\mathrm{W}_{i-1/2}^{n+1/2}, \mathrm{W}_{i+1/2}^{n+1/2})$ are solved and randomly sampled at a stable time Δt^{n+1}.

If $\hat{\mathrm{W}}_i^{n+1}(x, t)$ is the solution to $RP(\mathrm{W}_{i-1/2}^{n+1/2}, \mathrm{W}_{i+1/2}^{n+1/2})$, then the random sampling of the solution W_i^{n+1} is conducted through

$$\mathrm{W}_i^{n+1} = \hat{\mathrm{W}}_i^{n+1}(\theta^{n+1}\Delta x, \Delta t^{n+1}). \tag{4.14}$$

θ^{n+1} is a random number between zero and one (i.e. $\theta \in [0, 1]$) found from a Van der Corput pseudo-random number sequence [39]. The length of the time step Δt^{n+1} is determined by the Courant-Friedrich-Levy (CFL) criterion given by

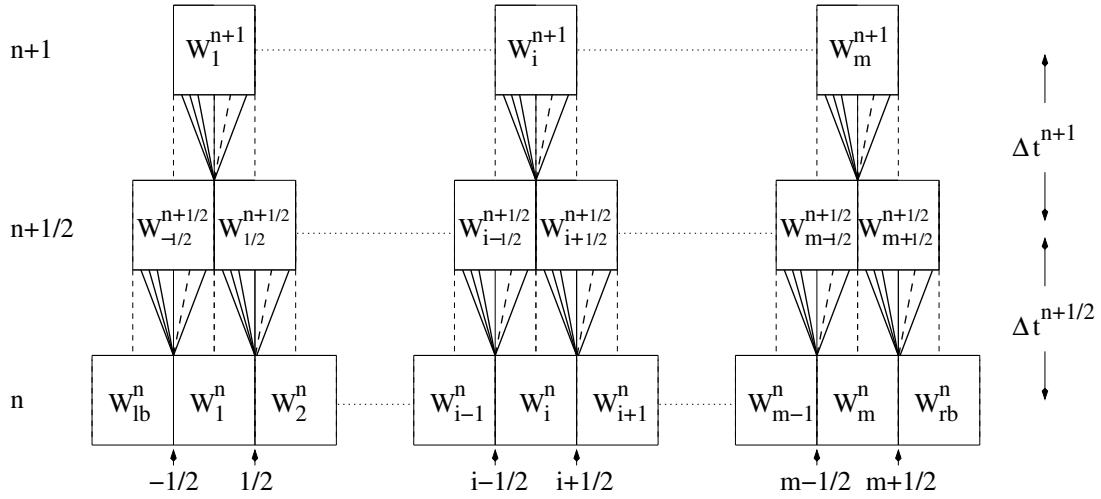

Figure 4.3: An illustration of the solution procedure for the Random Choice Method on a staggered grid.

$$\Delta t^{n+1} = C_{\text{CFL}} \frac{\Delta x}{|u_{\text{max}}^{n+1}| + c}. \tag{4.15}$$

$C_{\text{CFL}} = 0.45$ and $|u_{\text{max}}^{n+1}|$ is the maximum wave velocity existing throughout the domain at the time t^{n+1}.

The boundary conditions are illustrated in Figure 4.3 as W_{lb}^n for the left boundary and W_{rb}^n for the right boundary. For a closed pipe the left boundary condition is $W_{\text{lb}}^n = [\rho_1^n, -u_1^n, p_1^n]^T$ and the right boundary condition is $W_{\text{rb}}^n = [\rho_{\text{m}}^n, -u_{\text{m}}^n, p_{\text{m}}^n]^T$. Some simulations with a transmissive boundary (i.e. a non-reflecting end) have also been performed. These simulations used $W_{\text{rb}}^n = [\rho_{\text{m}}^n, u_{\text{m}}^n, p_{\text{m}}^n]^T$.

4.2.2 Combustion model

The conservation of mass and momentum in Equation (B.20) are reduced to $(\rho u)_x = 0$ and $(\rho u^2 + p)_x = 0$ for a steady flow. The conservation of mass and momentum over a steady flame therefore becomes

$$\rho_{\text{u}} u_{\text{u}} = \rho_{\text{b}} u_{\text{b}} = \text{M} \tag{4.16}$$

$$\rho_{\text{u}} u_{\text{u}}^2 + p_{\text{u}} = \rho_{\text{b}} u_{\text{b}}^2 + p_{\text{b}} \tag{4.17}$$

The subscript 'u' represents the unburned states and the subscript 'b' represents the burned states. Since $u_{\text{u}} = \text{M}/\rho_{\text{u}}$ and $u_{\text{b}} = \text{M}/\rho_{\text{b}}$ the conservation of momentum can be written as

$$\text{M}\frac{\text{M}}{\rho_{\text{u}}} + p_{\text{u}} = \text{M}\frac{\text{M}}{\rho_{\text{b}}} + p_{\text{b}}, \tag{4.18}$$

and finally

$$-\mathrm{M}^2 = \frac{p_\mathrm{b} - p_\mathrm{u}}{\frac{1}{\rho_\mathrm{b}} - \frac{1}{\rho_\mathrm{u}}}. \tag{4.19}$$

This is the Rayleigh line, which is a straight line in the p and $1/\rho$ plane. If one assumes that the flame position is locked and that the burning velocity of the flame is S, then $\mathrm{M} = S\rho_\mathrm{u}$.

The conservation of Energy in Equation B.20 is reduced to $(u(E+p))_x = 0$ for a steady flow. The conservation of Energy over a steady flame therefore becomes

$$u_\mathrm{u}(E_\mathrm{u} + p_\mathrm{u}) = u_\mathrm{b}(E_\mathrm{b} + p_\mathrm{b}). \tag{4.20}$$

Remember that $E = \rho e + (1/2)\rho u^2$ and that the specific enthalpy $h = e + p/\rho$. The conservation of energy can therefore be written as

$$\begin{aligned} h_\mathrm{b} - h_\mathrm{u} &= -\frac{1}{2}(u_\mathrm{b}^2 - u_\mathrm{u}^2) \\ &= -\frac{1}{2}\mathrm{M}^2\left(\frac{1}{\rho_\mathrm{b}^2} - \frac{1}{\rho_\mathrm{u}^2}\right), \end{aligned} \tag{4.21}$$

when the conservation of mass gives that $\rho_\mathrm{u}u_\mathrm{u} = \rho_\mathrm{b}u_\mathrm{b}$ and when $u_\mathrm{u} = \mathrm{M}/\rho_\mathrm{u}$ and $u_\mathrm{b} = \mathrm{M}/\rho_\mathrm{b}$. If Equation (4.19) is used for M^2, then the conservation of energy becomes

$$h_\mathrm{b} - h_\mathrm{u} = \frac{1}{2}(p_\mathrm{b} - p_\mathrm{u})\left(\frac{1}{\rho_\mathrm{b}} + \frac{1}{\rho_\mathrm{u}}\right). \tag{4.22}$$

The specific enthalpy $h = e + p/\rho$ may be written as $h = (\gamma/(\gamma-1))p/\rho$, when $e = (p/\rho)(1/(\gamma-1))$. The equation therefore changes to

$$\left(\frac{\gamma}{\gamma-1}\right)\left(\frac{p_\mathrm{b}}{\rho_\mathrm{b}} - \frac{p_\mathrm{u}}{\rho_\mathrm{u}}\right) - q = \frac{1}{2}(p_\mathrm{b} - p_\mathrm{u})\left(\frac{1}{\rho_\mathrm{b}} + \frac{1}{\rho_\mathrm{u}}\right) \tag{4.23}$$

when $h_\mathrm{u} = (\gamma/(\gamma-1))p_\mathrm{u}/\rho_\mathrm{u} + q$ and q is the heat of reaction. The equation can then finally be written as

$$\left(\frac{\gamma}{\gamma-1}\right)\left(\frac{p}{\rho} - \frac{p_\mathrm{u}}{\rho_\mathrm{u}}\right) - \frac{1}{2}(p - p_\mathrm{u})\left(\frac{1}{\rho} + \frac{1}{\rho_\mathrm{u}}\right) = q. \tag{4.24}$$

This is the Hugoniot curve, which gives the set of completely burned states ($\rho = \rho_\mathrm{b}, p = p_\mathrm{b}$) that can be assigned to a given unburned state by a detonation or a deflagration wave. If q and the unburned state are known, then the pressures p of the various possible burned states can be found as a function of the burned densities ρ by

$$p_\mathrm{Hc}(\rho) = \frac{\frac{p_\mathrm{u}}{\rho_\mathrm{u}}\left(\frac{\gamma+1}{\gamma-1}\right) - \frac{p_\mathrm{u}}{\rho} + 2q}{\frac{1}{\rho}\left(\frac{\gamma+1}{\gamma-1}\right) - \frac{1}{\rho_\mathrm{u}}}. \tag{4.25}$$

The subscript 'Hc' refers to Hugoniot curve.

Williams [40] states that the burned states (ρ_b,p_b) of a combustible gas can be related to the unburned states (ρ_u,p_u) through the intersection between the Rayleigh line and the

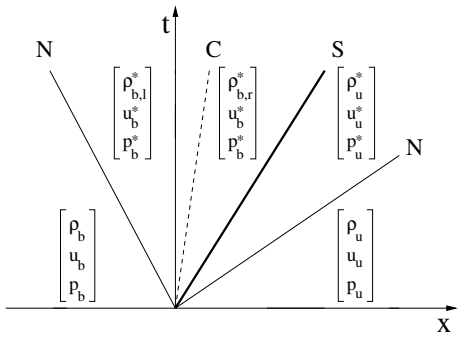

Figure 4.4: The combustion model in RCMLAB.

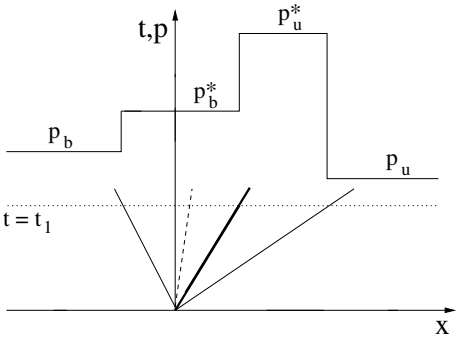

Figure 4.5: An example of a pressure solution for the combustion model in RCMLAB at the time t_1.

Hugoniot curve. A sketch of a Hugoniot curve together with the Rayleigh line is given in Figure 4.2. There may be two points of intersection between the Rayleigh line and the Hugoniot curve. The first intersection point is called 'weak' and the second intersection point is called 'strong'. The intersection point is called a Chapman-Jouguet (CJ) point when the Rayleigh line is a tangent to the Hugoniot curve. RCMLAB only takes into account the burned states which are either from weak deflagrations or from a CJ deflagration.

The combustion model treats the combustion wave as a discontinuity with a known burning velocity S. Since the burning velocity is known, the combustion process can be treated in essentially the same way as an ordinary non-reactive Riemann problem. The only difference is that the star region is divided into a burned and an unburned section. An illustration of the combustion model is given in Figure 4.4. 'N' is a nonlinear wave (i.e. shock or rarefaction), 'C' is the Contact discontinuity and 'S' is the burning velocity. p^*_{u} is first found by an iterative Newton-Rhapson procedure. When k $=$ u the state ρ^*_{u} is found with Equation (4.13) and u^*_{u} is found from $u^*_{\mathrm{u}} = u_{\mathrm{u}} + f_{\mathrm{u}}$. f_{u} is a function given by Equation (4.8). The burned states $\rho^*_{\mathrm{b,r}}$ and p^*_{b} are then found from the intersection of the Rayleigh line with the Hugoniot curve. When k $=$ b the state $\rho^*_{\mathrm{b,l}}$ is found with Equation (4.13) and u^*_{b} is found from $u^*_{\mathrm{u}} = u_{\mathrm{b}} - f_{\mathrm{b}}$. f_{b} is also a function given by Equation (4.8).

An example of a pressure solution for the combustion model at the time t_1, is shown in Figure 4.5. The wave pattern from Figure 4.4 is also plotted in Figure 4.5. Both of the nonlinear waves are shocks in this solution.

RCMLAB assigns a γ_{b} to grid cells which contain burned gas and a γ_{u} to grid cells which contain unburned gas. The flame position can therefore be determined by the position of the jump in the γ value. Table C.1 gives the values of the various q, γ_{u} and γ_{b} that have been used in the simulations for the different gas mixtures.

4.2.3 Burning velocity

Two different burning velocity models (BVM) have been used to calculate the one dimensional burning velocity in the simulations. One model (BVM1) uses experimental pressure records as input to calculate the burning velocity. The other model (BVM2)

uses the flow field right in front of the flame to calculate the burning velocity. A short description of the two models is given below.

BVM1: A model based burning velocity estimator

This model estimates the burning velocity from experimental pressure records. A version of the method has been presented by Bjerketvedt et al. [19]. The principle of the method is illustrated in Figure 4.6. A pressure wave is created by the flame at x_{l} at the time t^n. The magnitude of the pressure wave depends on the burning velocity S of the flame. This pressure wave propagates away from the flame in both directions. If a pressure transducer is located at x_{pt}, then the generated pressure wave in front of the flame will pass this pressure transducer at the time $t_{\text{pt}} = t^n + \Delta t$. The subscript 'pt' refers to the term pressure transducer. The time it takes for the pressure wave to propagate from the flame to the pressure transducer may be approximated to be $\Delta t \approx (x_{\text{pt}} - x_{\text{l}})/(c + u)$, where c and u are the speed of sound and the velocity field at the flame for the time t^n, respectively. A point x_{r} at the right hand side of x_{pt} is then chosen as $x_{\text{r}} = x_{\text{pt}} + (c - u)\Delta t$, where c and u now represent the conditions at the pressure transducer for the time t^n. The right running characteristic $(u + c)$ from the point x_{l} and the left running characteristic $(u - c)$ from the point x_{r} then arrive at the point x_{pt} at the approximated time t_{pt}.

An array of different burning velocities S is then used together with the combustion model to find the unburned states $\text{W}_{\text{l}}^n = [\rho_{\text{u}}^*, u_{\text{u}}^*, p_{\text{u}}^*]^T$ at x_{l} for the time t^{n}. (See Figure 4.4.) The solutions of the Riemann problems $RP(\text{W}_{\text{l}}^n, \text{W}_{\text{r}}^n)$ between the various states at x_{l} and the state at x_{r} for the time t^{n}, then give an array of $p^*(S)$. If p_{exp} is the experimental pressure recorded from the pressure transducer at x_{pt} for the time t_{pt}, then the value of S that gives $p^*(S) = p_{\text{exp}}$ is chosen as the burning velocity for the next time step. This is repeated at each time step through an interpolation between the various burning velocities and the error function which can be expressed as

$$\Delta p_{\text{e}}(S) = p_{\text{exp}} - p^*(S). \tag{4.26}$$

The subscript 'e' refers to the word error and the subscript 'exp' refers to the word experiment.

The pressure transducer behind the flame can also be used to estimate the burning velocity. The right hand sides of the Riemann problems then become the states $\text{W}_{\text{r}}^n = [\rho_{\text{b,r}}^*, u_{\text{b}}^*, p_{\text{b}}^*]^T$ and the left hand sides become $\text{W}_{\text{l}}^n = [\rho_{\text{l}}, u_{\text{l}}, p_{\text{l}}]^T$. The point x_{l} is found by $x_{\text{l}} = x_{\text{pt}} - (c + u)\Delta t$, where c and u represent the conditions at the pressure transducer at the time t^n. The value of Δt may be found by the approximation $\Delta t \approx (x_{\text{r}} - x_{\text{pt}})/(c - u)$, where c and u now represents the conditions at the flame at the time t^n. The time t_{pt} is finally found by $t_{pt} = t^n + \Delta t$.

The pressure transducer at the ignition wall has been used to estimate the burning velocity for the first 1.0 m of the flame propagation. A procedure different to the one described in the previous paragraphs was used for this pressure transducer. Since the pressure transducer is behind the flame, the right hand sides of the Riemann problems are of the form $\text{W}_{\text{r}}^n = [\rho_{\text{b,r}}^*, u_{\text{b}}^*, p_{\text{b}}^*]^T$. But the left hand side is now $\text{W}_{\text{l}}^n = [\rho_{\text{l}}, u_{\text{l}}, p_{\text{l}}]^T$ at the first grid cell. These Riemann problems are solved for the various burning velocities and then sampled at $x = 0$ in the local solutions. If the sampled solutions are $[\rho, u, p]^T$, then new

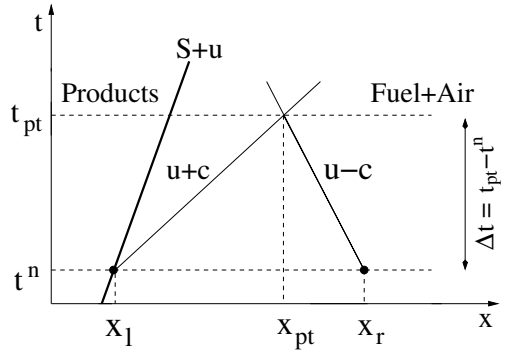

Figure 4.6: An illustration of the characteristics used by BVM1.

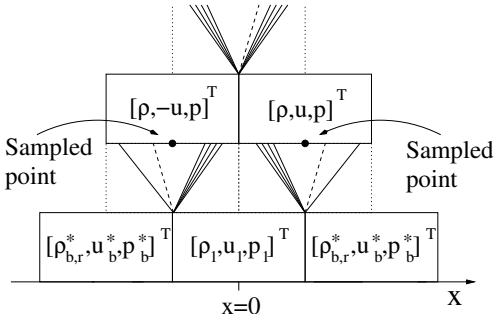

Figure 4.7: A sketch of the scheme used by BVM1 for the pressure transducer at the ignition wall.

Riemann problems of the form $RP([\rho, -u, p]^T, [\rho, u, p]^T)$ are solved to find the pressure $p^*(x_{\text{pt}}, t_{\text{pt}})$. This procedure is equivalent to the scheme illustrated in Figure 4.7. The time t_{pt} is approximated to be $t_{\text{pt}} \approx t^n + x_{\text{r}}/(c-u)$, where c and u are the speed of sound and the fluid velocity at the flame at the time t^n, respectively.

BVM2: A model based burning velocity simulator

This model uses the laminar burning velocity and the flow field right in front of the flame to simulate the burning velocity. Peters [10] has presented the following expression to calculate the turbulent burning velocity:

$$\frac{S_T}{S_L} = 1 + k_1 \left(\frac{u'}{S_L} \right)^n . \tag{4.27}$$

S_T is the turbulent burning velocity, S_L is the laminar burning velocity, u' is the velocity fluctuation, $n \in < 0.5, 1.0 >$ and k_1 is a constant that depends on the length scale ratio l_0/δ_L, where l_0 is the integral length scale and δ_L is the flame thickness. The equation is based on the effects of both small scale and large scale turbulence presented by Damköler [41]. For the limit $u' \to 0$ the equation gives $S_T \to S_L$.

Williams [40] has proposed that n should be close to 0.7 in Equation (4.27). If $S = S_T$ and the velocity fluctuations are written as a constant multiplied with the absolute value of the velocity field, i.e. $u' = k_3|u|$, then Equation 4.27 becomes

$$\begin{aligned} S &= S_L \left[1 + \left(k_2 \frac{u'_0}{S_L} \right)^{0.7} \right] \\ &= S_L \left[1 + \left(k_4 \frac{|u|}{S_L} \right)^{0.7} \right] . \end{aligned} \tag{4.28}$$

This equation is used to calculate the burning velocity in the simulations. The magnitude of the constant k_4 is tuned manually to fit the experimental results, but it is not changed during the simulation. Table 4.3 shows the value of k_4 that gave the best simulation results for the various equivalence ratios of hydrogen and air.

4.2.4 Obstacle model

A model for the area change at the obstacle has been added to RCMLAB. The model treats the obstacle as two different types of pipe cross section area changes. In the first half of the model the cross section area is monotonically decreasing over a number of grid cells. In the second half of the model the cross section area is monotonically increasing over an equal number of grid cells. The cross section area changes are implemented after the operator splitting method [42]. The equations for the modification of the primitive variables are given by Gottlieb [37] as

$$\begin{aligned} \rho &= \hat{\rho}\,[1 - \beta\hat{u}\Delta t] \\ u &= \hat{u} \\ p &= \hat{p}\,[1 - \gamma\beta\hat{u}\Delta t] \end{aligned}, \tag{4.29}$$

where $\hat{\rho}$, $\hat{u}$ and $\hat{p}$ are the unmodified variables at each time step, Δt is the time step and $\beta = (1/\mathrm{A})\mathrm{dA}/\mathrm{d}x$. The cross section areas over the obstacle are given by

$$\mathrm{A}(\xi) = (A_1 A_2)^{\frac{1}{2}} \exp\left\{ \ln\left[\left(\frac{A_1}{A_2} \right)^{\frac{1}{2}} \right] \cos\left(\frac{\pi\xi}{\tilde{L}} \right) \right\}, \tag{4.30}$$

where $\xi \in [0, \tilde{L}]$ and $\tilde{L}$ is the length of the local area change. In the first part of the obstacle model, A_1 is the cross section area of the pipe and A_2 is the cross section area of the obstacle opening. In the second part of the model, A_1 and A_2 are switched. The first derivative of the area may be written as

$$\frac{1}{\mathrm{A}} \frac{\mathrm{dA}}{\mathrm{d}x} = \frac{\pi}{2\tilde{L}} \ln\left(\frac{A_2}{A_1} \right) \sin\left(\frac{\pi\xi}{\tilde{L}} \right). \tag{4.31}$$

Figure 4.8 and Figure 4.9 show the pipe cross section area changes and the β-function for a pipe with an obstacle opening diameter of 20 mm. The diameter of the pipe was 107 mm. Figure 4.9 shows that β is a symmetric function over each local area change length $\tilde{L}$. This symmetry is an advantage since it reduces the numerical noise in the model [37].

Since the flow of a fluid trough orifice plates with sharp edges is known to create a reduced flow-area [37], a correction factor $C_d \leq 1.0$ was multiplied with the cross section area of the obstacle opening. The correction factor is given by

$$C_d = \frac{\pi}{\pi + 2 - 5s + 2s^2}, \tag{4.32}$$

where $s = (\gamma - 1)M_o^2/2$ and M_o is the Mach number of the flow inside the obstacle. The limit $M_o \to 0$ gives $C_d \to 0.611$. The best simulation results were achieved if the correction factor was set equal to unity when M_0 was close to 1.0. For the simulations with propane and methane, which have relatively low burning velocities between the ignition wall and the obstacle, the correction factor had to be reduced even further. In these simulations the correction factor was multiplied with a factor ranging from 0.35 to 0.75. The simulations with more reactive gas mixtures, such as stoichiometric hydrogen and air, were performed with $C_d = 1.0$ at all times.

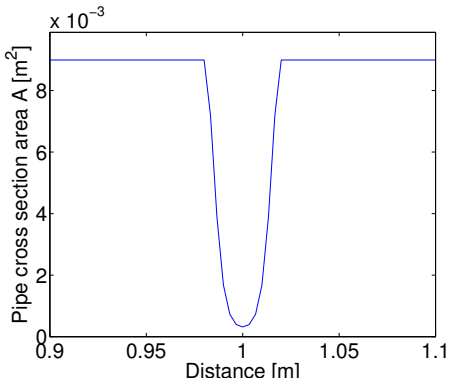

Figure 4.8: The pipe cross section area change for an obstacle opening diameter of 20 mm.

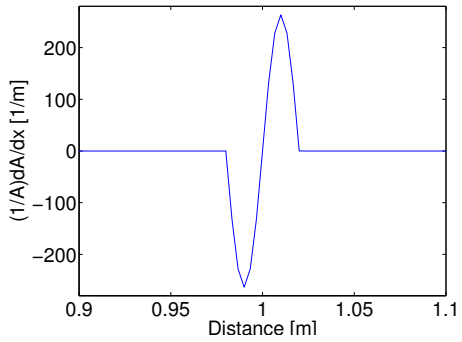

Figure 4.9: The β-function for an obstacle opening diameter of 20 mm.

4.2.5 Heat transfer and friction model

The total energy of the system is changed through friction and heat transfer at the pipe wall. Both heat convection and heat radiation reduce the potential energy of the system, while the pipe wall friction reduces the kinetic energy of the system. These changes in the system energy are implemented into RCMLAB by the operator splitting method. Both the heat convection and the heat radiation model assume that the pipe wall temperature T_w is constant and equal to the temperature T_0 outside the domain.

Heat convection and friction

The model for friction and heat convection is based on the work of Bjerketvedt [20] and it has previously been described by Kristoffersen [24]. A friction factor C_f is used together with the Reynolds analogy [47] to model the heat convection and wall friction in the different flow regimes. This means that the wall shear stress and the heat transfer rate are proportional in the boundary layer flow. The magnitude of the friction factor is further based on the Reynolds number as shown in Equation (4.33). Both the different flow regimes and friction factor equations are obtained from Kays and Crawford [45] for a fully developed flow in a circular pipe.

$$C_f = \begin{cases} 0, & \text{if} \quad 0 \leq \text{Re} < 1000 \quad \text{(laminar)} \\ 0.078(\text{Re})^{-0.25}, & \text{if} \quad 1000 \leq \text{Re} < 30000 \quad \text{(transition)} \\ 0.046(\text{Re})^{-0.20}, & \text{if} \quad 30000 \leq \text{Re} \quad \text{(turbulent)} \end{cases}, \tag{4.33}$$

The Reynolds number is given as $\text{Re} = |(\rho u D_p)/\mu|$, where μ is the viscosity of the gas. An approximation to the temperature dependence of the viscosity is given by the power law [46] as

$$\mu \approx \mu_0 \left(\frac{T}{T_0}\right)^{0.7}, \tag{4.34}$$

where the subscript '0' represents the reference values. The different values of μ_0 used in the simulations for the various gas mixtures, are listed in Table C.1.

Kays and Crawford [45] give the wall shear stress as

$$\tau_w = \alpha C_f \frac{\rho u^2}{2}, \tag{4.35}$$

where α is a wall specific factor. α was given the value of 1.0 in the simulations.

The heat convection at the pipe wall is defined by Eckert and Drake [43] as

$$\dot{Q}_c = h \left[T + \left(\frac{u^2}{2c_p} (\mathrm{Pr})^{1/3} \right) - T_0 \right], \tag{4.36}$$

when the pipe wall temperature is equal to the temperature outside the domain. In this equation T is the temperature, T_0 is the temperature outside the domain, Pr is the Prandtl number and h is the heat transfer coefficient. A Prandtl number of 0.7 has been used in the simulations. Applying the Reynolds analogy the heat transfer coefficient is also a function of the friction factor [44]: $h = (1/2)\alpha C_f c_p u$. Equation (4.36) can then be written as

$$\dot{Q}_c = \frac{1}{2}\alpha C_f \left[0.45\rho u^3 + \frac{\gamma}{\gamma - 1} u \left(p - \rho \frac{p_0}{\rho_0} \right) \right], \tag{4.37}$$

where ρ_0 and p_0 are the density and pressure outside the domain, $\gamma = c_p/c_v$ and $e = Tc_v = p/[(\gamma - 1)\rho]$. The energy at each time step then changes to

$$E = \hat{E} - \frac{4}{D_p}\dot{Q}_c \Delta t = \frac{p}{\gamma - 1} + \frac{1}{2}\rho u^2, \tag{4.38}$$

where $\hat{E} = \frac{\hat{p}}{\gamma - 1} + \frac{1}{2}\hat{\rho}\hat{u}^2$ and $\hat{\rho}$, $\hat{u}$ and $\hat{p}$ are the unmodified variables at each time step. When the reduced velocity due to friction is given as $u = \hat{u} - [4\tau_w/(\rho D_p)]\Delta t = \hat{u} - 2(\alpha C_f/D_p)\hat{u}^2 \Delta t$ and Equation (4.38) is solved with respect to p, the equations for the modified primitive variables become

$$\begin{aligned} \rho &= \hat{\rho} \\ u &= \hat{u} - 2\hat{u}^2 \left(\frac{\alpha C_f}{D_p} \right) \Delta t \\ p &= \hat{p} + \left(\frac{1}{2}\hat{\rho}(\hat{u}^2 - u^2) - \frac{4}{D_p}\dot{Q}_c \Delta t \right) (\gamma - 1) \end{aligned} \quad . \tag{4.39}$$

The factor $4/D_p$ is the hydraulic diameter of a circular pipe and it transforms the quantities from 'per unit surface area' to 'per unit volume' [37].

Radiant heat transfer

The modeling of the heat transfer has been changed to also account for the net heat flux caused by water vapor radiation. This feature is implemented into RCMLAB after a procedure presented by the VDI Heat Atlas [48]. The net radiant heat transfer between the gas and the pipe wall is given by

$$\dot{Q}_r = A_e \sigma \left(\frac{\varepsilon_w}{1-(1-\varepsilon_w)(1-A_v)} \right) (\varepsilon_g T_g^4 - A_v T_w^4), \tag{4.40}$$

where A_e is the exchange area, σ is the Stefan-Boltzmann constant, ε_g and ε_w is respectively the gas and wall emissivity and A_v is the absorptance of the gas.

The exchange area has been approximated to be the outer pipe wall of each pipe element, i.e. $A_e = \pi D_p \Delta x$. The radiation through the end walls of each pipe element are therefore not accounted for. The wall emissivity ε_w is given the value of 0.95, which is the emissivity of strongly oxidized iron [48]. The gas emissivity ε_g is given as

$$\begin{aligned} \varepsilon_g &= f_{\mathrm{H_2O}} \cdot \varepsilon_{\mathrm{H_2O}} \\ &= f_{\mathrm{H_2O}} \left\{ (0.747 - 0.168 \cdot 10^{-3} T_g) \left[1 - \exp\left(-F \cdot G\right) \right] \right\} \end{aligned} \quad , \tag{4.41}$$

where $f_{\mathrm{H_2O}}$ is a correction factor given by

$$f_{\mathrm{H_2O}} = 1 + (A^* - 1) \exp\left\{ -0.5 \left[\log\left(\frac{0.132 \left(\frac{T_g}{1000} \right)^2}{s_{eq} p_{\mathrm{H_2O}}} \right) \right]^2 \right\}, \tag{4.42}$$

and F, G and A^* are given respectively by

$$F = [1.785 - 0.039(s_{eq} p_{\mathrm{H_2O}}) + 0.2436(s_{eq} p_{\mathrm{H_2O}})^2](s_{eq} p_{\mathrm{H_2O}}) \tag{4.43}$$

$$G = 1 + \frac{0.11923}{0.137 + (s_{eq} p_{\mathrm{H_2O}})^{0.79}} \left[\frac{T_g}{1000} - 0.273 - \frac{0.99}{0.495 + (s_{eq} p_{\mathrm{H_2O}})^4} \right]^2 \tag{4.44}$$

$$A^* = \frac{p[1.888 - 2.053 \log(\tau)] \left[1 + 4.9 \left(\frac{p_{\mathrm{H_2O}}}{p} \right) \left(\frac{273}{T_g} \right)^{0.5} \right] + 1.1 \left(\frac{T_g}{1000} \right)^{-1.4}}{0.888 - 2.053 \log(\tau) + p \left[1 + 4.9 \left(\frac{p_{\mathrm{H_2O}}}{p} \right) \left(\frac{273}{T_g} \right)^{0.5} \right] + 1.1 \left(\frac{T_g}{1000} \right)^{-1.4}} \tag{4.45}$$

In these equations s_{eq} is the equivalent layer thickness given as $s_{eq} = 0.9(4V_e/A_e) = 0.9D_p$ and $p_{\mathrm{H_2O}}$ is the water vapor partial pressure. All pressures are in bar (100 kPa) and the following constrains are applied to equation (4.42) and (4.45).

$$f_{\mathrm{H_2O}} = \begin{cases} f_{\mathrm{H_2O}} & \text{if } f_{\mathrm{H_2O}} \leq A^* \\ A^* & \text{if } f_{\mathrm{H_2O}} > A^* \end{cases} \quad , \quad \tau = \begin{cases} 0.75 & \text{if } T_g \leq 750 \text{ K} \\ \frac{T_g}{1000} & \text{if } T_g > 750 \text{ K} \end{cases} \tag{4.46}$$

The absorptance A_v is given by

$$A_v = (f_{\mathrm{H_2O}} \cdot \varepsilon_{\mathrm{H_2O}}) \left(\frac{T_g}{T_w} \right)^{0.45} , \tag{4.47}$$

but the input parameters to the $\varepsilon_{\mathrm{H_2O}}$-function are changed here. The water vapor partial pressure is converted to $p_{\mathrm{H_2O}}(T_w/T_g)$, which is the value of the water vapor partial pressure at the wall temperature. The input temperature is changed to T_w.

If the radiant heat transfer is included in equations (4.39), then the equations change to

$$\begin{aligned} \rho &= \hat{\rho} \\ u &= \hat{u} - 2\hat{u}^2 \left(\frac{\alpha C_f}{D_p} \right) \Delta t \\ p &= \hat{p} + \left(\frac{1}{2}\hat{\rho}(\hat{u}^2 - u^2) - \frac{4}{D_p}(\dot{Q}_c + \dot{Q}_r)\Delta t \right) (\gamma - 1) \end{aligned} \quad . \tag{4.48}$$

These equations now account for the momentum loss caused by friction and the heat transfer caused by heat radiation and heat convection.

CO_2 is another combustion product that is of major importance in radiative heat transfer. The heat transfer model should therefore be changed to also account for CO_2 in the future.

4.3 Results and discussion

The RCMLAB program described in Section 4.2 has been used to perform one dimensional numerical simulations of gas explosions in pipes. The simulations presented in this section have the same fuel concentrations and use the same pipe types as the experiments in Chapter 3. The only exception is some simulations with a non reflecting end for an unobstructed pipe in Subsection 4.3.3.

Table 4.1 shows the simulation time and the number of time steps for RCMLAB simulations of a gas explosion at seven different grid resolutions. The simulations were performed for a hydrogen and air mixture in the 3.0 m pipe. The hydrogen volume percentage was 35 and the simulations lasted from the time of ignition to the time when the flame had propagated 1.0 m down the pipe. The estimated burning velocity was based on the experimental overpressure recorded at pressure transducer P0. (See Figure 3.8.) Table 4.1 shows that both the simulation time and the number of time steps increase nonlinearly when the number of grid cells is increasing. The simulation time is not only affected by the number of grid cells, but also by the size of the time step. A reduction of the grid cell size Δx will also reduce the size of the simulation time step Δt^{n+1}. (See Equation (4.15).) The simulations were performed with a DELL gx280, which had a CPU speed of 2.8 GHz. The total amount of memory was 512 MB and the operating system was SUSE Linux 9.1.

This section has been divided into tree subsections. Subsection 4.3.1 presents numerical simulations which start at the time of ignition and last until the flame is quenched at the opposite end wall. Subsection 4.3.2 presents numerical simulations of only the initial flame propagation. The term 'initial' refers in this case to the first 1.0 m of the flame propagation. These two groups of simulations used experimental pressure records as input to estimate the burning velocity. Subsection 4.3.3 presents numerical simulations with an alternative burning velocity model. Both the term 'blockage ratio' and the term 'obstacle opening diameter' are used for the area change at the obstacle. (The use of the terms depends on which is the best suited.) An overview of the two quantities can be found in the table in Figure 3.2.

Table 4.1: Simulation time and the number of time steps for RCMLAB simulations of a gas explosion at seven different grid resolutions. The simulations were performed for a hydrogen and air mixture in the 3.0 m pipe.

Scale	Number of grid cells	Simulation time [s]	Number of time steps
1	300	133	1297
2	600	237	2697
4	1200	577	5425
6	1800	1156	8201
8	2400	1671	10921
10	3000	2493	13641
15	4500	4855	20433

Table 4.2: An overview of the numerical simulations presented in Subsection 4.3.1.

Simulation configuration	Pipe type [m]	Fuel type	Fuel concentration (% volume)	Obstacle opening diameter [mm]
1	3.0	H_2	35.0	No obstacle
2	4.0	H_2	20.0	30
3	7.0	H_2	50.0	50
4	4.0	C_3H_8	4.0	50
5	4.0	CH_4	9.5	50

4.3.1 Gas explosions in closed pipes

Numerical simulations of gas explosions in closed pipes with premixed fuel and air at atmospheric conditions, have been performed. Table 4.2 gives a list of the numerical simulations that are presented in this subsection. These simulations used 1) the experimental pressure records from the experiments described in Chapter 3 as input to make an estimate of the burning velocity, 2) the experimental pressure record from pressure transducer P0 to estimate the burning velocity for the first 1.0 m of the flame propagation, and 3) a constant burning velocity when the flame was close to the end wall. The main purpose of performing these simulations was to see how well the burning velocity model managed to reproduce the experimental pressure records for the various pipe lengths, blockage ratios and fuel concentrations.

3.0 m pipe with hydrogen and air

The simulated and experimental overpressure from a gas explosion in the 3.0 m pipe is shown in Figure 4.10. The pipe was unobstructed and the hydrogen volume percentage was 35. The overpressures have been multiplied by two and they are plotted as a function of both the time and the pressure transducer position in the pipe. The simulated flame position is also plotted in the figure. Figure 4.11 shows the corresponding simulated burning

velocity. The vertical lines and the pressure transducer labels in Figure 4.11, indicate the use of the different experimental pressure records during the simulation. The burning velocity was held constant at 32 m/s after the flame had passed pressure transducer P5.

Subsection 3.3.1 gives a theoretical description of the early phases of the flame propagation for the 3.0 m pipe. That description is given in regard of the first 14 ms of the recorded overpressure at pressure transducer P0. (See Figure 3.8.) The same description can also be applied for the first 13.2 ms of the simulated burning velocity in Figure 4.11. The only exception is the spike at approximately 11.8 ms. It is assumed that this spike is caused by an elevated pressure at the x_{r} position in the burning velocity estimator model. This elevated pressure is caused by the first pressure wave that is propagating back up the pipe after it has been reflected off the end wall. Figure 4.10 shows that the reflected pressure wave is a shock when it reaches x_{r} at the time t^n in Figure 4.6. This shock wave will further have reached the x_{pt} position (the pressure transducer P3 in this case) at the time $t_{\mathrm{pt}} = t^n + \Delta t$. If the solution of the Riemann problem $RP(\mathrm{W}_{\mathrm{l}}^n, \mathrm{W}_{\mathrm{r}}^n)$ is of the form SCR, i.e. a shock wave and a contact surface together with a rarefaction wave, then the pressure p^* in the star region becomes too low compared to the pressure p_{exp} with the true value of S. The model therefore increases the burning velocity S to make p^* equal to p_{exp}. Remember that p_{exp} is the experimental pressure at x_{pt} for the time t_{pt}. A small step in the burning velocity of approximately 2.0 m/s can also be observed at about 10.8 ms. This occurs at the same time as BVM1 starts to use the experimental pressure from pressure transducer P3. The flame is at this time in the simulation, approximately 0.93 m from the ignition wall and the small step in the simulated burning velocity is most likely caused by a pressure difference in the recorded overpressure at the two pressure transducers.

The simulation results in Figure 4.10 shows that the reflected pressure wave hits the flame from the unburned gas side at approximately 13.2 ms. Figure 4.11 shows that the simulated burning velocity starts to decrease at that time. The burning velocity then temporally equals zero at approximately 13.9 ms. The pressure wave is further reflected off the ignition wall at 14.1 ms and it interacts with the flame from the burned gas side at approximately 15.0 ms. The burning velocity then decreases once more and it temporary equals zero at 15.2 ms. This type of behavior for a one dimensional burning velocity, may be a footprint of a three dimensional flame going through an inversion process and back. The inversion processes is most likely caused by the flow field generated by the propagating pressure wave. The pressure wave then reflects off the end wall for the second time at approximately 19.1 ms and it hits the flame from the unburned gas side at approximately 21.5 ms. Because of the rapid changes of the simulated burning velocity at this stage in the simulation, it is not possible to relate this last or any other later interactions directly to a change in the burning velocity.

Figure 4.12 shows the simulated overpressure multiplied with the specific heat capacity ratio ($p \cdot \gamma$) as a function of both distance and time. The darker regions to the left in the figure represent low pressures and the brighter regions to the right represent higher pressures. Both the flame position, the propagating pressure waves and the interactions between pressure waves and the reaction zone can be seen in this figure.

The first 11 ms of the simulation give pressures that are very similar to the experimental pressures. For the larger simulation times the differences in the pressures are mainly initiated by the incorrect peak in the burning velocity at 11.8 ms. Figure 4.10

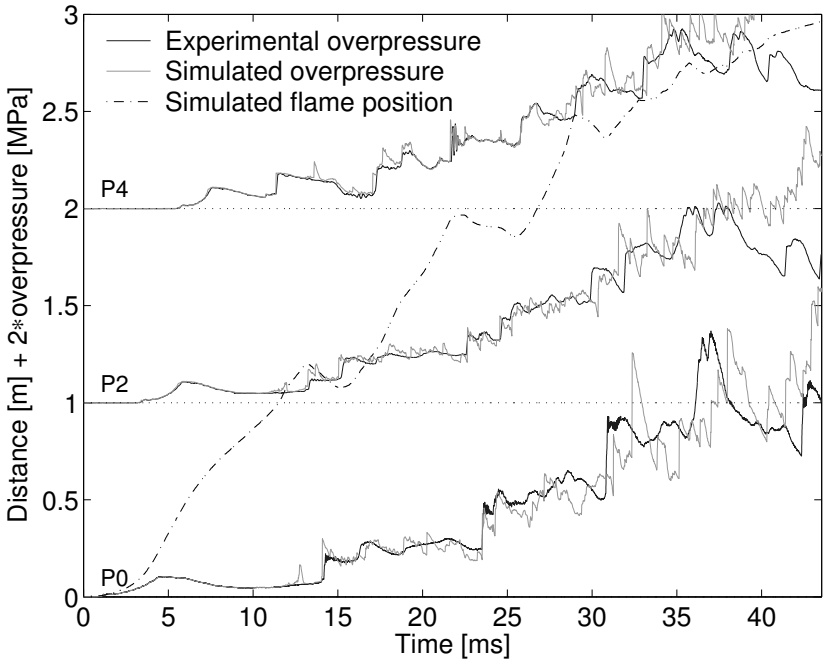

Figure 4.10: Experimental and simulated overpressure at pressure transducer P0, P2 and P4 in the 3.0 m pipe for a hydrogen volume percentage 35. The overpressures have been multiplied by two and they are shifted along the vertical axis to indicate the pressure transducer position in the pipe. (1.0 m corresponds to 1.0 MPa.)

shows that the simulated pressure becomes more noisy and that the complexity of the system increases as the flame propagates down the pipe. It is therefore assumed that the accuracy in the estimated burning velocity is decreasing with time. But the evolvement of the experimental and simulated overpressures are relatively similar even for the higher simulation times. The initial stages of the flame propagation indicate that there is some sort of coupling between the burning velocity and the flow field at the reaction zone.

The experimental overpressure in Figure 4.10 begins to drop when the flame is close to the end wall. This happens for times approximately larger than 35 ms. It is assumed that this pressure drop is related to both the heat loss to the surroundings and the time response of the piezo electrical pressure transducers.

4.0 m pipe with hydrogen and air

Figure 4.13 shows the experimental and simulated overpressure at pressure transducer P0, P1 and P3 for a gas explosion in the 4.0 m pipe. The overpressures have been multiplied by two and they are plotted as a function of both the pressure transducer location in the pipe and the time. The simulated flame position are also plotted in Figure 4.13. Figure 4.14 shows the corresponding simulated burning velocity. The obstacle opening diameter was 30 mm and the hydrogen volume percentage was 20.

Both the burning velocity and the flame propagation have an oscillating behavior between the ignition wall and the obstacle. The amplitudes of the burning velocity stay relatively equal but the periods decrease as the flame gets closer to the obstacle. The

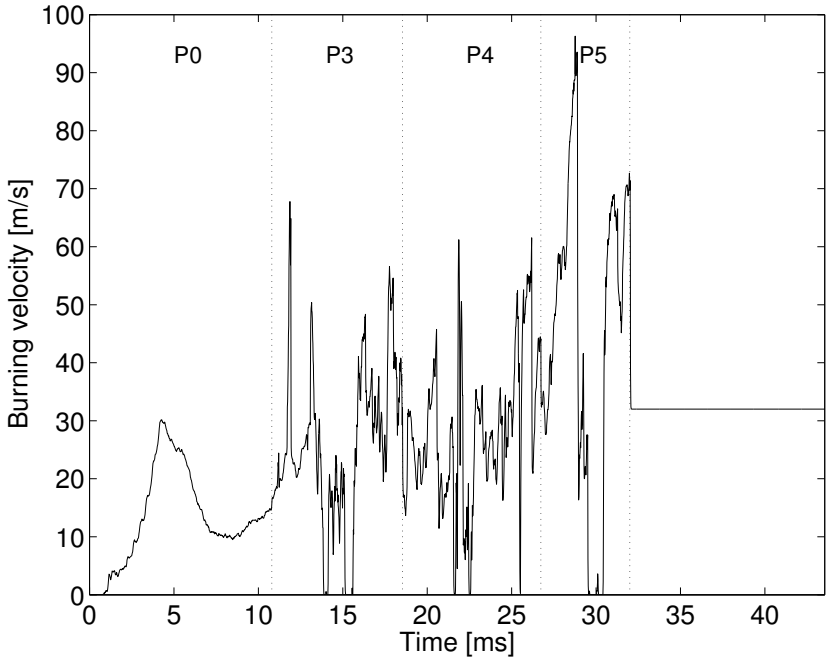

Figure 4.11: Simulated burning velocity for the 3.0 m pipe. The hydrogen volume percentage was 35. The vertical lines together with the pressure transducer labels indicate which pressure record that were used as input during the simulation.

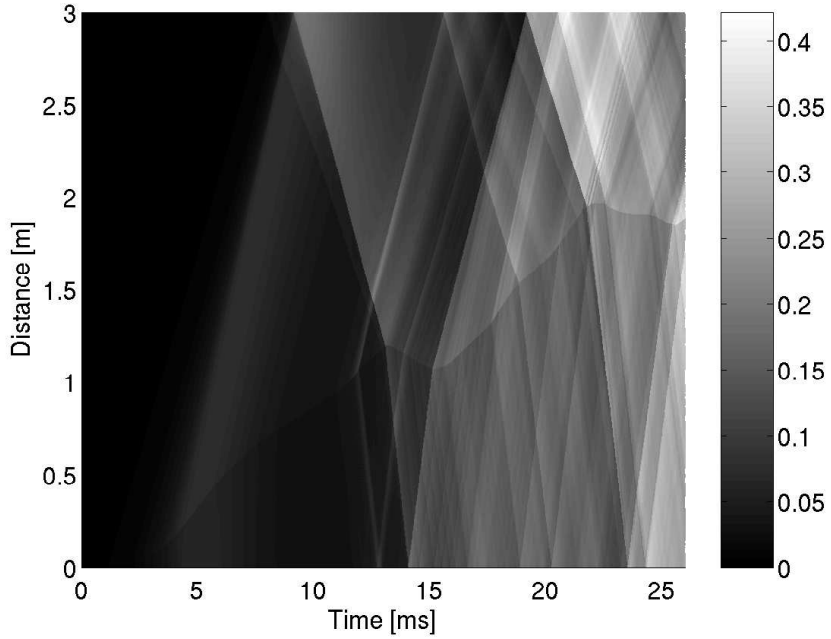

Figure 4.12: Simulated overpressure multiplied with the specific heat capacity ratio for the 3.0 m pipe. The darker regions to the left represent low pressures and the brighter regions to the right represent higher pressures. The hydrogen volume percentage was 35 and the gray-scale bar gives the value in MPa.

flame passes the obstacle at approximately 40 ms and Figure 4.14 shows that there is a large increase in the burning velocity at that time. The maximum burning velocity is 18 m/s before the obstacle and 145 m/s after the obstacle. The increased burning velocity after the obstacle creates a lead shock. Figure 4.13 shows that the distance between the flame and the lead shock increases as they propagate down the pipe. This may indicate a loose coupling between the obstacle caused shock and the reaction zone. Figure 4 at page 4 in Section A.2 (i.e. paper 2 in Appendix A), shows a simulation of a gas explosion in the 4.0 m pipe with an obstacle opening diameter of 20 mm and a hydrogen volume percentage of 30. In that simulation the flame and the lead shock do propagate down the pipe with almost the same speed.

The lead shock is reflected off the end wall at approximately 44.7 ms and it hits the flame from the unburned gas side at approximately 46.5 ms. It is difficult to relate this interaction to a specific change in the burning velocity because of the rapid changes in the burning velocity at that time. But it is interesting to see that the burning velocity remains high even after the collision. The burning velocity was held constant at 25 m/s when the flame had passed pressure transducer P5.

Some large differences between the experimental and simulated overpressure can be seen. The first major difference appears for pressure transducer P0 at approximately 42 ms. The obstacle caused shock is too weak in the simulation. This may be caused by a reduction of the shock when it goes through the obstacle model. Another difference appears at pressure transducer P1 at approximately 50 ms. In spite of these two differences there is good agreement between the experimental and simulated overpressure.

7.0 m pipe with hydrogen and air

Numerical results from the simulation of a gas explosion in the 7.0 m pipe, are shown in Figure 4.15, Figure 4.16 and Figure 4.17. The obstacle opening diameter was 30 mm and the hydrogen volume percentage was 50. Figure 4.15 shows the simulated flame position together with the simulated and experimental overpressure at pressure transducer P0, P1, P3 and P5. The overpressures have been multiplied by three and they are plotted as a function of both time and the pressure transducer location in the pipe. Figure 4.16 shows the simulated and experimental overpressure at pressure transducer P1. The experimental overpressure has been shifted 0.35 MPa in this figure. The simulated burning velocity is shown in Figure 4.17.

The flame uses approximately 17.4 ms to propagate from the ignition wall to the obstacle. This is under half of the time the flame used to propagate the same distance for the 4.0 m pipe in the previous sub subsection. The number of oscillations in the burning velocity is also reduced with approximately 50 percent compared to that simulation. These differences are mainly related to the differences in the equivalence ratio of the gas mixtures and the blockage ratio of the obstacles. But the discussion in Subsection 3.3 showed that the pipe length also could influence the initial flame propagation in an obstructed pipe. A numerical study of how the blockage ratio of the obstacle affects the initial flame propagation, is presented in Subsection 4.3.2.

Figure 4.17 shows that there is a large increase in the burning velocity when the flame passes the obstacle. The maximum burning velocity is 28 m/s before and 160 m/s after the obstacle. Figure 4.15 shows that the distance between the flame and the lead shock

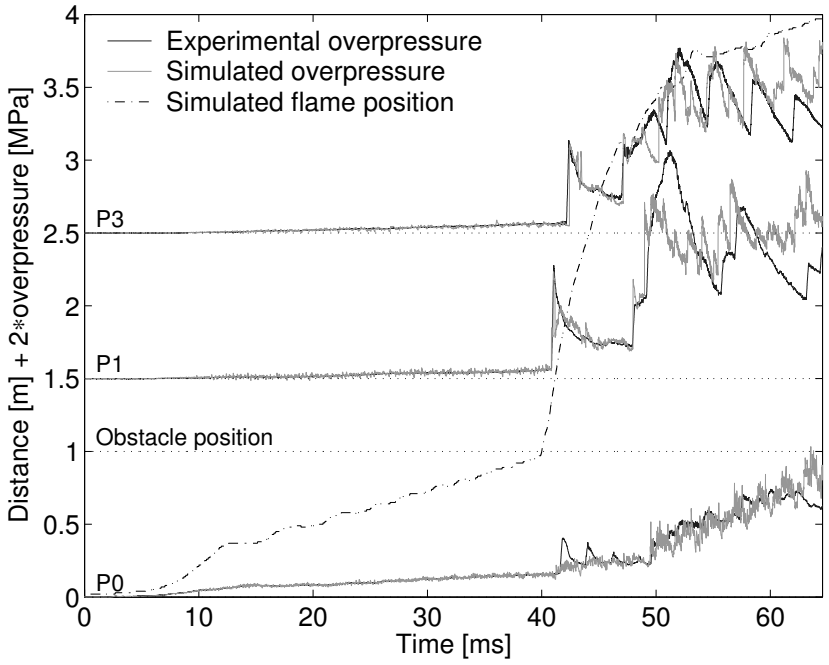

Figure 4.13: Simulated and experimental overpressure at pressure transducer P0, P1 and P3 in the 4.0 m pipe for $D_o = 30$ mm and a hydrogen volume percentage of 20. The overpressures have been multiplied by two and they are shifted along the vertical axis to indicate the pressure transducer position in the pipe. (1.0 m corresponds to 1.0 MPa.)

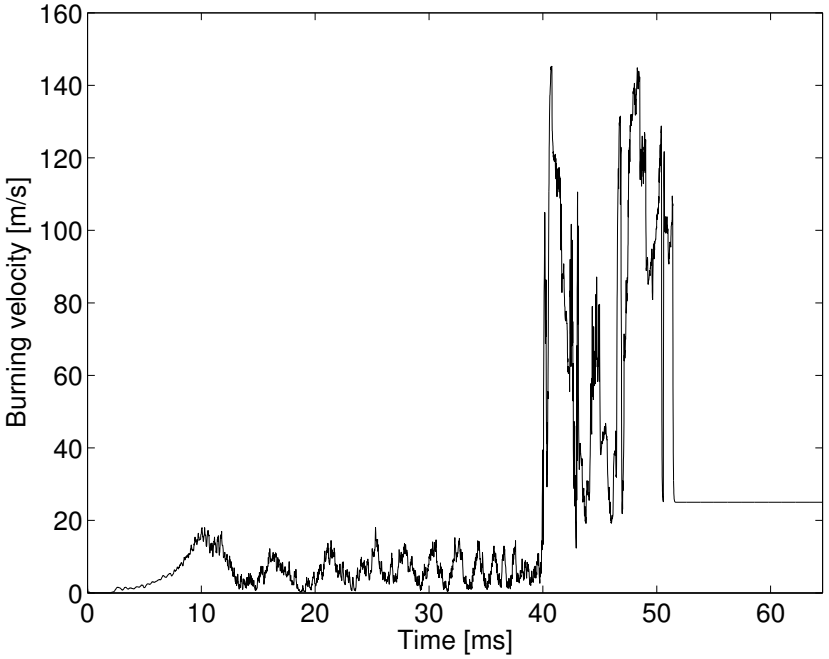

Figure 4.14: Simulated burning velocity for a hydrogen volume percentage of 20 in the 4.0 m pipe. The obstacle opening diameter was 30 mm.

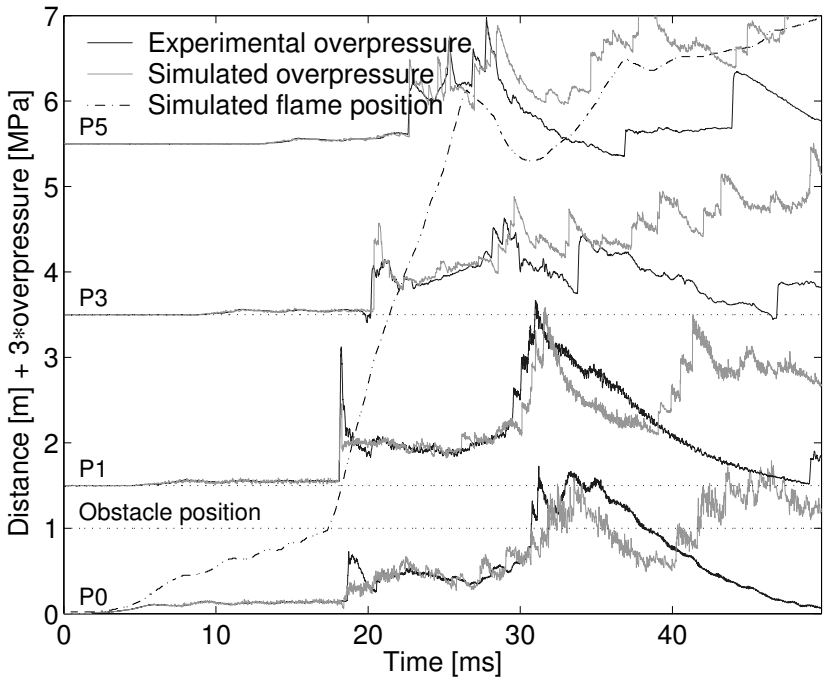

Figure 4.15: Simulated and experimental overpressure at pressure transducer P0, P1, P3 and P5 in the 7.0 m pipe for $D_0 = 50$ mm and hydrogen volume percentage of 50. The overpressures have been multiplied by three and they are shifted along the vertical axis to indicate the pressure transducer position in the pipe. (1.0 m corresponds to 1.0 MPa.)

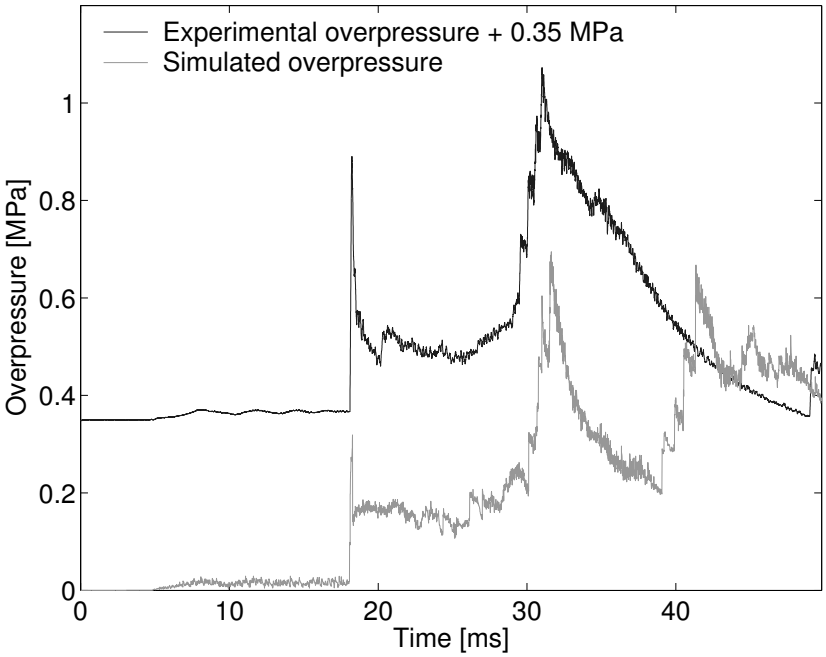

Figure 4.16: Simulated and experimental overpressure at pressure transducer P1 in the 7.0 m pipe. The hydrogen volume percentage was 50 and the obstacle opening diameter was 50 mm. The experimental overpressure has been shifted with 0.35 MPa.

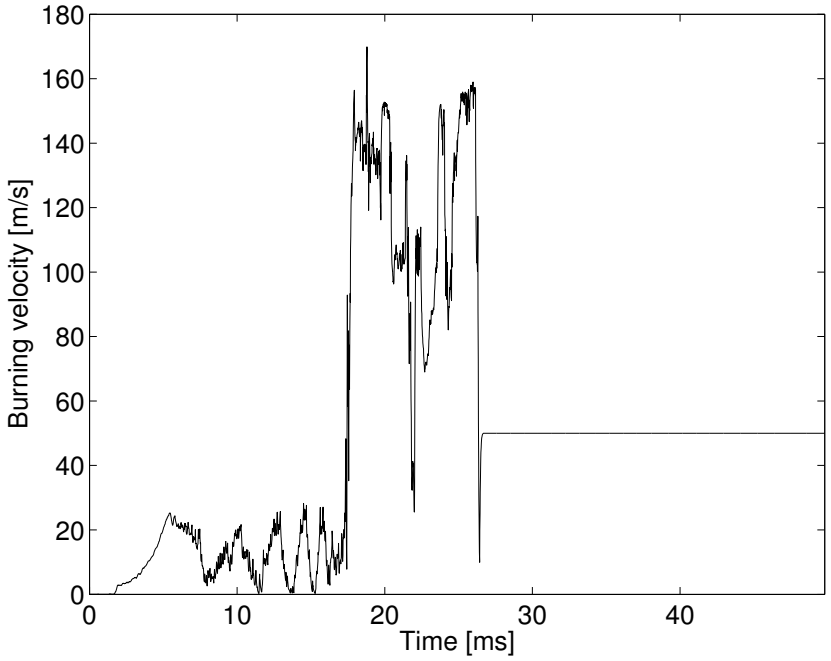

Figure 4.17: Simulated burning velocity for a hydrogen volume percentage of 50 and an obstacle opening diameter of 50 mm in the 7.0 m pipe.

increases as they propagate down the pipe. The maximum distance between the flame and the lead shock is 0.89 m. This maximum distance occurs at approximately 24.6 ms when the shock is reflected off the end wall. The reflected shock then hits the flame from the unburned gas side at approximately at 26.5 ms. The burning velocity was held constant at 50 m/s after this interaction.

Figure 4.16 shows that the obstacle caused shock at pressure transducer P1, is too low in the simulation compared to the one obtained in the experiment. The difference between the two shocks is 0.54 - 0.32 = 0.22 MPa. The experimental shock is created by an increased flame surface area and a turbulent flow field. RCMLAB will have difficulties to mirror this type of flame acceleration in a one dimensional burning velocity, when the flame surface area is large and the turbulence is high. But the differences between the simulated and experimental overpressures decrease as the lead shock propagates down the pipe. It can therfore be stated that generally there is a good agreement between the experimental and the simulated overpressure.

4.0 m pipe with propane and air

Figure 4.18 shows the experimental and simulated overpressure at pressure transducer P0, P1 and P3 for a gas explosion with propane and air in the 4.0 m pipe. The obstacle opening diameter was 50 mm and the propane volume percentage was 4.0. The overpressures have been multiplied by two and they are plotted as a function of both time and the pressure transducer position in the pipe. The corresponding simulated burning velocity is plotted in Figure 4.19. Because of the long simulation time required for propane and the level of noise generated by the obstacle model, the primitive variables $\mathrm{W} = [\rho, u, p]^T$ were filtered

between each time step. This was not done for any of the simulations involving hydrogen. The simulated flame position is also plotted in Figure 4.18.

As for the various simulations with hydrogen, there is an exponential growth in the burning velocity after the ignition. (See Figure 4.19.) But the exponential growth is much slower compared to the presented simulations with hydrogen. The simulated burning velocity has a local maximum of 5.6 m/s after approximately 28 ms. It is assumed that this first maximum is related to the quenching of the flame at the contact surfaces when it reaches the pipe wall in the radial direction. The further evolvement of the burning velocity shows that it becomes zero in the time interval ranging from 47 to 63 ms. This equals to the time period in which the flame propagation is negative for the first time in Figure 4.18. The negative flame speed is most likely caused by a pressure wave that propagates towards the ignition wall after it has been reflected off the opposite end wall. The flame speed then becomes positive again when this pressure wave has been reflected off the ignition wall and interacts with the flame from the burned gas side. A similar burning velocity evolvement was also observed for a blockage ratio of 0.572, but not for blockage ratios of 0.921, 0.965 and 0.991. Kristoffersen [24] has reported a similar evolvement of the burning velocity for RCMLAB simulations of propane and air gas explosions in a partly closed pipe with a length of 1.0 m. The oscillations that are superimposed on the burning velocity between 28 and 47 ms in Figure 4.19, have a period of approximately 2.5 ms. These oscillations may be caused by pressure waves that are reflected between the ignition wall and the obstacle.

The simulated flame position in Figure 4.18 shows that the flame passes the obstacle at approximately 72.6 ms. There is also a large increase in the burning velocity in Figure 4.19 at this time. The burning velocity is then stabilized at approximately 55 m/s until the experimental pressure from pressure transducer P2 is used as input by BVM1. The experimental pressure from pressure transducer P2 is used by BVM1 in the time range from approximately 75.0 to about 76.4 ms. The maximum burning velocity is higher than 90 m/s and the mean axial flame speed is 0.5 m/1.4 ms = 357 m/s during this time period. Figure 4.18 shows that the simulated shock in front of the flame is too high at pressure transducer P3 compared to the experimental pressure. This indicates that a burning velocity of 90 m/s is too high. The leading shock is reflected off the opposite end wall at approximately 79 ms and it interacts with the flame from the unburned gas side at approximately 82 ms. But the burning velocity has dropped to zero already at approximately 78 ms. This means that there is a 4 ms time difference between the time when the flame interacts with the reflected shock and the time when the burning velocity becomes zero. Figure 4.18 also shows that the sudden drop in the burning velocity at about 78 ms changes the flame speed. For the rest of the simulation the burning velocity changes too rapidly to relate it to any changes in the flame propagation. The burning velocity was held at 10 m/s when the flame had passed pressure transducer P5.

The pressure difference between the experimental and simulated overpressure at the end of the simulation in Figure 4.18, is relatively large and approximately equal to 0.15 MPa at the different pressure transducers. Some attempts were made to adjust the wall specific factor α in the heat transfer model (see Equation (4.35)), but an increased α also affected the periods of the propagating waves. The pressure difference may therefore mainly be related to the nature of the pressure transducers. The pressure transducers can

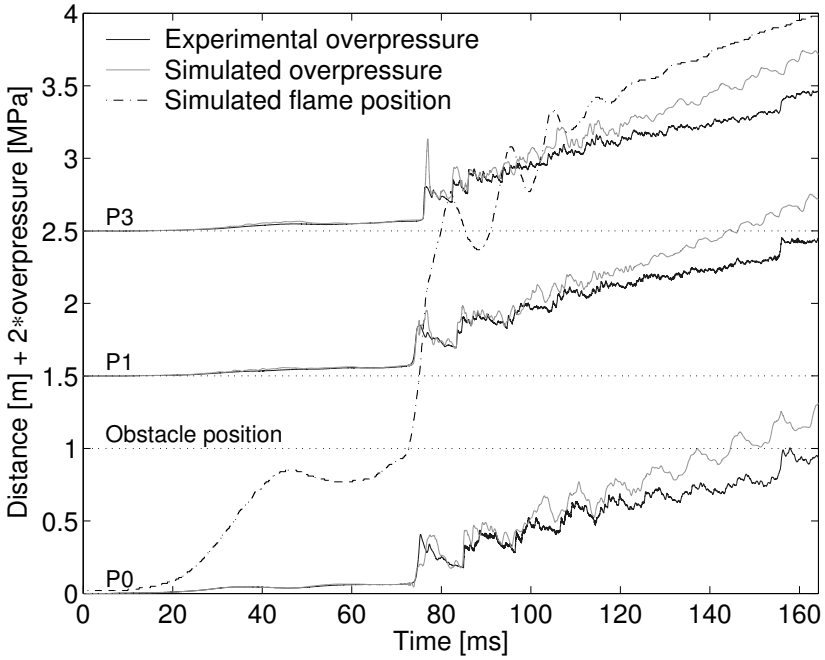

Figure 4.18: Simulated and experimental overpressure at pressure transducer P0, P1 and P3 in the 4.0 m pipe, for $D_0 = 50$ mm and a propane volume percentage of 4.0. The overpressures have been multiplied by two and they are shifted along the vertical axis to indicate the pressure transducer position in the pipe. (1.0 m corresponds to 1.0 MPa.)

not keep their voltage charge for a long time. The experimentally recorded overpressures will therefore become lower as the pressure transducers are loosing charge.

Even though there are some uncertainties related to the simulated burning velocity, there is still good agreement between the simulated and experimental overpressure. There is especially a high level of similarity at pressure transducer P5. A plot of the experimental and simulated overpressure at pressure transducer P5 is shown in Figure 4.20.

4.0 m pipe with methane and air

The experimental and simulated overpressure at pressure transducer P0, P1 and P3 for a gas explosion with premixed methane and air in the 4.0 m pipe, are shown in Figure 4.21. The equivalence ratio was equal to 1.0 and the obstacle opening diameter was 50 mm. Both the experimental and simulated overpressures have been multiplied by two and they are plotted as a function of time and the pressure transducer location in the pipe. The simulated flame position is also plotted in Figure 4.21 and Figure 4.22 shows the corresponding simulated burning velocity. As for the simulations with propane in the previous sub subsection, the primitive variables W$= [\rho, u, p]^T$ have been filtered between each time step.

The first 95 ms of the simulated burning velocity is relatively similar to the first 75 ms of the simulated burning velocity with propane in Figure 4.19. Both simulations have an obstacle opening diameter of 50 mm and a stoichiometric mixture of fuel and air. The local maximum of 4.4 m/s in the burning velocity for methane occurs after 28.5 ms.

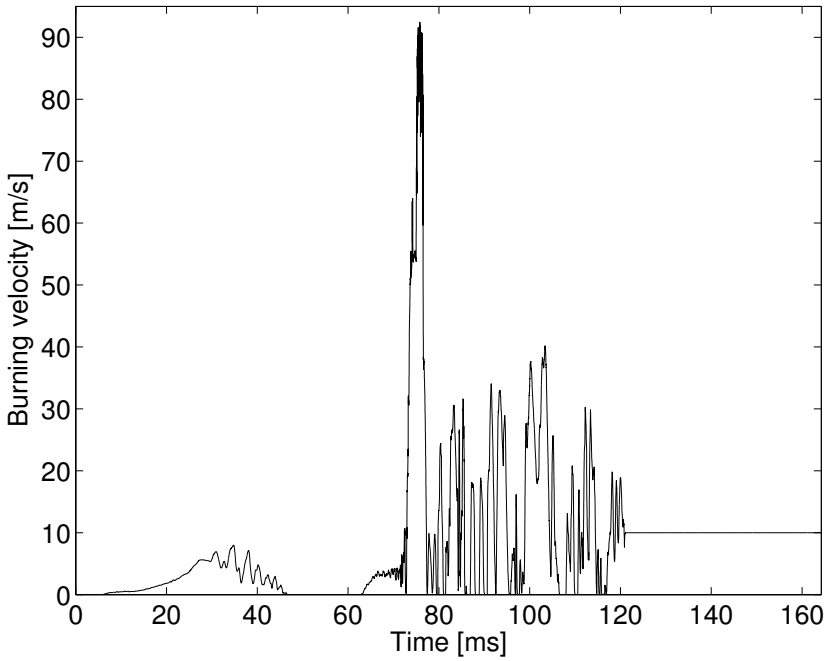

Figure 4.19: Simulated burning velocity for a propane volume percentage of 4.0 and an obstacle opening diameter of 50 mm in the 4.0 m pipe.

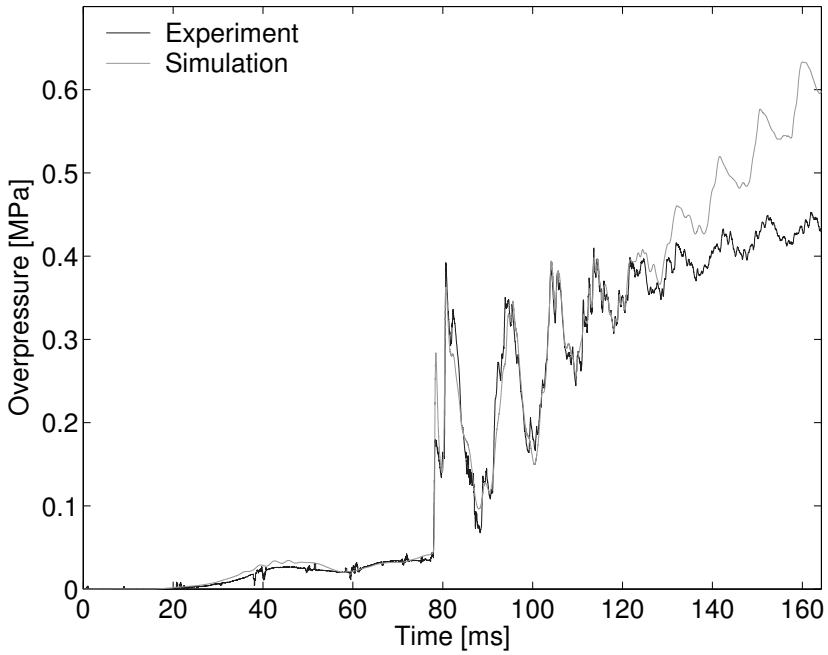

Figure 4.20: Simulated and experimental overpressure at pressure transducer P5 in the 4.0 m pipe. The propane volume percentage was 4.0 and the obstacle opening diameter was 50 mm.

This is a slightly lower burning velocity than the one that was obtained in the simulation with propane. A further discussion of this first stage of the flame propagation is given in Subsection 4.3.2. After the local maximum, the burning velocity stays close to 2.5 m/s before it becomes zero at 72 ms. The burning velocity becomes zero at the same time as the flame speed becomes negative for the first time. (See Figure 4.21.) The negative flame speed can, as for the simulations with propane, be related to the interaction between the flame and a pressure wave that has been reflected off the opposite end wall. The burning velocity remains zero until 90.3 ms. This is also the time at which the flame speed becomes positive again in Figure 4.21. It is further interesting to see that the flame almost managed to pass the obstacle before it interacted with the reflected pressure wave.

The flame passes the obstacle at approximately 95.1 ms. The simulated burning velocity then reaches a temporary peak of 41.8 m/s, before it decreases and reaches zero at 109.3 ms. Unlike in the simulation with propane there is no shock formation behind the obstacle. The obstacle caused pressure wave propagates down the pipe and it is reflected off the end wall at approximately 103.5 ms before it interacts with the flame from the unburned gas side at about 108.3 ms. This interaction occurs just before the flame speed becomes negative for the second time in Figure 4.21. Figure 4.23 shows the simulated flame speed divided by five together with the simulated burning velocity. The time period in the figure reaches from 100 to 138 ms after the ignition. This time period corresponds to the flame propagating from 1.0 to 3.3 m in the pipe, i.e. from the obstacle to 0.7 m away from the end wall. Figure 4.23 shows that there is some consistency between the flame speed and burning velocity. The burning velocity becomes zero just before or approximately at the time when the flame speed decreases and becomes negative. The burning velocity also becomes larger than zero approximately at the same time as the flame speed is fastest towards the ignition wall. Figure 4.23 shows that the simulated flame speed is between -110 and 190 m/s. It is interesting to see that both the maximum and minimum flame speed are relatively equal between each oscillation. Like in the simulations with propane, there is a difference between the simulated and experimental overpressure at the end of the simulation. This difference is approximately 0.2 MPa at the various pressure transducers. The burning velocity was kept at 8.0 m/s after the flame had passed pressure sensor P5.

It can be stated that there is good agreement between the experimental and simulated overpressure. As for the simulation with propane, the similarity was highest at pressure transducer P5. The simulated and experimental overpressure at pressure transducer P5 are shown in Figure 4.24.

4.3.2 Initial flame propagation

Experimental pressure records from pressure transducer P0 have been used together with a model based burning velocity estimator (i.e. BVM1) to simulate the initial flame propagation of gas explosions in a closed pipe with a single obstacle. The main purpose of performing these simulations, was to see how the blockage ratio of the obstacle affected the flame propagation between the ignition wall and the obstacle. The presented results are mainly from gas explosion simulations in the 4.0 m pipe. Obstacle opening diameters ranging from 10 to 70 mm and three different fuels premixed with air, have been used

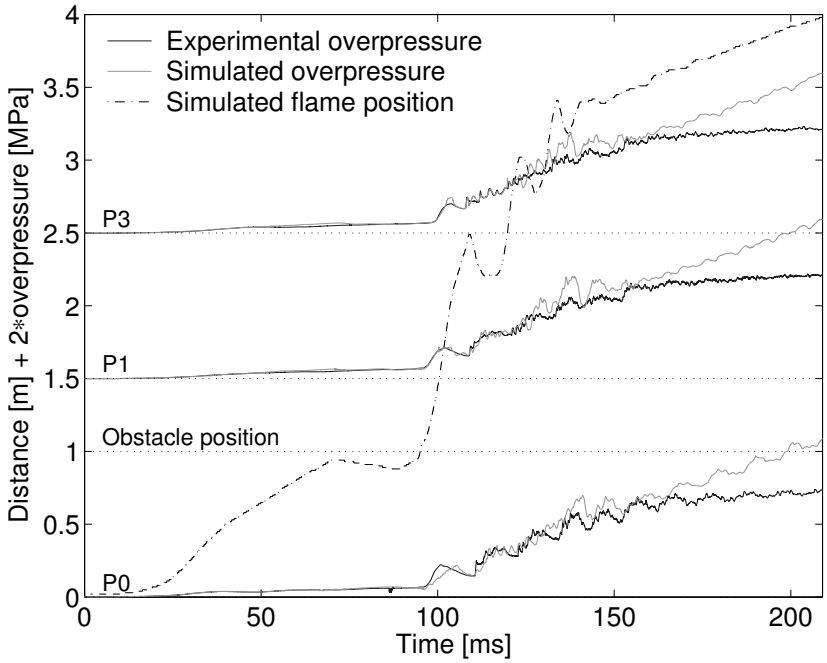

Figure 4.21: Simulated and experimental overpressure at pressure transducer P0, P1 and P3 in the 4.0 m pipe, for $D_0 = 50$ mm and a methane volume percentage of 9.5. The overpressures have been multiplied by two and they are shifted along the vertical axis to indicate the pressure transducer position in the pipe. (1.0 m corresponds to 1.0 MPa.)

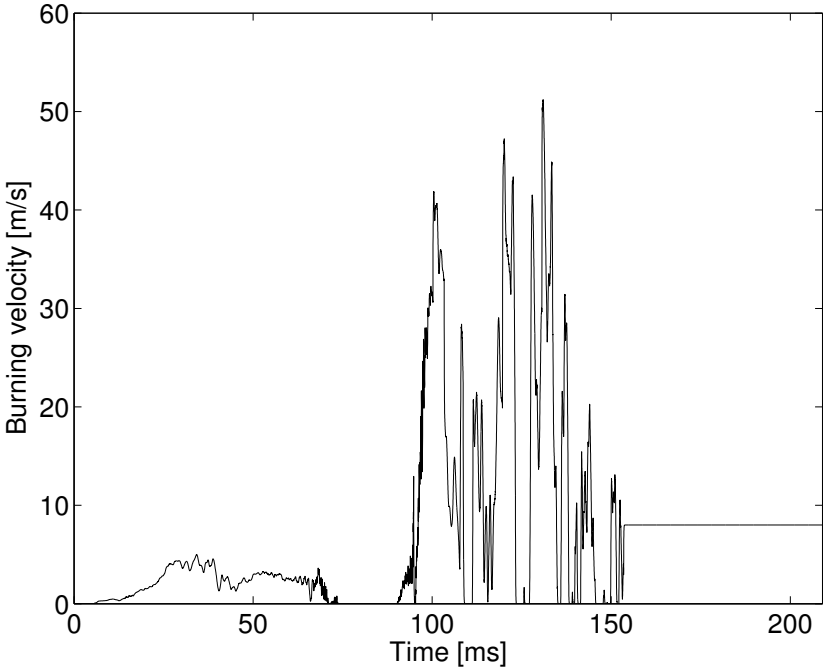

Figure 4.22: Simulated burning velocity in the 4.0 m pipe. The methane volume percentage was 9.5 and the obstacle opening diameter was 50 mm.

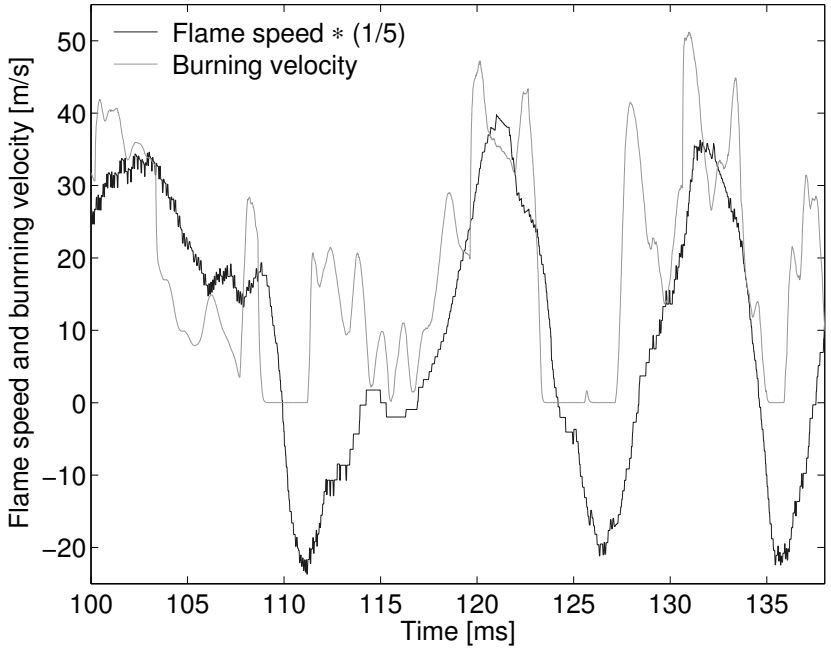

Figure 4.23: Simulated burning velocity and flame speed in the 4.0 m pipe, for a methane volume percentage of 9.5 and an obstacle opening diameter of 50 mm. The simulated flame speed has been divided by five.

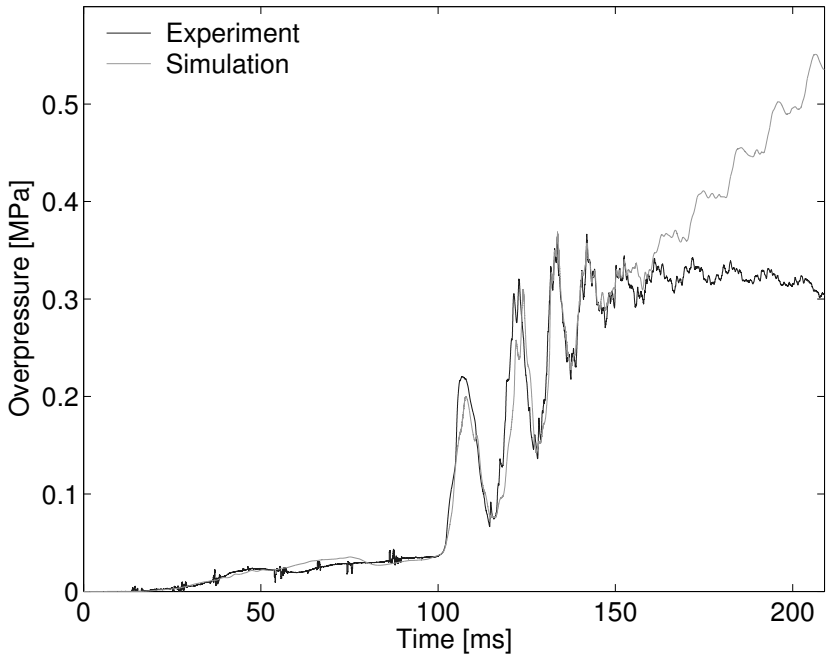

Figure 4.24: Simulated and experimental overpressure at pressure transducer P5 in the 4.0 m pipe. The methane volume percentage was 9.5 and the obstacle opening diameter was 50 mm.

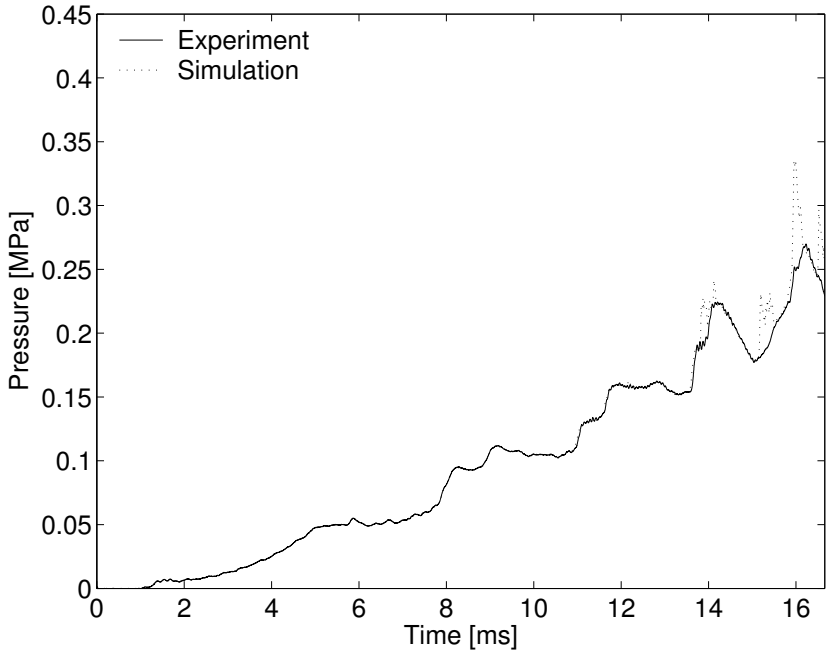

Figure 4.25: Simulated and experimental overpressure at pressure transducer P0 for a hydrogen volume percentage of 30 in the 4.0 m pipe. The obstacle opening diameter was 30 mm.

in the simulations. The fuels were hydrogen, propane and methane. Each fuel is presented separately. The results from the simulations with propane and methane, are only discussed from the time of ignition to the time when the flame is assumed to have reached the pipe wall in the radial direction.

Hydrogen and air

The numerical simulations manage to reproduce the experimental pressures to a large extent. An example of this is shown in Figure 4.25. This figure shows the first 16.7 ms of the simulated and experimental overpressure at pressure transducer P0 in the 4.0 m pipe. The obstacle opening diameter was 30 mm and the hydrogen volume percentage was 30. The model for the area change at the obstacle is the main source of numerical noise in this phase of the simulation. The generated noise is amplified with time and it appears as sharp pressure peaks in the simulated pressure as the flame gets closer to the obstacle.

Figure 4.26 shows the simulated burning velocities in the 4.0 m pipe for obstacle opening diameters of 30, 50 and 70 mm. The hydrogen volume percentage was 30. As for the experimental overpressure in Figure 3.11, there is a first phase that is unaffected by the blockage ratio of the obstacle. But after approximately 5.5 ms the burning velocities become dependent on the obstacle opening diameter. These differences are initiated by the interaction between the flame and the first pressure wave that is reflected off the obstacle. Figure 3.11 shows these interactions as small pressure peaks at approximately 5.7 ms. This means that the burning velocity only depends on the pipe diameter and the equivalence ratio of the gas mixture, until the flame interacts with the first reflected pres-

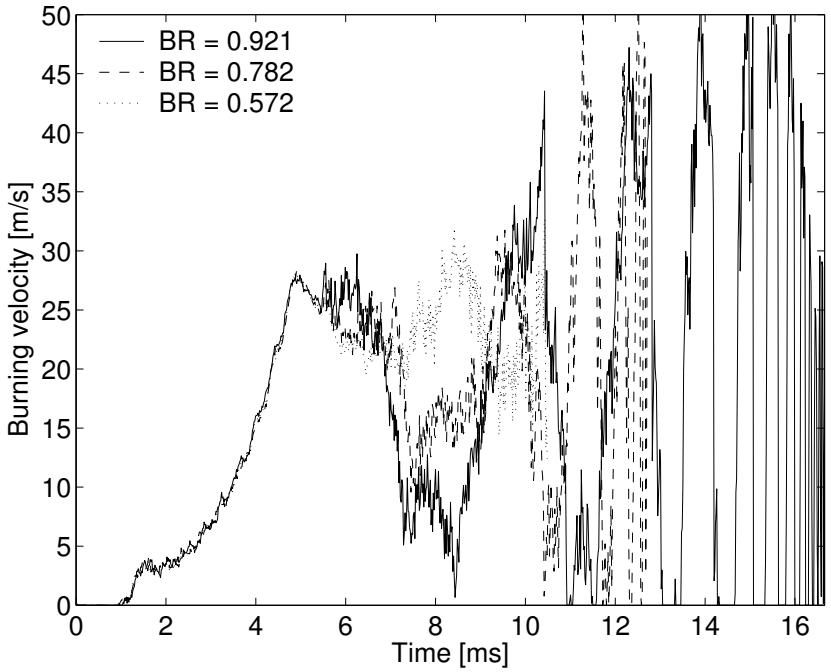

Figure 4.26: Simulated burning velocities for a hydrogen volume percentage of 30 in the 4.0 m pipe. The obstacle opening diameters were 30, 50 and 70 mm.

sure wave. The rest of the simulated burning velocity is highly dependent on the blockage ratio. The oscillating behavior of the simulated burning velocities, may be related to interactions between the flame and the propagating pressure waves. If the flow field created by these pressure waves is strong enough, then the flame may go through an inversion process.

Figure 4.27 and Figure 4.28 show the simulated flame positions and the simulated flame speeds (i.e. with respect to the pipe) for the three different blockage ratios in the previous paragraph. The flame has both an increased oscillating behavior and a reduced mean axial velocity for the higher blockage ratios. This type of behavior is most likely caused by hydrodynamic effects. It is interesting to observe that for obstacle opening diameters of 30 mm and 50 mm, the flame speeds after the first possible inversion in Figure 4.28, are approximately the same value of 150 m/s as they were before. This result can also be seen as almost parallel regions of the flame propagation in Figure 4.27. A corresponding simulation for the 3.0 m pipe (i.e. zero blockage ratio) gave a lower mean axial flame speed for the initial flame propagation, than the one that was obtained for an obstacle opening diameter of 70 mm in the 4.0 m pipe. This result indicates that a blockage ratio of 0.572 is close to some optimum blockage ratio configuration for the highest mean axial flame speed for the first 1.0 m of the flame propagation. The first 1.0 m of the flame propagation in the 3.0 m pipe was without any pressure wave interactions.

Simulations with a hydrogen volume percentage of 20 in the 4.0 m pipe, showed interactions between the flame and the first reflected pressure wave, already before the flame had reached the pipe wall in the radial direction. These interactions indicate that the burning velocity is dependent on the blockage ratio of the obstacle even before the flame has

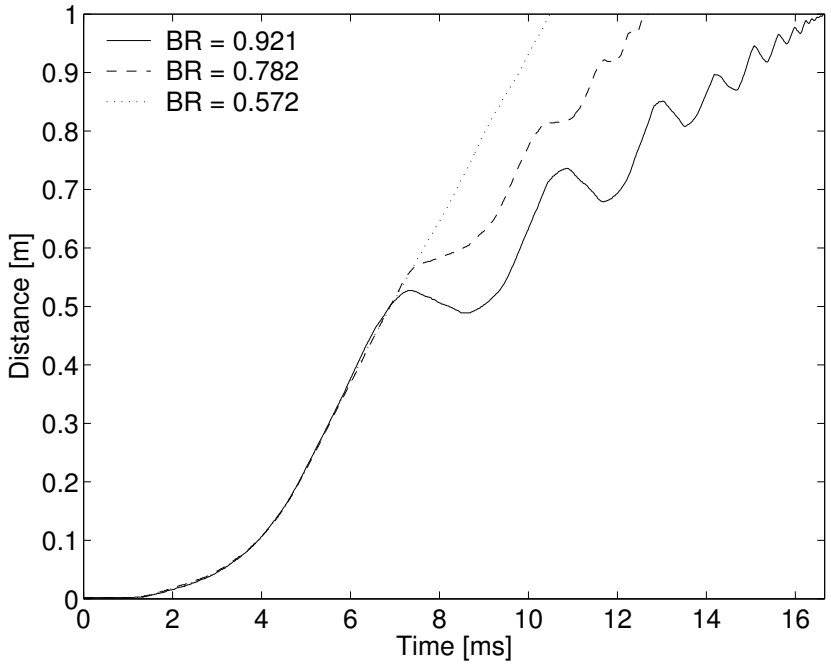

Figure 4.27: Simulated flame positions for a hydrogen volume percentage of 30 in the 4.0 m pipe. The obstacle opening diameters were 30, 50 and 70 mm.

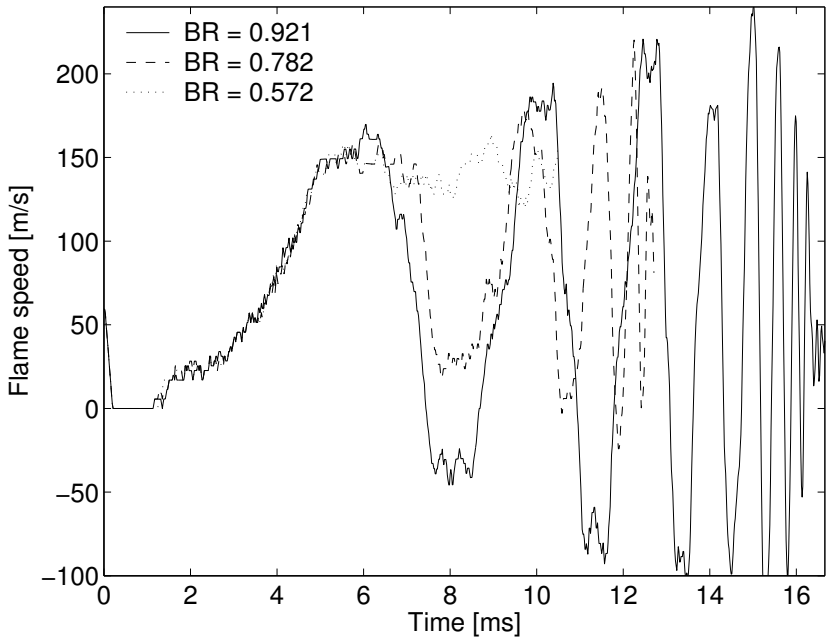

Figure 4.28: Simulated flame speeds for a hydrogen volume percentage of 30 in the 4.0 m pipe. The obstacle opening diameters were 30, 50 and 70 mm.

Table 4.3: Asymptotic burning velocities from simulations in a transmissive end version of the 3.0 m pipe. k_4 is given in Equation (4.28).

H_2 (% volume)	S_a [m/s]	k_4
20	7.9	0.35
30	26.4	0.42
35	31.4	0.40
50	17.7	0.35

Table 4.4: Parameters used in Figure 4.29 to scale the burning velocity and the time. $S_L(\Phi)$ is found from [9].

H_2 (% volume)	t_w [ms]	S_L [m/s]
20	13.3	1.3
30	4.9	2.5
35	4.3	2.9
50	5.5	2.8

reached the pipe side wall in the radial direction. Figure 4.14 shows the simulated burning velocity for an obstacle opening diameter of 30 mm and a hydrogen volume percentage of 20 in the 4.0 m pipe. The first local maximum of 18.0 m/s occurs approximately 10 ms after the ignition. A corresponding simulation in the 3.0 m pipe, showed that the flame reached the pipe wall in the radial direction before it interacted with the pressure wave that had been reflected off the end wall. The first local maximum of the burning velocity in that simulation, was 8.5 m/s and it occurred after approximately 13.5 ms. These results agree with Guénoche [2], who states that the flame tends to reach the radial pipe wall sooner when a constriction that hinders the longitudinal flow of unburned gas is present. It is also interesting to note that the flame uses 52 ms to propagate the first 1.0 m in the 3.0 m pipe, but only 40 ms in the 4.0 m pipe. This indicates a higher mean axial flame speed with an increasing blockage ratio, which is quite the opposite of what has been observed for the more reactive mixtures. One explanation could be that the mean axial velocity of the flame in the 3.0 m pipe, is reduced due to interactions with pressure waves that are reflected off the end walls. For the more reactive mixtures, the first 1.0 m of the flame propagation in the 3.0 m pipe was without these interactions.

Scaled burning velocities from simulations with hydrogen volume percentages of 20, 30, 35 and 50 are shown in Figure 4.29. The simulations lasts from the time of ignition to the time t_w when the flame reaches the pipe wall in the radial direction. t_w is assumed to be the first local maximum of the burning velocity. The laminar burning velocities $S_L(\Phi)$ were found from Reference [9] for a pressure of 0.1 MPa and a temperature of 300 K. The values of t_w and $S_L(\Phi)$ for the various equivalence ratios, are listed in Table 4.4. The differences in the exponential growth of the scaled burning velocities for the various equivalence ratios, do almost reflect the laminar burning velocities. The largest increase in the scaled burning velocity occurs for hydrogen volume percentages of 30 and 35, whereas the increase for the hydrogen volume percentage of 20 is slightly lower than the increase for the hydrogen volume percentage of 50.

Propane and air

Figure 4.30 shows the simulated burning velocities for stoichiometric mixtures of propane and air in the 4.0 m pipe. The obstacle opening diameters were 10, 20, 30, 50 and 70 mm.

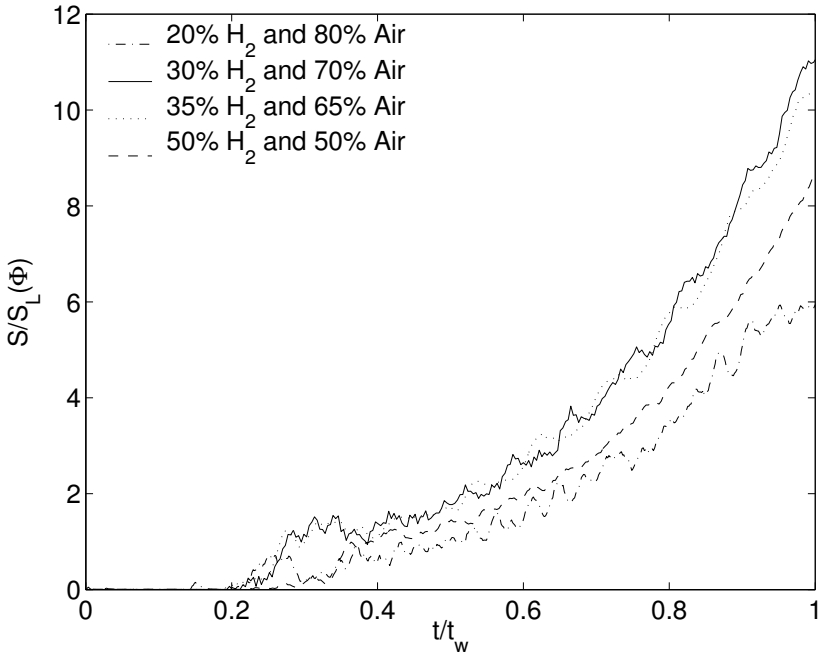

Figure 4.29: Scaled burning velocities for simulations with hydrogen volume percentages of 20, 30, 35 and 50. The simulations last from the time of ignition to the time when the flame reaches the pipe wall in the radial direction.

The simulations last from the time of ignition to the time t_w when the flame reaches the pipe wall in the radial direction. Only experimental pressure records from pressure transducer P0 have been used to estimate the burning velocities. (See Subsection 3.3.3 for a discussion of these experimental pressure records.) As for the simulation with hydrogen, t_w is assumed to be the time when the burning velocity reaches its first maximum. S_w is the magnitude of this first maximum. Table 4.5 lists the values of t_w and S_w for the various blockage ratios. The laminar burning velocity S_L for a stoichiometric mixture of propane and air, is 0.42 m/s [50] at atmospheric conditions. In Figure 4.31 S_L together with t_w have been used to scale the simulated burning velocities obtained for the various blockage ratios.

As for the experimental overpressures in Figure 3.26 and Figure 3.27, the first few milliseconds of the simulated burning velocity are similar for all the blockage ratios. But at approximately 11.0 ms they start to evolve differently. These differences are most likely caused by the interaction between the flame and the first pressure wave reflected off the obstacle. The burning velocities then become higher for the larger blockage ratios. The rest of the evolvement of the simulated burning velocities are relatively unstructured and it is difficult to relate the individual changes and the differences between the various blockage ratios, to specific events. But it is interesting to see that the burning velocity becomes constant or even decreases between 17.0 and 25.0 ms for the blockage ratios of 0.965 and 0.921. Based on the simulation results in Figure 4.30 it is not possible to determine how the blockage ratio of the obstacle affect the time t_w when the flame reaches the pipe wall in the radial direction. The magnitude of S_w is also relatively similar for the various blockage ratios. The only exception is S_w for the blockage ratio of 0.991. Even

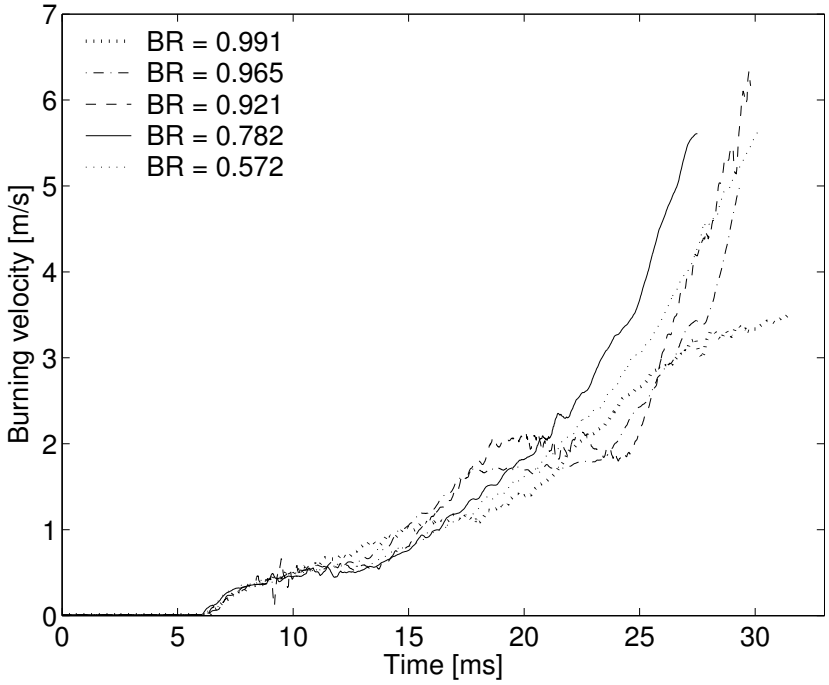

Figure 4.30: Burning velocities for simulations with a propane volume percentage of 4.0 and obstacle opening diameters of 10, 20, 30, 50 and 70 mm.

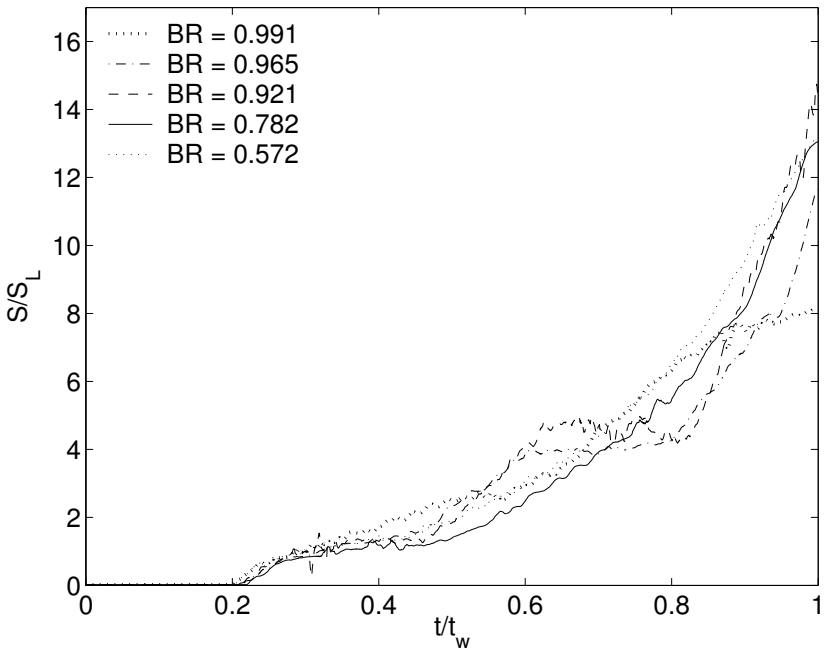

Figure 4.31: Scaled burning velocities for simulations with a propane volume percentage of 4.0 and obstacle opening diameters of 10, 20, 30, 50 and 70 mm.

Table 4.5: The time of appearance t_w and the magnitude S_w of the first local maximum in the simulated burning velocity for stoichiometric mixtures of fuel and air in the 4.0 m pipe. The fuels were propane and methane.

Blockage ratio	Obstacle opening diameter [mm]	C_3H_8		CH_4	
		t_w [ms]	S_w [m/s]	t_w [ms]	S_w[m/s]
0.991	10	31.6	3.50	31.6	3.28
0.965	20	29.4	5.01	–	–
0.921	30	29.8	6.34	35.7	5.84
0.782	50	27.5	5.61	28.5	4.20
0.572	70	30.3	5.67	31.3	4.73

though S_w is considerably lower for the blockage ratio of 0.991, the flame still reaches the pipe wall in the radial direction at approximately the same time as for the other blockage ratios. The theoretical t_w calculated from Equation (2.4) is 33.1 $\pm$ 2.5 ms and slightly larger than the values listed in Table 4.5. This might indicate that the pressure build-up in front of the flame due to the obstacle, makes the flame reach the pipe wall in the radial direction sooner compared to the case without a constriction. This phenomenon has been reported also by Guénoche [2] and the experiments performed by Popov [87] showed that the flame speed in the radial direction right after the ignition, varies as the inverse of the pipe length for short and closed pipes.

The scaled burning velocities in Figure 4.31 show that the maximum burning velocity for an obstacle opening diameter of 30 mm is 15 times the laminar burning velocity. The corresponding value for a stoichiometric mixture of hydrogen and air in Figure 4.29, is 11. But unlike in the simulations with propane (in Figure 4.31), the flame reaches the radial pipe wall without any pressure wave interactions for the simulations with hydrogen (in Figure 4.29).

Methane and air

Experimental pressure records from pressure transducer P0, have been used by RCMLAB to estimate the burning velocity in gas explosions with premixed methane and air in the 4.0 m pipe. The obstacle opening diameters were 10, 30, 50 and 70 mm and the equivalence ratio of the gas mixture was 1.0. The simulated burning velocities for the various blockage ratios are shown in Figure 4.32. These simulations last from the time of ignition to the time t_w when the flame reaches the pipe wall in the radial direction. As for the simulations with propane in the previous sub subsection, t_w is assumed to be the time when the burning velocity reaches its first maximum and S_w is the magnitude of this first maximum. The different values of t_w and S_w obtained for the various blockage ratios, are listed in Table 4.5. t_w together with the laminar burning velocity S_L, have been used to scale the various burning velocities in Figure 4.33. The laminar burning velocity of a stoichiometric mixture of methane and air, is 0.38 m/s at atmospheric conditions [50]. A discussion of the experimental pressure records that were used as input in the simulations,

is given in Subsection 3.3.4.

There are many similarities between the estimated burning velocities for methane (Figure 4.32 and Figure 4.33) and the estimated burning velocities for propane (Figure 4.30 and Figure 4.31). Table 4.5 shows that the times t_w are slightly larger and that the velocity S_w is as much as 1.4 m/s lower, for the simulations with methane compared to the simulations with propane. The largest difference between the two gas mixtures occurs for the blockage ratio of 0.921. For this blockage ratio the difference in t_w is approximately 5.9 ms. There is also an interesting decrease in the scaled burning velocity between 19.0 and 22.5 ms in Figure 4.33 for this blockage ratio. A similar evolvement can also be observed in the simulations with propane for this blockage ratio. (See Figure 4.31.)

As for the simulations with propane, it is not possible to determine how the blockage ratio of the obstacle affects t_w and S_w in a general way. But both the propane and the methane simulations have a S_w that is considerably lower for the blockage ratio of 0.991 than for the other blockage ratios. Since the time t_w is relatively similar for the various blockage ratios, this reduced burning velocity is most likely caused by a reduced flame surface area. The pressure build up in front of the flame due to the hindering of the flow of unburned gas through the obstacle, is known to flatten the flame [2]. Figure 3.27 and Figure 3.30 show that the pressure build up at pressure transducer P0 is strongest for the blockage ratio of 0.991. It is therefore likely that the flame in these pipe configurations has the smallest flame surface area at the time t_w. The simulations did also show that the burning rate of the flame [kg/(s·m^2)], had a similar evolvement as the burning velocity. This means that also the burning rate for the blockage ratio of 0.991 was considerable lower for both the propane and methane simulations.

If Equation (2.4) is used for the methane mixture to predict the time when the flame reaches the pipe wall in the radial direction, then t_w becomes 36.6 $\pm$ 2.8 m/s. This value is larger than the simulated values of t_w listed in Table 4.5. The stoichiometric methane and air flame is therefore, as for the simulations with propane, assumed to reach the radial pipe wall sooner than it would have done without a constriction.

The maximum burning velocity in Figure 4.33, is 15 times the laminar burning velocity and it occurs for an obstacle opening diameter of 30 mm. The corresponding value for propane in Figure 4.29 is also 15.

4.3.3 Alternative burning velocity model

Numerical simulations of gas explosions in pipes with premixed hydrogen and air have been performed with RCMLAB and an alternative burning velocity model (BVM2). A description of the model is given in Subsection 4.2.3. The main objective of performing the simulations was to see how well the model managed to reproduce the experimental data. Simulation results from both obstructed and unobstructed pipes are presented in this subsection.

The first phase of the simulations were performed with a constrained burning velocity in order to reproduce the first pressure structure from the experiments. A simplified version of the theory of Clanet and Searby [1] was used in this constrained phase to estimate the flame surface area at each time step. The flame surface area was then used together with the laminar burning velocity and the pipe cross section area, to calculate

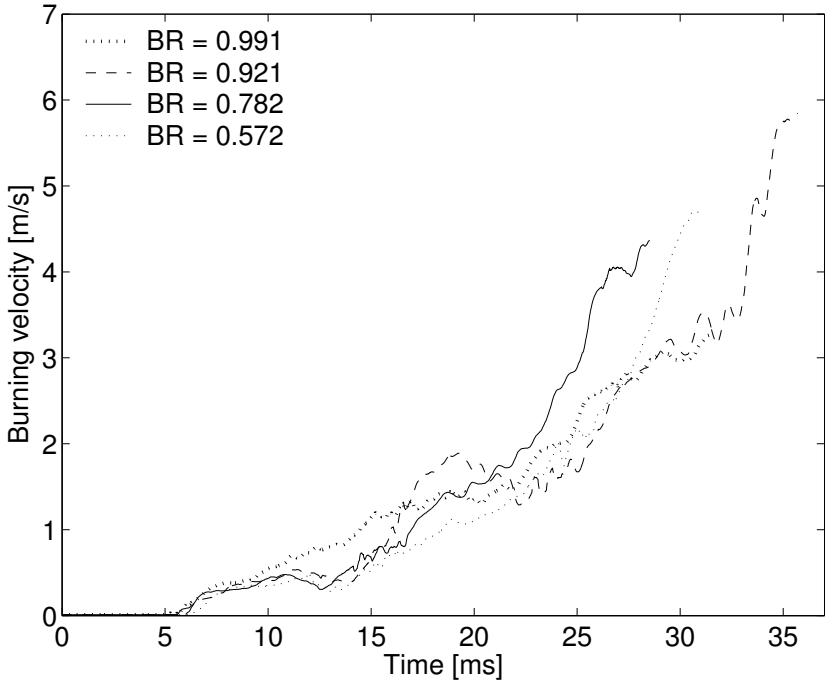

Figure 4.32: Burning velocities for simulations with a methane volume percentage of 9.5 and obstacle opening diameters of 10, 30, 50 and 70 mm.

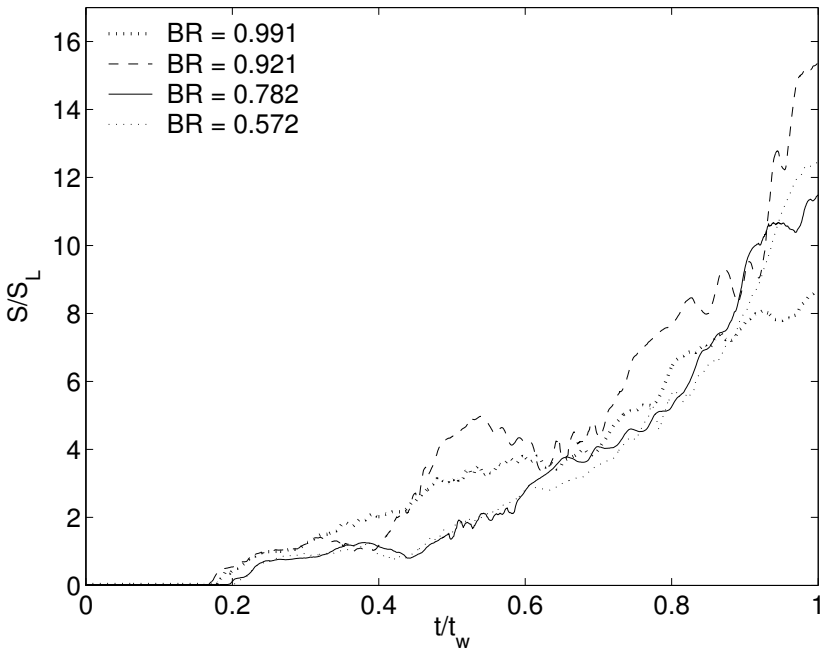

Figure 4.33: Scaled burning velocities for simulations with a methane volume percentage of 9.5 and obstacle opening diameters of 10, 30, 50 and 70 mm.

the burning velocity. When the constrained flame had reached the side wall in the radial direction, Equation (4.28) was used together with the flow field right in front of the flame, to calculate burning velocity for the rest of the simulation.

The constrained phase of the simulations assumed that the flame surface area was equal to the surface area of a cylinder and a hemisphere added together. The surface of the cylinder that faced towards the ignition wall, was not included because of the quenching of the flame at the contact surfaces. The burning velocity in the radial direction was considered as constant and the flame reached the pipe wall at

$$t_w = C_\Phi \cdot \frac{D_p}{2S_\Phi} \quad , \tag{4.49}$$

where C_Φ is a constant, D_p is the pipe diameter and S_Φ is a constant burning velocity. The location of the flame tip in the axial direction x_f, was assumed to follow

$$x_f = \frac{D_p}{2} \cdot e^{\frac{t-t_{sp}}{\tau}} \quad , \tag{4.50}$$

where $t_{sp} = 0.10 \cdot (D_p/2S_\Phi)$, $\tau = D_p/(4\sigma S_\Phi)$ and $\sigma = \rho_u/\rho_b$ is the expansion ratio. The subscript 'sp' refers to the word spherical. If A_{cyl} is the surface area of the cylinder and A_{hsp} is the surface area of the hemisphere, then the total flame surface area can be written as

$$\begin{aligned} A_f &= A_{cyl} + A_{hsp} \\ &= 2\pi(y_f \cdot x_f - (y_f)^2) + 2\pi(y_f)^2 \\ &= 2\pi(y_f \cdot x_f) \end{aligned} \quad , \tag{4.51}$$

where $y_f = D_p \cdot (t/t_w)$ is the radius of the cylinder and the hemisphere. If $A_p = \pi(D_p/2)^2$ is the pipe cross section area, which would be the flame surface area of a plane laminar flame, then the constrained burning velocity can be written as

$$S_f = S_\Phi \cdot \frac{A_f}{A_p}, \quad t \in < 0, t_w > . \tag{4.52}$$

The two quantities C_Φ and S_Φ had to be tuned manually for each simulation to make the simulated overpressures fit the experimental overpressures for this first phase of the simulations. Both the determination of the ignition time and the actual equivalence ratio of the gas mixture in the experiments affect the value of the two parameters. Table 4.6 lists the various values of C_Φ and S_Φ that were used with the different gas mixtures. The corresponding laminar burning velocities at atmospheric conditions obtained from Reference [9] are also listed in Table 4.6. The largest difference between S_Φ and S_L occurs for a hydrogen volume percentage of 35. Clanet and Searby [1] reported that $C_\Phi = 0.26 \pm 0.02$ for propane and air mixtures and that $C_\Phi = 0.22$ for the acetylene and air experiments of Starke and Roth [61]. The value of C_Φ in Table 4.6 for a hydrogen volume percentage of 20, is as low as 0.16. In the experiments of Clanet and Searby [1] the equivalence ratios were in the range from 0.6 to 1.3, whereas the equivalence ratios were in the range from 0.5 to 1.0 in the experiments of Starke and Roth [61]. Clanet and Searby [1] also included an uncertainty in the equation for the time t_{sp}, but this quantity

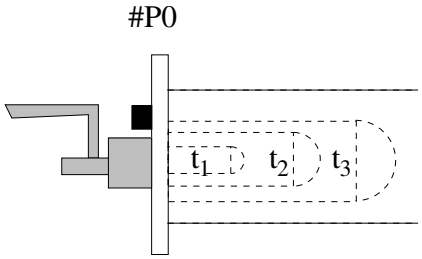

Figure 4.34: A sketch of the flame structure at three different simulation times for the constrained phase of the flame propagation. The flame surface is build up by a cylinder and a hemisphere [1].

Table 4.6: The two constants C_Φ and S_Φ used in the constrained phase of the flame propagation. S_L is the corresponding laminar burning velocity at atmospheric conditions [9].

H_2 (% volume)	C_Φ	S_Φ [m/s]	S_L [m/s]
20	0.160	0.70	1.30
30	0.260	2.80	2.50
35	0.295	3.70	2.90
50	0.270	2.65	2.80

has not been tuned directly for these simulations. Figure 4.34 shows a sketch of the constrained flame structure at three different simulation times.

Unobstructed pipes

Numerical simulations of gas explosions in unobstructed pipes with premixed hydrogen and air have been performed. The presented simulation results are mainly from simulations in the 3.0 m pipe, but simulation results from pipes with one non-reflecting end are also presented.

Figure 4.35 shows the simulated and experimental overpressure at pressure transducer P0, P2 and P4 in the 3.0 m pipe. The hydrogen volume percentage was 35 and Equation (4.52) was used to calculate the burning velocity for the first 4.1 ms of the simulation. The overpressures have been multiplied with two and they are plotted as a function of both the pressure transducer location in the pipe and time. Figure 4.35 shows that the simulated overpressure becomes too high after 4.1 ms, i.e. when the burning velocity is calculated by Equation (4.28). But the evolvement of the simulated pressure at the pressure trancduser positions is still relatively similar to the evolvement of the experimental pressure. The first pressure wave is reflected off the end wall at approximately 9.0 ms and it hits the flame from the unburned gas side at approximately 12.3 ms. It is then reflected off the ignition wall at approximately 13.8 ms and it hits the flame from the burned gas side at approximately 15.3 ms. Figure 4.36 shows the first 25 ms of the simulated burning velocity. The corresponding simulated burning velocity from the 3.0 m pipe presented in Subsection 4.3.1 is also plotted in Figure 4.36. The two burning velocities start to differ after approximately 4.5 ms. For BVM1 the burning velocity starts to decrease at 4.5 ms but for BVM2 it remains high. This is because BVM2 only takes into account the velocity field in the axial direction right in front of the flame. It will therefore stay high until the flame interacts with the first pressure wave reflected off the end wall. This un-reduced burning velocity is causing the high overpressure seen in Figure 4.35.

Figure 4.37 shows the simulated and experimental overpressure at pressure transducer P0 in the 3.0 m pipe. The hydrogen volume percentage was 35. Three different constraints have been used on the burning velocity. The first constrain reproduces the experimental overpressure to a high extent. The two other constrains used $0.5 \cdot S_\Phi$ and $2 \cdot S_\Phi$ in Equation

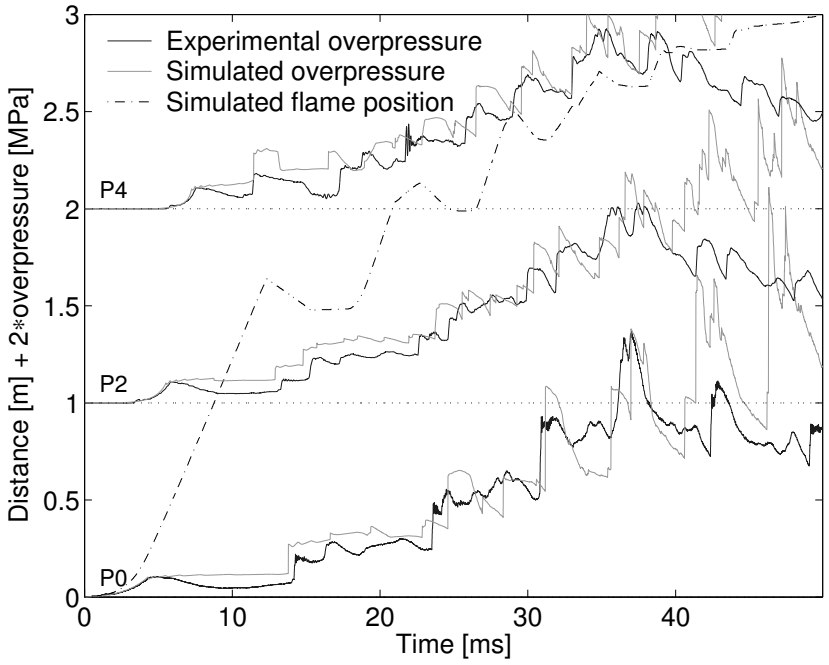

Figure 4.35: Simulated and experimental overpressure at pressure transducer P0, P2 and P4 in the 3.0 m pipe for a hydrogen volume percentage of 35. The overpressures have been multiplied by two and they are shifted along the vertical axis to indicate the pressure transducer position in the pipe. (1.0 m corresponds to 1.0 MPa.)

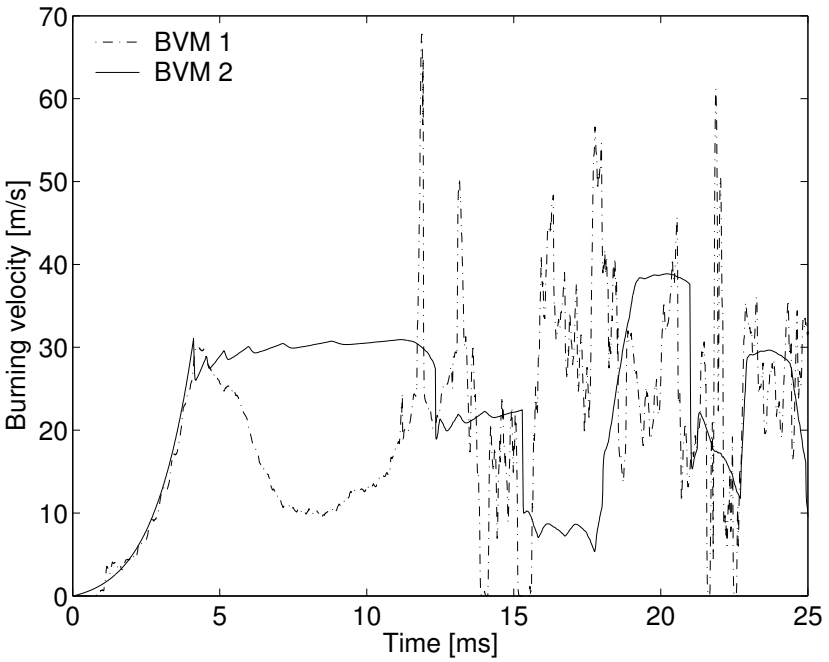

Figure 4.36: The first 25 ms of the simulated burning velocity in the 3.0 m pipe for two different burning velocity estimator models. The hydrogen volume percentage was 35.

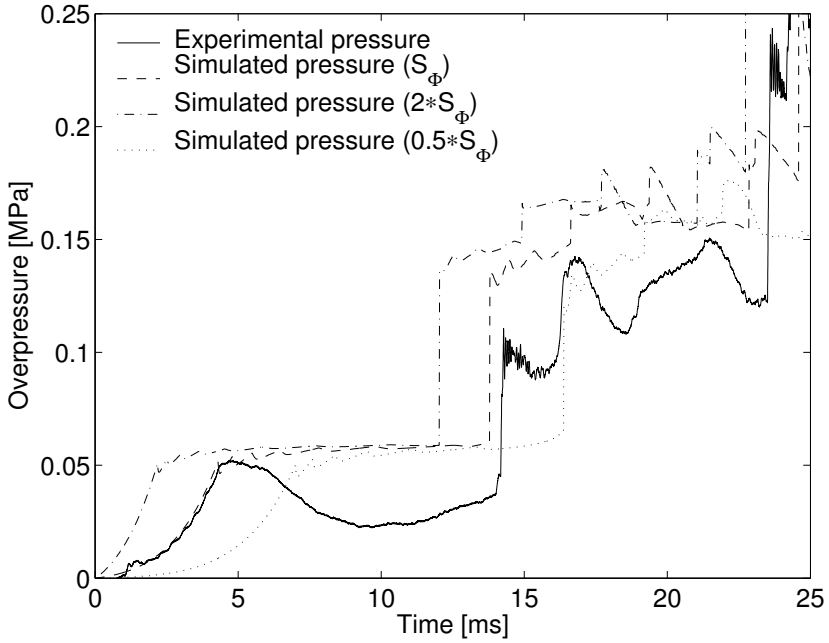

Figure 4.37: The first 25 ms of the experimental and simulated overpressure at pressure transducer P0 in the 3.0 m pipe. Three different constrains have been used on the burning velocity and the hydrogen volume percentage was 35.

(4.52). Figure 4.38 shows the corresponding simulated burning velocity. Both of these two figures show that the different constraints shift the simulation results in time.

A 3.0 m pipe with one transmissive (i.e. non-reflecting) end has been used in gas explosion simulations. This pipe is equivalent to the 3.0 m pipe in Figure 3.2, but with the right end wall replaced with a transmissive end. Figure 4.39 shows the first 17.0 ms of the simulated burning velocities for five different scenarios. Each of these simulations were conducted with one of the following changes to Equation (4.52); 1) a too large t_w, 2) a too small t_w, 3) a too large S_Φ, 4) a too small S_Φ and 5) $t_w = 0$ i.e. the burning velocity was only calculated by Equation (4.28). The simulations were conducted for a hydrogen volume percentage of 35. Figure 4.39 shows that the burning velocities, regardless of the constrained phase, goes asymptotically towards a burning velocity S_a of approximately 31.4 m/s. A similar evolvement was also observed for other equivalence ratios. Table 4.3 gives a list of these asymptotic burning velocities for the various equivalence ratios together with k_4 from Equation (4.28). The simulations showed that the asymptotic value of the burning velocity was strongly connected to the value of k_4. For example, if k_4 was changed from 0.35 to 0.34 for a hydrogen volume percentage of 50, then S_a went from 17.7 to 16.9 m/s. Figure 4.39 also shows that the unconstrained burning velocity has a different shape and that it increases faster than the constrained ones.

Obstructed pipes

Numerical simulations of gas explosions in an obstructed pipe with premixed hydrogen and air have been performed. The simulation results presented in this subsection are

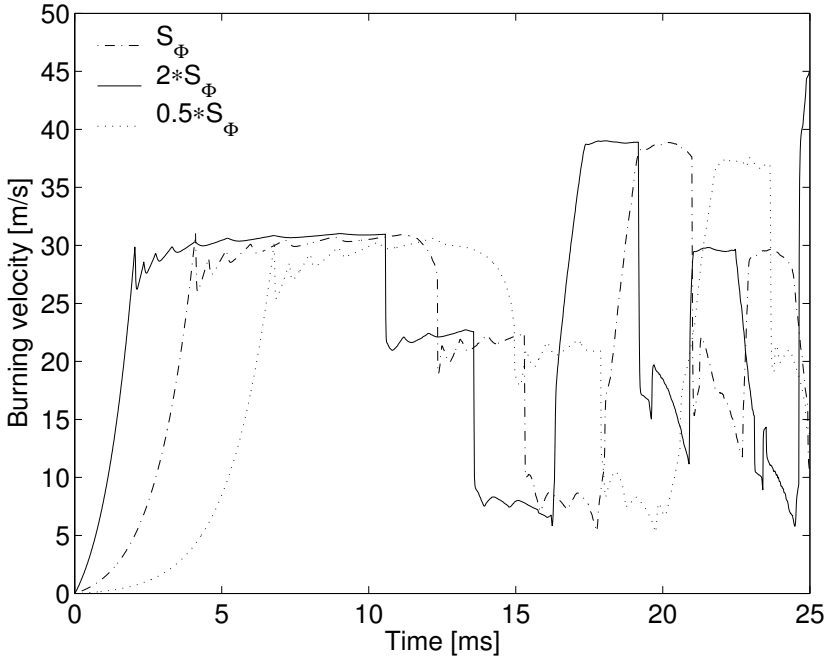

Figure 4.38: The first 25 ms of the simulated burning velocity in the 3.0 m pipe. Three different constrains have been applied and the hydrogen volume percentage was 35.

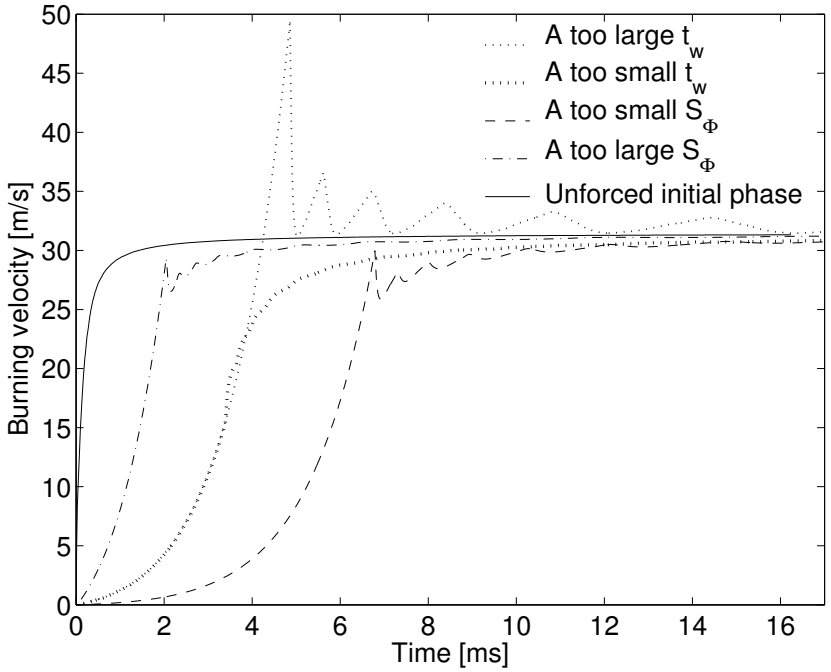

Figure 4.39: Simulated burning velocity for five different constrains in a transmissive end version of the 3.0 m pipe. The hydrogen volume percentage was 35.

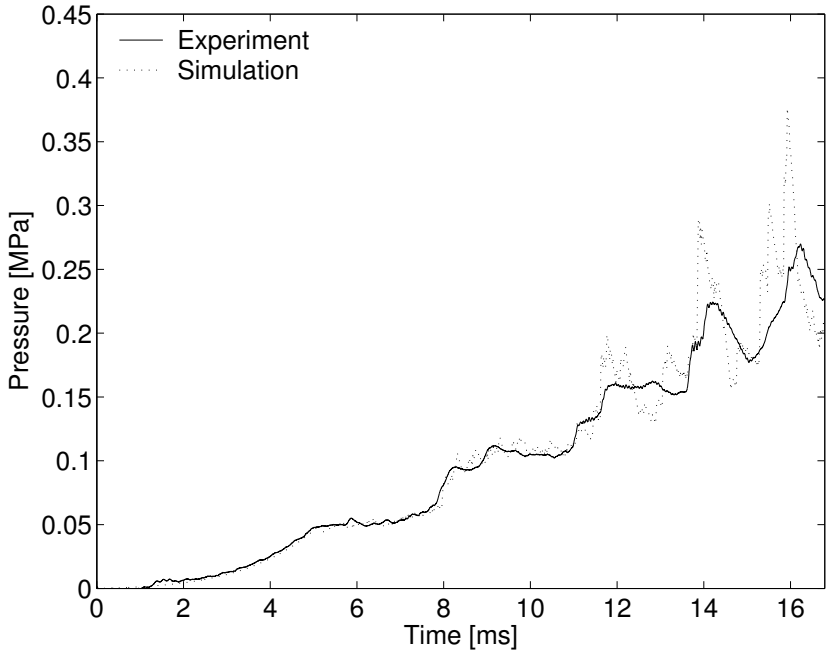

Figure 4.40: Simulated and experimental overpressure at pressure transducer P0 for a hydrogen volume percentage of 30 in the 4.0 m pipe. The obstacle opening diameter was 30 mm.

mainly from stoichiometric mixtures of hydrogen and air in the 4.0 m pipe, but simulations with other equivalence ratios have also been performed. The obstacle opening diameters were 30, 50 and 70 mm. The primary focus of these simulations was to see how the burning velocity model responds to various combinations of obstacle opening diameters and equivalence ratios. BVM2 can not model the turbulent flame acceleration behind the obstacle and only the initial flame propagation has therefore been studied in these simulations.

The numerical simulations manage to reproduce the experimental overpressures quite satisfactorily for the more reactive mixtures. An example of this is shown in Figure 4.40. This figure shows the first 16.7 ms of the simulated and experimental overpressure at pressure transducer P0. The hydrogen volume percentage was 30 and the obstacle opening diameter was 30 mm. It is assumed that the burning velocity model amplifies the propagating pressure waves when they interact with the flame. This together with the numerical noise created by the obstacle model, can be seen as sharp and increasing pressure signals as the flame gets closer to the obstacle.

Figure 4.41 and Figure 4.42 show the simulated burning velocities and the simulated flame positions for three different blockage ratios in the 4.0 m pipe. The hydrogen volume percentage was 30 and the obstacle opening diameters were 30, 50 and 70 mm. The burning velocities are calculated by Equation (4.28) after approximately 5.0 ms and the flame interacts with the first pressure wave at approximately 6.2 ms. A comparison between these simulation results (Figure 4.41 and Figure 4.42) and the simulation results presented in Figure 4.26 and Figure 4.27, shows that the two burning velocity models produce quite similar results.

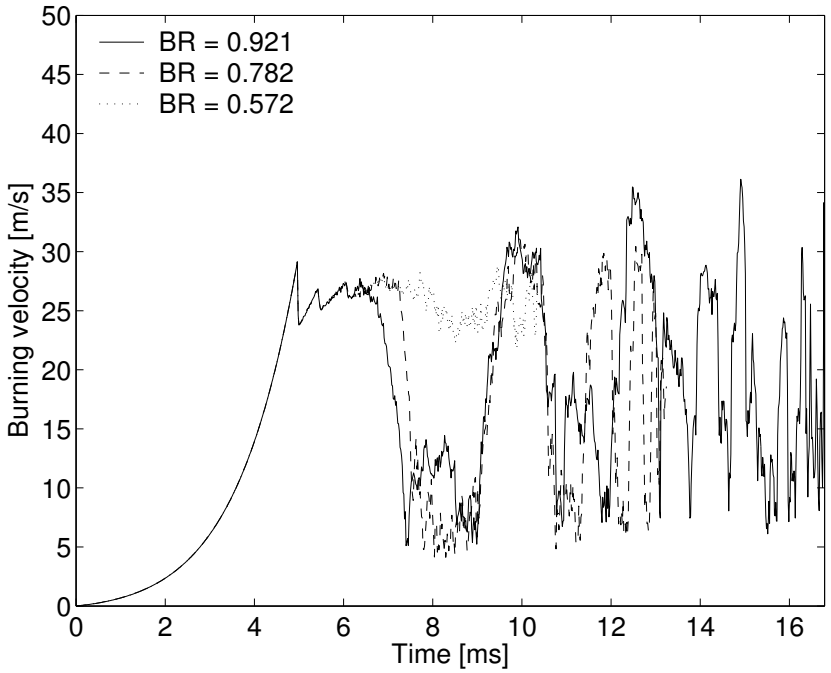

Figure 4.41: Simulated burning velocities for obstacle opening diameters of 30, 50 and 70 mm in the 4.0 m pipe. The hydrogen volume percentage was 30.

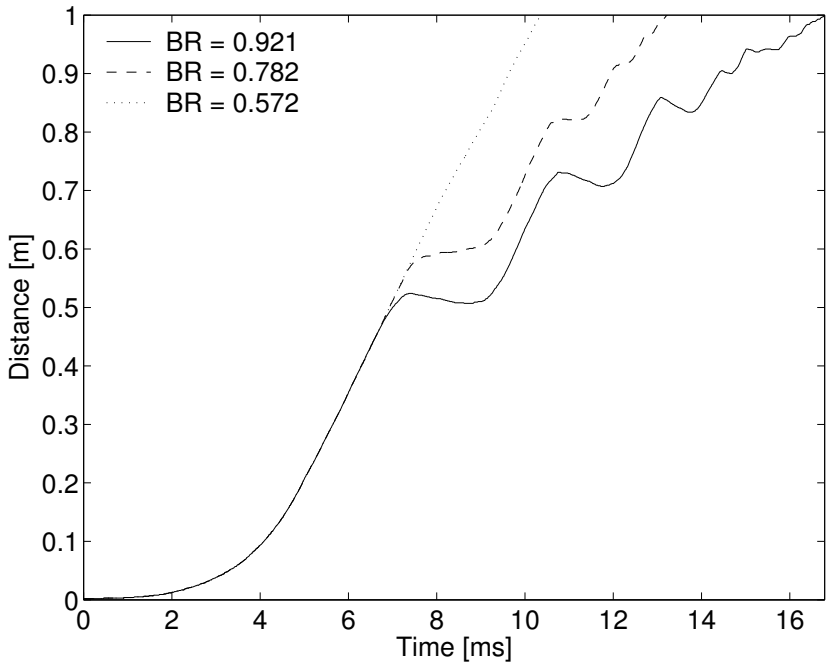

Figure 4.42: Simulated flame positions for obstacle opening diameters of 30, 50 and 70 mm in the 4.0 m pipe. The hydrogen volume percentage was 30.

BVM2 is dependent on having the initial flow field established correctly before it can operate on its own. This was more clearly revealed during the work with the less reactive gas mixtures. It has been shown in Subsection 4.3.2 that for a hydrogen volume percentage of 20, the first pressure wave interacts with the flame before the flame has reached the pipe wall in the radial direction. This influenced the first stages of the flame propagation and t_w became a function of also the obstacle opening diameter. If the applied constraint on the burning velocity was based on the t_w from the unobstructed pipe (i.e. the 3.0 m pipe), then the simulations were not able to reproduce the initial phase of the experimental overpressures. In the 3.0 m pipe, the flame reached the pipe wall in the radial direction before it interacted with any pressure waves.

4.4 Conclusions

The main conclusions derived from the numerical simulations can be summarized as follows:

1. A one dimensional numerical code named RCMLAB has been used to simulate gas explosions in closed and single obstructed pipes. Three different pipes and various equivalence ratios of premixed fuel and air have been used in the simulations. The pipes had inner lengths of 3.0, 4.0 and 7.0 m. Both the 4.0 and the 7.0 m pipe had an obstacle installed 1.0 m down the pipe from the ignition wall. The fuels were hydrogen, propane and methane. The blockage ratio of the obstacle was ranging from 0.572 to 0.991. This is equivalent to obstacle opening diameters ranging from 70 to 10 mm. Corresponding experimental pressure records have been used for validation of the numerical results.

2. RCMLAB together with BVM1 managed to reproduce the experimental pressure recordings for a large variety of both fuel and air mixtures and pipe configurations. BVM1 estimates the burning velocity by comparing the simulated pressure at the flame position for the present simulation time t^n, with the recorded experimental overpressure at a pressure transducer for the time $t^n + \Delta t$. The simulations especially managed to reproduce the experimental pressure recordings at pressure transducer P0. There was a high level of similarity between the simulated and experimental overpressure at this pressure transducer location for the first phase of the flame propagation after the ignition. RCMLAB can therefore be used to validate the simulation results from other multidimensional Computational Fluid Dynamics codes for this first phase. On the other hand BVM1 is not suitable to simulate the strong deflagrations and the DDTs which occur right behind some of the obstacles for the most reactive gas mixtures. BVM1 did also experience difficulties when the flame was close to the opposite end wall. But it is believed that this problem is mostly related to the nature of the pressure transducers that were used to measure the experimental overpressure.

3. The simulations with RCMLAB and BVM2 in the 4.0 m pipe managed to reproduce the experimental pressure recordings quite well. These simulations lasted from the time of ignition to the time when the flame had reached the obstacle. BVM2 uses

only the laminar burning velocity and flow field right in front of the flame to estimate the burning velocity. The model can therefore only handle flame phenomena which are directly associated with the propagating pressure waves. The model can not handle three dimensional effects like flame inversion caused only by a reduced flame surface area (i.e. not caused by an interaction with a pressure wave) or the turbulent flame acceleration behind an obstacle. The initial flow field inside the pipe must also be established before the model can operate on its own.

4. The numerical simulations have shown that the pressure structure which is created during the time of ignition to the time when the flame reaches the pipe side wall in the radial direction, is of significant importance for the flame propagation in closed pipes. This pressure wave will both be reflected off the obstacle and the end walls. The reflected pressure wave then interact with the reaction zone from both the unburned and the burned gas side. The simulations with BVM2 in the 4.0 m pipe show that this pressure wave is the most dominant factor for the flame propagation between the ignition wall and the obstacle. The rest of the flame propagation, i.e. from the obstacle to the end wall, depends on the flame acceleration caused by the turbulent flow field behind the obstacle.

5. The simulations with BVM1 and stoichiometric mixtures of hydrogen and air, showed that flame propagation between the ignition wall and the obstacle is highly dependent on the blockage ratio of the obstacle. The obstacle may increase or decrease the mean axial flame speed.

6. A model for the area change at the obstacle has been added to RCMLAB. The model works best with more reactive gases where the flow Mach number in the obstacle is close to unity. But the model also works satisfactorily for less reactive gases, if a correction factor smaller than one is multiplied to the obstacle opening cross section area.

7. The heat transfer model in RCMLAB has been upgraded to also account for the net heat flux caused by water vapor radiation. A discussion of how the radiant heat transfer model affects the simulated flame propagation, is not presented in this thesis. But it was observed that 1) the model generally has little effect on the first 1.0 m of the flame propagation and 2) the effect of the model increases with time.

8. The simulations with stoichiometric mixtures of propane and air in the 4.0 m pipe, indicate that the time t_w, in which the flame reaches the pipe side wall in the radial direction, is relatively unaffected by the blockage ratio of the obstacle. The same indication was also seen for the simulations with stoichiometric mixtures of methane and air.

9. The simulated burning velocity at the time t_w for a stoichiometric mixture of hydrogen and air in the 4.0 m pipe, is 11 times the laminar burning velocity. The corresponding ratio for propane and methane is 15.

Chapter 5

Conclusions

The main conclusions of this thesis are presented in this chapter. A short summary of the work is given in Section 5.1 before the main conclusions are listed in Section 5.2. Some recommendations for further research are presented in Section 5.3.

5.1 Summary

Gas explosions in pipes have been studied both experimentally and numerically. The main objective of this work was to develop numerical models that could be used together with RCMLAB [17, 18] to simulate flame acceleration and deflagration to detonation transition (DDT). But the initial studies of flame propagation in closed and single obstructed pipes, showed that more knowledge of the first phases of the flame propagation was required before a DDT model could be developed. The primary focus of this thesis has therefore been to see how the flame propagation between the ignition wall and the obstacle in a closed pipe with a single obstacle, is affected by the blockage ratio of the obstacle. Both hydrogen, carbon monoxide, propane and methane have been used, but most of the work has been done with hydrogen.

The gas explosion experiments were primarily performed to provide a set of data for validation of the numerical simulations with RCMLAB. But the data set obtained from the experiments is unique and it has exposed conditions that affect the flame propagation and transition to detonation in pipes. RCMLAB is a one dimensional numerical code which uses the random choice method (RCM) to solve the local Riemann problems between each grid cell. New models have been added to RCMLAB and these models have 1) made RCMLAB applicable to new pipe geometries and 2) brought RCMLAB closer to becoming a predictive numerical code for simulation of gas explosions in pipes. The work presented in this thesis has covered combustion regimes ranging from laminar flames and weak deflagrations to DDTs and self sustaining detonation waves.

5.2 Main conclusions

The main conclusions of this thesis are listed below. The list is in a non prioritized order.

1. Gas explosion experiments in closed and single obstructed pipes have been performed with premixed fuel and air at various equivalence ratios. The experiments were originally performed to provide a set of experimental data for validation of the numerical simulations. Three different pipes together with seven different obstacles and four different fuels, were used in the experiments. The experimental overpressures were measured with pressure transducers. The pipes had an inner diameter of 107 mm and lengths of 3.0, 4.0 and 7.0 m. The four fuels were hydrogen, propane, methane and blends of carbon monoxide and hydrogen.

2. A data acquisition and recording unit consisting of piezo electrical pressure transducers, amplifiers, PCI sampling boards and a laboratory computer, has been used to measure, digitize and store the experimental overpressures. The obtained pressure records are from weak deflagrations, strong deflagrations, DDTs and self sustaining detonations. The time response of the unit was sufficient to measure the shock and detonation waves caused by the obstacle. But the recorded pressures for the less reactive gas mixtures were generally lower than the theoretical constant volume combustion pressures. It is believed that this phenomenon is related to the nature of the pressure transducers. The piezo electrical material in the pressure transducers can not hold the voltage charge for a long time and the measured overpressure therefore becomes lower than the actual value when the flame is close to the opposite end wall.

3. The set of blockage ratios and equivalence ratios of hydrogen and air that gives a DDT after the obstacle for the 4.0 m pipe, has been found. DDTs were observed for equivalence ratios ranging from 0.79 to 1.95 and for blockage ratios ranging from 0.572 to 0.965. This is equivalent to hydrogen volume percentages ranging from 25 to 45 and for obstacle opening diameters ranging from 70 to 20 mm. There was a higher concentration of DDTs on the rich fuel side and the most optimum conditions for DDTs after the obstacle was created with a blockage ratio of 0.921. The various detonations propagated down the pipe with an overpressure of 1.4 MPa or higher and the mean axial detonation velocity between the pressure transducers were close to the theoretical CJ detonation velocity near the pipe end.

4. The experimental configurations that gave a transition to detonation after the obstacle, show good agreement with the DDT criterion presented by Peraldi et al. [160] for an obstacle filled tube (i.e. $D_o \geq \lambda_d$). But the experimental results also indicate that the radial distance between the pipe side wall and the obstacle opening, is a limiting length scale in the type of pipe geometries applied in this work. This possible DDT criterion may be written as $(D_p - D_o) \geq 2\lambda_d$.

5. One dimensional numerical simulations of gas explosions in closed and single obstructed pipes have been performed with RCMLAB. The simulations were performed with various fuel and air mixtures at different equivalence ratios, and with various pipes and obstacle opening diameters. There is a relatively high level of similarity between the simulated overpressures at the different pressure transducer positions in the pipe and the experimental overpressures. Simulations with RCMLAB can therefore be used as a tool to enhance the understanding of flame propaga-

tion in closed and single obstructed pipes. Important parameters such as the average burning velocity and the average burning rate can be estimated using RCMLAB.

6. A model for the area change at the obstacle has been added to RCMLAB. The model is implemented into the code after the operator splitting method. The model of the obstacle is essential in the presented simulations, since the obstacle controls the level of pressure build up in front of the flame and reflects the propagating pressure waves that interact with the flame.

7. Two different methods have been used to calculate the burning velocity in the numerical simulations. One model calculated the burning velocity as a function of both the flow field right in front of the flame and the laminar burning velocity of the gas mixture. This method of simulating the burning velocity showed that the flame propagation in closed and single obstructed pipes is strongly influenced by the first pressure structure that is created from the time of ignition to the time when the flame reaches the pipe side wall in the radial direction. This was clearly shown by the simulations in the 4.0 m pipe with a stoichiometric mixture of hydrogen and air. In these simulations the flame propagation between the ignition wall and the obstacle was completely dominated by this pressure wave. The other burning velocity model used experimental pressure records as input to estimate the burning velocity. This model showed that the pressure wave that is created after the obstacle, is the dominant factor for the flame propagation between the obstacle and the end wall.

8. Both the experiments and the numerical simulations have demonstrated that the flame propagation between the ignition wall and the obstacle is affected by the obstacle opening diameter. The increasing overpressure at P0 with increasing blockage ratio, is mainly caused by the hindering of fluid flow through the orifice plate and not by an increased burning rate. It was also observed that the mean axial flame speed between the ignition wall and the obstacle generally decreased with increasing blockage ratio.

9. The various simulations with RCMLAB have shown that the pressure evolvement for a gas explosion in a closed and single obstructed pipe has similarities to the pressure behavior of an acoustic system. A simplified description of the process can be presented as follows. Once the initial pressure structure of the gas explosion is created, the system will begin to oscillate. The general pressure level in the pipe is enhanced by the combustion process of the unburned gas, but the main oscillations are caused by the initial pressure structure that is reflected off the obstacle and the end walls. The initial pressure structures refers to the pressure structure that is created from the time of ignition to the time when the flame reaches the pipe wall in the radial direction, but also the pressure or shock wave that is created by the turbulent combustion behind the obstacle. The numerical simulations have further shown that even though there are little correspondence between the burning velocity and the flame and pressure wave interactions for the later stages in the simulations, there can still be a a high level of similarity between the simulated and experimental pressures. One should therefore not be so straight forward to make the conclusion that a combustion model is working correctly just based on

the fact that the simulation manages to reproduce the experimental overpressure. The validation of a numerical code used for predictive analysis, should therefore not solely be based on overpressure measurements. This conclusion is in agreement with Reference [172]. The simulations with RCMLAB have also shown that it is relatively easier to reproduce the experimental overpressure in a system that has a continuous and positive flame acceleration, than in a system where the flame acceleration becomes negative.

10. A unique data set has been obtained from the experiments. This data set may also be applied by others in the development of numerical codes and models. Even though the pipe geometry appears to be simple, the flame propagation becomes challenging from a computational fluid dynamics point of view, because of the relative large distance between the ignition wall and the obstacle. This large distance causes several flame and reflected pressure wave interactions before the flame reaches the obstacle.

5.3 Further research

Some recommendations for further research are given in the list below. This list contains both experimental and numerical projects, but also general recommendations on how to improve the experimental setup.

1. The numerical work with RCMLAB, BVM1 and the experimental pressure records have shown that BVM1 can be applied to characterize different fuels. RCMLAB and BVM1 together with the experimental pressure records from pressure transducer P0 should therefore be used to develop a curve fitted formula that describes the average burning rate of gas explosions in pipes, from the time of ignition to the time when the flame reaches the pipe side wall in the radial direction. The calculated burning rate should be a function of both the internal pipe diameter, the fuel type and the equivalence ratio of the gas mixture.

2. It is believed that the piezo electrical crystal in the Kistler 603B and 7001 pressure transducers loses its voltage charge too fast for the less reactive gas mixtures. The data acquisition and recording unit should therefore be changed in such a way that it also manages to measure the actual experimental overpressures at larger time scales. The trigger signal that is sent from the ignition unit to the data acquisition and recording unit, should also be changed to give the exact time of ignition.

3. Water vapor is condensed on the pipe wall in each experiment and the moisture was not completely removed from the pipe during the gas refilling phase. Experiments should therefore be performed to see if this moisture has an affect on the flame propagation, such as the detonation velocity.

4. The method that has been used to model the area change at the obstacle, should also be tested for the conditions at the open end, for simulations of gas explosions in pipes with one open end. Such simulations should be compared with corresponding experimental data.

5. The current version of RCMLAB handles only burning velocities up to CJ deflagrations. The code should therefore be changed to also handle DDTs and detonations. The heat transfer model should also be updated to account for the net heat flux caused by CO_2 radiation.

6. Both the experiments with propane and methane in the 4.0 m pipe, indicated that the flame was quenched at the obstacle for a blockage ratio of 0.991. This phenomenon could be investigated further with a high speed camera in an experiment where the 3.0 m pipe behind the obstacle is replaced by a transparent plastic bag.

7. This study has shown that even if there is a high level of similarity between the experimental and the simulated overpressure, there is still some uncertainty related to the accuracy of the simulations. Experiments with flame position detectors should therefore be performed to validate the numerical simulations further.

8. The limiting conditions for a transition to detonation behind the obstacle, for premixed hydrogen and air at various equivalence ratios, need to be investigated further. The two length scale criteria proposed in this thesis, are not based on a sufficiently large and detailed data set to be regarded as absolute. There might also exist other DDT criteria for the type of pipe configurations used in this study. Additional experiments should therefore be performed to study the DDT phenomenon further. Such an experimental study should have a higher resolution in both the hydrogen volume percentages and the obstacle opening diameters to make the border between DDT and no-DDT clearer. The experimental study should also be performed in a sufficiently long pipe to avoid interactions between the flame and pressure waves reflected off the opposite end wall. Detonation cell size measurements should also be made.

9. A transition to detonation behind the obstacle might occur as a result of both turbulent mixing in the jet and reflected pressure waves from the gas containment [6]. The experiments in this thesis have been performed in a non-transparent steel tube and it is therefore difficult to know if the DDTs occurred in the turbulent flame jet or close to the boundary of the gas confinement. Experiments should therefore be performed to gain more knowledge of the locations of the onset of detonation for the various pipe configurations. Such knowledge might enhance the understanding of the various DDT processes and can be useful in the determination of the critical criteria for DDT in this type of pipe geometries.

Appendix A

Papers

Paper 1 V. Knudsen, K. Vaagsaether and D. Bjerketvedt: *Experiments with hydrogen-air explosions in a closed pipe with a single obstacle*, Proc. of the European Combustion Meeting, 2005.

Paper 2 V. Knudsen, K. Vaagsaether and D. Bjerketvedt: *An experimental study of hydrogen-air gas explosions in a single obstructed pipe*, Proc. of the First Baltic Combustion Meeting, 2005.

A.1 Paper 1

(6 pages)

Experiments with hydrogen-air explosions in a closed pipe with a single obstacle.

V. Knudsen*, K. Vaagsaether and D. Bjerketvedt
Department of Technology,
Telemark University College,
Kjølnes ring 56, NO-3918 Porsgrunn, Norway

Abstract
Flame propagation and Detonation Deflagration Transition (DDT) in a 4 m long circular steel pipe with a single obstacle and an inner diameter of 0.107 m, have been studied experimentally. Premixed hydrogen-air at atmospheric pressure were the combustible gas mixtures used. The experimental results are in agreement with comparable reported experiments. The main purpose of performing the experiments was to provide a set of data for evaluation of numerical codes and models. A one Dimensional (1D) numerical code based on the Random Choice Method (RCM), have been used for the preliminary simulations of the flow and flame propagation in the pipe.

Introduction

In most practical cases there is a Flame Acceleration (FA) after a weak ignition of a combustible premixed gas. This initial acceleration is caused by instabilities of the flame. The flame gets wrinkled and this increases the flame area. It is the difference between the densities of the burned and unburned gas and diffusive-thermal effects that creates the instabilities. Dorofeev [8] states that there is a relationship between the expansion ratio $\sigma = \rho_u/\rho_b$, (where ρ_u is the density of the unburned gas and ρ_b is the density of the burned gas), and the magnitude of the flame acceleration. The further development of the flame velocity is closely related to the geometry of the confinement. It is known that obstructions of various kinds provides a good environment for FA. The fluid flow caused by the combustion processes increases the flame surface around obstacles. This type of flow may also generate turbulence. If the turbulence is not so intense that it leads to local quenching of the flame, it will contribute to (or dominate) the FA process. Turbulence effects the flame by an increase of the flame surface area and by an increase of the local transport of heat and reactants in the combustion zone. If the flame acceleration is sufficiently large, DDT is likely to occur.

This work have been concentrated on hydrogen-air gas explosions at atmospheric conditions in a pipe with an obstacle. Flame propagation and DDT has been the main focus in this study.

Specific Objectives

The main purpose of performing the experiments was to provide a set of hydrogen data for evaluation of the two numerical codes RCMLAB [2] and FLICLAB [9]. These numerical codes has been created with the intention of 1) making tools to simulate gas explosions in pipes and 2) to develop a DDT describing model.

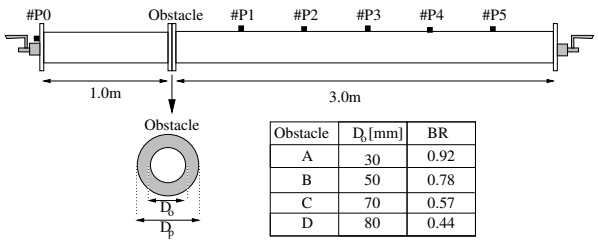

Obstacle	D_o [mm]	BR
A	30	0.92
B	50	0.78
C	70	0.57
D	80	0.44

Figure 1: The experimental setup used. Six pressure transducers are placed along the pipe as indicated on the sketch.

Experimental setup

The experiments have been carried out on a 4.0 m long circular steel pipe with an inner diameter of 0.107 m. The pipe was closed at both ends and had a spark ignition source in one end. An obstacle i.e. an orifice plate with a centred circular opening, was installed 1.0 m down the pipe from the ignition source. This obstacle ensured strong turbulence and caused DDT in some of the experiments. Four orifice plates with different opening diameter were used. The opening diameters were 30, 50, 70 and 80 mm, equivalent to Blockage Ratios (BR) of 0.92, 0.78, 0.57 and 0.44. The combustible gas mixtures were premixed hydrogen-air at atmospheric pressure and with a fuel concentration ranging from 10% to 50% in steps of 5%. To measure the pressure six transducers were mounted in the pipe. (The pressure transducers used

*Corresponding author: vegeir.knudsen@hit.no

was Kistler 7001 and Kistler 603B). One transducer was placed at the end wall close to the ignition source (P0), and the rest at 1.5 m (P1), 2.0 m (P2), 2.5 m (P3), 3.0 m (P4) and 3.5 m (P5) down the pipe.

To ensure gas homogeneity, the pipe was slightly tilted with the ignition end elevated. A sketch of the pipe and the distribution of the pressure transducers is shown in Figure 1.

Numerical simulations

Bjerketvedt and Mjaavatten [1] have developed a one dimensional numerical code to simulate gas explosion in pipes. This code is written in Matlab and has successfully been tested on a different set of pipes at various propane-air mixtures by Kristoffersen et al. [3] and [4]. A very short summarize of the numerical code can be stated as follows: Experimental pressure records are used as input. These pressure records are used to estimate the burning velocity *S* of the combustible gas mixture. This burning velocity is then fed back in to a combustion model of the code. With knowledge of the burning velocity the code is capable of simulating the flow and flame propagation in the pipe. To verify the simulation results, the simulated pressure records can be compared with the experimental pressure records.

The original version of the method used for estimation of the burning velocity is described by Bjerketvedt et al. [2], and the new version is described by Kristoffersen [4].

RCMLAB (as the numerical code is named) uses the RCM to solve the Euler equations of Gas Dynamics on a staggered grid in 1D. In essence the RCM solves the local Riemann Problems (RP) between grid cells and sample the solution for the next time step at random. This random sampling is carried out after a Van der Corput procedure on the local RPs. A good presentation of the RCM can be found in Toro [7].

The thermodynamic data used in the code were determined by the software packages SuperSTATE and Cantera. The pipe was modeled as 1D planar geometry with $X \times 100$ grid cells per meter. X is the scale factor for the grid size.

The obstacle (turbulizer) inside the pipe, was coded in to RCMLAB after a model presented by Gottlieb [5]. This model is a first order corrections of the primitive variables. The primitive variables are ρ = density, u = speed and p = pressure, and the corrected values are written as

$$\begin{aligned} \rho &= \hat{\rho}[1 - \beta\hat{u}\Delta t] \\ u &= \hat{u} \\ p &= \hat{p}[1 - \gamma\beta\hat{u}\Delta t] \end{aligned} \tag{1}$$

where $\hat{\rho}$, $\hat{u}$ and $\hat{p}$ are the uncorrected values, γ are the specific heat capacity ratio and $\beta = (1/A) \cdot dA/dx$. In the model A is used as the pipe cross section area and dA is the pipe cross section area change caused by the turbulizer. The obstacle is further defined to be $X \times 8$ cells sizes big.

For the version of RCMLAB applied in this study, there is not incorporated a model for the energy loss to the surroundings. But there is work in progress on creating a model for heat loss using a Reynolds analogy, and a model for radiation using the Stefan-Boltzmann equation. The absence of an energy loss model is assumed to mainly result in a lower estimated burning velocity *S*.

Results and Discussion

Two examples of the pressure records obtained in the experiments are shown in Figure 2 and Figure 3. Figure 2 is an example of a typical obtained pressure record with DDT and a detonation after the obstacle. We observe a wave that travels down the pipe with a pressure peak of approximately 1.4 - 2.0 MPa. It was also typical for the experiments with a detonation that the first wave front created the highest pressure of the recording for each sensor. Figure 3 is an example of an obtained pressure record with a deflagration after the obstacle. The pressure records are strongly related to the strength of the deflagration. But the pressures are much lower and the first wave front travels at a much lower speed than it was observed for the experiments with a detonation.

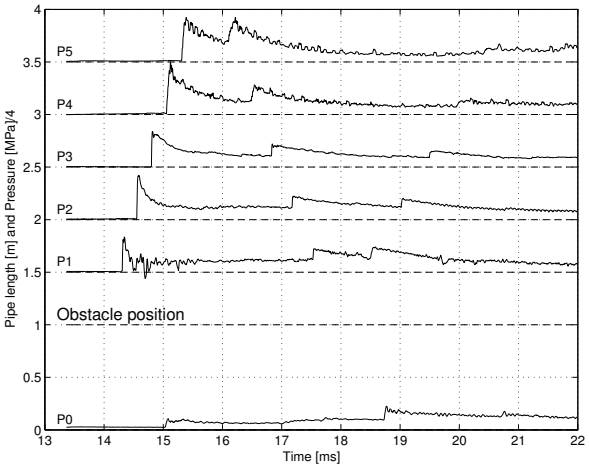

Figure 2: A detonation wave from the experiments for a blockage ratio of 0.78 and 30%H_2. The maximum pressure of P2 is about 1.67 MPa.

There is a listing in Table 1 showing which of the experiments that experienced a DDT between the obstacle and the pressure transducer P1. Experiments with DDT have been marked with a + sign and experiments without a DDT have been marked with a - sign. We did not observe any DDTs for the lowest blockage ratio. For some blockage ratios we observed that the same mixture

Table 1: A DDT matrix showing which of the experiments that did have a DDT. BR is the blockage ratio and $\%H_2$ is the fuel percentage of hydrogen. The + sign indicates a DDT and a - sign indicates no DDT.

BR \ $\%H_2$	10	10	15	15	20	20	25	25	30	30	35	35	40	40	45	45	50	50
0.92	-	-	-	-	-	-	-	+	+	+	+	+	+	+	+	-	-	-
0.78	-	-	-	-	-	-	-	-	+	+	+	+	+	+	-	-	-	-
0.57	-	-	-	-	-	-	-	-	-	-	+	-	-	-	-	-	-	-
0.44	-	-	-	-	-	-	-	-	-	-	-	-	-	-	-	-	-	-

concentration could give DDT in one experiment and no DDT for an another experiment. This effect was observed for a blockage ratio of 0.92 with 25 and 45 $\%H_2$, and for a blockage ratio of 0.57 with 35 $\%H_2$. This effect can rely on both the unrepeatable nature of turbulence and on the small fuel concentration variations between each experiment. It was also observed high pressures (1.8 - 2.6 MPa) at the transducer P5 with a blockage ratio of 0.57. These high pressures were observed for hydrogen concentrations from 30 to 40 $\%$ and are a result of a DDT in the precompressed gas after the shock has reflected off the end wall.

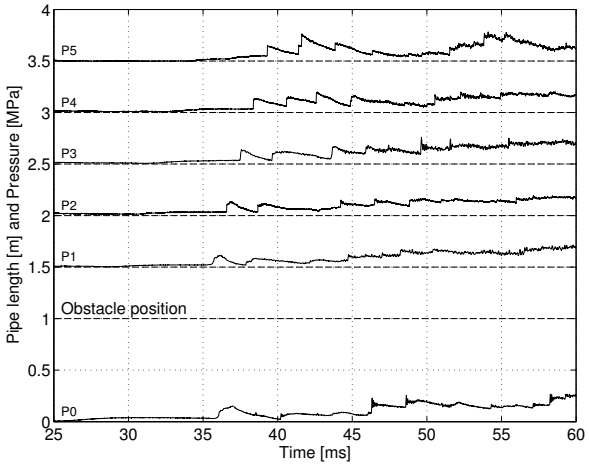

Figure 3: A deflagration wave from the experiments for a blockage ratio of 0.44 and 20$\%H_2$. The maximum pressure of P5 is about 0.25 MPa.

In Figure 4 the theoretical CJ detonation velocity (obtained from SuperSTATE) for a fluid with the initial conditions $u = 0$ m/s, $p = 0.1$ MPa and $T = 300$ K, are plotted against the measured detonation velocities for the various blockage ratios. The measured values are the averaged speed of the pressure waves between the pressure sensors P3 and P5. Figure 10 shows that the number of small pressure waves in front of the detonation at transducer P1 increases with an increase of the blockage ratio. Even for a blockage ratio of 0.44, the gas is no longer at its initial state when the detonation wave passes the last sensor P5. The gas was therfore already preheated and moving when the combustion zone passed the transducers. This condition will effect the detonation velocity and can be an explanation for the low detonation velocities measured for some of the experiments. The low detonation velocity was mainly observed for a blockage ratio of 0.92.

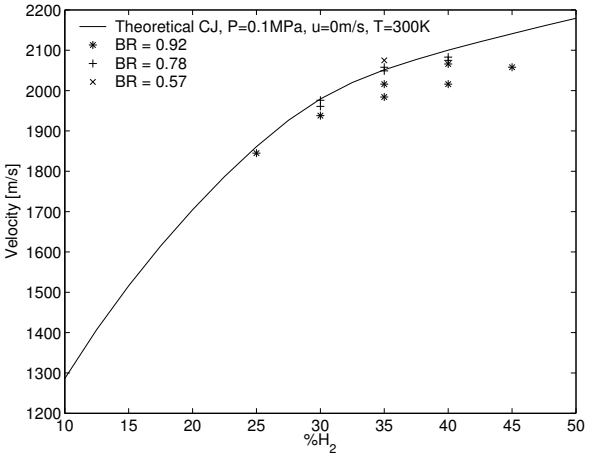

Figure 4: Theoretical CJ detonation velocity and measured detonation velocities averaged between sensors P3 and P5.

The orifice diameter to detonation cell size ratio (D_o/λ_d), is plotted against the hydrogen fuel percentage for the four different orifice diameters in Figure 5*. The experimental results have also been marked in the figure. (* indicates DDT, ∘ indicates no DDT and × indicates the critical situations discussed above). It can bee seen from the figure that we experienced DDT up to a $D_o/\lambda_d \approx 8.5$. This result is not too far from the limit of 7 proposed by Üngüt et al. [12]. For the 30 mm orifice (i.e. BR = 0.92) DDTs were observed for orifice diameter to detonation cell size ratio smaller than 3 on the lean side and 2 on the rich side. Scaling with cell size λ_d alone seems to be insufficient for the DDT process in the present geometry.

*The data for λ_d is obtained from Kaneshige et al. [11] and Ciccarelli et al. [10].

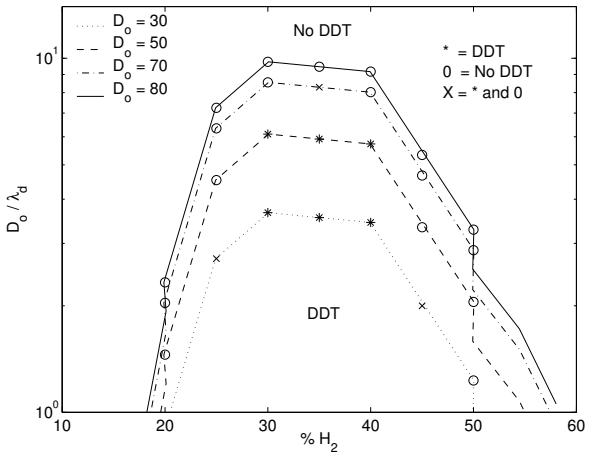

Figure 5: An overview of the experimental results as a function of the orifice diameter to detonation cell size ratio and the hydrogen fuel percentage. (* is the experiments with DDT, ∘ is the experiments with no DDT and × is the experiments both with and without DDT).

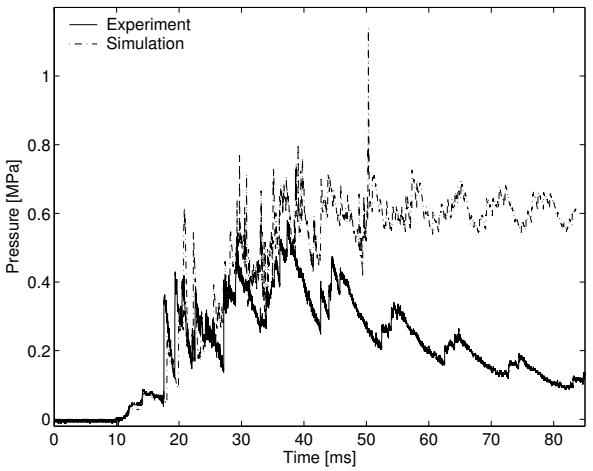

Figure 6: The simulated and experimental pressure record at sensor P5 for a blockage ratio of 0.44 and a stoichiometric gas mixture.

The preliminary numerical simulations of the pipe did not manage to recreate the experimental pressure records in full detail. We belive this is mainly caused by the insufficient modeling of the obstacle and there is work in progress trying to approve this model. An example of the simulated pressure at P5 is shown in Figure 6 for a blockage ratio of 0.44 and a stoichiometric gas mixture. The associated simulated burning velocity and density are shown in Figure 7 and Figure 8. The initial flame propagation (i.e times approximately smaller than 10 ms) seems to be predicted quite well. However the burning velocity drops to zero when the flame is close to the obstacle. We belive that this is also a result of the insufficient modeling of the obstacle. When the flame has passed the obstacle there is a rapid increase in the velocity because of the increased turbulence. A visualization of the flame propagation and the propagation of the pressure waves, are given by the density plot in Figure 8. The burned gas is shown as the darker areas to the left in the figure.

In Figure 6 the experimental pressure starts to drop after the flame has reached the end wall. (This happens for times approximately larger than 40 ms). The pressure drop is related to both the heat loss to the surroundings and to the time response of the piezo electrical pressure transducers.

Table 2: The simulated flame jet velocity (v_{fj}) in the obstacle for the four blockage ratios and a stoichiometric gas mixture. The + sign indicates DDT in the experiment and the - sign indicates no DDT in the experiment.

BR	0.92	0.78	0.57	0.44
v_{fj} [m/s]	401	296	115	44
DDT	+	+	-	-

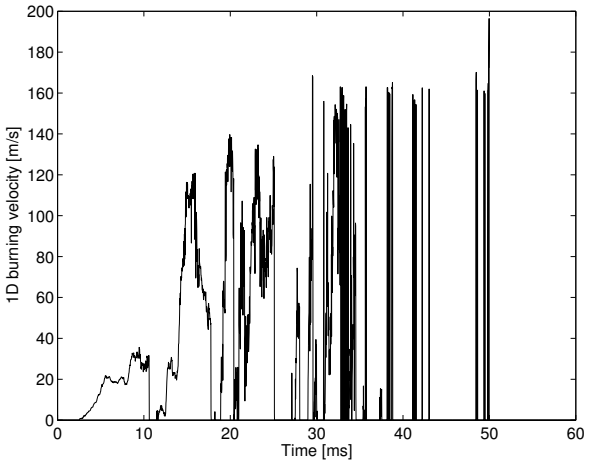

Figure 7: The simulated burning velocity for a blockage ratio of 0.44 and a stoichiometric gas mixture.

MacKay et al. [6] have studied flame-jet ignition of large fuel-air clouds. They have looked in to the criteria of DDT as a function of the initial flame jet velocity v_{fj} and the ratio of mixture critical tube diameter to tube diameter (d_c/D_o). According to MacKay et al. there exist a minimum flame jet velocity of about 600 m/s required for DDTs in sensitive fuel-air mixtures and that this minimum velocity increases with decreasing mixture sensitivity. Table 2 shows the simulated v_{fj} in the obstacle for the four different blockage ratios at stoichiometric mixture. The simulated velocities are rather low compared to the criteria above. It is assumed that these low velocities also are related to the insufficient modeling of the obstacle. It was observed that small changes of the obstacle model resulted in dramatically changes of the velocity

fields inside the obstacle. It is also important to state that the fluid velocities inside the obstacle can be much larger than it appears from Table 2.

In relation to the simulated flame jet velocities discussed above, the experimental pressure recordings at sensor P0 and P1 are shown in Figure 9 and Figure 10 for the four different blockage ratios and 35 $\%H_2$. The two figures indicates the time dependent pressure differences over the obstacle as a function of the blockage ratio.

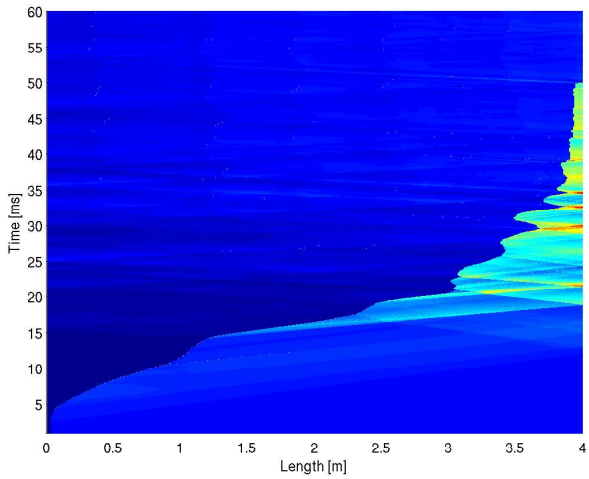

Figure 8: The simulated density record of the 4 m pipe at transducer P1 with a blockage ratio of 0.44 and a stoichiometric gas mixture. There is no DDT for this simulation.

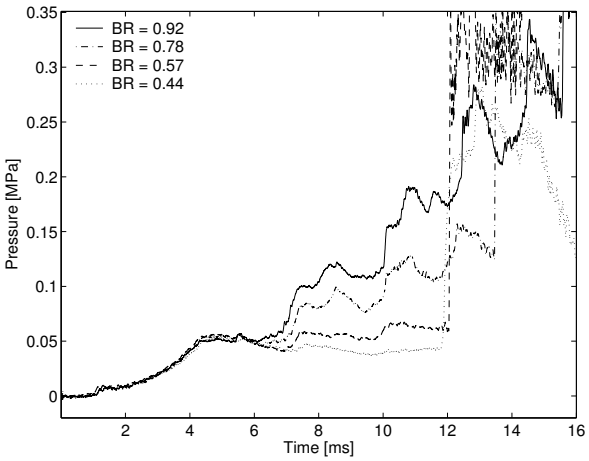

Figure 9: The difference in the experimantal pressure evolvement at P0 for the four different blockage ratios and 35$\%H_2$.

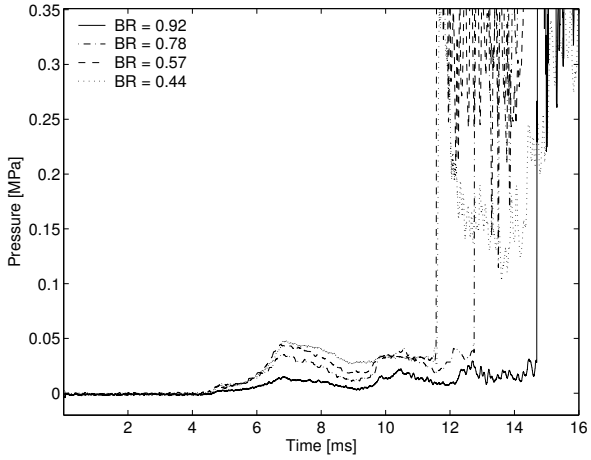

Figure 10: The difference in the experimental pressure evolvement at P1 for the four different blockage ratios and 35$\%H_2$.

Conclusions

A set of experimentally determined pressure records with hydrogen-air mixtures in a pipe with a single obstacle and the length of 4 m are obtained. The preliminary numerical reproductions of the experimental pressure records, are done with a high level of accuracy for the initial flame propagation.

DDTs was observed when the orifice diameter (D_o) to detonation cell size (λ_d) ratio was smaller than 8.5 for the 50 mm orifice and smaller than 2 to 3 for the 30 mm orifice.

This dataset will now be used for evaluations and testing of Computational Fluid Dynamics (CFD) codes.

Acknowledgments

Support from The Norwegian Defense Estates Agency and Strategisk Høgskole-program - The Research Council of Norway, is gratefully acknowledged.

References

[1] D. Bjerketvedt, A. Mjaavatten, Simulation of gas dynamic flow with a Matlab version of the random choice method, Proceedings of the Nordic Matlab Conference, 2001.

[2] D. Bjerketvedt, K. Kristoffersen, Knut Vaagsaether, A. Mjaavatten, A. O. Thomas, A method for estimating the burning velocity in a tube by using experimental pressure records and the 1-D RCMLAB code, Proceedings of Combustion Science and Technology, 2004.

[3] K. Kristoffersen, K. Vaagsaether, D. Bjerketvedt, G. O. Thomas, Experimental Thermal and Fluid Science 28, (2004),723-728.

[4] K. Kristoffersen, Gas explosions in process pipes, Norwegian University of Science and Technology and Telemark University College, Norway, 2004.

[5] J. Gottlieb, Random-Choice Method for solving one-dimensional unsteady flows in ducts, shock tubes and blast-wave simulators, Institute for Aerospace Studies, University of Toronto, 1986.

[6] D. J. MacKay, S.B. Murray, I. O. Moen, Twenty-Second Symposium (international) on Combustion/The Combustion Institute, (1988), 1339-1353.

[7] E. F. Toro, Riemann Solvers and Numerical Methods for Fluid Dynamics, Springer, Germany, 1999.

[8] S. B. Dorofeev, Journal de physique IV,12, (2002).

[9] K. Vaagsaether, D. Bjerketvedt, Gas explosion simulation with flux limiter centred method, Submitted for the 20th ICDERS, 2005.

[10] G. Ciccarelli, T. Ginsberg, J. Boccio, C. Economos, K. Sato, M. Kinoshita. Combustion and Flame, 99(2):212-220, (1994).

[11] M. Kaneshige and J.E. Shepherd, Detonation database, Technical Report FM97-8, GALCIT, July 1997. See also the electronic hypertext version at http://www.galcit.caltech.edu/detn_db/html/.

[12] A. Üngüt, P. Shuff, Combustion Science and Technology, Vol 63, (1989), 75-87.

A.2 Paper 2

(4 pages)

An Experimental Study of Hydrogen-Air Gas Explosions in a Single Obstructed Pipe.

V. Knudsen, K. Vaagsaether and D. Bjerketvedt

Department of Technology, Telemark University College, Porsgrunn, NO

Abstract

A closed tube with a single internal obstacle has been used to study gas explosions in hydrogen-air mixtures. The main objective of the experiments was to provide a set of experimental data for validation of numerical codes and models. A numerical code based on the Random Choice Method (RCM) has been updated and preliminary runs of the code show promising results.

Introduction

It is well known that turbulent flow right in front of a flame in a combustible gas mixture may lead to strong flame acceleration and increased flame speed. The turbulence increases the transport of heat and reactants in the reaction zone, but it also increases the flame surface area. One common way to increase the turbulence in a gas explosion experiment, is through the introduction of obstacles. Different types of obstacles create different levels of turbulence and flow patterns for the reactive flow. The experiments in this study have been done with one single obstacle. This obstacle configuration was chosen both to ensure strong turbulence inside the pipe and to keep the geometrical complexity at a fairly low level. The main objective for performing the experiments was to get a set of experimental data for evaluation of numerical simulations. The primary focus of this experimental study was to see how the blockage ratio (BR) of the obstacle and the equivalence ratio (Φ) of the premixed hydrogen-air influenced the flame propagation. If the flame acceleration is sufficiently large, a Deflagration to Detonation Transition (DDT) is likely to take place.

Experimental Setup

The tube used in the experiments was a closed, smooth and circular steel pipe with a single internal obstacle. The pipe was 4.0 m long and had an inner diameter of 107 mm. Both the end walls of the pipe were plane, and an electrical spark plug (< 30 kV) was mounted in the center of one of them. 1.0 m down the pipe from this weak ignition source, an obstacle was installed inside the pipe. The obstacle was an orifice plate with a single centered circular opening. A total of 6 Kistler pressure transducers were distributed in the pipe. One transducer was installed on the end wall very close to the spark plug (P0). The rest of the transducers were mounted 1.5 m from the spark plug (P1) and every 0.5 m down the pipe (P2-P5). 7 different obstacles with BRs ranging from 0.441 to 0.996, and 9 different fuel concentrations with equivalence ratios ranging from 0.26 to 2.33, have been used. This is equivalent to obstacle opening diameters ranging from 5 mm up to 80 mm and volume fuel concentrations of hydrogen ranging from 10 percent up to 50 percent. All the experiments were done at atmospheric pressure and with the ignition end of the pipe slightly elevated. This small tilting of the pipe was done to ensure homology in the combustible gas mixtures. A sketch of the experimental setup is shown in Figure 1.

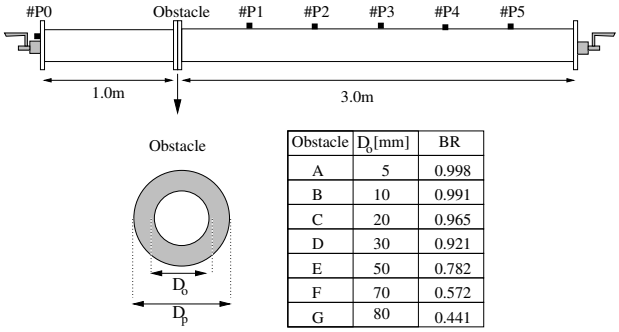

Obstacle	D_o[mm]	BR
A	5	0.998
B	10	0.991
C	20	0.965
D	30	0.921
E	50	0.782
F	70	0.572
G	80	0.441

Figure 1: Experimental setup.

Table 1: Experimental DDT matrix.

BR	$\%H_2$								
	10	15	20	25	30	35	40	45	50
0.998	○	○	○	○	○	○	○	○	○
0.991	○	○	○	○	○	○	○	○	○
0.965	○	○	○	○	×	×	○	○	○
0.921	○	○	○	×	●	●	●	×	○
0.782	○	○	○	○	●	●	●	○	○
0.572	○	○	○	○	○	×	○	○	○
0.441	○	○	○	○	○	○	○	○	○

Numerical Simulations

A one dimensional (1D) numerical code based on the RCM and designed to simulate gas explosions in pipes [1], has been updated with new models both for heat transfer and for the area change at the obstacle. The obstacle model has been changed to implement the orifice plate as two different types of monotonically changing cross section areas. First the area of the pipe is set to decrease over $X \cdot 4$ grid cells and then it is set to increase again over $X \cdot 4$ new grid cells. (X is the scale parameter that controls the total number of grid cells). The cross section area changes are implemented after the operator splitting method [5] and equation 1.

$$\frac{1}{A(x)}\frac{\partial A(x)}{\partial x} = \frac{\pi}{2L}\ln\left(\frac{A_2}{A_1}\right)\sin\left(\frac{\pi x}{L}\right) \tag{1}$$

L is the length of the local area change and $A(x)$ is the cross section area of the pipe given by equation 2. In the first part of the obstacle model, A_1 is the cross section area of the pipe and A_2 is the cross section area of the obstacle. In the second part of the model, A_1 and A_2 are switched.

$$A(x) = (A_1A_2)^{\frac{1}{2}}\exp\left[\ln\left((\frac{A_1}{A_2})^{\frac{1}{2}}\right)\cos\left(\frac{\pi x}{L}\right)\right] \tag{2}$$

The heat transfer model has been changed to also account for the net heat flux caused by radiation. This feature is implemented into the numerical code after a method presented in [3]. The heat transfer model now treats the changes in the potential energy through heat radiation and heat conduction. Both of these two processes assumes that the pipe wall temperature is constant. The same model treats the changes in kinetic energy through a reduced fluid velocity. The reduced velocity is caused by the pipe wall friction.

Results and Discussion

The set of BRs and percentages of hydrogen that gives a DDT after the obstacle for this experimental setup, is shown by the DDT matrix in Table 1. '○' represent experiments without DDT, '×' represent experiments with parallels both with DDT and without DDT (critical values), and '●' represent experiments with DDT. The matrix shows that there is a higher concentration of DDTs on the rich fuel side of the gas mixtures. Experiments with DDT had pressure peaks close to 1.6 MPa or higher for each transducer after the obstacle.

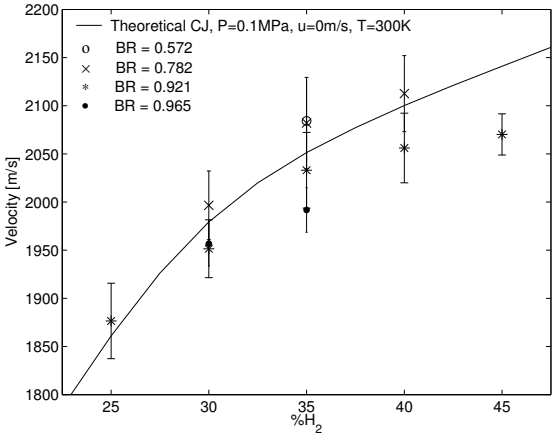

Figure 2: Theoretical and experimental detonation velocities.

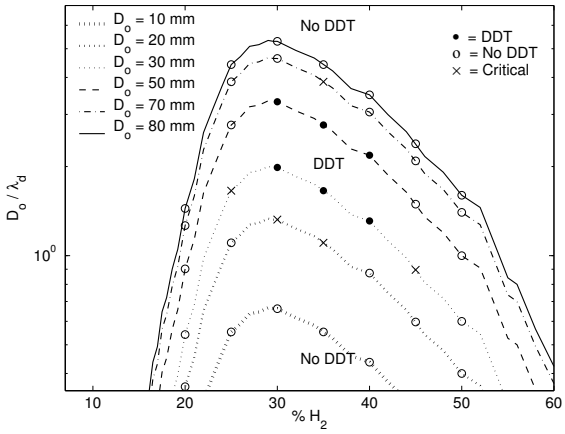

Figure 3: Experimental results versus detonation celle sizes.

These pressure peaks were in most cases created by the first shock wave that propagated down the pipe. The velocity of these waves were close to the theoretical CJ-detonation velocities near the end of the pipe. Figure 2 shows the experimental and the theoretical CJ detonation velocities as a function of the hydrogen percentage. The error bars on the experimental velocities indicate the standard deviation for each BR and percentage of hydrogen combination. It can easily be seen from the figure that the experimental detonation velocities decrease with increasing BR values. This may be caused by the pressure waves in front of the detonation wave [2].

Figure 3 shows the experimental DDT results as a function of both the obstacle opening diameter to detonation celle size ratio (D_o/λ_d) and the hydrogen percentage. This figure uses the same notation as Table 1 and the data for λ_d is obtained from [6, 7]. The figure shows that experiments with DDT have a D_o/λ_d in the range from 0.9 to 3.9. Lindstedt et al. [4] have reported values of $D_o/\lambda_d \approx 0.71$ for DDTs in stoichiometric gas mixtures of hydrocarbons and air. They used Shchelkin spirals with varying lengths as obstacles and found that a BR of 0.44 gave the most optimum conditions for flame acceleration. We found that a BR of 0.921 is the most efficient BR for our experimental setup. Another comparable study [8] reports that DDTs in fuel-air mixtures can occur as local explosions both in the flame jet and near the boundary of the gas confinement. Since our experiments are done in a steel tube, it is hard to know where the transitions actually take place. This needs to be investigated further.

The result from a preliminary run of the numerical code for a strong deflagration in a stoichiometric gas mixture with an obstacle opening of 20 mm, is shown in figure 4 and 5. Figure 4 shows the simulated pressure at pressure transducer positions P0, P1, and P3 versus the experimental obtained pressure records. The simulated flame position is also plotted in this figure. The corresponding burning velocity is plotted in Figure 5.

Conclusions

A set of experimental pressure records of hydrogen-air gas explosions at atmospheric conditions in a closed and single obstructed pipe have been obtained. The set of BRs and fuel concentrations that gives a DDT after the obstacle has been found. A numerical

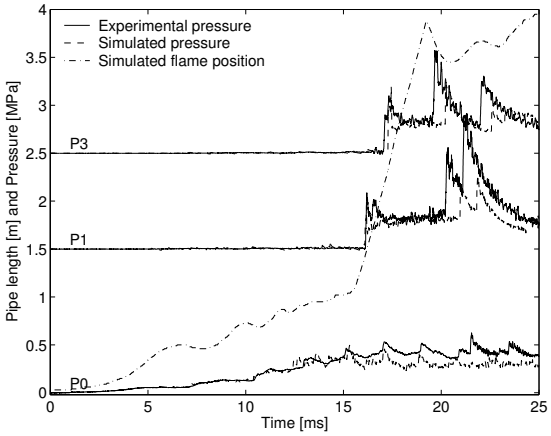

Figure 4: Simulated and experimental pressure together with flame position.

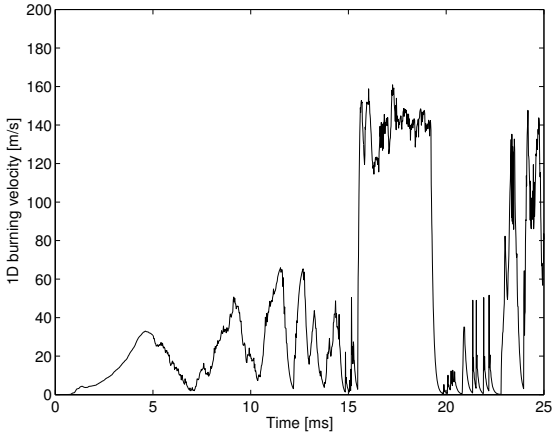

Figure 5: Simulated burning velocity.

code for simulation of gas explosions in pipes has been updated and preliminary runs of the code show promising results.

Acknowledgments

Support from The Norwegian Defense Estates Agency and Strategisk Høgskole-program - The Research Council of Norway, is gratefully acknowledged.

References

[1] D. Bjerketvedt, A. Mjaavatten, Simulation of gas dynamic flow with a Matlab version of the random choice method, Proc. of the Nordic Matlab Conference, 2001.

[2] V. Knudsen, K. Vaagsaether, D. Bjerketvedt, Experiments with hydrogen-air explosions in a closed pipe with a single obstacle, Proc. of the European Combustion Meeting, 2005.

[3] VDI heat atlas, VDI-Verlag GmbH, 1993.

[4] R. P. Lindstedt, H. J. Michels, Combust. Flame, 76 (2) (1989) 169-181.

[5] J. Gottlieb, Random-Choice Method for solving one-dimensional unsteady flows in ducts, shock tubes and blast-wave simulators, Institute for Aerospace Studies, University of Toronto, 1986.

[6] C.M. Guirao, R. Knystautas, J. Lee, W. Benedick, M. Berman, Hydrogen-air detonations, 19th Symp. Int. Combust. Proc., pages 583-590, 1982.

[7] M. Kaneshige, J.E. Shepherd, Detonation database, Technical Report FM97-8, GALCIT, July 1997. Electronic version at http://www.galcit.caltech.edu/detn_db/html.

[8] I. O. Moen, D. Bjerketvedt, T. Engebretsen, A. Jenssen, B. H. Hjertager, J. R. Bakke, Combust. Flame, 75 (1994) 297-308.

Appendix B

The Euler equations

This appendix gives a short introduction to the homogenous Euler equations for a compressible and inviscid flow. Section B.1, Section B.2 and Section B.3 give a brief derivation of the equations for conservation of mass, momentum and energy. Section B.4 presents the Euler equation on the conservative form. The derivations presented in this chapter are mainly based on the lecture notes by Langtangen [15] and the book by White [16].

B.1 The equation of continuity

The total mass of a collection of particles that occupies the material volume $V(t)$, can be written as

$$M(t) = \int_{V(t)} \rho(\vec{r}, t) \mathrm{d}V. \tag{B.1}$$

ρ is the density [kg/m^3]. The conservation of mass then gives that

$$\frac{\mathrm{d}M(t)}{\mathrm{d}t} = \frac{\mathrm{d}}{\mathrm{d}t} \int_{V(t)} \rho(\vec{r}, t) \mathrm{d}V = 0 \tag{B.2}$$

when the volume $V(t)$ is followed. Reynolds transport theorem removes the time dependent integration domains and gives that

$$\frac{\mathrm{d}M(t)}{\mathrm{d}t} = \int_{V} \frac{\partial \rho}{\partial t} \mathrm{d}V + \int_{\partial V} \rho \vec{u} \cdot \vec{n} \mathrm{d}S = 0, \tag{B.3}$$

where $\vec{u}$ is the velocity vector [m/s] and $\vec{n}$ is the normal vector. The integral form of the equation of continuity then becomes

$$\int_{V} \frac{\partial \rho}{\partial t} \mathrm{d}V + \int_{\partial V} \rho \vec{u} \cdot \vec{n} \mathrm{d}S = 0. \tag{B.4}$$

The Gauss theorem transform the surface integral to a volume integral and the equation can now be written as

$$\int_V \frac{\partial \rho}{\partial t} \mathrm{d}V + \int_V \nabla \cdot (\rho \vec{u}) \mathrm{d}V = 0. \tag{B.5}$$

This equation can also be written as

$$\int_V \left(\frac{\partial \rho}{\partial t} + \nabla \cdot (\rho \vec{u}) \right) \mathrm{d}V = 0. \tag{B.6}$$

Since the integral is arbitrary the integrand can be removed. The equation is therefore reduced to

$$\frac{\partial \rho}{\partial t} + \nabla \cdot (\rho \vec{u}) = 0. \tag{B.7}$$

This is the differential form of the equation of continuity.

B.2 The equation of motion

Newton's second law states that

$$\frac{\mathrm{d}}{\mathrm{d}t} \vec{I} = \vec{F}, \tag{B.8}$$

where $\vec{I}$ is the momentum and $\vec{F}$ is the total external force. The external forces are both the surface forces and the body forces. Body forces are 'distant' forces that is acting in each point of the body. Gravity is an example of a body force. Surface forces are distributed along the surface of a body or of an internal part of the body. If $\boldsymbol{\sigma}$ is the stress tensor and $\vec{b}$ is the vector acceleration of the body [m/s^2], then Equation (B.8) transforms to

$$\frac{\mathrm{d}}{\mathrm{d}t} \underbrace{\int_V \rho \vec{u} \mathrm{d}V}_{\text{momentum}} = \underbrace{\int_{\partial V} \boldsymbol{\sigma} \cdot \vec{n} \mathrm{d}S}_{\text{surface force}} + \underbrace{\int_V \rho \vec{b} \mathrm{d}V}_{\text{body force}}. \tag{B.9}$$

By applying Reynolds transport theorem on the left hand side the equation, the equation transforms to

$$\int_V \frac{\partial}{\partial t} (\rho \vec{u}) \mathrm{d}V + \int_{\partial V} (\rho \vec{u}) \vec{u} \cdot n \mathrm{d}S = \int_{\partial V} \boldsymbol{\sigma} \cdot \vec{n} \mathrm{d}S + \int_V \rho \vec{b} \mathrm{d}V. \tag{B.10}$$

This is the equation of motion in the integral form. If the Gauss theorem is applied on the surface integrals and every thing is moved to the left hand side, then the equation can be written as

$$\int_V \left(\frac{\partial}{\partial t} (\rho \vec{u}) + \nabla \cdot (\rho \vec{u} \vec{u}) - \nabla \cdot \boldsymbol{\sigma} - \rho \vec{b} \right) \mathrm{d}V = 0. \tag{B.11}$$

Since the volume V is arbitrary the integrand can be removed. The differential form of the equation of motion then can be written as

$$\frac{\partial}{\partial t}(\rho\vec{u}) + \nabla\cdot(\rho\vec{u}\vec{u}) = \nabla\cdot\boldsymbol{\sigma} + \rho\vec{b}. \tag{B.12}$$

B.3 The energy equation

The first law of thermodynamics can be written as

$$\frac{\mathrm{d}}{\mathrm{d}t}(K+E) = W + Q. \tag{B.13}$$

This law states that the time rate of change to the total energy of a system, is equal to the sum of the heat transfer and the work done to the system per time unit. K is total kinetic energy, E is total internal energy, W is work and Q is heat transfer. Equation B.13 can then be written as

$$\begin{aligned}\frac{\mathrm{d}}{\mathrm{d}t}\Bigg(\underbrace{\frac{1}{2}\int_V \rho\vec{u}\cdot\vec{u}\mathrm{d}V}_{\text{kinetic energy}} + \underbrace{\int_V \rho e\mathrm{d}V}_{\text{internal energy}}\Bigg) = \\ \underbrace{\int_{\partial V}\vec{n}\cdot\boldsymbol{\sigma}\cdot\vec{u}\mathrm{d}S}_{\text{work by surface forces}} + \underbrace{\int_V \rho\vec{b}\cdot\vec{u}\mathrm{d}V}_{\text{work by body forces}} - \underbrace{\int_{\partial V}\vec{q}\cdot\vec{n}\mathrm{d}S}_{\text{heat transfer}} + \underbrace{\int_V \rho h\mathrm{d}V}_{\text{internal heat source}}.\end{aligned} \tag{B.14}$$

In this equation e is the internal energy per unit mass, $\vec{q}$ is the heat transfer out of the system and h is the internal heat source. Chemical reactions are an example of an internal heat source and both translational, rotational and vibrational energy are included in the internal energy. By applying Reynolds transport theorem on the left hand side of the equation it transforms the energy equation on the integral form

$$\begin{aligned}\frac{1}{2}\int_V \frac{\partial}{\partial t}(\rho\vec{u}\cdot\vec{u})\mathrm{d}V + \frac{1}{2}\int_{\partial V}\rho(\vec{u}\cdot\vec{u})\vec{u}\cdot\vec{n}\mathrm{d}S + \int_V \frac{\partial}{\partial t}(\rho e)\mathrm{d}V + \int_{\partial V}(\rho e)\vec{u}\cdot\vec{n}\mathrm{d}S = \\ \int_{\partial V}\vec{n}\cdot\boldsymbol{\sigma}\cdot\vec{u}\mathrm{d}S + \int_V \rho\vec{b}\cdot\vec{u}\mathrm{d}V - \int_{\partial V}\vec{q}\cdot\vec{n}\mathrm{d}S + \int_V \rho h\mathrm{d}V.\end{aligned} \tag{B.15}$$

If the Gauss theorem is applied on the surface integrals and every thing is moved to the left hand side, then the equation can be written as

$$\begin{aligned}\int_V \Bigg(\frac{1}{2}\frac{\partial}{\partial t}(\rho\vec{u}\cdot\vec{u}) + \frac{1}{2}\nabla\cdot(\rho\vec{u}(\vec{u}\cdot\vec{u})) + \frac{\partial}{\partial t}(\rho e) + \nabla\cdot(\rho e\vec{u}) - \\ \nabla\cdot(\boldsymbol{\sigma}\cdot\vec{u}) - \rho\vec{b}\cdot\vec{u} + \nabla\cdot\vec{q} - \rho h\Bigg)\mathrm{d}V = 0.\end{aligned} \tag{B.16}$$

Since the volume V is arbitrary the integrand can be removed. The equation then reduces to

$$\frac{\partial}{\partial t}E + \nabla \cdot (E\vec{u}) = \nabla \cdot (\boldsymbol{\sigma} \cdot \vec{u}) + \rho\vec{b} \cdot \vec{u} - \nabla \cdot \vec{q} + \rho h. \tag{B.17}$$

This is the differential form for the energy equation and $E \equiv \rho e + \frac{1}{2}\rho\vec{u} \cdot \vec{u}$.

B.4 The equations of gas dynamics

Section B.1, B.2 and B.3 give a brief derivation of the equations for conservation of mass, momentum and energy. The equations were

$$\begin{aligned} \frac{\partial \rho}{\partial t} + \nabla \cdot (\rho\vec{u}) &= 0 \\ \frac{\partial}{\partial t}(\rho\vec{u}) + \nabla \cdot (\rho\vec{u}\vec{u}) &= \nabla \cdot \boldsymbol{\sigma} + \rho\vec{b} \\ \frac{\partial}{\partial t}E + \nabla \cdot (E\vec{u}) &= \nabla \cdot (\boldsymbol{\sigma} \cdot \vec{u}) + \rho\vec{b} \cdot \vec{u} - \nabla \cdot \vec{q} + \rho h \end{aligned} \tag{B.18}$$

The stress tensor in the equations for conservation of momentum and energy, can be written as $\boldsymbol{\sigma} = -p\mathbf{I} + \mu(\nabla\vec{u} + (\nabla\vec{u})^T)$, where $\mathbf{I}$ is the identity matrix and p is the pressure [Pa]. If one assumes no body forces (i.e. $\vec{b} = 0$), no heat transfer (i.e. $\vec{q} = 0$), no internal heat generation (i.e. $h = 0$) and no friction (i.e. $\mu = 0$), then the equations are reduced to

$$\begin{aligned} \frac{\partial \rho}{\partial t} + \nabla \cdot (\rho\vec{u}) &= 0 \\ \frac{\partial}{\partial t}(\rho\vec{u}) + \nabla \cdot (\rho\vec{u}\vec{u} + p\mathbf{I}) &= 0 \\ \frac{\partial}{\partial t}E + \nabla \cdot ((E + p)\vec{u}) &= 0 \end{aligned} \tag{B.19}$$

because $\nabla \cdot (\boldsymbol{\sigma} \cdot \vec{u}) = \nabla \cdot (-p\mathbf{I} \cdot \vec{u}) = \nabla \cdot (p\vec{u})$. These are the conservative form of the homogeneous Euler equations for a compressible and inviscid flow. In only one space dimension these equations are further reduced to

$$\begin{aligned} \frac{\partial}{\partial t}\rho + \frac{\partial}{\partial x}(\rho u) &= 0 \\ \frac{\partial}{\partial t}(\rho u) + \frac{\partial}{\partial x}(\rho u^2 + p) &= 0 \\ \frac{\partial}{\partial t}E + \frac{\partial}{\partial x}((E + p)u) &= 0 \end{aligned} \tag{B.20}$$

and $E = \rho e + \frac{1}{2}\rho u^2$.

Appendix C

Thermodynamic data

Table C.1 gives an overview of the thermodynamic data used in the simulations with RCMLAB. The data are based on SuperSTATE and Reference [16, 45, 56]. Some of the entries in the table are approximated values. These approximations are made from the mole fractions of the different elements in the gas mixture.

Table C.1: An overview of the thermodynamic data used by RCMLAB for the various gas mixtures. μ_0 is the reference viscosity at room temperature, γ is the ratio of the specific heats, c_v is the specific heat at constant volume and q is the heat of reaction.

Fuels		Unburned			Burned			Heat of reaction
Type	Concentration (% volume)	μ_0 [N·s/m]	γ	c_v [kJ/(kg·K)]	μ_0 [N·s/m]	γ	c_v [kJ/(kg·K)]	q [J/kg]
H_2	20.0	$1.48{\cdot}10^{-5}$	1.400	884.2	$1.55{\cdot}10^{-5}$	1.263	1238.2	$2.40{\cdot}10^{6}$
H_2	30.0	$1.34{\cdot}10^{-5}$	1.401	997.0	$1.47{\cdot}10^{-5}$	1.244	1421.6	$3.63{\cdot}10^{6}$
H_2	35.0	$1.30{\cdot}10^{-5}$	1.401	1065.2	$1.42{\cdot}10^{-5}$	1.245	1516.3	$3.85{\cdot}10^{6}$
H_2	50.0	$1.14{\cdot}10^{-5}$	1.402	1340.5	$1.32{\cdot}10^{-5}$	1.262	1839.8	$3.93{\cdot}10^{6}$
C_3H_8	4.0	$1.82{\cdot}10^{-5}$	1.368	767.7	$1.54{\cdot}10^{-5}$	1.248	1198.9	$3.01{\cdot}10^{6}$
CH_4	9.5	$1.78{\cdot}10^{-5}$	1.332	827.5	$1.53{\cdot}10^{-5}$	1.238	1376.3	$2.62{\cdot}10^{6}$

Bibliography

[1] C. Clanet and G. Searby, On the ”tulip flame” phenomenon, Combustion and flame, (1996), 105, 225-238.

[2] H. Guénoche, in: G. H. Markstein (Ed.), Non-steady flame propagation, Pergamon, Oxford, 1964.

[3] C.M. Guirao, R. Knystautas, J. Lee, W. Benedick, M. Berman, Hydrogen-air detonations, Proc. Combust. Inst., 19th, pages 583-590, 1982.

[4] M. Kaneshige, J.E. Shepherd, Detonation database, Technical Report FM97-8, GALCIT, July 1997. Electronic version at http://www.galcit.caltech.edu/detn_db/html.

[5] R. P. Lindstedt, H. J. Michels, Deflagration to detonation transitions and strong deflagrations in alkane and alkene air mixtures, Combust. Flame, 76 (2) (1989) 169-181.

[6] I. O. Moen, D. Bjerketvedt, T. Engebretsen, A. Jenssen, B. H. Hjertager, J. R. Bakke, Transition to detonation in a flame jet, Combust. Flame, 75 (1989) 297-308.

[7] R. K. Kumar, G. W. Koroll, M. Heitsch and E. Studer, Carbon monoxide - hydrogen combustion characteristics in severe accident containment conditions, Nuclear energy agency, Committee on the safety of nuclear installations, 2000.

[8] J. Modic, Carbone monoxide and COHb concentration in blood in various circumstances, Energy and Buildings, 35 (2003) 903-907.

[9] T. IIjima and T. Takeno, Effects of temperature and pressure on burning velocity, Combust. Flame, 65 (1986) 35-43.

[10] N. Peters, Turbulent combustion, Cambridge University Press, Cambridge, 2000.

[11] N. Peters, Length scales in laminar and turbulent flames, Numerical approaches to combustion modeling, American Institute of Aeronautics and Astronautics, 1991, 155-182, Washington, DC.

[12] S. B. Dorofeev, Flame acceleration and DDT in gas explosions, Journal de Physique, IV, 12, pr.7: pages 3-10, 2002.

[13] C. R. L. Bauwens, L. Bauwens and I. Wierzba, Analysis and Simulation of Accelerating Flames, 41st AIAA/ASME/SAE/ASEE Joint Propulsion Conference & Exhibit, 2005.

[14] J. P. Laviolette, A. J. Higgins, J. H. S. Lee, Interaction between a flame and a rarefaction, Proc. of the 19th ICDERS, 2003.

[15] H. P. Langtangen, Lecture notes: Mathematical modeling of flow, heat transfer and deformation, University of Oslo, Oslo, 2003.

[16] F. M. White, Viscous fluid flow, McGraw-Hill, 1991.

[17] D. Bjerketvedt and A. Mjaavaten, Simulation of gas dynamic flow with a matlab version of the random choice method (RCM), Proceedings of the Nordic conference, 2001.

[18] D. Bjerketvedt, K. Vaagsaether, K. Kristoffersen, A. Mjaavatten, G. Thomas and R. Bambrey, Simulation of gas explosions with a Matlab version of the random choice Method (RCM), Journal de Physique IV France **12**, 247-251, 2002.

[19] D. Bjerketvedt, K. Kristoffersen, K. Vaagsaether, A. Mjaavatten and G. Thomas, A method for estimating the burning velocity in a tube by using experimental pressure records and the 1-D RCMLAB code, Combustion science and technology, 2004.

[20] D. Bjerketvedt, Re-Initiation of detonation across an inert region, PhD-Thesis, Norwegian University of Science and Technology, Norway, 1985.

[21] D. Bjerketvedt, J. R. Bakke and K. van Wingerden, Gas explosion handbook, Journal of Hazardous Materials, volume 52, pages 1-150, 1997.

[22] D. Bjerketvedt and A. Mjaavatten, A hydrogen-air explosion in a process plant: A case history, Presented at the International Conference oh Hydrogen Safety, Pisa, Italia, 2005.

[23] K. Kristoffersen, K. Vaagsaether, D. Bjerketvedt and G. O. Thomas, Propane-air pipe explosion experiments. Data for estimation of 1-D burning velocity in slow regimes, Experimental thermal and fluid science 28, 723-728, 2004.

[24] K. Kristoffersen, Gas explosions in process pipes, PhD-Thesis, Norwegian University of Science and Technology and Telemark University Collage, Norway, 2004.

[25] SuperSTATE, Version 2.1, Combustion Dynamics Ltd., 1998.

[26] Octave, University of Wisconsin, Electronic version at http://www.gnu.org/software/octave/.

[27] MATLAB, The MathWorks, Inc, Electronic version at http://www.mathworks.com/.

[28] OpenSSH, The OpenBSD Project, Electronic version at http://www.openssh.com/.

[29] S. K. Godunov, A finite difference method for the computation of discontinuous solutions of the equations of fluid dynamics,(Russian) Mat. Sb. (N.S.) 47 (89), 271-306, 1959.

[30] J. Glimm, Solutions in the large for nonlinear hyperbolic systems of equations, communications of pure and applied mathematics 18, 695-715, 1965.

[31] J. Glimm, J. Grove and Y. Zhang, Numerical calculation of Rayleigh-Taylor and Richtmyer-Meshkov instabilities for three dimensional axi-symmetric flows in cylindrical and spherical geometries. Preprint, SUNY at Stony Brook, 1999.

[32] J. Glimm, M. J. Graham, J. Grove, X. L. Li, T. M. Smith, D. Tan, F. Tangerman and Q. Zhang, Front tracking in two and three dimensions, Computers & Mathematics with Applications, Volume 35, Issue 7, Pages 1-11, 1998.

[33] A.J. Chorin, Random choice solutions of hyperbolic systems, Journal of computational physics 22, 517-533, 1976.

[34] A.J. Chorin, Random choice methods with applications to reacting gas flow, Journal of computational physics 25, 253-272, 1977.

[35] T. Saito and I. I. Glass, Application of random-choice method to problems in shock and detonation-wave dynamics, Technical report UITAS 240, Institute for aerospace studies, University of Toronto, 1979.

[36] E. F. Toro, Riemann solvers and numerical Methods for fluid dynamics, Springer-verlag, Berlin, 1999.

[37] J. Gottlieb, Random-choice method for solving one-dimensional unsteady flows in ducts, shock tubes and blast-wave simulators, AC-Laboratorium Spiez, Switzerland, 1986.

[38] R. J. Leveque, Finite volume methods for hyperbolic problems, Cambridge university press, Cambridge, 2002.

[39] J. M. Hammersley and D. C. Handscombe, Monte Carlo Methods, Chapman and Hall, 1964.

[40] F. A. Williams, Combustion theory, Perseus books, Massachusetts, 1985.

[41] D. Damköler, Der einfluß der turbulenz auf die flammengeschwindigkeit in gasgemischen, Z. Elektrochem. 46, 601-652, 1940.

[42] G. A. Sod, A numerical study of converging cylindrical shock, Journal of fluid mechanics, vol. 83, pages 785-794, 1977.

[43] E. R. G. Eckert and R.M. Drake, Analysis of heat and mass transfer, 3rd edition, Hemisphere publishing corporation, New York, 1987.

[44] H. Schlichting and K. Gersten, Boundary Layer Theory, 8th edn, Springer-Verlag, Berlin, 2000.

[45] W. M. Kays and M. E. Crawford, Convective heat and mass transfer, 3rd edition, McFraw-Hill, New York, 1993.

[46] W. Sutherland, The viscosity of gases and molecular force. Philosophical Magazine, Vol. 5, pages 507-531, 1893.

[47] O. Reynolds, On the extent and action of the heating surface for steam boilers, Manchester Literary and Philosophical Society, Vol 14, pages 7-12, 1874.

[48] Verein Deutscher Ingenieure VDI, VDI Heat Atlas, English edition, VDI-Verlag GmbH, Düsseldorf, Germany, 1993.

[49] J. Warnatz, U. Maas and R.W.Dibble, Combustion, 3rd edition, Springer-Verlag Berlin Heidelberg, Germany, 2001.

[50] I. Glassman, Combustion, second edition, Academic press inc., San Diego, California, 1987.

[51] R. Knystautas, C. Guirao, J.H. Lee, and A. Sulmistras. Measurement of cell size in hydrocarbon-air mixtures and predictions of critical tube diameter, critical initiation energy, and detonability limits. In Prog. Astronaut. Aeronaut., volume 94, pages 23-37, 1984.

[52] R. Knystautas, J.H. Lee, I. Moen and H. GG. Wagner, Direct initiation of spherical detonation by a hot turbulent gas jet, Proc. Comb. Inst., 17th, pages 1235-1245, 1978.

[53] I.O. Moen, J.W. Funk, S.A. Ward, G.M. Rude, and P.A. Thibault. Detonation length scales for fuel-air explosives. In Prog. Astronaut. Aeronaut., volume 94, pages 55-79, 1984.

[54] H.D. Beeson, R.D. McClenagan, C.V. Bishop, F.J. Benz, W.J. Pitz, C.K. Westbrook, and J.H.S. Lee. Detonability of hydrocarbon fuels in air. In Prog. Astronaut. Aeronaut., volume 133, pages 19-36, 1991.

[55] H. Le Chatelier and O. Boudouard, Limits of flammability of gaseous mixtures, Bull. Soc. chim. (Paris), 19, 483-488, 1898.

[56] G. L. Borman and K. W. Ragland, Combustion Engineering, McGraw-Hill, 1998.

[57] S. Kondo, K. Takizawa, A. Takahashi and K. Tokuhashi, Extended Le Chatelier's Formula for Carbon Dioxide Dilution Effect on Flammability Limits, Journal of Hazardous Materials, In Press, 2006.

[58] R. S. Chue, J. F. Clarke and J. H. Lee, Chapman-Jouguet deflagrations, Proc. The Royal Society of London, Series A, pages 607-623, 1993.

[59] J. M. Austin and J. E. Shepherd, Detonations in hydrocarbon fuel blends, Comb. Flame, 132, (2003), 73-90.

[60] J. M. Austin, The role of instability in gaseous detonation, PhD-Thesis, California Institute of Technology, California, 2003.

[61] R. Starke and P. Roth, An experimental investigation of flame behavior during cylindrical vessel explosions, Comb. Flame, 66, (1986), 249-259.

[62] J. Buckmaster, P. Calvin, A. Liñán, M. Matalon, N. Peters, G. Sivavshinsky and F. A. Williams, Combustion theory and modeling, Proc. Comb. Inst., 30th, (2005), 1-19.

[63] W. Breitung, C. K. Chan, S. B. Dorofeev, A. Eder, B. E. Gelfand, M. Heitsch, R. Klein, A. Malliakos, J. E. Shepherd, E. Studer and P. Thibault, Flame Acceleration and Deflagration to Detonation Transition in Nuclear Safety, State-of-the-Art Report by a Group of Experts, OECD Nuclear Energy Agency NEA/CSNI/R7, 2000.

[64] J. Chomiak, Turbulent reacting flows, Internal report 00/2, Chalmers university of technology, Göteborg, 2000.

[65] D. L. Chapman, On the rate of explosion in gases, Philos. Mag. 47, 90-104, 1899.

[66] E. Jouguet, On the propagation of chemical reactions in gases, J. de mathematiques pures et appliquers 6, 347, 1905.

[67] Y. B. Zeldovich, On the theory of of the propagation of detonation in gaseous systems, Zhur. Eksp. Teor. Fiz. 10, 542-568, 1940.

[68] Ya. B. Zeldovich,V. B. Librovich, G. M. Makhviladze and G. I. Sivashinsky, On the development of detonation in a non-uniformly preheated gas, Astronaut Acta, 15, pages 313-321, 1970.

[69] Ya. B. Zeldovich, S. M. Kogarko and N. N. Simonov, An experimental investigation of spherical detonation of gases, Sov. Phys.-Tech. Phys., 1, pages 1689-1713, 1956.

[70] J. von Neumann, Theory of detonation waves, OSRD Rep. No. 549, 1942.

[71] W. Döring, On detonation processes in gases, Ann. phys. 43, 421-436, 1943.

[72] J. H. S. Lee, Dynamic parameters of gaseous detonations, Annual review of fluid mechanics, Vol. 16: 311-336, 1984.

[73] J. H. Lee, R. Knystautas and C. K. Chan, Turbulent flame propagation in obstacle-filled tubes, Proc. Comb. Inst., 20th, pages 1663-1672, 1984.

[74] J. H. Lee, R. Knystautas and N. Yoshikawa, Photochemical initiation of gaseous detonations, Astronautica Acta, 5, pages 971-982, 1978.

[75] J. H. S. Lee, R. Knystautas and A. Freiman, High speed turbulent deflagrations and transition to detonation in H_2-air mixtures, Combustion and flame, 56, pages 227-239, 1984.

[76] P. A. Urtiew and A. K. Oppenheim, Experimental observations of the transition to detonation in an explosive gas, Proceedings of the Royal Society of London. Series A, Vol. 295, pages 13-28, 1966.

[77] K. I. Shchelkin and Y. K. Torshin, Gas dynamics of combustion, Mono book corp., Baltimore, 1965.

[78] C. K. Westbrook, Chemical kinetics of hydrocarbon oxidation in gaseous detonations, Combustion and Flame. Vol. 46, 191-210, 1982.

[79] S. S. Shy, W. J. Lin and K. Z. Peng, High-intensity turbulent premixed combustion: General correlations of turbulent burning velocities in a new cruciform burner, Proc. Comb. Inst., 28th, 561-568, 2000

[80] R. G. Abdel-Gayed, D. Bradley and M. Lawes, Turbulent burning velocities - a general correlation in terms of straining rates, Proc. Royal Soc. London, A 414, 389-413, 1987.

[81] R. G. Abdel-Gayed, D. Bradley, M. N. Hamid and M. Lawes, Lewis number effects on turbulent burning velocity, Proc. Comb. Inst., 20th, pages 505-512, 1984.

[82] D. Bradley, How fast can we burn?, Proc. Comb. Inst., 24th, 247-262, 1992.

[83] D. Bradley, A. K. C. Lau and M. Laws, Flame stretch rate as a determinant of turbulent burning velocity, Phil. Trans. R. Soc. London, A 338, 359-387, 1992.

[84] E. H. W. Schmidt, H. Steinicke and U. Neubert, Flame and schlieren photographs of combustion waves in tubes, Proc Comb. Inst., 4th, 658-666, 1952.

[85] S. A. S. Jones and G. O. Thomas, Pressure hot-wire and laser Doppler anemometer studies of flame acceleration in long tubes, Combustion and flame, Vol. 87, 21-32, 1991.

[86] O. C. De C. Ellis, Flame movement in gaseous explosive mixtures, (Part 2), Fuel in science and practice, 7, 502, 1928.

[87] V. A. Popov, The initial propagation distance of flames in closed tubes, (In Russian), Izvest. Akad. Nauk SSSR, Otdel. Tekh Nauk 1956, No. 3, 116, 1956.

[88] A. Combe, C. Meyer and M. Thiery , Étude de la propagation des flammes dans un vase á reaction formé de deux chambres reliées par un canal, Rev. Inst. Franç. Pétrole, 13, 1435, 1958.

[89] M. W. Evens, M. D. Scheer, L. J. Schoen and E. L. Miller, A study of high velocity flames developed by grids in tubes, Proc. Comb. Inst., 3th, 168-176, 1948.

[90] I. O. Moen, S. B. Murrey, D. Bjerketvedt, A. Rinnan, R. Knystautas and J. H. Lee, Diffraction of detonation from tubes into large fuel-air explosive cloud, Proc. Comb. Inst., 19, 635-644, 1982.

[91] I. O. Moen, A. Sulmistras, G. Thomas, D. Bjerketvedt, and P.A. Thibault, Influence of cellular regularity on the behavior of gaseous detonations, Astronaut. Aeronaut., volume 106, pages 220-243, 1986.

[92] I. O. Moen, M. Donato, R. Knystautas and J. H. Lee, The influence of confinement on the propagation of detonations near the detonability limits, Proc. Comb. Inst., 18th, pages 1615-1622, 1980.

[93] I. O. Moen, Transition to detonation in fuel-air explosive clouds, Journal of Hazardous Materials, 33, pages 159-192, 1993.

[94] M. Mallard and H. Le Chatelier, Recherches experimentales et theoriques sur la combustion des mélanges gazeux explosifs, Annales de Mines, Paris series 8, 274-568, 1883.

[95] D. Dunn-Rankin and R. F. Sawyer, Tulip flames: changes in shape of premixed flames propagating in closed tubes, Experiments in fluids, 24 , 130-140, 1998.

[96] D. Dunn-Rankin, P. K. Barr and R. F. Sawyer, Numerical and Experimental study of "tulip" flame formation in a closed vessel, Proc. Comb. Inst., 21th, 1291-1301, 1986.

[97] G. D. Salamandra, T. V. Bazhenova and I. M. Naboko, Formation of detonation wave during combustion of gas in combustion tube, Proc. Comb. Inst.,7th, 851-855, 1958.

[98] A. C. Egerton, O. A. Saunders, A. H. Lefebvre and N. P. W. Moore, Some observations by schlieren technique of the propagation of flames in a closed vessel, Proc. Comb. Inst., 4th, 396-402, 1952.

[99] Y. K. Pu, J. Hu and J. Jarosinski, Detailed study of flammability limits in propane-air mixtures under gravity and micro gravity conditions, Proc. Baltic Comb. Meeting, 1, 133-136, 2005.

[100] G. H. Markstein, A shock-tube study of flame front-pressure wave interactions, Proc. Comb. Inst, 6th, 387-398, 1956.

[101] G. H. Markstein (Ed.), in: G. H. Markstein (Ed.), Non-steady flame propagation, Pergamon, Oxford, 1964.

[102] G. H. Markstein, Instability in combustion waves, Proc. Comb. Inst., 4th, 1952.

[103] F. R. S. Taylor, The instability of liquid surfaces when accelerated in a direction perpendicular to their planes,Pt. I, Proc. Royal Soc. London, A 201, 192-196, 1950.

[104] A. Pocheau and C. W. Kwon, in: Colloque de l'A.R.C. Modélisation de la combustion dans les moteurs à piston (C.N.R.S.-P.I.R.S.E.M.Ed.), Paris, p. 62, 1989.

[105] R. D. Richtmyer, Taylor instability in shock acceleration of compressible fluids, Communications in Pure and Applied Mathematics, vol. 13, 297-319, 1960.

[106] J. W. Rayleigh, Scientific papers, Vol. II, Cambridge university press, 1900.

[107] D. Thompson (Ed.), The Oxford compact English dictionary, Oxford university press, 1996.

[108] Y. N. Denisov and Y. K. Troshin, On the mechanism of detonative combustion, Proc. Comb. Inst., 8th, pages 600-610, 1960.

[109] Y. N. Denisov and Y. K. Troshin, Pulsating and spinning detonations in channels, Dokl. Akad. Nauk. S.S.S.R. 125, 110, 1959.

[110] Y. N. Denisov and Y. K. Troshin, Structure of gaseous detonations in channels, Z. Tech. Phys. 30, 450, 1960.

[111] B. V. Voitsekhovsky, V. V. Mitrofanov and M. E. Topchain, Structure of a detonation front in gases, Izd. Sib. Otd. Nauk. S.S.S.R., 1963.

[112] B. E. Gelfand, S. M. Frolov and M. A. Nettleton, Gaseous detonations - a selective review, Prog. Energy Combust. Sci., Vol. 17, pages 327-371, 1991.

[113] C. M. Coats, Coherent structures in combustion, Prog. Combust. Sci., Vol. 22, pages 427-509, 1996.

[114] V. V. Bychkov and M. A. Liberman, Dynamics and stability of premixed flames, Physics reports, 325, pages 115-237, 2000.

[115] P. Clavin, Dynamic behavior of premixed flame fronts in laminar and turbulent flows, Progress in Energy and Combustion Science, Volume 11, Issue 1, Pages 1-59, 1985.

[116] M. Barrére and F. A. Williams, Comparison of combustion instabilities found in various types of combustion chambers, Proc. Comb. Inst., 16th, pages 169-181, 1976.

[117] A. Liñán and F. A. Williams, Fundamental aspects of combustion, Oxford Engineering Science Series 34, Oxford University press, New York, 1993.

[118] L. Landau, On the theory of slow combustion, Acta Physicochimica, USSR, 19, pages 77-85, 1944.

[119] G. Darrieus, Propagation d'un front de flamme, unpublished works presented at La Technique Moderne in 1938 and at Congrès de Mécanigue Appliguée Paris 1945.

[120] E. E. Meskov, Instability of a shock wave accelerated interface between two gases, NASA Tech. Trans. F-13, 074, 1970.

[121] S. I. Abarzhi, K. Nishihara and J. Glimm, Rayleigh-Taylor and Richtmyer-Meshkov instabilities for fluids with a finite density ratio, Physics Letters A, Volume 317, Issues 5-6, 27, Pages 470-476, 2003.

[122] S. K. Zhdanov, Nonlinear theory of Kelvin-Helmholtz instability, Physica D: Nonlinear Phenomena, Volume 87, Issues 1-4, Pages 375-379, 1995.

[123] Lord Kelvin (W. Thomson), Hydrokinetic solutions and observations, Phil Mag. 10, pages 155-168, 1871.

[124] H. L. F. von Helmholtz , Über discontinuirliche Flüssigkeitsbewegungen, Monatsbericht Akad. Wiss. Berlin S, pages 215-228, 1868.

[125] M. S. Ruderman, L. Brevdo and R. Erdélyi, Kelvin-Helmholtz absolute and convective instabilities of, and signaling in, an inviscid fluid-viscous fluid configuration, Proceedings of the Royal Society of London, A 460, pages 847-874, 240.

[126] S. B. Dorofeev, M. S. Kuznetsov, V. I. Alekseev, A. A. Efimenko and W. Breitung, Evaluation of limits for effective flame acceleration in hydrogen mixtures, Journal of Loss Prevention in the Process Industries, Volume 14, Issue 6, Pages 583-589, 2001.

[127] S. Dorofeev, Thermal quenching and re-ignition of mixed pockets of reactants and products in gas explosions, Presented at the 31st international symposium of combustion, Germany, 2006.

[128] S. Dorofeev, M. Kuznetsov, V. Alekseev, A. Efimenko and W. Breitung, Evaluation of limits for effective flame acceleration in hydrogen mixtures, Journal of Loss Prevention in the Process Industries, 14, pages 583-589, 2001.

[129] S.R. Tieszen, M.P. Sherman, W.B. Benedick, J.E. Shepherd, R. Knystautas, and J.H.S. Lee. Detonation cell size measurements in hydrogen-air-steam mixtures. In Prog. Astronaut. Aeronaut., volume 106, pages 205-219, 1986.

[130] G. Ciccarelli, T. Ginsberg, J. Boccio, C. Economos, K. Sato, and M. Kinoshita. Detonation cell size measurements and predictions in hydrogen-air-steam mixtures at elevated temperatures. Combust. Flame, 99(2): pages 212-220, 1994.

[131] W.B. Benedick, R. Knystautas, and J.H.S. Lee. Large-scale experiments on the transmission of fuel-air detonations from two-dimensional channels. In Prog. Astronaut. Aeronaut., volume 94, pages 546-555, 1984.

[132] V. N. Gamezo, T. Ogawa and E. S. Oran, Numerical simulations of flame propagation and DDT in obstructed channels filled with hydrogen-air mixture, Presented at the 31st international symposium of combustion, Germany, 2006.

[133] P. Thibault, Y. K. Liu, C. Chan, J. H. Lee, R. Knystautas, C. Guirao, B. Hjertager and K. Fuhre, Transmission of an explosion through an orifice, Proc. Comb. Inst, 19th, pages 599-606, 1982.

[134] M. Kuznetsov, V. Alekseev, Y. Yankin and S. Dorofeev, Slow and fast deflagrations in hydrocarbon-air mixtures, Combustion Science and Technology, 174, pages 157-172, 2002.

[135] M. Kuznetsov, V. Alekseev, I. Matsukov and S. Dorofeev, DDT in hydrogen-oxygen mixtures in smooth tubes, In: Proceedings of the 19th International Colloquium on the Dynamics of Explosions and Reactive Systems, Hakone, Japan, 2003.

[136] M. Kuznetsov, V. Alekseev, I. Matsukov and S. Dorofeev, DDT in a smooth tube filled with a hydrogen-oxygen mixture, Shock waves 14, 3, pages 205-215, 2005.

[137] M. Kuznetsov, G. Ciccarelli, S. Dorofeev, V. Alekseev, Yu. Yankin and T. H. Kim, DDT in methane-air mixtures, Shock waves, 12, pages 215-220, 2002.

[138] C. Chan, I. O. Moen and J. H. S. Lee, Influence of confinement on flame acceleration due to repeated obstacles, Combustion and flame, 49, pages 27-39, 1983.

[139] V. I. Alekseev, M. S. Kuznetsov, Yu. G. Yankin and S.B. Dorofeev, Experimental study of flame acceleration and the deflagration-to-detonation transition under conditions of transverse venting, Journal of Loss Prevention in the Process industries, 14, pages 591-596, 2001.

[140] F. Tamanini and J. L. Chaffee, Turbulent vented gas explosions with and without acoustically-induced instabilities, Proc. Comb. Inst., 24th, pages 1845-151, 1992.

[141] J. C. Leyer and N. Manson, Development of vibratory flame propagation in short closed tubes and vessels, Proc. Comb. Inst, 13th, pages 551-558, 1970.

[142] G. O. Thomas and R. J. Bambrey, Some observations of the controlled generation and onset of detonation, Shock waves, 12, pages 13-21, 2002.

[143] M. Berthelot and P. Vielle, Sur la vitesse de propagation des phènoménes explosivs dans les gaz, C. R. Acad. Sci., Paris 94, pages 101-108, seance du 16 Janvier; pages 822-823, seance du 27 Mars; 95, pages 151-157, seance de 24 Juillet, 1882.

[144] G. D. Roy, S. M. Frolov, A. A. Borisov and D. W. Netzer, “Pulse detonation propulsion: challenges, current status and future perspective”, Progress in Energy and Combustion Science, 30, pages 545-672, 2004.

[145] P. D. O. Connor, L. N. Long and J. B. Anderson, The direct Simulation of detonations, Invited paper: AIAA/ASME/SAE/ASEE Joint Propulsion Conference, Sacramento CA, 2006.

[146] A. M. Bartenev and B. E. Gelfand, Spontaneous initiation of detonations, Progress in Energy and Combustion Science, 26, 1, pages 29-55, 2000.

[147] H. Steen and K. Schampel, Experimental investigations on the run-up distance of gaseous detonations in large pipes, 4th International Symposium on Loss Prevention and Safety Promotion in Process Industries, 82, pages E23-E33, 1983.

[148] J. Li, W. H. Lai, K. Chung and F. K. Lu, Uncertainty analysis of deflagration-to-detonation run-up distance, Shock Waves, 14, 5, pages 413-420, 2005.

[149] M. Hattwig, Detonationsanlaufstrecken von gasgemischen in Rohren großen druchmessers, Amts- und Mitteilungsblatt der Bundesanstalt für Materialprüfung (BMA), Berlin, 10, pages 274-278, 1980.

[150] W. Bartknecht, Brenngas- und staubexplosionen forschungsbericht F 49 des bundesinstitus für arbeitsschuntz (now: Bundesanstalt für unfallforschung und arbeitsshuntz, Dortmund), 1971.

[151] L. E. Bollinger, M. C. Fong and R. Edse, Experimental measurements and theoretical analysis of detonations induction distances, ARS-Journal, 31, pages 588-595, 1961.

[152] L. E. Bollinger, Experimental detonation velocities and induction distance in hydrogen air mixture, AIAA-Journal, 2, pages 131-133, 1964.

[153] L. E. Bollinger, G. C. Smith, F. J. Tomazic and R. Edse, Formation of detonation waves in flowing hydrogen oxygen and Methane oxygen mixtures, AIAA-Journal, 4, pages 1773-1776, 1966.

[154] I. Ginsburgh and W. L. Bulkly, Hydrocarbon-air detonations ... industrial aspects, Chem. Engng. Progr., Vol 59, pages 82-86, 1963.

[155] W. Baumann and H. Gg. Wagner, EinfiuSS der frischgasströmung auf die beschleunigungen von flammen und den anlaufvorgang von detonationen für electrochemie, 65, pages 895-898, 1961.

[156] K. Chatrathi, J. E. Going and B. Grandestaff, Flame propagation in industrial scale piping, Process Safety Progress, 20(4), 286-294, 2001.

[157] L. He, A scaling analysis of the critical conditions for a deflagration-to-detonation transition, Combustion Theory and Modeling, 4, pages 107-122, 2000.

[158] J. E. Sheperd and J. H. S. Lee, On the transition from deflagration to detonation, pages 439-487 in: Major research topics in combustion, M. Y. Hussaini, A. Kumar and R. G. Voigt, Springer Verlag, New York, 1992.

[159] A. A. Vasiliev, Geometric limits of gas detonation propagation, Fiz. Goreniya. Vzryre 18, pages 132-136, 1982.

[160] O. Peraldi, R. Knystautas and J. H. Lee, Proc. comb. Inst, 21th, pages 1629-1637, 1986.

[161] A. Teodorczyk, J. H. S. Lee and R. Knystautas, Propagation mechanism of quasi-detonations, Proc. Comb. Inst., 22th, pages 1723-1731, 1988.

[162] V. V. Mitrofanov and R. I. Soloukhin, The diffraction of multi front detonation waves, Sov. Phys.-Dokl. 9, 1055, 1965.

[163] D. J. Mackay, S. B. Murray and I. O. Moen, Flame-jet igniton of large fuel-air clouds, Proc. Comb. Inst., 22th, pages 1339-1353, 1988.

[164] A. Üngüt and P. J. Shuff, Deflagration to detonation transition from a venting pipe, Combustion Science and Technology, Vol. 63, pages 75-87, 1989.

[165] FLACS, A FLame ACceleration Simulator, Electronic information at http://www.gexcon.com.

[166] EXSIM, Computational fluid dynamic analysis of combustion hazards, Electronic information at http://www.exsim.com.

[167] AutoReaGas, Software for modeling of gas explosions and subsequent blast effects, Electronic information at http://www.century-dynamics.com/index.htm.

[168] D. B. Spalding, The Influences of Laminar Transport and Chemical Kinematics on the Time-Mean Reaction Rate in a Turbulent Flame, Proc. Comb. Inst., 17th, pages 431-440, 1978.

[169] D. Veynante, Large eddy simulation for turbulent combustion, Proc. European Combustion Meeting, CD-rom, 2005.

[170] D. Veynante and L. Vervisch, Turbulent combustion modeling, Progress in Energy and Combustion Science, 28, pages 193-266, 2002.

[171] J. Janicka and A. Sadiki, Large eddy simulation of turbulent combustion systems, Proc. Comb. Inst., 30 th, Issue 1, pages 537-547, 2005.

[172] C. J. Lea and H. S. Ledin, A review of the state-of-the-art in gas explosion modeling, Health & safety Laboratory, Fire and explosion group, Hampur Hill, Buxton, SK179JN, 2002.

[173] E. Salzano, F. S. Marra, G. Russo, J. H. S. Lee, Numerical simulation of turbulent gas flames in tubes, Journal of Hazardous Materials, A95, pages 233-247, 2002.

[174] N. R. Popat, C. A. Catlin, B. J. Arntzen, R. P. Lindstedt, B. H. Hjertager, T. Solberg, O. Saeter and A. C. Van den Berg, Investigations to improve and assess the accuracy of computational fluid dynamic based explosion models, Journal of Hazardous Materials, Volume 45, pages 1-25, 1996.

[175] European Industrial Gases Association (EIGA), Hydrogen transportation pipelines, IGC Document 121/04/E.

[176] P. Kinsmann and J. Lewis, Report on a second study of pipeline accidents using the Health and Safety Executive's risk assessment programs MISHAP and PIPERS, Health and Safety Executive [HSE] Research Report, 063, 2002.

[177] D. S. Burgess and M. G. Zabetakis, "Detonation of a flammable cloud following a propane pipeline break. The December 9, 1970, Explosion In Port Hudson, MO.", U.S. Bureau of Mines, Washington, 1973.

[178] Statens forvaltningstjeneste - Informasjonsforvaltning (In Norwegian), Hydrogen som fremtidens energibærer, Norges offentlige utredninger (NOU), 11 , 2004.

[179] Hydrogen and fuel cells in Norway - Who's who ?, Birkebeinerlaugets bedriftsutvikling (BBU): Edited by D. Sanne, 1st Edition, 2006.

[180] IEA Agreement on the production and utilization of hydrogen, International energy agency (IEA), Annual report: Edited by M. R. de Valladares, 2005.

[181] HySafe, Safety of Hydrogen as an Energy Carrier, Electronic information at http://www.hysafe.org/.

[182] HySafe, HySafe 1st Periodic Report, Executive Summary, (http://www.hysafe.org/), 2005.

[183] J. P. Longwell, E. S. Rubin and J. Wilson, Coal: Energy for the future, Progress in Energy and Combustion Science, Volume 21, Issue 4, pages 269-360, 1995.

[184] Mark J. Prins, Krzysztof J. Ptasinski and Frans J.J.G. Janssen, From coal to biomass gasification: Comparison of thermodynamic efficiency, Energy (In Press), Corrected Proof, 2006.

[185] J. L. Alcock, L. C. Shirvill, and R. F. Cracknell, Compilation of existing safety data on hydrogen and comparative fuels, Report: EIHP - Contract N° ENK6-CT2000-00442, 2001.

[186] G. A. Karim, I. Wierzba and S. Boon, Some considerations of the lean flammability limits of mixtures involving hydrogen, International Journal of Hydrogen Energy, Volume 10, Issue 2, pages 117-123, 1985.

[187] K. T. Løyland, In Norwegian: Utredning av eksplosjonsfare for ovnsgass ved ER-AMET Norway AS, Master-thesis, Telemark University College, Siv-09-05, 2005.

[188] D. C. Wilcox, Basic Fluid Mechanics, 2nd Edition, D C W Industries, 2000.